Time-optimized Radio Frequency pulse design within hardware and sequence constraints for multiband MRI

Abo Seada, Samy

Awarding institution:
King's College London

Time-optimized Radio Frequency pulse design within hardware and sequence constraints for multiband MRI

Samy Abo Seada

A thesis submitted in partial fulfilment of the requirement
for the degree of **Doctor of Philosophy** of **King's College London**

September 2018
School of Biomedical Engineering & Imaging Sciences
King's College London

Abstract

Over the past few decades Magnetic Resonance Imaging (MRI) has become a clinically important medical imaging modality, thanks to its superior soft tissue contrast over computed tomography (CT), and the benefit of imaging deep anatomies which is challenging with ultrasound technology. In addition, unlike CT and PET it does not make use of ionizing radiation. This makes MRI well-suited for at-risk patient populations, as well as an indispensable modality for healthcare research.

Unfortunately MRI is also expensive, largely due to the cost of hardware involved and its maintenance. Adding to this problem, MR acquisition times are typically longer than comparable CT examinations, which can make MRI scans uncomfortable experiences, and economically speaking decreases patient throughput. Both of these disadvantages are addressed by reducing MR scan durations, where parallel imaging methods such as SENSE, GRAPPA and compressed sensing have had success in the past decade. Acceleration in parallel imaging however comes at a cost in signal-to-noise ratio (SNR) as MR images are formed from undersampled data.

Multiband techniques (a.k.a. Simultaneous Multi-Slice) reduce scan time by exciting and acquiring signal from multiple slices simultaneously, and consequently using multiple receiver coils for unfolded reconstruction. This type of acceleration has an SNR benefit over parallel imaging, for a fixed echo-time, as when no in-plane undersampling is used the SNR cost is solely due to multi-channel reconstruction. However challenges in multiband imaging arise in the design of multiband RF pulses, which can take significantly longer to transmit and consequently lead to lower acquired signal, due to relaxation. Exciting multiple slices also places significant demand on current hardware, in terms of coping with higher RF power, and higher frequency demands for both RF and gradient systems. Upgrading hardware is not always an option, due to the cost involved. In addition, higher RF power requirements for exciting multiple slices can also lead to increased patient heating, measured as specific absorption rate (SAR), which needs to be considered for MRI safety.

The work presented in this thesis seeks to improve multiband RF pulse design techniques by three means; firstly, we demonstrate practical hardware considerations for implementing time-optimized multiband pulses. This includes considerations for RF transmission

hardware for phase-optimized, time-shifted and root-flipped multiband RF pulses, as well as gradient hardware considerations for using time-variable selection gradients, which have been shown to greatly enhance multiband RF performance. Based on such considerations, we propose the use of amplitude modulated multiband RF pulses, as well as the design of time-variable gradient waveforms with smooth shapes, which significantly reduce demands on MR hardware when necessary.

Secondly, time-shifted and root-flipped multiband pulses can have misaligned spin-echo signals for different slices, which can lead to different T_2 and T_2^* contrast; these effects have been investigated and discussed.

Thirdly, using the hardware considerations we have implemented multiband RF pulses with time-variable selection gradients in a cardiac bSSFP sequence, one of the most clinically relevant examinations of our time. Although the shortest RF pulses are thought to be optimal for rapid MR, they do not directly lead to the shortest acquisition time due to patient heating, as this is limited by SAR. We reformulated the RF pulse design problem to reduce image acquisition duration directly which can result in shorter breath-hold periods and improved image quality.

Acknowledgements

The work undergone for this thesis would never be possible without my supervisors, Shaihan and Jo, and I'm incredibly grateful for all the hours you both spent with me. During my PhD Shaihan has always been around for help, with kindness and awesome excitement for new ideas. While Jo had the insane duty of running the department, during meetings his piercing attentiveness made this work discover otherwise dark corners of knowledge. This thesis would not be the same work without the extra enthusiasm you both put into the project, and aside from the productivity achieved you have taught me to enjoy the process of research, acknowledging failure and persisting, which is a trait impossible to describe in metrics.

Equally in effort this work has been possible thanks to Anthony, with who I experimented during countless evenings over the course of this project. It is fair to say that without Anthony this thesis could have been a 4 year-long mathematical exercise with nowhere near this amount of experimental data. The skills of an experimentalist are invaluable to the work as practical as this and require Anthony's blend of patience, persistence and humour to get things to actually work, as well as enjoying the journey of doing so.

It is not always obvious how an office environment can make you feel, and much like good health you might not know until you miss it. I would like to thank everyone in our physics group, as well as all the great people in perinatal imaging. I have learned, laughed and had so much fun during my time here with people who are amazing in what they do, but also kind, collaborative and self-less in their attitudes.

I would like to thank my parents Nagwa and Mahmoud, for just about everything they have done for me. The first thing I can think of is, thank you for giving me toys as a child, but also for supporting me, my actions and beliefs until this day as a slightly older child. This carries on to the rest of my family, my awesome siblings, Omar, Rana and Ahmed, his wife Yana and my niece Maya, whose smile and baby-chat brings anyone to a happier place.

I'm also insanely grateful for having the best friends that anyone could wish for around me, many of who I have known ever since I moved to London. This includes Leo, Steph, Sam, Karen and George who I have lived with for so long it might count as my first

marriage. Together we have made the best memories for eachother, and time only makes them sweeter. This also includes some high-school companions who never parted ways since childhood, Lieuwe, Jesse, Juan who keeps flying in from Amsterdam to ignite the fun, and the rest of a group which is feeling better knit as years pass by, Fotis, Marijn, Jul and Yann. It is no understatement to say that we are a product of our environment, and I feel blessed to have my best friends around me.

And finally to Jenny, whose unconditional love supports me every day, and makes my life a living dream. Here's to the adventures ahead...

Contents

Contents
_____

List of Figures

List of Tables

Chapter 1

Introduction

1.1 MRI background

MRI is made possible by a quantum property of atomic nuclei, known as quantum spin. This property describes an intrinsic angular momentum $\vec{J}$, which produces a magnetic moment $\vec{\mu}$ in the same direction

$$\vec{\mu} = \gamma \cdot \vec{J} \tag{1.1}$$

where γ is the gyromagnetic ratio, which is specific to the atomic nuclei of interest. MR signal originates from the nuclei of hydrogen atoms, which are formed of singular protons, for which the gyromagnetic ratio $\gamma = 267.5 \; rad \; s^{-1}T^{-1}$. In thermal equilibrium, an ensemble of magnetic moments (i.e. a collection of protons together) are directed in random directions, with an overall effect that cancels out the effect of the individual magnetic moments. When an external magnetic field B_0 is applied, more magnetic moments will on average align with respect to the direction of this field and the net magnetization will experience torque about this direction. The ensemble effect of magnetic moments is described by a magnetization vector $\vec{M}$, and the torque will cause rotational motion of the magnetization vector, known as nuclear precession. This can be described by the equation of motion

$$\frac{d\vec{M}}{dt} = \gamma \vec{M} \times \vec{B_0} \tag{1.2}$$

where the cross-product implies that precession occurs about the direction of the external magnetic field. Moreover, this precession occurs at a rate known as the Larmor frequency

$$\omega_0 = \gamma B_0. \tag{1.3}$$

In the transverse directions, perpendicular to the direction of B_0, magnetic moments all have different phases, which annuls any net ensemble effect.

When a radio-frequency (RF) pulse, $B_1(t)$, is applied perpendicularly to the direction of the external field, we can use the equation of motion to describe the spatially varying

magnetisation in the laboratory frame (x, y, z).

$$\frac{d\vec{M}}{dt} = \gamma \vec{M} \times \vec{B} = \gamma \vec{M} \times (\vec{B_0} + \vec{B_1}) \tag{1.4}$$

where

$$\vec{B_1}(t) = \hat{B}(t)_{envelope}[cos(\omega t + \phi)\vec{x} - sin(\omega t + \phi)\vec{y}] \tag{1.5}$$

and where ω is the the modulation frequency of the radio-frequency pulse, and ϕ is the phase-offset. The modulation frequency ω is set to the Larmor frequency to synchronise with precession.

As MRI takes place at the Larmor frequency, it is useful to introduce a rotating frame of reference (x', y', z').

$$\vec{x'} = cos(\omega t)\vec{x} - sin(wt)\vec{y} \tag{1.6}$$

$$\vec{y'} = sin(\omega t)\vec{x} + cos(wt)\vec{y} \tag{1.7}$$

$$\vec{z'} = \vec{z} \tag{1.8}$$

the equation of motion can be rewritten as

$$\frac{\partial \vec{M}'}{\partial t} = \gamma(\vec{M}' \times \vec{B}_{eff}) \tag{1.9}$$

where B_{eff} is the local effective field in the rotating frame which is experienced as a combination of all present magnetic fields. When the rotating frame is set to rotate at the Larmor frequency, the contribution from the main field to the effective field cancels and only the B_1-field matters.

Before an RF pulse is applied, the magnetization vector is fully aligned with the external field, in a state known as thermal equilibrium. As the RF pulse is applied, the magnetization vector tilts away from the its equilibrium direction along $\vec{B_0}$. The cross-product in Equation 1.9, implies that an RF pulse applied on the x'-axis will cause the magnetisation vector to rotate the z-y plane about the y'-axis. The angle between the magnetization vector, before and after the RF pulse has been applied is known as the flip-angle, and is calculated as

$$\theta = \gamma \int_0^T B(\tau)d\tau \tag{1.10}$$

1.1.1 Relaxation

The equation of motion can be extended to include relaxation terms

$$\frac{\partial \vec{M}'}{\partial t} = \gamma(\vec{M}' \times \vec{B}_{eff}) - \frac{M_{xy}}{T_2} - \frac{(M_z - M_0)}{T_1} \tag{1.11}$$

where M_{xy} is a composite vector representing transverse magnetization $M_{xy} = M_x\vec{x} + M_y\vec{y}$ in the transverse plane, and $M_z = M_z\vec{z}$. M_0 is a constant value representing the magnitude of the magnetization vector immediately after a 90° RF pulse has been applied, and T_1

and T_2 are relaxation parameters, and are unique to specimen. By Equation 1.11, they describe how the magnetization vector recovers to the equilibrium state after an RF pulse. For the special case after an RF pulse which results in a 90º flip-angle, this recovery is described by

$$M_{xy} = M_0 e^{-t/T_2}, \qquad (1.12)$$

$$M_z = M_0(1 - e^{-t/T_1}). \qquad (1.13)$$

These two relaxation procedures occur simultaneously, as well as a third process known as spin dephasing. This is caused by B_0-field inhomogeneities within a pixel of any MR measurement, which results in a distribution of spin orientations and thus loss of phase coherence. This is governed by a parameter known as T_2', however as this affects almost all measurements of transverse magnetization, it is commonly inferred from a better known parameter T_2^* given by

$$\frac{1}{T_2^*} = \frac{1}{T_2} + \frac{1}{T_2'} \qquad (1.14)$$

An important distinction between T_2 and T_2' is that the former is a decay term which is irreversible, whilst the latter is reversible by applying a subsequent RF pulse. This is covered in more detail in section 1.3.3. These three effects are shown in Figure 1.1, for a 90º RF pulse example.
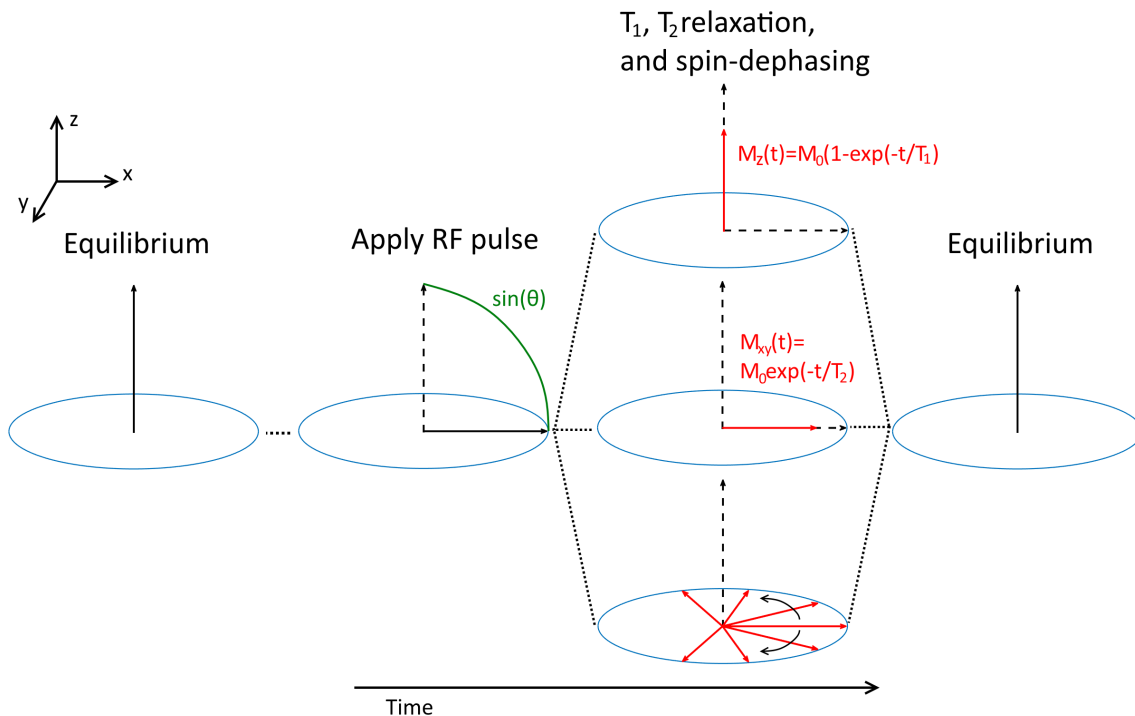
Figure 1.1: An illustration of the magnetization vector in a 3D space. After the application of an 90º RF pulse, the magnetization vector is aligned in the transverse xy plane. After this, two relaxation parameters T_1 and T_2 describe the exponential recovery of longitudinal and transverse components of the magnetization vector. Simultaneously to these processes the transverse magnetization also experiences spin dephasing, caused by local field inhomogeneities and governed by T_2'. After sufficient time, the magnetization vector returns to the equilibrium state.

1.1.2 Signal detection

The signal in MRI is detected by positioning a receiver coil close to the region of interest to increase the SNR of measurements. According to Faraday's law of induction, time-varying magnetic flux through a looped coil induces a current into the loop, which generates a voltage across the coil ports known as an electromotive force (emf). The magnetic flux Φ can be expressed in terms a time-dependent magnetisation vector $\vec{M}$

$$\Phi_M(t) = \int_{sample} d^3r \vec{B}^{receive}(\vec{r}) \cdot \vec{M}(\vec{r}, t) \tag{1.15}$$

where $\vec{B}^{receive}(\vec{r})$ is the magnetic field per unit current that, due to reciprocity, would be produced if the coil were located at a distant spatial point $\vec{r}'$. For a current loop, the vector potential at such a distant point can be found as

$$\vec{A}(\vec{r}') = \frac{\mu_0}{4\pi} \oint \frac{I d\vec{l}}{|\vec{r} - \vec{r}'|} \tag{1.16}$$

Using the curl relationship between the magnetic field and vector potential $\vec{B} = \vec{\nabla} \times \vec{A}$ we can write $\vec{B}^{receive}$ as

$$\vec{B}^{receive}(\vec{r}') = \frac{\vec{B}(\vec{r})}{I} = \vec{\nabla}' \times \left(\frac{\mu_0}{4\pi} \oint \frac{d\vec{l}}{|\vec{r} - \vec{r}'|} \right). \tag{1.17}$$

The emf produced by this time-varying flux is thus

$$\begin{aligned} emf &= -\frac{d}{dt} \Phi_M(t) \\ &= -\frac{d}{dt} \int_{sample} d^3r \vec{M}(\vec{r}, t) \cdot \vec{B}^{receive}(\vec{r}) \end{aligned} \tag{1.18}$$

It is important to recall Equation 1.2, which showed that magnetisation precesses about the direction of the external field, and so only the transverse component of the total magnetisation vector is time-varying, and hence detectable.

1.1.3 Spatial localization in MRI

All topics thus far are relevant to nuclear magnetic resonance. Magnetic Resonance Imaging (MRI) uses spatially localised NMR signals to form images. This is done using gradient coils which can produce linearly varying magnetic field gradients as a function of space. Gradient fields are required in three orthogonal directions, to spatially resolve signals from each orientation. When active, gradient fields vary the magnetic field strength such that in the rotating frame

$$\omega(\vec{r}) = \gamma B(\vec{r}) = \gamma \vec{G} \cdot \vec{r} \tag{1.19}$$

When all gradients are turned off, and a B_1-field is transmitted at the Larmor frequency, all nuclei within the reach of the transmit antenna will interact with it. When the same scenario happens with a linear field gradient present, only the nuclei within a certain

frequency band will interact, which will allow for measurements in spatially defined positions.

Image formation can be done by spatially exciting a frequency band $\Delta\omega$ in one direction, which is known as slice-selective excitation. In direction z this corresponds to a slice spanning over space Δz.

$$\Delta\omega = \gamma G_{slice} \cdot \Delta z \tag{1.20}$$

Where the gradient amplitude G_{slice} can control the slice-thickness. However within this slice, all nuclei will spin coherently and cannot be spatially isolated unless the other two gradients directions are used to create controlled incoherence. The MRI signal which is measured from Equation 1.18 can be written as

$$s(\vec{r}, t) = \int \rho(\vec{r})e^{i\gamma \int_0^t \vec{G}(\tau)\cdot\vec{r}d\tau}d\vec{r} \tag{1.21}$$

where ρ is representative of spin density, and $i = \sqrt{-1}$. Defining a parameter $\vec{k}(t)$ as

$$\vec{k}(t) = \frac{\gamma}{2\pi}\int_0^t \vec{G}(\tau)d\tau \tag{1.22}$$

Allows us to rewrite Equation 1.21 as

$$s(\vec{r}, \vec{k}) = \int \rho(\vec{r})e^{i2\pi\vec{k}\cdot\vec{r}}d\vec{r} \tag{1.23}$$

which is the familiar Fourier transform, where the spatial frequency variable $\vec{k}$ has units $1/m$, and is directly controlled by the gradient waveforms.

This formalism allows us to describe a simple example of forming a 2D image, by sampling a 2D spatial frequency domain known as k-space. Although this is physically a continuous spatial frequency space, it is sampled discretely and so must adhere to minimum sampling requirements. Specifically, the density at which we sample k-space, Δk, is inversely proportional to the field-of-view (FOV) in our reconstructed 2D image. An insufficient sampling density will result in image aliasing. Similarly, the range of acquired k-space will determine the pixel size in the image domain.

A typical 2D k-space acquisition method is to start at the center of k-space, move towards the edge of k-space with so-called prewind gradients, and acquire a straight line in one direction. This can be repeated starting from a range of different edges, as shown in Figure 1.2.

The RF and gradient waveforms for acquiring a 2D k-space are shown in Figure 1.3. The straight acquisition line across k_x is achieved by what is known as the read-out gradient, during which k-space data are acquired. The read-out gradient ensures that different spatial positions will experience a different field-strength, and thus precess slower or faster according to the Larmor equation. This is therefore known as frequency encoding. The prewind gradient before the read-out gradient moves the current position from the center to the edge of k-space. This causes spin dephasing across the transverse plane, which adds
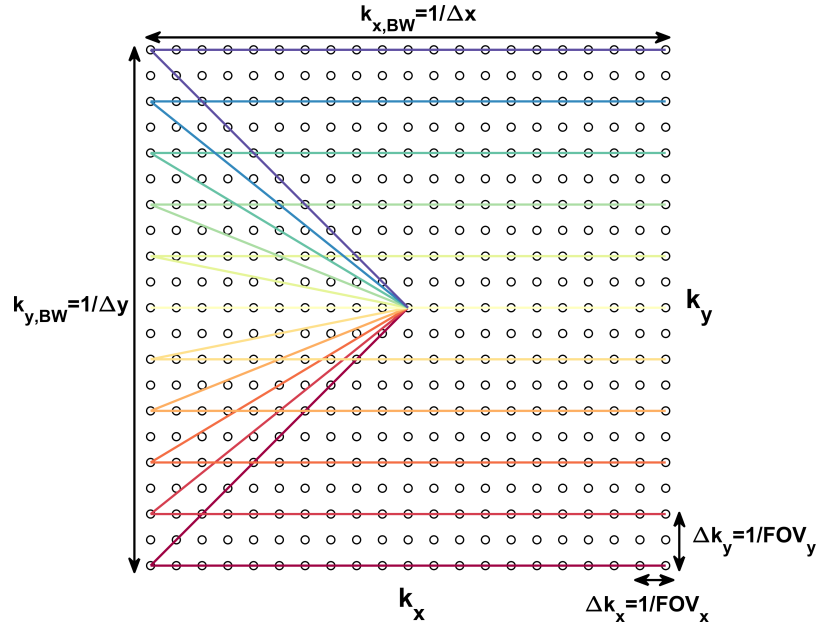
Figure 1.2: An illustration of 2D k-space, which is related to a 2D image by the Fourier transform. Coloured traces show k-space trajectories for a simple acquisition scheme, acquiring 1 line of k-space per RF pulse, starting from the center of k-space. Sampling bandwidth (or range) k_{BW} and density Δk are inversely proportional to pixel resolution and Field-of-View respectively. A sequence diagram for acquiring this k-space is shown in Figure 1.3.

to signal dispersion. This period of dephasing is then followed by rephasing from the read-out gradient, which implies that the measured gradient echo peaks when the k_x-center is crossed.

The time between the center of an RF pulse (i.e. specifically, the point about which an RF pulse is symmetric) and the center of acquisition window is known as the sequence echo-time, abbreviated as TE.

The phase-encoding gradient in Figure 1.3 applies a space-dependent phase-shift in the corresponding direction. In terms of k-space, it moves the acquisition point from the center along the phase-encoding direction k_y, in time before read-out commences. The gradient area of the phase-encoding waveform controls the positioning of the phase-encoding direction.

For this simple example it is already possible to determine imaging considerations. Image resolution is determined by the range of k-space data acquired. However as for most 2D images, higher spatial frequencies also have smaller coefficient amplitudes. Noise in MRI is broadly uniform across frequency as it is caused by thermal noise, and so higher spatial frequencies suffer from a low signal-to-noise ratio (SNR). Another limitation is that large k-space bandwidth require large gradient areas, and gradient hardware is limited in amplitude. Any time-stretching of gradient waveforms at fixed amplitude comes at a cost in echo-time, which again results in lower SNR. The image FOV is related to the density of k-space sampling Δk, and needs to be big enough to cover the region of interest.
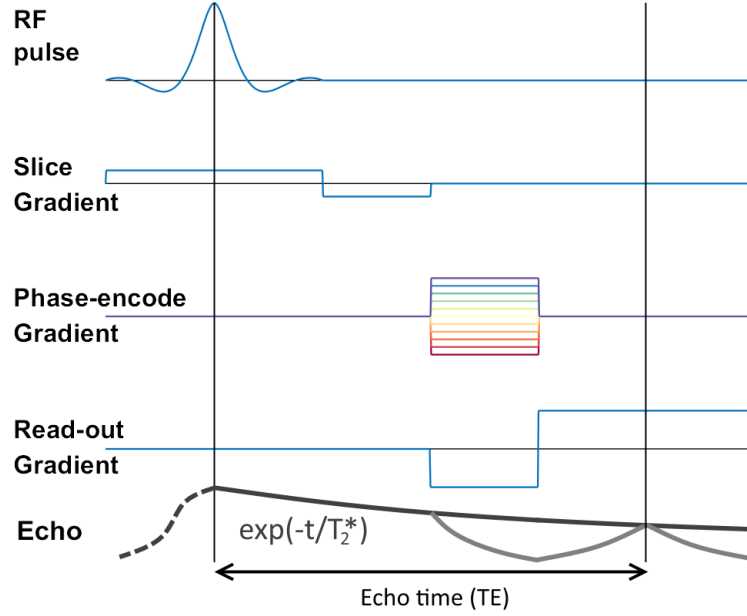
Figure 1.3: A sequence diagram for a 2D gradient-echo acquisition, showing RF and gradient waveforms as well an animated echo throughout the sequence. RF pulse is scaled to achieve a flip-angle, as determined by Equation 1.10. The slice gradient is necessary for spatial excitation, and is scaled to achieve a slice-thickness according to Equation 1.20. The followed negative lobe is the slice-rewind, which ensures coherent phase across the slice profile for maximum signal. The phase encode and read-out prewind gradient ensure correct localization in k-space. Whilst the read-out prewind amplitude is consistent for a sequence, the phase-encoding amplitude is different for different sequence repetitions, to acquire different k-space lines. These two can overlap with the slice-rewind gradient. The read-out gradient is used for traversing k-space whilst the ADC takes measurements of spatial frequencies. During the RF pulse, the echo signal increases and starts decreasing due to T_2^*. During the read-out prewind, the signal is further dephased. The read-out gradient is on during data acquisition, and measurements are made while crossing a line in 2D k-space. The first half of the read-out gradient rephases the gradient-echo such that it peaks when crossing the center of k_x.

Sampling density in the frequency encoding direction can be easily achieved, as it relates to the sampling rate of the analogue-to-digital converter (ADC) of the acquisition system. However to ensure high sampling density in the phase-encoding direction, more phase-encoding steps in k-space are required, which increase the number of sequence repetitions (measured in repetition-time, abbreviated as TR) in an overall sequence. It is therefore common for anisotropic FOV imaging, to have the read-out direction along the larger FOV and the phase-encoding along the shorter FOV.

1.2   Radio Frequency Pulse Design

The challenge of RF pulse design is to design a $B_1(t)$ waveform to ensure the excitation of a desired transverse magnetisation profile $M_{xy}(\vec{r})$. The change in magnetisation in the presence of B_1 pulses and gradients, in the rotating frame and neglecting relaxation, is

given by the Bloch equations

$$
\begin{pmatrix} \dot{M}_x \\ \dot{M}_y \\ \dot{M}_z \end{pmatrix} = \gamma \begin{pmatrix} 0 & \vec{G} \cdot \vec{r} & -B_{1,y} \\ -\vec{G} \cdot \vec{r} & 0 & B_{1,x} \\ B_{1,y} & -B_{1,x} & 0 \end{pmatrix} \begin{pmatrix} M_x \\ M_y \\ M_z \end{pmatrix} \tag{1.24}
$$

We can express the change in transverse magnetisation, over space r and time t, as:

$$
\dot{M}_{xy}(\vec{r}, t) = -i\gamma \vec{G}\vec{r} M_{xy}(\vec{r}, t) + i\gamma B_1(t) M_z(\vec{r}, t) \tag{1.25}
$$

where $B_1(t) = B_{1,x}(t) + iB_{1,y}(t)$ and $M_{xy} = M_x + iM_y$. In the above expression, there is no closed form solution for $B_1(t)$ given a specific $M_{xy}(r, t)$ because $M_z(r, t)$ is a time-varying function coupled with $M_{xy}(r, t)$.

1.2.1 Small-Tip Angle Design

One way to simplify Equation 1.25 is to assume that the longitudinal magnetisation remains constant during B_1 transmission. This turns the matrix form of the Bloch equations from a system of coupled linear differential equations to one where M_x and M_y are decoupled from M_z. It can be shown that by making this assumption, the transverse magnetization at the end of the pulse duration T is [1].

$$
M_z \approx M_0 = \text{constant} \tag{1.26}
$$

$$
M_{xy}(\vec{r}, T) = i\gamma M_0 \int_0^T B_1(t) e^{-i\gamma \vec{r} \int_t^T \vec{G}(s)ds} dt \tag{1.27}
$$

Moreover, assuming a constant-valued gradient for slice-selection, Equation 1.26 can be further simplified to

$$
M_{xy}(\vec{r}, T) = i\gamma M_0 \phi(\vec{r}) \int_0^T B_1(t) e^{i\gamma \vec{r} \cdot \vec{G} t} \tag{1.28}
$$

where $\phi(\vec{r}) = exp(-i\gamma GT\vec{r})$ is a constant value representative of a space-dependent phase-roll. This assumption thus results in a Fourier transform relation between the B_1-shape and the resultant slice-profile M_{xy}. The small-tip angle approximation framework is valid for pulses with low flip angles. However, in practice this approximation can work for flip angles of 45°, but becomes problematic for up to 90° as well as higher flip angles, as the assumption in Equation 1.26 becomes progressively invalid.

The most common desired excitation profile is a rectangle in the frequency domain which, according to the Fourier transform, corresponds to a sinc pulse of infinite duration under the small-tip approximation. A sinc pulse is defined as

$$
sinc(\omega t) = \frac{sin(\omega t)}{\omega t} \tag{1.29}
$$

Infinite pulse durations are practically impossible, and sinc pulses are apodized for practical implementation.

$$
B_1(t) = \begin{cases} A(t) \cdot sinc\left(\frac{N_s t}{T}\right) & \text{for -T/2 < t < T/2} \\ 0 & \text{elsewhere} \end{cases} \tag{1.30}
$$

Where N_s is the number of sidelobes retained, and T is the RF pulse duration. The apodization function $A(t)$ can simply be a rectangular function, or a windowing function such as a Hamming window which allows a trade-off between transition ripples and transition width. From Equation 1.29 to Equation 1.30 we have substituted

$$\omega = N_s/T \tag{1.31}$$

An interesting result from this relation is that the slice-bandwidth and RF pulse duration remain linked by a dimensionless parameter. This is known as the time bandwidth product (TBP), and is used as a parameter to define slice-quality. The more sidelobes included, the higher the time bandwidth product and thus the closer a magnetisation profile will match a perfect rectangle. The cost of higher slice quality is longer RF pulse durations, which can result in longer echo-times and thus lower SNR.

1.2.2 Shinnar-Le Roux Pulse Design

The Shinnar-Le Roux (SLR) algorithm is a more sophisticated approach to RF pulse design, and more common for large-tip angle pulse design. It regards the pulse envelope as a series of hard pulses rather than a continuous-shaped pulse. It then makes use of the spin-domain description of the magnetisation vector, and an assumption known as the hard-pulse approximation, to find the series of hard pulses required to achieve a desired magnetisation.

Cayley-Klein rotation parameters

According to Euler's rotation theorem, any rotation R can be described using three angles (ϕ, θ, ψ) as $R = R_z(\psi)R_x(\theta)R_z(\phi)$ where $R_z(\phi)$ represents a rotation about the z-axis with angle ϕ. The matrix form of the Bloch equations in the rotating frame (ignoring relaxation) is given by Equation 1.24, repeated below

$$\begin{pmatrix} \dot{M}_x \\ \dot{M}_y \\ \dot{M}_z \end{pmatrix} = \gamma \begin{pmatrix} 0 & Gr & -B_{1,y} \\ -Gr & 0 & B_{1,x} \\ B_{1,y} & -B_{1,x} & 0 \end{pmatrix} \begin{pmatrix} M_x \\ M_y \\ M_z \end{pmatrix}$$

for which $\vec{M}(T) = R\vec{M}(0)$ is a solution, where R is a 3×3 orthonormal matrix which can be described using Euler angles. An RF pulse can be considered as a piece-wise constant function, made up of N time-steps of length Δt such that pulse duration $T = N \cdot \Delta t$. An example of this is shown in Figure 1.4.

During each time-step the magnetisation vector $\vec{M}$ undergoes a rotation. After a sequence of N time-steps, the total rotation can be found as the product of all previous rotations

$$R_N = R_{N-1}R_{N-2}..R_1 \tag{1.32}$$

18
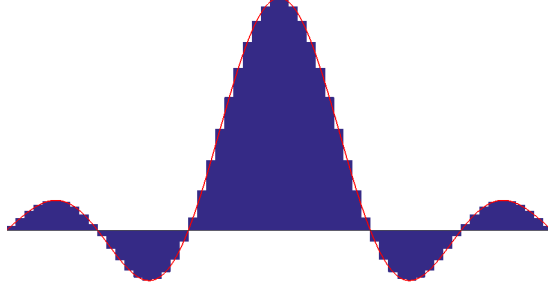
Figure 1.4: A discretised sinc-shaped RF pulse. During each time-span Δt the magnetisation vector undergoes a rotation

Using Cayley-Klein rotation parameters, the 3x3 rotation matrix can also be represented by a 2x2 unitary matrix.

$$Q = \begin{pmatrix} \alpha & -\beta^* \\ \beta & \alpha^* \end{pmatrix} \tag{1.33}$$

where α and β are Cayley-Klein parameters which are related to Euler angles (ϕ, θ, ψ) as

$$\alpha = e^{(\psi+\phi)/2} cos\frac{\theta}{2} \tag{1.34}$$

$$\beta = ie^{(\psi-\phi)/2} sin\frac{\theta}{2} \tag{1.35}$$

These parameters can be rewritten when using a specified axis of rotation $\vec{n}$ and a single rotation angle ϕ.

$$\alpha = cos\frac{\phi}{2} - in_z sin\frac{\phi}{2} \tag{1.36}$$

$$\beta = -i(n_x + in_y) sin\frac{\phi}{2} \tag{1.37}$$

where $\vec{n}$ is the vector representing the axis of rotation and ϕ is the rotation angle. The rotation angle and axis during a single constant piecewise time-step, j, are

$$\phi_j = -\gamma \Delta t \sqrt{|B_{1,j}|^2 + (Gr)^2} \tag{1.38}$$

$$\vec{n}_j = \frac{\gamma \Delta t}{|\phi_j|}(B_{1,x}, B_{1,y}, Gr) \tag{1.39}$$

and the Cayley-Klein rotation parameters during this time-step are

$$a_j = cos\frac{\phi_j}{2} - in_{z,j} sin\frac{\phi_j}{2} \tag{1.40}$$

$$b_j = -i(n_{x,j} + in_{y,j}) sin\frac{\phi_j}{2} \tag{1.41}$$

where symbols a and b are used rather than α and β to distinguish between rotation parameters and spinor state parameters, as well as following the notation used by Pauly et al. [2]. The spin-domain rotation matrix during this time-step is

$$Q_j = \begin{pmatrix} a_j & -b_j^* \\ b_j & a_j^* \end{pmatrix} \tag{1.42}$$

The total rotation after N time steps is again the product of all piece-wise rotations

$$Q_N = Q_{N-1}Q_{N-2}..Q_1 \tag{1.43}$$

which is the spin-domain analogue of Equation 1.32. Once the spinor state parameters α_N and β_N (i.e. the rotation parameters at the end of pulse) have been determined, the magnetisation can be calculated from the following relations

$$
\begin{pmatrix} M_{xy}^+ \\ M_{xy}^{+*} \\ M_z^+ \end{pmatrix} =
\begin{pmatrix}
(\alpha^*)^2 & -\beta^2 & 2\alpha^*\beta \\
-(\beta^*)^2 & \alpha^2 & 2\alpha\beta^* \\
-\alpha^*\beta^* & -\alpha\beta & \alpha\alpha^* - \beta\beta^*
\end{pmatrix}
\begin{pmatrix} M_{xy}^- \\ M_{xy}^{-*} \\ M_z^- \end{pmatrix} \tag{1.44}
$$

We can now derive some useful representations from this matrix. For example, assuming an initial condition of $M^- = [0, 0, M_0]$, the transverse magnetization of an excitation profile can be written as

$$M_{xy}^+ = 2\alpha^*\beta M_0 \tag{1.45}$$

Because these are just scalar multiplications, these calculations are extremely fast, making them very useful.

State-space representation

At any time-point j, the spinor states α_j and β_j are given by the series of rotations propagated through all previous time-points.

$$
\begin{pmatrix} \alpha_j & -\beta_j^* \\ \beta_j & \alpha_j^* \end{pmatrix} =
\underbrace{\begin{pmatrix} a_j & -b_j^* \\ b_j & a_j^* \end{pmatrix}}_{Qj} \cdots
\begin{pmatrix} a_0 & -b_0^* \\ b_0 & a_0^* \end{pmatrix} \tag{1.46}
$$

The rotation matrix Q_j has symmetric redundancy as it can be represented with only one of its two columns. Here we follow the method in [2] and use the first column of the 2x2 rotation matrix to represent a 2x1 spinor state.

$$
\begin{pmatrix} \alpha_j \\ \beta_j \end{pmatrix} =
\begin{pmatrix} a_j & -b_j^* \\ b_j & a_j^* \end{pmatrix}
\begin{pmatrix} \alpha_{j-1} \\ \beta_{j-1} \end{pmatrix} \tag{1.47}
$$

This is called the state-space representation of the RF pulse. The initial states α_0 and β_0 can be found by evaluating Equations 1.36 and 1.37 for the case of no rotation ($\phi_0 = 0$) which gives

$$\alpha_0 = cos\frac{0}{2} - in_z sin\frac{0}{2} = 1 \tag{1.48}$$

$$\beta_0 = -i(n_{x,j} + in_{y,j})sin\frac{0}{2} = 0 \tag{1.49}$$

Hard-pulse approximation

The spin domain rotation matrix can be decomposed as two separate matrices. The first matrix isolates the effect due to the B_1-field, while the second isolates the effect of the gradient-induced precession that the magnetisation vector undergoes. This approximation can be expressed as

$$Q_j = \begin{pmatrix} a_j & -b_j^* \\ b_j & a_j^* \end{pmatrix} \approx \begin{pmatrix} C_j & -S_j^* \\ S_j & C_j \end{pmatrix} \begin{pmatrix} z^{\frac{1}{2}} & 0 \\ 0 & z^{-\frac{1}{2}} \end{pmatrix} \tag{1.50}$$

where

$$C_j = cos(\gamma |B_{1,j}| \Delta t/2) \tag{1.51}$$

$$S_j = ie^{i\angle B_{1,j}} sin(\gamma |B_{1,j}| \Delta t/2) \tag{1.52}$$

$$z = e^{i\gamma Gr\Delta t} \tag{1.53}$$

An important concept is that in reality we know that they are two simultaneous processes, but according to the hard-pulse approximation they can be separated as two separate sequential rotations. This approximation becomes increasingly accurate as the number of time-steps increases, or equivalently if the time-step Δt decreases. An illustration of the hard-pulse approximation is shown in Figure 1.5.
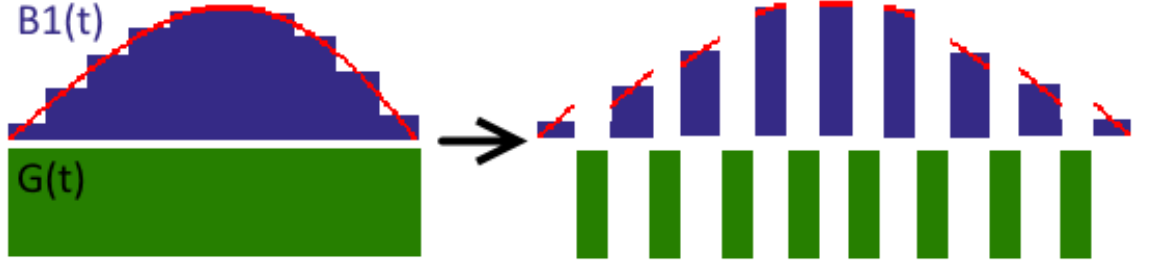
Figure 1.5: An illustration of the hard-pulse approximation. The rotations that are in reality occurring simultaneously can be regarded as separate rotations. The effect from the gradient is a pure gradient-induced precession, represented as a rotation about the z-axis and the effect from the RF pulse is a tilt of the magnetization vector about the transverse plane

Forward SLR transform

Using the hard-pulse approximation, the state-space representations from Equation 1.47 can then be rewritten as

$$\begin{pmatrix} \alpha_j \\ \beta_j \end{pmatrix} = z^{1/2} \begin{pmatrix} C_j & -S_j^* \\ S_j & C_j \end{pmatrix} \begin{pmatrix} 1 & 0 \\ 0 & z^{-1} \end{pmatrix} \begin{pmatrix} \alpha_{j-1} \\ \beta_{j-1} \end{pmatrix} \tag{1.54}$$

We define the spinor state variables A_j and B_j as

$$\tilde{\alpha}_j = z^{j/2} \alpha_j \tag{1.55}$$

$$\tilde{\beta}_j = z^{j/2} \beta_j \tag{1.56}$$

such that the half angles from the Equation 1.50 are eliminated for convenience. We can then rewrite Equation 1.47 as

$$\begin{pmatrix} \tilde{\alpha}_j \\ \tilde{\beta}_j \end{pmatrix} = \begin{pmatrix} C_j & -S_j^* z^{-1} \\ S_j & C_j z^{-1} \end{pmatrix} \begin{pmatrix} \tilde{\alpha}_{j-1} \\ \tilde{\beta}_{j-1} \end{pmatrix} \tag{1.57}$$

From Equation 1.57 we can see that the spinor state variables $\tilde{\alpha}_j$ and $\tilde{\beta}_j$ are actually $j-1$ order polynomials in z^{-1}. Furthermore, at the end of the pulse of length $T = N \cdot \Delta t$ the slice profile under the hard-pulse approximation can be characterised by spinor state variables $\tilde{\alpha}_N(z)$ and $\tilde{\beta}_N(z)$ as

$$\tilde{\alpha}_N(z) = \sum_{n=0}^{N-1} \hat{\alpha}_n z^{-n} \tag{1.58}$$

$$\tilde{\beta}_N(z) = \sum_{n=0}^{N-1} \hat{\beta}_n z^{-n} \tag{1.59}$$

where $\tilde{\alpha}_N(z)$ and $\tilde{\beta}_N(z)$ are $N-1$ order polynomials in z^{-1}, and $\hat{\alpha}_n$ and $\hat{\beta}_n$ are discrete-time coefficients of the polynomials. As stated, the polynomials are z-transforms of the discrete-time sequences $\hat{\alpha}_n$ and $\hat{\beta}_n$, and $z = e^{i\gamma Gr \Delta t}$ (Equation 1.53) which can be written more generally as

$$z = e^{2\pi i k/N} = e^{i\omega} \tag{1.60}$$

making these expressions equivalent to the familiar Discrete Fourier Transform (DFT). This concludes how a time-discretised RF pulse can be transformed to two finite-order polynomials.

Inverse SLR transform

It is also possible to iterate from two DFT functions to an RF pulse by inverting the matrix in Equation 1.57, to find

$$\begin{pmatrix} \tilde{\alpha}_{j-1} \\ \tilde{\beta}_{j-1} \end{pmatrix} = \begin{pmatrix} C_j & S_j^* \\ -S_j z & C_j z \end{pmatrix} \begin{pmatrix} \tilde{\alpha}_j \\ \tilde{\beta}_j \end{pmatrix} \tag{1.61}$$

This is a recursion, where on the left-hand side $\tilde{\alpha}_{j-1}$ and $\tilde{\beta}_{j-1}$ are polynomial of one order less than $\tilde{\alpha}_j$ and $\tilde{\beta}_j$ on the right-hand side. This means that one of the terms in $\tilde{\alpha}_{j-1}$ and $\tilde{\beta}_{j-1}$ must equate to zero. For example, in a single iteration we can write

$$\tilde{\beta}_j(z) = \hat{\beta}_0 + \hat{\beta}_1 z^{-1} + ... + \hat{\beta}_{j-1} z^{-(j-1)}$$

$$\tilde{\alpha}_j(z) = \hat{\alpha}_0 + \hat{\alpha}_1 z^{-1} + ... + \hat{\alpha}_{j-1} z^{-(j-1)}.$$

Expanding $\tilde{\beta}_{j-1}$ from Equation 1.61 gives us (dropping the argument for clarity)

$$\tilde{\beta}_{j-1} = z^1 (-S_j \tilde{\alpha}_j + C_j \tilde{\beta}_j)$$

$$= -S_j (\hat{\alpha}_0 z^1 + \hat{\alpha}_1 + ... + \hat{\alpha}_{j-1} z^{-(j-2)})$$

$$+ C_j (\hat{\beta}_0 z^1 + \hat{\beta}_1 + ... + \hat{\beta}_{j-1} z^{-(j-2)}).$$

Since $\tilde{\beta}_{j-1}$ is a $j-2$ order polynomial, there cannot be a z^1 term, and this term must equate to zero.

$$\tilde{\beta}_{j-1} = \underbrace{(...)}_{\text{j-2-order poly}} + \underbrace{(-S_j\hat{\alpha}_0 + C_j\hat{\beta}_0)z^1}_{=0} \tag{1.62}$$

$$-S_j\hat{\alpha}_0 + C_j\hat{\beta}_0 = 0. \tag{1.63}$$

A similar relation can be shown for the $\tilde{\alpha}_{j-1}$ iteration.

From Equations 1.63, 1.51 and 1.52 we thus have that

$$\frac{\hat{\beta}_0}{\hat{\alpha}_0} = \frac{S_j}{C_j} = \frac{ie^{i\theta_j}sin(\phi_j/2)}{cos(\phi_j/2)} \tag{1.64}$$

where ϕ_j is the fractional flip angle of the jth time-step, and θ_j is the phase of the RF pulse. Solving this for ϕ_j and θ_j gives us

$$\phi_j = 2arctan\left|\frac{\hat{\beta}_0}{\hat{\alpha}_0}\right| \tag{1.65}$$

$$\theta_j = \angle\left(-i\frac{\hat{\beta}_0}{\hat{\alpha}_0}\right) \tag{1.66}$$

and finally, the RF waveform at iteration step j is given by

$$B_{1,j} = \frac{1}{\gamma\Delta t}\phi_j e^{i\theta_j} \tag{1.67}$$

which concludes the inverse SLR transform.

SLR polynomial design

With the inverse SLR transform we have a direct mapping between designing polynomials and designing RF pulses with prescribed transverse magnetization profiles. The design of such SLR polynomials is generalized by filter design. A filter is a control system where the output is a function of its input as well as its inherent characteristics. Of particular interest are Linear Time-Invariant (LTI) filters, which can be fully characterised by an impulse response $\beta(n)$. The output $y(n)$ of a LTI filter can be reproduced by convolving the input $x(n)$ with linearly-scaled, time-shifted versions of the characteristic impulse response function.

$$y(n) = \sum_{k=-\infty}^{\infty} x(k)\beta(n-k) = x(n) * \beta(n) \tag{1.68}$$

This is a fundamental property for LTI filters and allows us to analyse them using tools such as the Fourier transform. The impulse response $\beta(n)$ equals the system output when the input is an impulse function $\delta(t)$. We are often interested in the frequency behaviour of LTI filters by describing them in the frequency domain.

$$\tilde{\beta}_k = \sum_{n=-\infty}^{\infty} \beta_n e^{-2\pi ikn/N} \tag{1.69}$$

LTI filters are classified between finite impulse response (FIR) and infinite impulse response (IIR) filters. FIR filters rely only on current and past inputs, but not on past outputs as infinite impulse response (IIR) filters do. The impulse response of FIR filters is of finite length N, and Equation 1.69 becomes

$$\tilde{\beta}_k = \sum_{n=0}^{N-1} \beta_n e^{-2\pi i k n/N} \tag{1.70}$$

which is the same expression the earlier SLR polynomials $\tilde{\alpha}_N(z)$ and $\tilde{\beta}_N(z)$ using Equations 1.59 and 1.60. This is the reason why FIR filter design and SLR RF pulse design are linked. Going forward, we will use $\tilde{\beta}_k$ to denote the frequency profile of both SLR polynomials and FIR filters, which have time-domain coefficients $\tilde{\beta}_n$. The hat-symbol used for time-domain coefficients for SLR-polynomials are dropped for convenience.

In Equation 1.70 our filter is written as a polynomial with coefficients (i.e. a sum of products). An alternative expression is the factored form (product of factors), which can be written as

$$\tilde{\beta}_k = \sum_{n=0}^{N-1} \beta_n e^{-2\pi i k n/N} = \beta_0 \prod_{n=1}^{N-1} (1 - r_n e^{-2\pi i k/N}) \tag{1.71}$$

where r_n are the roots of polynomial coefficients β_n. Roots can be found by evaluating the eigenvalues of the companion matrix of the coefficients. Complex valued roots can be plotted on the complex plane, where the unit circle is given by the expression $e^{-2\pi i k/N}$. The roots will usually appear on or around the unit circle, and their angular position with respect to the real-axis corresponds to the frequency at which they become significant. Roots which relate to stopband behaviour will generally appear on the unit circle at stopband frequencies (angles), whilst roots which relate to passband behaviour will appear away from the unit circle and passband frequencies (angles). It is thus important to note that, whilst SLR design is generally expressed in polynomial representation, the root representation is an equivalent way of representing the SLR design, where frequencies are expressed as angular position on the complex plane.

There are two important rules which govern the positioning of roots. The first rule is that for real-valued filters, the roots must be positioned symmetrically about the real axis. Algebraically, this means that r_k and r_k^* come in pairs. The second rule is that for time-symmetric filter coefficients, the roots must appear in anti-symmetry about the real axis, on equiangular radial lines. Algebraically, this means that r_k and r_k^{-1} come in pairs. These two rules can also be combined, which is why for linear-phase filters (which are both time-symmetric, and real-valued) roots come in pairs of r_k, r_k^*, r_k^{-1} and $(r_k^*)^{-1}$. This is illustrated for three different filters in Figure 1.6.

Radio Frequency pulse design with the SLR transform

With the forward and inverse SLR processes in place, we now have a unique transformation between an RF pulse and a set of two polynomials $\tilde{\alpha}_k$ and $\tilde{\beta}_k$. The designed polynomials
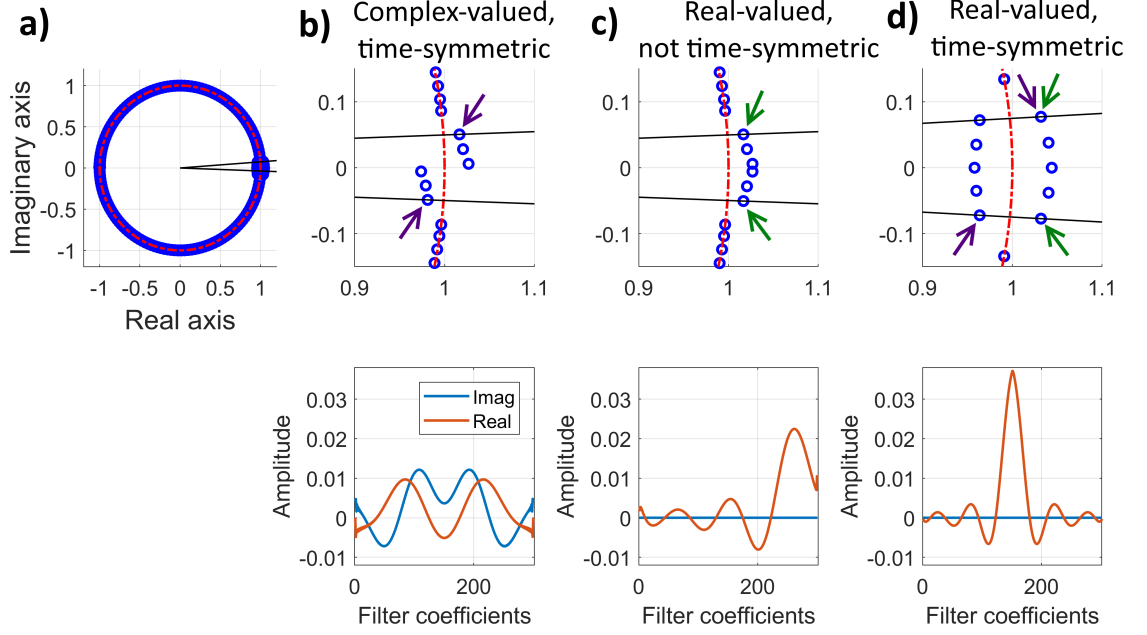
Figure 1.6: a) A root-pattern of a conventional linear-phase filter. **b)** Shows a zoomed in version around the passband roots, with two radial lines through the outer passband roots. This is a quadratic-phase filter, where the roots appear anti-symmetric about the real axis (purple arrows), on equiangular radial lines. This filter is therefore time-symmetric, but complex-valued as there is no symmetry about the real axis. **c)** Shows a different filter (minimum-phase), where the passband roots remain symmetrical about the real-axis (green arrows). The filter is therefore real-valued, but not time-symmetric. **d)** Shows the roots for a linear-phase filter, which are symmetric about the real axis (green arrows), which imply real-valued filter coefficients. Additionally, roots are anti-symmetric about the real axis, on equiangular radial lines (purple arrows), which imply time-symmetric filters. Minimum-phase and quadratic-phase filters are discussed in sections 1.2.5 and 1.2.6 respectively.

must satisfy the Cayley-Klein magnitude constraint:

$$|\tilde{\alpha}_k|^2 + |\tilde{\beta}_k|^2 = 1 \tag{1.72}$$

We design $\tilde{\beta}_k$ subject to our desired magnetisation, and choose $\tilde{\alpha}_k$ to satisfy the above magnitude constraint. The scaling of $\tilde{\beta}_k$ sets the desired flip angle $\theta(\omega)$, using the relation

$$\tilde{\beta}_k = sin(\theta(\omega)/2)\frac{\tilde{\beta}'_k}{max|\tilde{\beta}'_k|} \tag{1.73}$$

The magnitude profile of $\tilde{\alpha}_k$ can then be found as

$$|\tilde{\alpha}_k| = \sqrt{1 - |\tilde{\beta}_k|^2} \tag{1.74}$$

Although we have specified a magnitude profile for $\tilde{\alpha}_k$, the phase profile is unspecified. It can be shown that the minimum pulse-energy is achieved when $\tilde{\alpha}_k$ has a minimum-phase structure. This can be found by taking the Hilbert transform of the log-magnitude profile [2, 3].

$$\angle\tilde{\alpha}_k = \mathcal{H}\{\ln|\tilde{\alpha}_k|\} \tag{1.75}$$

where $\mathcal{H}\cdot$ denotes the Hilbert transform operator and ln denotes the natural logarithm. Finally $\tilde{\alpha}_k$ is thus found as

$$\tilde{\alpha}_k = |\tilde{\alpha}_k|e^{i\mathcal{H}\{\ln(|\tilde{\alpha}_k|)\}} \tag{1.76}$$

Our RF pulse $B_1(t)$ can then be found using the inverse SLR algorithm as in section 1.2.2.

$$B_1(t) = \mathcal{ISLR}(\tilde{\beta}_k, \tilde{\alpha}_k) \tag{1.77}$$

A single N-1 order polynomial, designed to match our desired magnetization profile can be transformed to an RF pulse in time. The workflow of designing a RF pulse using SLR is shown in Figure 1.7. Note that the forward and inverse SLR transform is non-linear, but completely deterministic. The performance of $\tilde{\beta}_k$ filter designs can be assessed using the
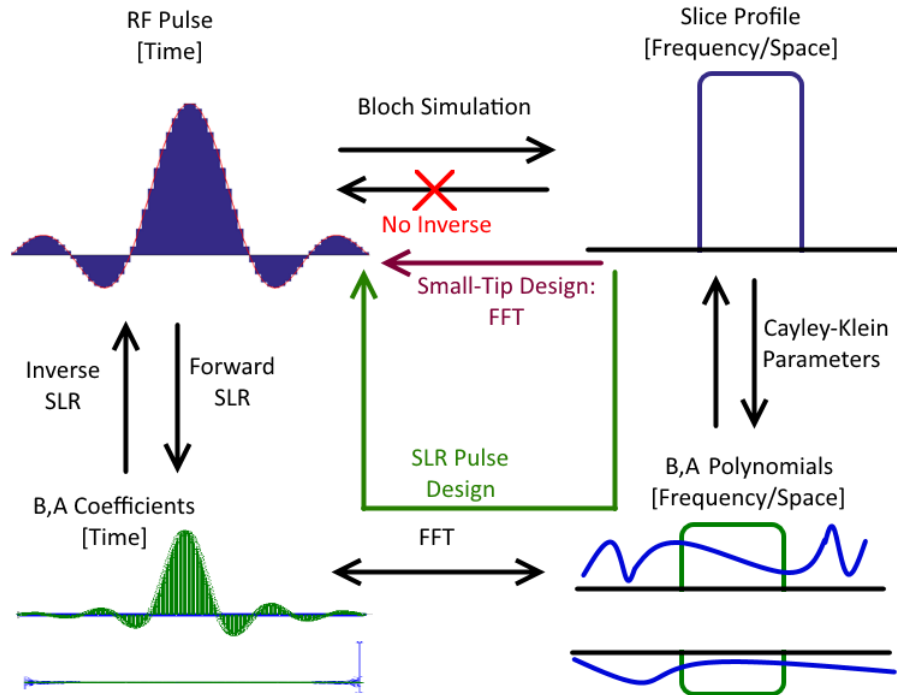
Figure 1.7: Illustration of the workflow for designing RF pulses using the SLR transform. Ultimately, what we are trying to do is to invert the Bloch equations such that we can get a RF pulse given a desired slice profile. A direct inversion is impossible, but the small-tip angle approximation tells us that transverse magnetisation and the RF pulse are related by the Fourier transform. The SLR transform allows you to start with a slice profile, expressed as a N-1 order polynomial, and deduct a set of two polynomials using CK parameters. The polynomials are related to coefficients by the DFT. The inverse SLR transform maps a set of two sequences to an RF pulse.

D_∞ function. This is a empirically derived function related to filter order estimation [4] and is available in Pauly's RF toolbox. Pauly et al [2] linked the design of RF pulses via the SLR transform with the design of FIR filters by deriving the following equation:

$$D_\infty(\delta_1, \delta_2) = TBP \cdot W \tag{1.78}$$

where TBP denotes time bandwidth product and W denotes fractional transition band (i.e. normalised edge between passband and stopband), and δ_1 and δ_2 denote the pass-band

and stop-band ripple respectively. This is the key relationship that allows the parametric RF pulse design based on FIR polynomial design. It explains that the TBP of a pulse is dependent on the desired slice ripples as well as the transition width. In [2] the relationship between the filter ripples (δ_1, δ_2) and magnetization profile ripples (δ_1^e, δ_2^e) are derived for different desireable applications. Once $D_\infty(\delta_1, \delta_2)$, TBP and W are set, we can define a desired filter frequency response $|\tilde{\beta}_d|$ as

$$|\tilde{\beta}_d(e^{i\omega})| = \begin{cases} 1 & \text{for } \omega \text{ in passbands} \\ 0 & \text{for } \omega \text{ in stopbands} \end{cases} \tag{1.79}$$

Two common approaches to designing $\tilde{\beta}_k$ are the least-squares and the optimal FIR methods. The least-squares approach minimises the integrated squared error between the desired and realised frequency.

$$\arg\min_{\beta_n} \int_0^\pi |\tilde{\beta}_d - \tilde{\beta}_k|^2 d\omega. \tag{1.80}$$

When using this cost function, the maximum error will always appear on the transition edges. This is a L_2 norm problem, and a benefit of this approach is that it is well-established, very fast to solve and produces stable results. The optimal FIR solution is an L_∞ solution, which minimises the maximum error. The cost function in this case is

$$\arg\min_{\beta_n} \max_\omega |\tilde{\beta}_d - \tilde{\beta}_k| \tag{1.81}$$

and can be designed by the Parks-McClellan algorithm [5]. Optimal FIR filters have the property that the ripple is equally large across the entire band. Linear-phase FIR design algorithms are available as functions in Matlab using the functions "firls" and "firpm".

Another approach is to rewrite the filter design problem as a convex optimization problem [6,7]. This can be written as

$$\arg\min_{\beta_n} \quad \delta \tag{1.82}$$

$$\text{subject to} \quad -\delta \leq \tilde{\beta}_d - \tilde{\beta}_k \leq \delta \quad \omega \quad \text{in passbands}$$

$$0 \leq \tilde{\beta}_d - \tilde{\beta}_k \leq \delta\frac{\delta_2}{\delta_1} \quad \omega \quad \text{in stopbands}$$

which gives similar solutions to the least-squares approach, but improves it by always ensuring the ripple constraint is met.

1.2.3 Linear-phase refocusing SLR pulse

To design an SLR spin-echo refocusing pulse, the equivalent $\tilde{\beta}_N$ filter needs to be constrained to ripples [2]

$$\delta_1 = \delta_1^e/4 \tag{1.83}$$

$$\delta_2 = \delta_2^e/\sqrt{2}. \tag{1.84}$$

This designs an RF refocusing pulse, assuming that the FID signals inbetween the excitation and refocusing pulse are perfectly crushed using crusher gradients. This is however an RF refocusing pulse designed in isolation from an excitation pulse.

1.2.4 Matched-excitation refocusing SLR pulse

It is possible to take advantage of having a paired excitation and refocusing pulse into the SLR framework. To do this, we can use Equation 1.73 to design a $\theta = \pi/2$ excitation pulse for an excitation profile which is matched to a refocusing profile $\tilde{\beta}_N$. Using the notation $\tilde{\beta}_{90}$ and $\tilde{\beta}_{180}$ to denote the $\tilde{\beta}_k$ frequency profiles of the excitation and refocusing profiles respectively, we can write

$$\tilde{\beta}_{90} = \tilde{\beta}_k sin(\theta/2) = \frac{\tilde{\beta}_k}{\sqrt{2}}. \tag{1.85}$$

Assuming ideal crusher gradients, a refocusing profile is given by $\tilde{\beta}_k = \tilde{\beta}_{180}^2$, and thus Equation 1.85 can be rewritten as

$$\tilde{\beta}_{90} = \frac{\tilde{\beta}_{180}^2}{\sqrt{2}} \tag{1.86}$$

The transverse magnetization for a spin-echo profile in Cayley-Klein parameters is given by

$$M_{xy,se} = 2\tilde{\alpha}_{90}\tilde{\beta}_{90}\tilde{\beta}_{180}^2 \tag{1.87}$$

Which is the product of an excitation profile and a refocusing profile. $|\tilde{\alpha}_{90}|$ can be expressed in terms of $|\tilde{\beta}_{90}|$, and in this case also in terms of $|\tilde{\beta}_{180}|$ as

$$|\tilde{\alpha}_{90}| = \sqrt{1 - \frac{|\tilde{\beta}_{180}|^4}{2}} \tag{1.88}$$

Substituting Equations 1.86 and 1.88 into Equation 1.87 allows us to express the magnitude of the spin-echo profile as

$$|M_{xy,se}| = 2\sqrt{1 - \frac{|\tilde{\beta}_{180}|^4}{2}} \frac{|\tilde{\beta}_{180}|^2}{\sqrt{2}}|\tilde{\beta}_{180}|^2 \tag{1.89}$$

$$= \sqrt{2}|\tilde{\beta}_{180}|^4 \sqrt{1 - \frac{|\tilde{\beta}_{180}|^4}{2}} \tag{1.90}$$

In the stop-band regions we expect maximum ripples of $|M_{xy,se}| = \delta_2^e$ and $|\tilde{\beta}_{180}| = \delta_2$ in the slice-profile and filter respectively. To derive the stopband ripple relation we can rewrite Equation 1.90 to

$$\delta_2^e = \sqrt{2}|\delta_2|^4 \left(1 - \frac{|\delta_2|^4}{2}\right)^{1/2} \tag{1.91}$$

Since $|\delta_2|^4 \approx 0$ Equation 1.91 can be rewritten as

$$\delta_2^e = \sqrt{2}|\delta_2|^4 \underbrace{\left(1 - \frac{|\delta_2|^4}{2}\right)^{1/2}}_{\approx 1} \tag{1.92}$$

Making the stop-band ripple relation

$$\delta_2 = \left(\frac{\delta_2^e}{\sqrt{2}}\right)^{1/4} \tag{1.93}$$

Similarly, the ripple relation for the passband can be derived between the maximum slice-profile ripple $|M_{xy,se}| = 1 - \delta_1^e$ and the maximum filter passband ripple $|\tilde{\beta}_{180}| = 1 - 2\delta_1$ (following the definitions from [2]) by rewriting Equation 1.90

$$1 - \delta_1^e = \sqrt{2}(1 - 2\delta_1)^4 \left(1 - \frac{(1-2\delta_1)^4}{2}\right)^{1/2} \tag{1.94}$$

The terms in brackets can be rewritten using the binomial approximation, generally written as

$$(1 + x)^n \approx (1 + nx) \qquad \text{if} \qquad |x|n << 1 \tag{1.95}$$

Which allows us to rewrite Equation 1.94 as

$$
\begin{aligned}
1 - \delta_1^e &= \sqrt{2}(1 - 8\delta_1)\left(1 - \frac{(1-8\delta_1)}{2}\right)^{1/2} \\
&= \sqrt{2}(1 - 8\delta_1)\left(\frac{1}{2}(1 + 8\delta_1)\right)^{1/2} \\
&= (1 - 8\delta_1)(1 + 4\delta_1) \\
&= 1 - 4\delta_1 - \underbrace{32\delta_1^2}_{\approx 0} \\
&= 1 - 4\delta_1
\end{aligned}
$$

And finally

$$\delta_1 = \frac{\delta_1^e}{4} \tag{1.96}$$

which are also found in [7].

1.2.5 Minimum-and maximum-phase SLR pulse

Minimum-phase RF pulses produce slice-profiles which contain a non-linear phase across the slice. This property makes them unsuitable as either an excitation or refocusing pulse. They can be used as saturation pulses, or when paired with another minimum-phase RF pulse to produce a refocused echo. The gain in using such pulses is that, for the same TBP as linear-phase pulses, they have narrower transition widths, or equivalently for the same transition width they can have smaller ripples.

The SLR framework allows for the design of optimal minimum-phase FIR filters. For a minimum-phase filter with length N, this can be done by first designing a linear-phase FIR filter with length 2*N-1, adjusting the ripples to $2\delta_1$ and $\delta_2^2/2$, and by using an adjusted D_∞ function

$$D_{\infty,min} = \frac{1}{2}D_{\infty,lin}(2\delta_1, \delta_2^2/2) \tag{1.97}$$

The linear-phase FIR filter is then transformed to a minimum-phase pulse using the Discrete Hilbert Transform (DHT) [3]. The Hilbert transform effectively removes half of the
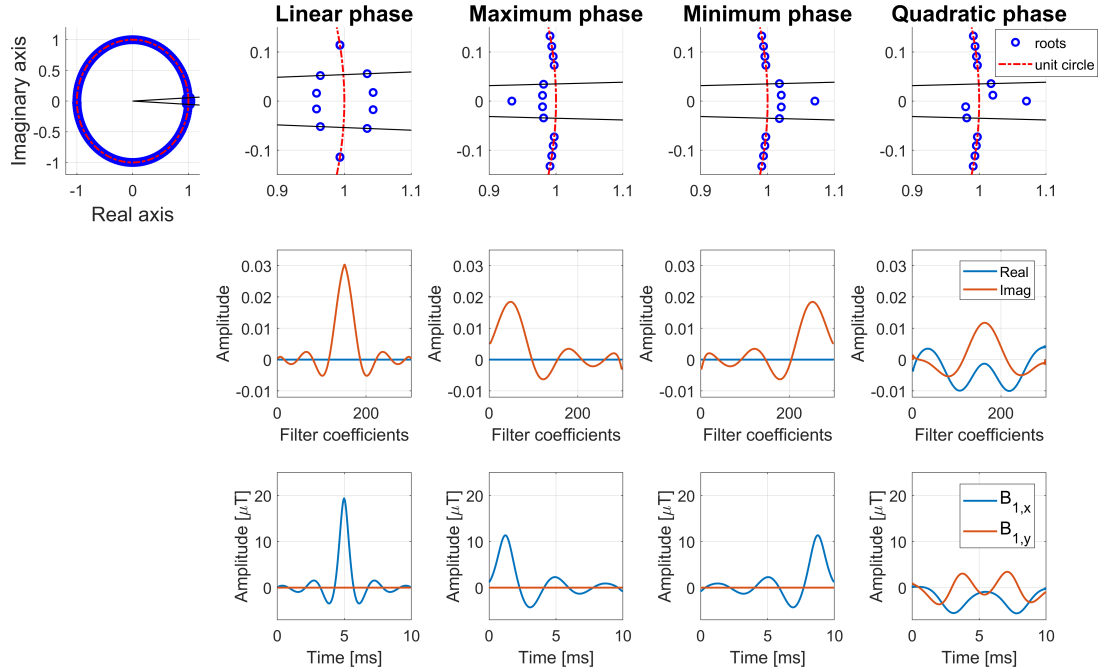
Figure 1.8: Top-row: A plot of polynomial roots on the complex plane. The unit circle is also plotted in the red dotted line for comparison. Linear-phase filters have passband roots alternating about the unit circle. Maximum-phase and minimum-phase filters have all their roots inside and outside the unit circle respectively. A Minimum-phase filter is simply a time-reversed maximum-phase filter, which is equivalent to conjugating and inverting (i.e. "flipping" all the roots. Quadratic-phase filters can be designed by flipping all the roots of a minimum-phase filter which have negative imaginary components, as shown in the top-right figure. **Middle row:** Flipping the roots alters the temporal profile of the filter coefficients as shown. Linear-phase pulses have symmetric filter responses. Maximum-phase filter coefficients have most of their RF aligned at the start of the RF pulse, and the opposite holds for minimum-phase filters. Quadratic-phase pulses show most evenly distributed RF energy over the duration of the filter coefficients. **Bottom row:** Temporal profiles of the corresponding SLR RF pulses, fixed for a duration of 10ms. The temporal profiles resemble the filter coefficients but are not the same.

roots of the linear-phase filter. Plotting the root-representation from Equation 1.71 on the complex plane can reveal this. In addition, the RF pulse is now highly asymmetric, with most of the energy aligned to the end of the RF pulse.

A maximum-phase pulse can be designed by conjugating all the roots as $r_k = r_k^*$. Doing this to all the roots is equivalent to time-reversing all the filter coefficients. This process leads to a change in the phase-profile of $\tilde{\beta}_k$, but retains the original magnitude profile, subject to rescaling by a single real-valued scalar.

1.2.6 Quadratic-phase SLR pulse

Quadratic-phase pulses also produce slices with non-linear phase profiles, making them similar to minimum-phase pulses. Quadratic-phase pulses additionally benefit from having a lower peak RF amplitude than equivalent minimum-phase designs [8]. This is of great

Pulse type	δ_1	δ_2	D_∞	$D_\infty(1\%)$	CK M_{xy}
$\pi/2$ Excitation	$\sqrt{\delta_1^e/2}$	$\delta_2^e/\sqrt{2}$	$D_\infty(\delta_1,\delta_2)$	1.44	$2\tilde{\alpha}_k^*\tilde{\beta}_k$
π se refocusing	$\delta_1^e/4$	$\sqrt{\delta_2^e}$	$D_\infty(\delta_1,\delta_2)$	1.73	$\tilde{\beta}_k^2$
π se " (min ϕ)	$\delta_1^e/2$	$\delta_2^e/2$	$1/2 \cdot D_\infty(\delta_1,\delta_2)$	1.17	$\tilde{\beta}_k^2$
π me refocusing	$\delta_1^e/4$	$(\delta_2^e/\sqrt{2})^{1/4}$	$D_\infty(\delta_1,\delta_2)$	1.44	$\sqrt{2}|\tilde{\beta}_k|^4\sqrt{1-|\tilde{\beta}_k|^4/2}$
π me " (min ϕ)	$\delta_1^e/2$	$\sqrt{\delta_2^e}/(2\sqrt[4]{2})$	$1/2 \cdot D_\infty(\delta_1,\delta_2)$	0.88	$\sqrt{2}|\tilde{\beta}_k|^4\sqrt{1-|\tilde{\beta}_k|^4/2}$

Table 1.1: Summary of ripple relations used throughout this thesis. δ_1 and δ_2 are the filter passband and stopband ripple expressions in terms of desired magnetisation slice-profile ripple δ^e. The D_∞ column shows how to define the function for further processing. For minimum-phase designs the $\delta_{1,2}$ expression shown here already incorporate the adjusted ripples from Equation 1.97. The $D_\infty(1\%)$ column is the corresponding D_∞ function evaluated for 1% ripples, and high values correspond to more constrained designs. Minimum-phase and matched-excitation designs are thus less constrained, allowing for better ripple or transition width performance.

importance for RF saturation pulses with very high TBP and thus high peak RF amplitude requirements. A simple way of designing quadratic-phase RF pulses [9] is to first design a minimum-phase RF pulse with the desired properties, and then transform it into a quadratic-phase pulse by replacing all roots on the lower-half of the unit circle (i.e. all roots with negative imaginary components) by their inverse conjugates. Algebraically, an eligible root r_k is replaced by $(r_k^*)^{-1}$. This procedure is known as "flipping", and flipping individual roots alters the time-alignment of the relevant spectral energy, leading
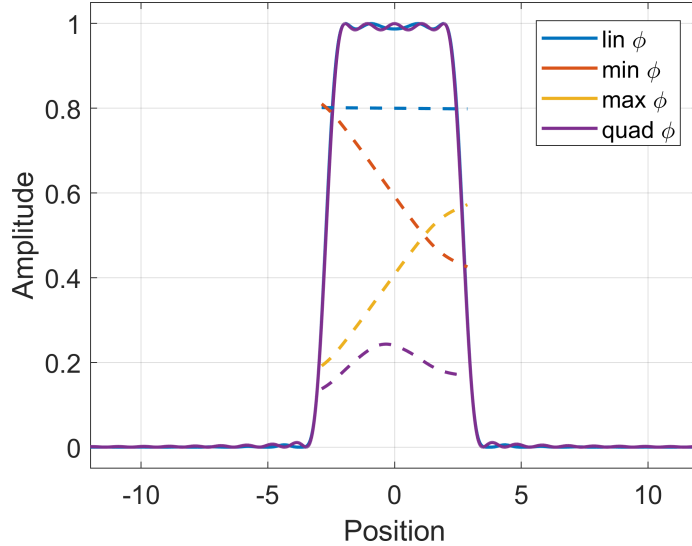
Figure 1.9: Refocusing profiles of the four different RF pulses shown in Figure 1.8. The slice-profile match in $|M_{xy}|$ but have different phase profiles $\angle(M_{xy})$. Linear-phase profiles have constant phase through the slice, indicating that they have no overall phase-contribution on previous phase profiles, as expected from 180° refocusing pulses. Minimum, maximum and quadratic phase profiles are non-linear, and thus would lead to signal loss across the slice. Note that the minimum and maximum phase profiles are roughly conjugates of each other. The magnitude slice-profile between linear and non-linear phase pulses does not perfectly match, however they are designed to have equivalent ripples and transition width.

to different RF shapes, which will be used extensively in Chapters 2 and 3.

Better results in terms of B_1-reduction can be achieved using L_2 [10] or L_∞ [8] filter design approaches, and it is also possible to further enhance B_1-performance by using higher polynomial-phase designs [11]. In this thesis however it was important to design quadratic-phase RF pulses which had matched slice properties as linear-phase and minimum-phase RF pulses, and so a design derived from a minimum-phase RF pulse was best suited.

Figure 1.8 shows the root-patterns, filter coefficients and subsequent RF pulses for a π spin-echo refocusing pulse in the case of linear, maximum, minimum and quadratic-phase pulses with TBP=8.

In this example we have designed all pulses with the convex optimization approach to have equivalent ripples of $\delta_1 = \delta_2 = 0.01$ and transition width, such that these pulses can be directly compared against each other. This is pertinent for a meaningful comparison of RF pulses, with equivalent slice characteristics as conducted in chapters 2 and 4. To obtain equivalent transition width, Equations 1.78 and 1.97 are used to set the time bandwidth product of the minimum-phase (and thus maximum and quadratic-phase pulses) as following

$$W_{lin} = W_{min}$$
$$\frac{D_\infty(\delta_1, \delta_2)}{TBP_{lin}} = \frac{1/2 \cdot D_\infty(2\delta_1, \delta_2^2/2)}{TBP_{min}}$$
$$TB_{min} = TB_{lin} \frac{D_\infty(2\delta_1, \delta_2^2/2)}{2D_\infty(\delta_1, \delta_2)} \tag{1.98}$$

The slice-profiles for the RF pulses in Figure 1.8 are shown in Figure 1.9. By using the correct ripple relations, and setting the TBP as in Equation 1.98 we can indeed design RF pulses with equivalent slice-profiles. However it needs to be noted that the slice-profiles do not perfectly match, but only have equivalent transition and ripples to a high enough degree. Such small inconsistencies are inherited from the SLR method. The spin-echo refocusing example from Figures 1.8 and 1.9 can be repeated for matched-excitation design using the ripple relations in Table 1.1.

1.2.7 Multiband RF pulse design

Multiband Imaging

Multiband imaging is the practice of exciting multiple slices (i.e. frequency bands), and thus acquiring k-space data from multiple slices simultaneously. The earliest methods in multiband imaging stemmed from studies where multiple slices were excited for an SNR benefit [12, 13], due to the signal being reconstructed from twice as many samples but in the same amount of time as single-slice imaging. This has also been used in volume imaging [14]. Larkman et al used multiband pulses for accelerated imaging, by

using coil sensitivities to separate the slices [15]. Such multi-coil reconstruction has been greatly improved by acquiring slices with CAIPIRINHA, which intentionally moves aliasing in space such that the slice unfolding process is better conditioned. This is done by altering the phase distribution for different slices [16, 17]. An implementation of this was shown in Nunes et al [18] by k-space ramps in the slice-select direction. This was later improved by blipped-CAIPI, [19] which avoids signal dephasing caused by the earlier method. The blip-area depends on the slice-separation and the shift pattern desired. This is an intuitive result when considering SMS acquisition and reconstruction as a 3D multidimensional framework [20], where multiband data with aliased slices is compared to volumetric MRI acquired with undersampling in the slice-direction. It is furthermore also possible combine undersampling in both phase-enoding and slice-encoding direction [20]. A range of multiband reconstruction techniques have been proposed, such as 3D SENSE [20], 3D GRAPPA [21] and slice-GRAPPA [19, 22].

Brain MRI has been the main domain for multiband imaging, especially for higher temporal resolution in functional MRI and to collect more data in difussion sequences [23]. In the latter, an interesting development is MB combined with gSlider [24]. Other imaging methods include MB TSE sequences combined with WAVE-CAIPI [25]. Multiband applications have also been tested on cardiac bSSFP applications [26–28] as well as in combination with quantitave imaging, such as magnetic resonance fingerprinting [29–31] and triple echo steady-state imaging [32, 33].

The limitation on the acceleration factor for multiband imaging depends on a range of factors, including the number of receiver coils, and the coil geometry in use, but also on the number of slices excited, and whether this fits in within sequence SAR and hardware constraints. The latter factor was prominent and got people investigating pulse design techniques to reduce the peak B_1 amplitude. For a review on multiband imaging readers are referred to Barth et al. [34]. The rest of this section will focus on existing multiband RF pulse design methods.

Phase-optimizing

The small-tip angle approximation simplifies the relation between B_1 pulses and resultant transverse magnetisation to a Fourier relation [1]. This is pertinent to multiband pulse design, since the simplest method for producing a multiband pulse $b(t)$ is to take a singleband pulse $p(t)$ and multiply it by a modulation function $f(t)$ [15]

$$b(t) = p(t) \sum_{n=1}^{MBF} e^{i\omega_n t} = p(t)f(t). \tag{1.99}$$

Here ω_n are the frequency offsets for the replica slices, numbered from $n = 1$ to MBF (multiband factor). The Fourier convolution theorem dictates that in the Fourier domain

$$\tilde{b}(\omega) = \tilde{p}(\omega) * \tilde{f}(\omega) \tag{1.100}$$

where $\tilde{f}(\omega)$ is an array of delta functions centered on ω_n.

The problem with this technique is that the peak amplitude increases linearly with the number of slices. The peak power demanded from RF amplifiers relates quadratically to the peak amplitude, making such designs unfeasible. An illustration of this is shown in Figure 1.10.
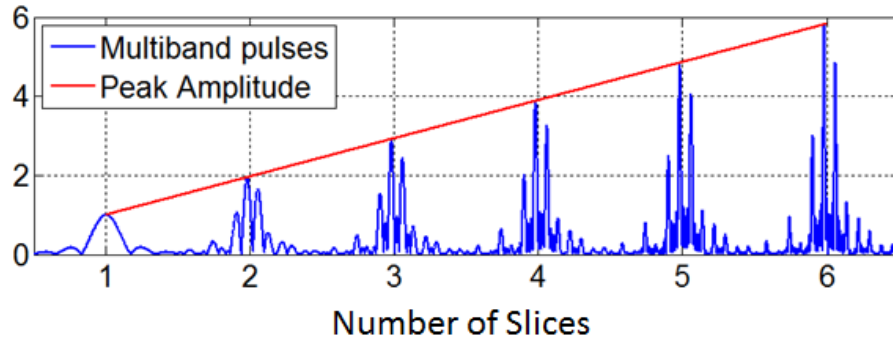
Figure 1.10: The relationship between peak amplitude of an RF pulse and the number of slices it excites is linear. This becomes problematic for peak power demands on RF hardware, which scales quadratically with peak RF amplitude.

One solution to the peak-amplitude problem is to offset the phase for individual slices of the modulation function $f(t)$, since the phase-offset of each slice does not necessarily need to be aligned [35–37]. Adding phase-offset values ϕ_n to the modulation function implies

$$f(t) = \sum_{n=1}^{MBF} e^{i(\omega_n t + \phi_n)} \qquad (1.101)$$

where ϕ_n can vary between -180º and 180º. The peak amplitude of $|f(t)|$ can be minimized by numerically optimizing the values of ϕ_n. When MBF is odd valued, the central slice must be dealt with separately. Note that the optimal set of phase-offsets for a multiband factor is independent of the single-band pulse $p(t)$. The slice separation is also independent assuming that the modulation envelope $f(t)$ is significantly faster than the single-band envelope, which is not always true for low slice separations. This is a straight-forward and thus a common method for designing multiband pulses. It preserves the linear-phase structure of excitation profiles, and thus can be used for both gradient-echo and spin-echo sequences. This can be combined with CAIPIRINHA excited phase-offsets [38] which requires a more constrained optimization for $f(t)$. Alternatively, the unconstrained optimization can be combined with blipped-CAIPI [19].

Time-shifting

Another possibility is to temporally offset individual single-band waveforms in time to avoid constructive interference as much as possible, as shown by Goelman [36] and more recently by Auerbach [39]. This technique can be combined with phase-optimization for

each singleband waveform. The aggregated multiband pulse is characterised as

$$b(t) = \sum_{n=1}^{MBF} p(t - \tau_n)e^{i(\omega_n t + \phi_n)} \tag{1.102}$$

where τ_n is the temporal-shift variable for each single-band pulse. In contrast to phase-optimizing, the optimal solution depends on the singleband waveform $p(t)$ so optimal time and phase-offsets must be evaluated for each design case. The bandwidth of the composite MB pulse is the same as each underlying singleband pulse. An illustration of a time-shifted design is shown in Figure 1.11.
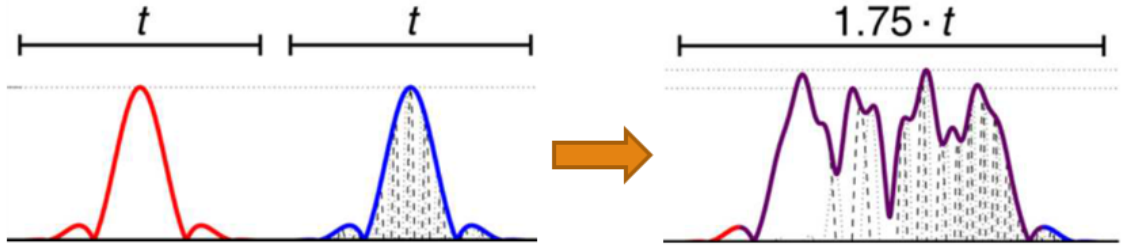
Figure 1.11: An illustration for the time-shifting technique. Two singleband pulses are temporally offset and summed together. Adapted from [39]

Root-flipping

Root-flipping, as proposed by Sharma et al [7], takes a direct approach to multiband pulse design using the Shinnar Le-Roux (SLR) method [2]. First, a maximum-phase multiband filter is designed using the techniques described in section 1.2.5. As shown, when roots are plotted on the complex plane, they are scattered around the unit circle. Flipping passband roots inside or outside the unit circle redistributes the contributions associated with those frequencies across the duration of the filter coefficients β_n. The filter coefficients are then used to evaluate $\tilde{\alpha}_k$ using Equations 1.74, 1.75 and 1.77. An illustration of this is shown in Figure 1.12. The optimal root-flipped pulse will have a root-pattern which results in an RF pulse with the minimum peak RF amplitude. An exhaustive search strategy to find this root-pattern would be computationally impractical, and so a Monte-Carlo approach is taken to iteratively start from a maximum-phase pulse and randomly select a number of roots to flip outside the unit circle. This concept is an extension to the design of quadratic-phase pulses in the single-band case, and has also been shown to be effective for high TBP inversion pulses [40] as well as useful for gSlider difussion imaging [41].

VERSE

Phase-optimization, time-shifting and root-flipping optimize B_1-envelopes for constant-valued selection gradient waveforms, as it allows for the parametric SLR design. However
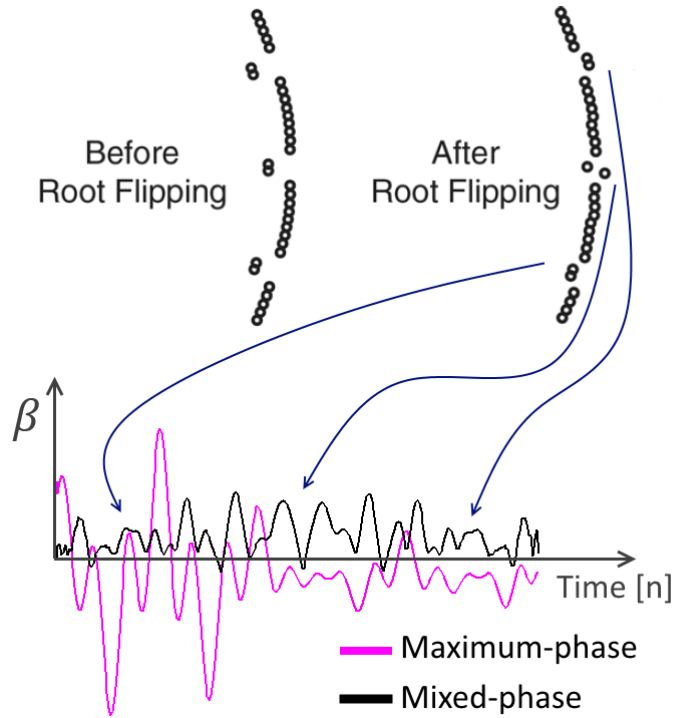
Figure 1.12: An illustration of the effect of flipping polynomial roots on the β_n, and subsequently the RF pulse. Only one combination of root-flip pattern is shown, and by randomizing the pattern iteratively we can find the combination that leads to the minimum RF peak amplitude. Adapted from [7]

once designed, the RF and gradient waveforms can be reshaped using Variable-Rate Selective Excitation (VERSE) [42]. The key to the VERSE-method is that the magnetisation vector at the end of transmission of B_1 and gradient fields depends on the total rotation per unit time rather than the rate of rotation. Mathematically, the rotation Θ of the magnetisation vector during a period Δt can be expressed as

$$\Theta = \gamma(B_1 + \vec{G} \cdot \vec{r})\Delta t = \omega \Delta t \tag{1.103}$$

For a given RF and gradient waveform it is possible to reduce all B_1 and gradient amplitudes by a value α, and increase the period Δt by the same value. The resulting magnetisation vector will be the same as long as the net rotation is maintained. Taking this further, for RF and gradient waveforms $B_1(k)$ and $G(k)$ with a fixed sampling time Δt, we can define a time-variable $\alpha(k)$ of equal length. VERSE waveforms can then be written as

$$B_1^v(k) = \alpha(k) \cdot B_1(k), \tag{1.104}$$

$$G_1^v(k) = \alpha(k) \cdot G(k), \tag{1.105}$$

$$t^v(k) = t(k)/\alpha(k) \tag{1.106}$$

where $\alpha(k)$ can be found subject to desired constraints. A simple example of this is shown in Figure 1.13, where the peak RF amplitude is reduced by using two different gradient amplitudes across the pulse duration. The minimization allows one to constrain the
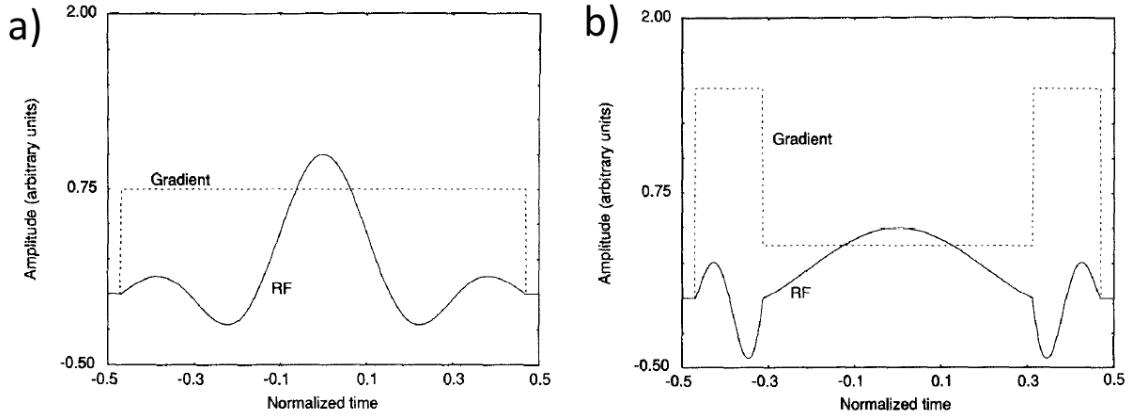
Figure 1.13: An illustration of the workings of the VERSE algorithm adapted from the original publication [42]. The original waveforms (a) are manipulated to have two distinct rates of excitaiton. The gradient amplitude is increased when the original RF amplitude is low, and decreased down when the RF amplitude is high.

solution for a system peak B_1 amplitude, peak gradient amplitude and peak gradient slew-rate. The downside any time-variable gradient technique is that the change in gradient amplitude causes the slice profile at off-resonant frequencies to degrade.

Time-optimal VERSE designs

The VERSE algorithm can also be reframed to a time-optimal problem, which was first explored by Hargraves et al. [43]. Lustig et al. in [44] provided a comprehensive closed-form solution for the problem of faster k-space coverage during the receive phase of a sequence. The same concept can be translated to the transmit phase, which was shown by Lee et al. [45]. This study improves on the original VERSE method by formalising it in a more mathematically rigid framework, supporting a non-iterative solution, and an extension to multi-dimensional and parallel transmit pulse design.

The time-optimal algorithm takes as an input a combination of RF and gradient waveforms, and evaluates a excitation transmit trajectory based on these two waveforms. The path can be described as

$$C(p) = (x(p), y(p), z(p)) \tag{1.107}$$

where p is the path in 3D k-space. As the waveforms are played, the path has a varying velocity and acceleration which are two differentials, which makes time-optimal design too difficult. When the path is broken up into small line segments and the path p is reparametrised as an Euclidean arc-length with a variable s, Equation (1.107) can be rewritten as

$$C(s) = (x(s), y(s), z(s)) \tag{1.108}$$

where s is a k-space variable, which is defined as

$$s(t) = \gamma \int_0^t G(\tau) d\tau \tag{1.109}$$

37

which has a domain between $[0, L]$, L being the length of the path. In this new definition the velocity at each line-segment is constant (assuming the line segment is sufficiently small) and the acceleration is equal to the curvature at that specific point along the curve. In other words, the magnitude of velocity can be written as

$$|C'(s)| = 1 \tag{1.110}$$

and the magnitude of acceleration is equal to the curvature at that line-segment. More-over, the curvature can be found as the reciprocal of the radius of a circle touching the path.

$$|C''(s)| = \kappa(s) = \frac{1}{r(s)} \tag{1.111}$$

The circle has equivalent first and second derivatives as the line segment. This property from the arc-length parametrisation allows the time-optimal problem to be reduced in complexity. An illustration of a path in terms of arc-length is shown in Figure 1.14.
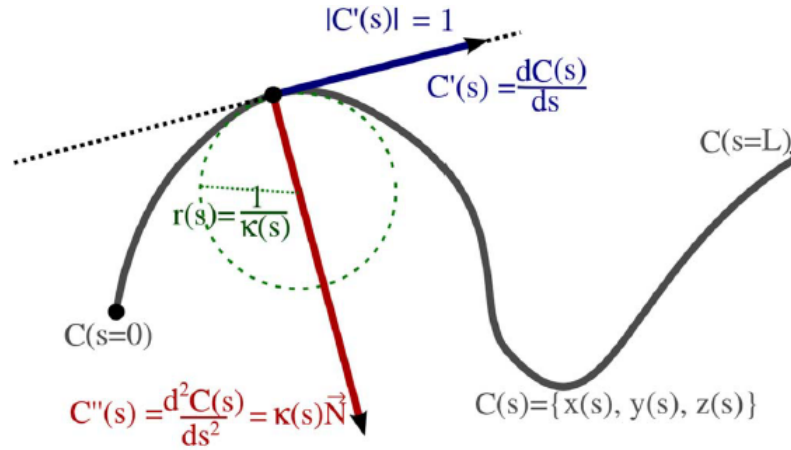
Figure 1.14: Parametrization in arc-length space for the time-optimal VERSE algorithm. Adapted from [44]

The time-optimal gradient trajectory can be calculated for any trajectory in k-space, and was originally proposed for data acquisition [44]. The contribution from Lee et al. [45] is the addition of an RF-amplitude constraint, which is incorporated as an additional gradient constraint. This modified algorithm designs a combination of VERSE RF and gradient waveforms $B_1^v(s)$ and $G^v(s)$ that take the quickest route from start to end subject to hardware constraints. The slice-profile before and after VERSE will be preserved as long as the ratio $W(s)$ is

$$W(s) = \frac{B_1(s)}{G(s)} = \frac{B_1^v(s)}{G^v(s)} \tag{1.112}$$

These waveforms can be converted from s to a regular path p (which simply corresponds to time) by inverting Equation 1.109.

An example of applying time-optimal VERSE on a multiband 4 RF pulse is shown in Figure 1.15. In this example a 4.9-fold reduction in pulse duration could be achieved, compared to a phase-optimized RF pulse. Such time-optimal VERSE implementations have been

used in the ISMRM multiband RF pulse challenge [46] as well as for other multiband applications [47], and is used in chapters 4 and 5 of this thesis. It is worth nothing that the work discussed in this chapter only uses a single gradient during transmit which results in a 1D k-space trajectory.
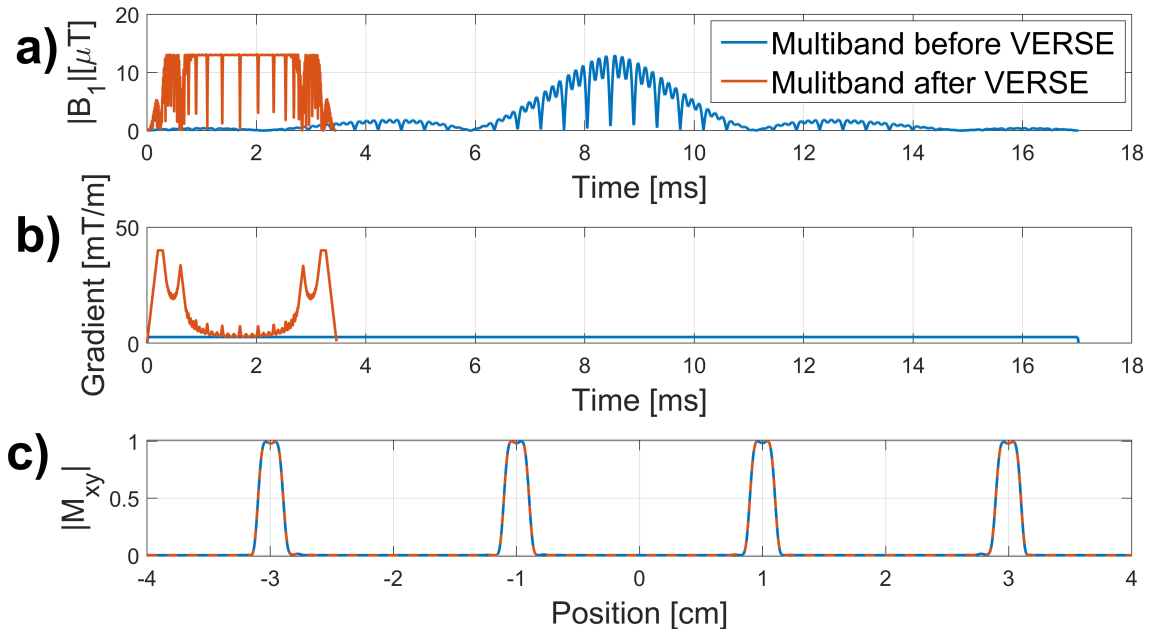
Figure 1.15: An example of applying time-optimal VERSE on a phase-optimized Multiband 4 pulse results in a 4.9-fold reduction in pulse duration. **a)** shows both RF pulses subject to a 13 μT peak-amplitude constraint. **b)** shows both gradient, where the VERSE gradient is subject to a peak amplitude of 40 mT/m and a peak slew-rate of 200 $mT/m/ms$. **c)** shows both slice-profile overlapping, to clarify that the resultant slice profile remains unchanged.

PINS and Multi-PINS

In 2011, Norris et al. [48] introduced a multiband pulse design method which intentionally causes aliasing in the spatial domain. From Fourier theory, we know that discretised time-signals have Fourier transforms which are periodic at the sampling frequency. In the PINS method this relationship is used for multiband excitation by undersampling a singleband RF pulse, which means that replicas of the slices appear at frequencies lower than the original Nyquist frequency. The relative separation between the slices can be controlled by the undersampling rate, whilst the slice thickness can be controlled by the gradient strength. This is illustrated in Figure 1.16.

In the ideal case of having infinitely short RF subpulses, an inifinite number of slices would be excited. In reality however RF subpulses have finite sampling duration, which can be seen as convolving the RF subpulses with a rect-function. According to the convolution theorem this corresponds to the sinc-modulation of the excited slices, which is an undesired effect. PINS pulses are designed by alternating undersampled RF blips, with gradient blips in between. The gradient area of all gradient blips needs to correspond to that of
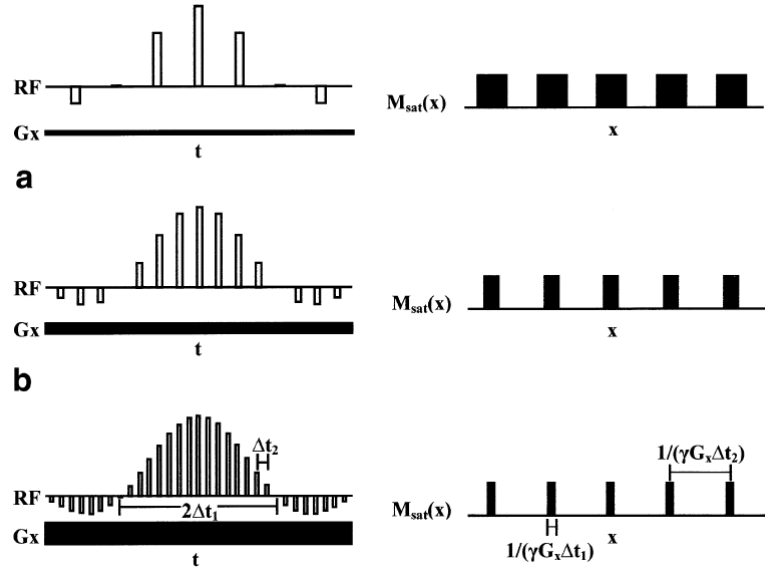
Figure 1.16: Three different methods of under-sampling a sinc waveform, and their associated excitation profile. Different sampling rates and pulse bandwidths can be used to control the multi-slice saturation profile. Note that these are not PINS pulses, as the power does depend on the number of slices. Adapted from [49]

the equivalent constant gradient. The alternating gradient blips mean that no gradient is active during RF transmission, and from the perspective of the excitation transmit trajectory RF blips appear infinitely short, which avoids the sinc-modulation of excited slices. A later technique proposed by Eichner et al [50], where RF during gradient blips were replaced by samples of conventional multiband pulses. The relative contributions between PINS and multiband excitation can be optimized to reduce pulse duration or pulse energy. An illustration of this is shown in Figure 1.17.

1.3   Bloch equation simulations

1.3.1   Matrix decomposition

To assess the performance of RF pulses, the magnetisation vector in the context of B_1 and gradient fields $\vec{G}$, based on the Bloch equations can be solved. Ignoring relaxation effects, the Bloch equations can be written in matrix form as shown in Equation 1.24. This is a system of ordinary differential equations, which can be solved by using matrix decomposition to evaluate its matrix exponential. The general solution is given by the equation

$$\vec{M} = \vec{\sigma}e^{\lambda t} \tag{1.113}$$

where σ and λ are eigenvector and eigenvalues of the 3x3 rotation matrix, respectively. Computationally, the RF and gradient waveforms are discretised in time, and the magne-
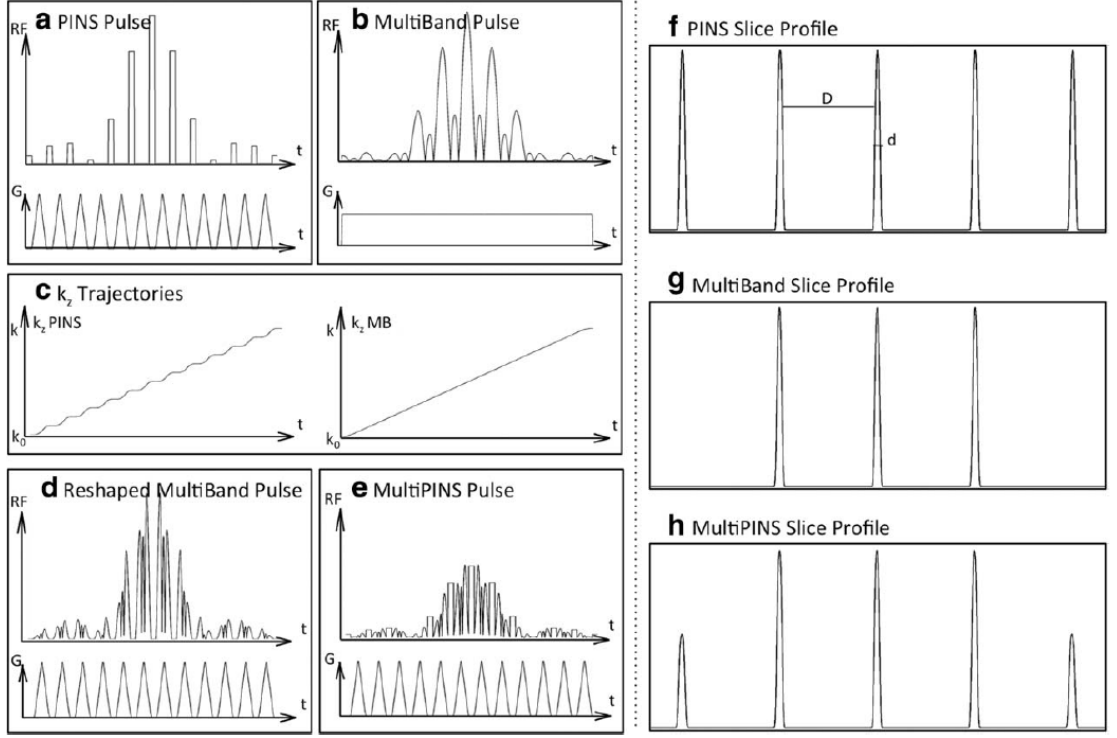
Figure 1.17: a) A PINS pulse as proposed by [48]. **b)** A typical multiband pulse. **c)** The two k_z moments for the PINS (left) and multiband case (right) as a function of time. Because the PINS gradient waveform is turned on-and off repeatedly, the integral function shows a step-wise behaviour. **d)** An altered multiband pulse to follow the gradient trajectory of the PINS pulse. This can be designed using VERSE. **e)** A plot of a Multi-PINS pulse, where the altered multiband pulse is played out when the gradient is on, and the PINS pulse is played out when it is off. **f-h)** Slice profiles as annotated, with slice-separation D and slice-thickness d. Complete figure adapted from [50].

tization vector can be calculated iteratively using

$$\vec{M}_t = \vec{C}\vec{\sigma}e^{\lambda\Delta t}\vec{M}_{t-1} \tag{1.114}$$

Where Δt is the sampling time, and C is set using initial conditions $\vec{C} = \vec{M}_{t-1}\vec{\sigma}^{-1}$. This evaluation includes eigen-decomposition and a matrix inversion, and is computationally expensive. However, it makes no other assumptions about the structure of the matrix and is thus numerically reliable.

1.3.2 Cayley-Klein representation

The spinor representation of the Bloch equations has already been introduced in the context of the SLR transform. The Cayley-Klein parameters can be found for any RF pulse, regardless of how it is designed, using the forward SLR method as described in section 1.2.2. A spin-domain rotation matrix is given by (similar to Equation 1.42)

$$Q = \begin{pmatrix} \alpha & -\beta^* \\ \beta & \alpha^* \end{pmatrix} \tag{1.115}$$

The relationship between the magnetisation vector and the Cayley-Klein parameters is shown in Equation 1.44, repeated here for convenience.

$$\begin{pmatrix} M_{xy}^+ \\ M_{xy}^{+*} \\ M_z^+ \end{pmatrix} = \begin{pmatrix} (\alpha^*)^2 & -\beta^2 & 2\alpha^*\beta \\ -(\beta^*)^2 & \alpha^2 & 2\alpha\beta^* \\ -\alpha^*\beta^* & -\alpha\beta & \alpha\alpha^* - \beta\beta^* \end{pmatrix} \begin{pmatrix} M_{xy}^- \\ M_{xy}^{-*} \\ M_z^- \end{pmatrix}$$

Assuming an initial magnetisation $M^- = (0, 0, M_0)^T$, The transverse magnetisation after an excitation pulse is given by

$$M_{xy,exc} = 2\alpha^*\beta M_0 \tag{1.116}$$

It is also possible to simulate a rewind gradient in this framework. A gradient-induced rotation causes a phase-profile over position x given by

$$\phi(x) = -x\gamma \int_0^T G(t)dt \tag{1.117}$$

where T is the gradient duration. This will produce a rotation expressed in spin domain as

$$R_{rew} = \begin{pmatrix} e^{-i\phi/2} & 0 \\ 0 & e^{i\phi/2} \end{pmatrix} \tag{1.118}$$

Therefore, any state-space rotation in Equation 1.115 followed by a gradient induced rotation is given by

$$Q \cdot R_{rew} = \begin{pmatrix} \alpha e^{-i\phi/2} & -\beta^* e^{i\phi/2} \\ \beta e^{-i\phi/2} & \alpha^* e^{i\phi/2} \end{pmatrix} \tag{1.119}$$

Comparing Equations 1.115 and the first column in 1.119 shows that both α and β are multiplied by a term $exp(-i\phi(x)/2)$. We can thus rewrite Equation 1.116 as

$$M_{xy,exc,rew} = 2\alpha^*\beta e^{-i\phi} \tag{1.120}$$

which gives the known result, that a slice-gradient after an excitation pulse results in a space-dependent phase-roll.

Another interesting application is the simulation of a spin-echo profile. In this case the initial magnetisation can be assumed to be $M^- = (M_{xy}, M_{xy}, 0)^T$, and so the transverse magnetization after the refocusing pulse is

$$M_{xy}^+ = (\alpha^*)^2 M_{xy}^- - \beta^2 M_{xy}^{-*} \tag{1.121}$$

Placing crusher gradients around a refocusing pulse alters the state-space rotation to

$$R_c Q R_c = \begin{pmatrix} \alpha e^{-i\phi} & -\beta^* \\ \beta & \alpha^* e^{i\phi} \end{pmatrix} \tag{1.122}$$

Comparing matrices 1.115 and 1.122 as before, we see that the α term has been multiplied by a term $exp(-i\phi)$, whilst the β term is unchanged. We can thus rewrite Equation 1.121 as

$$M_{xy}^+ = (\alpha^*)^2 e^{i2\phi(x)} M_{xy}^- - \beta^2 M_{xy}^{-*} \tag{1.123}$$

In this expression, only the first term is affected by the crusher gradients. Given that the crusher gradients surrounding the refocusing pulse will create a sufficiently large phase-roll across the slice profile, the integrated signal will sum this term to zero. Thus Equation 1.123 can be rewritten as

$$M_{xy}^+ = -\beta^2 M_{xy}^{-*} \tag{1.124}$$

Another useful property of spin-domain representation is that we can simulate Cayley-Klein parameters for different RF pulses, and assess a composite slice profile. For example, a spin-echo sequence formed of an excitation pulse, followed by a rewind gradient, crusher gradients and a refocusing pulse can all be found as

$$M_{xy,comp} = 2\alpha_{exc}\beta_{exc}^* e^{i\phi_{rew}}\beta_{ref}^2 M_0 \tag{1.125}$$

Finally, for any of these cases it is also possible to investigate the resulting longitudinal magnetization, when starting from $M^- = (0, 0, M_0)^T$, as

$$M_z^+ = (|\alpha| - |\beta|)M_0 \tag{1.126}$$

and this can be scaled in terms of flip-angle (between 0-180º) as

$$FA(x) = \arccos(M_z(x)) \tag{1.127}$$

This representation is computationaly faster than the matrix-decomposition technique, and allows for B_1 and B_0 inhomogeneity terms. However it is not possible to include relaxation terms.

1.3.3 Bloch-equation spin-echo simulations

To assess the spin-echo behaviour of excitation and refocusing pulses, T_2^* needs to be simulated.

Spin-echoes occur when two RF pulses are played, interleaved with a time-period during which spinors within a voxel are dephasing. The peak of the spin-echo will occur at twice the dephasing period, when spinors are rephased as a consequence of the second RF pulse. The mechanism which allows for spin-echoes is T_2^*, which is a combination of both T_2 and T_2' given by

$$T_2^* = \Big(\frac{1}{T_2} + \frac{1}{T_2'}\Big)^{-1}. \tag{1.128}$$

Here T_2 is the relaxation parameter for transverse magnetization, and T_2' describes the loss of local phase coherence in a measured voxel. Importantly, T_2' is a decay term which is reversible by applying a subsequent RF pulse, whilst T_2 is irreversible. The spin-echo signal is generally observed to peak according to T_2 decay, and in addition decay away exponentially in time. It can therefore be assumed that the off-resonant frequencies which lead to the T_2' effects are Lorentzian distributed, with full-width-half-maximum spread ΔB_0 such that

$$T_2' = 2\pi/(\gamma\Delta B_0). \tag{1.129}$$

In order to simulate spin-echo effects both T_2 and T_2^* need to be simulated simultaneously. T_2 and T_1 can be simulated by adding relaxation terms to Equation 1.24

$$\begin{pmatrix} \dot{M}_x \\ \dot{M}_y \\ \dot{M}_z \end{pmatrix} = \gamma \begin{pmatrix} -1/T_2 & \vec{G}\cdot\vec{r} & -B_{1,y} \\ -\vec{G}\cdot\vec{r} & -1/T_2 & B_{1,x} \\ B_{1,y} & -B_{1,x} & -1/T_1 \end{pmatrix} \begin{pmatrix} M_x \\ M_y \\ M_z \end{pmatrix} + \begin{pmatrix} 0 \\ 0 \\ M_0/T_1 \end{pmatrix} \tag{1.130}$$
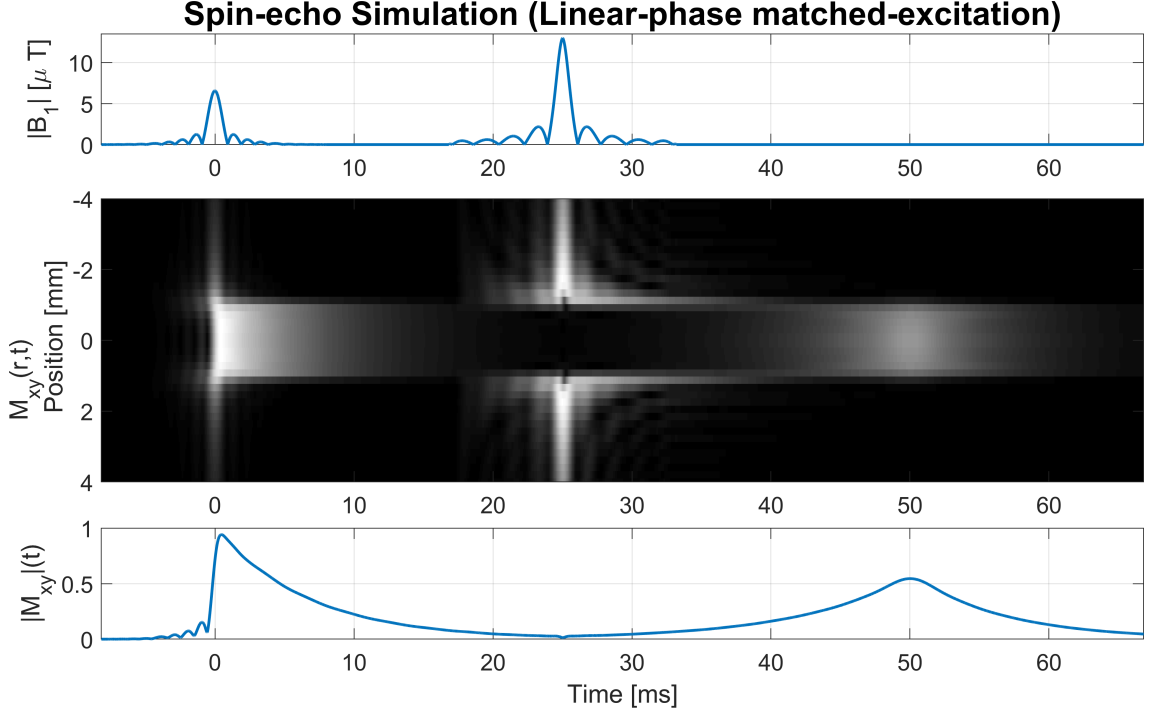
Figure 1.18: A 90-180° spin-echo simulation using matched-excitation refocusing pulses for a 2mm slice. The top row shows RF pulses, and the middle row shows the magnitude of the evolution of transverse magnetisation. The bottom row shows the integrated signal across the slice. The signal peaks shortly after the center of the excitation pulse, before decaying away exponentially due to T_2'. The refocusing pulse is peaked at t=25ms, and hence the echo-time TE=50ms. The Lorentzian weighting in the imaginary spatial direction ensures an exponential T_2' decay

To simulate the T_2', the distribution of spinors can be modelled as a distribution of isochromates with a range of precession frequencies that describe a Lorentzian distribution. Integrating across all isochromats will sum to the signal expected within one imaging voxel. If all isochromats are in-phase this will result in maximal signal, and vice-versa when all isochromats are perfectly out of phase, the overall signal will be annulled. An ensemble of isochromats can be represented by a sum of complex exponentials and the integral can be expressed as:

$$\int_{f_0}^{f_1} A(f)e^{i2\pi ft}df = a(t) \tag{1.131}$$

Here $a(t)$ is observed to be an exponentially decaying function of the type

$$a(t) = e^{-t/T_2'} = e^{-tR_2'} \tag{1.132}$$

and so $A(f)$, which is the Fourier transform of $a(t)$, is the Lorentzian function

$$A(f) = \frac{1}{\pi} \left(\frac{R_2'}{(R_2')^2 + f^2} \right) \tag{1.133}$$

We therefore know that ΔB_0 has the shape of a Lorentzian.

Figure 1.19: A 90-180º spin-echo simulation using a matched-excitation quadratic-phase refocusing pulse, similar to Figure 1.18. The RF pulses in the top row have a move even B_1-amplitude distribution, allowing them to be much shorter. The quadratic-phase refocusing pulse is 4.5ms compared to the 16.4ms refocusing duration in the linear-phase case. This is achieved by exciting and refocusing different sections of the slice over time, which results in a slight spatial slope in the refocused echo (middle row, around TE=50ms)

Computationally, T_2 relaxation can be modelled by solving Equation 1.130, and dephasing within each voxel can be modelled by an imaginary spatial axis in the Bloch equations. Simulating an ensemble of isochromats on this spatial axis with a background gradient $G_{\Delta B_0}$, emulates the dephasing of isochromats in the transverse plane. Integrating for a range of frequencies $f = \frac{k}{T_2'}$ leads to a realistic evolution within a voxel, where the values of k needs to be determined. The imaginary background gradient can be set as

$$G_{\Delta B_0} = \frac{2\pi k}{\gamma \Delta z T_2'} \tag{1.134}$$

where Δz denotes the voxel-size.

We can thus retrieve an exponentially decaying T_2' effect by multiplying the spatial axis by an Lorentzian weighting function. Alternatively it is possible to simulate a non-uniformly distributed spatial axis with a Lorentzian density, which should give a similar effect. The Bloch equations can be solved using a range of matrix exponential solvers. Furthermore,

the definition of f should be chosen with care. If not enough frequency-points are chosen (i.e. not enough isochromats within each voxel) a "ghost" spin-echo can occur without a second RF pulse present. Similarly, the domain of f needs to be sufficiently large to capture the spectral characteristics of the Lorentzian.

In theory the two RF pulses can have any two flip-angles, as any initial RF pulse will produce some transverse magnetisation, and any subsequent RF pulse will rephase some transverse magnetisation to form a spin-echo. The highest signal is achieved when using a 90° excitation pulse followed by a 180° refocusing pulse. Such an example is shown in Figure 1.18 for a linear-phase matched-excitation RF pulse, designed as described in section 1.2.4 with TBP=8. This example used $T_2 = 80ms$, $T_2^* = 45ms$, $T_1 = \infty$ and an echo-time of $50ms$. An equivalent quadratic-phase simulation is shown in Figure 1.19, with notably shorter RF pulses. Specifically, the linear-phase refocusing pulse was 16.4ms, whereas the quadratic-phase refocusing pulse was only 4.5ms. From close inspection it can be seen that due to the quadratic phase-structure of this pulse, different sections of the slice become excited and refocus at different times.

1.4 MRI engineering

Multiband MRI can often place significant demands on MR hardware. This is particularly true for transmit hardware involved in generating RF and gradient waveforms. For RF transmission, pulse envelopes are specified by the MR user in the console room and transferred to an equipment room for amplification, which are subsequently transmitted by an RF transmit coil.

Gradient waveforms are similarly amplified and transmitted by gradient coils. A diagram of the MR equipment involved is shown in Figure 1.20.

This section will cover transmit hardware specifications related to this thesis.

1.4.1 RF transmission

RF pulses as specified by the host computer are considered as envelopes. An RF pulse consists of both a real and imaginary component

$$B_1(t) = B_{1,x}(t) + iB_{1,y}(t).$$

Another useful complex representation is in terms of magnitude and phase

$$B_1(t) = |B_1(t)|e^{i\angle(B_1(t))} \tag{1.135}$$

On our Philips 3T Achieva (Philips Healthcare, Best, The Netherlands) system in particular, complex RF envelopes are specified as signed amplitude modulation and signed fre-
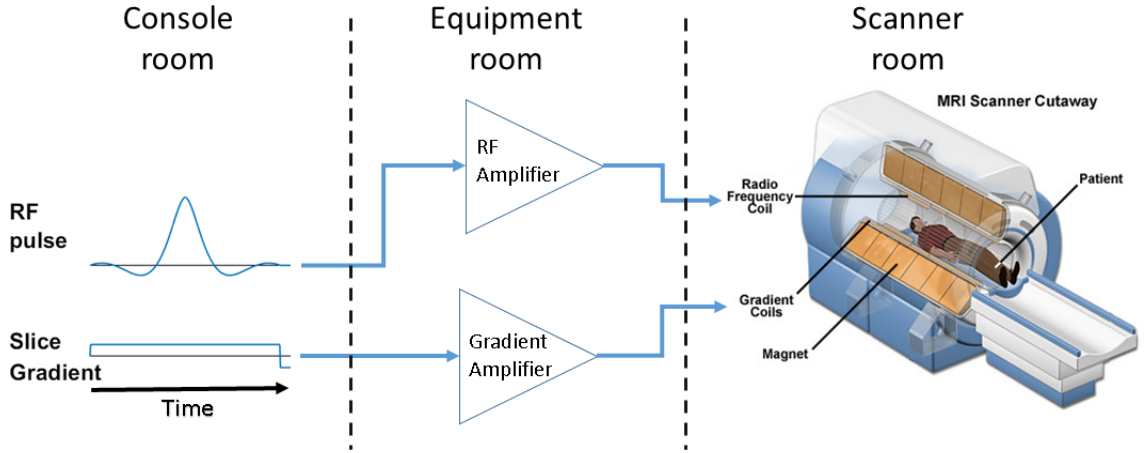
Figure 1.20: Diagram of RF and gradient hardware. Both RF and gradient waveforms are specified in the console room by the MR user. RF pulses are amplified in an separate equipment room, before being transmitted by the RF coil in the scanner room. Gradient waveforms are also amplified, before being sent to the gradient coils. The RF coil is relatively smaller and designed to deposit RF energy as effectively as possible. Gradient coils are larger, and designed to create a spatially varying magnetic field which is as linear as possible. The main superconducting magnet is significantly larger and remains on at all times.

quency modulation waveforms. We can rewrite Equation 1.135 as an FM-waveform

$$B_1(t) = B_{1,AM}(t)e^{i\Theta} \tag{1.136}$$

$$= B_{1,AM}(t)e^{i(2\pi f_i(t)t)} \tag{1.137}$$

where $f_i(t)$ is the instantaneous frequency, given by

$$f_i(t) = f_0 + B_{1,FM}(t) \tag{1.138}$$

Where f_0 is a constant carrier frequency, and $B_{1,FM}$ can be found as the derivative of the instantaneous phase defined as

$$\Phi_i = \int \frac{d\Phi}{dt}dt = 2\pi f_0 t + 2\pi \int_0^t B_{1,FM}(\tau)d\tau \tag{1.139}$$

Once $B_{1,AM}$ is found, the RF envelope is then further modulated at the instantaneous frequency, which includes the Larmor frequency f_0

$$\vec{B}_{1,\omega_0}(t) = B_{1,AM}(t)[cos(2\pi f_i(t) + \phi)\vec{x} - sin(2\pi f_i(t) + \phi)\vec{y}] \tag{1.140}$$

where ϕ is an additional phase-offset. This highly modulated RF waveform is then fed through a high power voltage amplifier, placed in a separate equipment room to prepare it for transmission. The composite B_{1,ω_0} pulse can be transmitted by two perpendicular coils, or with a single quadrature coil with an 90° phase-induced delay to one of the terms. The RF transmit coil needs to be finely tuned to have low self-reflection at and around the Larmor frequency, and avoid generating local hotspots which lead to SAR limits. Furthermore, the voltage required to achieve a certain flip-angle needs to be calibrated based on the imaging sample. RF power amplifiers typically have high output bandwidth, of the range of 100-500kHz.

1.4.2 Gradient systems

Gradient waveforms are specified by the MR user in a similar manner as RF waveforms, as determined by a desired pulse sequence. In the equipment room gradient waveforms are amplified by current amplifiers, which generally have high power demands for fast switching. Current and gradients waveforms are related by

$$I(t) = \frac{G(t)}{\eta} \tag{1.141}$$

where η is a measure known as gradient efficiency. The voltage across gradient terminals, ignoring resistive losses, is

$$V = L\frac{dI}{dt}. \tag{1.142}$$

For the typical case of a gradient slope, rising to gradient amplitude G at gradient slew-rate SR over period τ, the power demands can be shown to be

$$P = V \cdot I = \frac{LG^2}{\eta^2 \tau} = \frac{LG \cdot SR}{\eta^2}. \tag{1.143}$$

This means for a given peak power limit, gradient amplitude and slew-rate can be traded off against each other. Once the gradient current is amplified, it is fed through the gradient coils. These are designed to produce a spatially varying magnetic field, which vary linearly as a function of space [51]. This generally means that gradient coil designs require many coil windings in proximity, which leads to a high self-inductance, which as Equation 1.143 shows further increases power demands.

Small deviations in realized gradient fields can cause image artefacts. Such deviation can occur due to eddy currents which are caused by time-varying magnetic fields inducing currents in surrounding conductive material, such the gradient coils themselves. A common method for reducing such errors is to use gradient pre-emphasis [52] and active gradient shielding [53].

More sophisticated approaches aim to correct for time-dependent effects, by modelling induced eddy currents as exponentially decaying sinusoids [54, 55]. However this can be difficult to characterize, and might not take into account gradient errors due to other sources such as mechanical vibration [56] or amplifier bandwidth. A more recent approach is to model the entire gradient system as a linear-time invariant systems (LTIS), and thus their composite effect as a linear combination of their response functions [57]. Once the impulse response function is known, the realized gradient can be found using convolution

$$G_{actual}(t) = G_{demand}(t) * h(t). \tag{1.144}$$

The Fourier transform of $h(t)$ is the frequency response of the gradient system. Generally speaking, this corresponds to a low-pass filter with a cut-off frequency of 7-22kHz [57–59], which is about an order of magnitude lower than common RF systems.

1.5 Peripheral Nerve Stimulation prediction

Using time-variable selection gradients, as will be shown later in this thesis, poses an important question surrounding peripheral nerve stimulation (PNS) safety. Time-optimal RF and gradient design will almost always result in gradients running at the maximum slew-rate for most of the time, which over the course of an MRI sequence implies fast gradient switching and could thus lead to PNS. This section will review the existing literature surrounding PNS safety, and specifically how systems evaluate PNS safety.

1.5.1 PNS background

PNS is caused by the electrical stimulation of nerves. Experience of PNS has been described as "sensations of stimulations" as well as from "discomfort" to "painful" and "local sharp pain" [60]. Moreover, the anatomic region of experience can vary across patients [60] and some include a small twitch across the bridge of the nose, contractions at the base of the spine and on the medial surface of the thigh [61].

The gradient coil responsible for creating a longitudinal magnetic field gradient creates a linearly varying B_z-field along this direction. In addition it also creates transverse field contributions very near to the coil but this typically does not result in magneto stimulation [61]. For the transverse x and y gradients this is different, as they are designed to have a linear B_z field across their respective direction, as only the B_z components affects MR imaging. However they also always produce B_x and B_y fields which are typically larger than their B_z components. Figure 1.21 shows the different behaviour for longitudinal and transverse gradient coils.
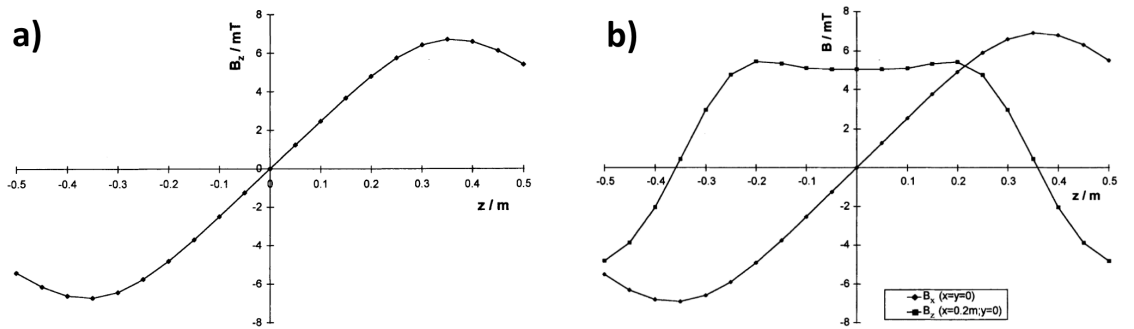
Figure 1.21: a) The B_z field along z, produced by a longitudinal (FH) gradient coil. **b)** Shows the B_z field as well as the B_x field, away from isocenter, along the FH-direction for a transverse gradient coil. The gradient coil is designed to have a linearly varying B_z component along x (not shown here), and a flat B_z component along z. The linearly varying B_x component is a byproduct of this design. Figure adapted from [61].

Time-varying magnetic fields induce electric fields **E**, which are linked by Faraday's law of induction [61–63]

$$\oint \mathbf{E} \cdot d\mathbf{s} = \frac{d}{dt} \int^A \mathbf{B} \cdot d\mathbf{A} \tag{1.145}$$

where d**s** is a line element vector, **B** is the magnetic flux density, d**A** is an area element vector and A is the area bounded by the contour integral. Equation 1.145 can be simplified when assuming an uniform magnetic field along a perpendicular circular cross-section with radius r

$$E(r) = \frac{r}{2}\frac{d\mathbf{B}}{dt}. \tag{1.146}$$

A similar relation can be used for elliptical bodies [62,63] by introducing a variable $0.5 \leq c \leq 1$ which aligns the magnetic field with the circular body (0.5 for longitudinal, 1 for transverse)

$$E(r) = c \cdot r \frac{d\mathbf{B}}{dt}. \tag{1.147}$$

In words, induced electric fields are proportional to the rate of changing magnetic fields and the surface area across where they flow. This explains why the AP-gradient coil is particularly likely to cause PNS in supine-positioned patients.

Whilst this explains the induced electric fields, the link between fields and nerve stimulation can be explained by considering electrophysiology. Pioneering work in 1901 by Weiss [61] investigated how neural excitation was linked to the strength of stimuli and the duration for which the stimuli were applied for. This lead to so-called "strength duration" curves, which describe how strong and long stimuli need to be to excite certain nerves, and can be characterised by two terms known as "chronaxie" and "rheobase". Rheobase is a stimuli level below which no stimulation is possible, regardless of stimulus duration. At twice this level, stimulation occurs with minimum energy, and the duration for which this occurs is known as chronaxie [61]. These concepts are shown in Figure 1.22.

Such strength-duration curves are expressed in electric field [V/m], or when multiplied by conductivity σ it can equivalently be expressed as current density. Using the expression in Equation 1.147 we can relate stimulation level from electric fields to dB/dt, which is a more intuitive expression for MRI sequences.

Reilly modelled [65] myelinated nerves as a circuit model, known as the spatially extended nonlinear node (SENN) model. This models myelinated nerves, which have high conduction properties and thus low stimulation thresholds. The stimulation properties of this circuit-model can be characterised using differential equations, however Reilly found that when this circuit was stimulated using a square-wave pulse, it produced a strength duration curve which could be characterised using the simple expression

$$I(\tau) = \frac{I_0}{1 - e^{-\tau/\tau_m}} \tag{1.148}$$

where $\tau_m = R_m C_m$ are circuit parameters to be tuned to fit experimental data, which is quoted to be roughly $0.15ms$. I_0 is conceptually equivalent to a rheobase stimulation level. This can be re-expressed to change in magnetic field [62]

$$\frac{dB(t)}{dt} = \frac{B_0}{1 - e^{-t/\tau_m}}. \tag{1.149}$$
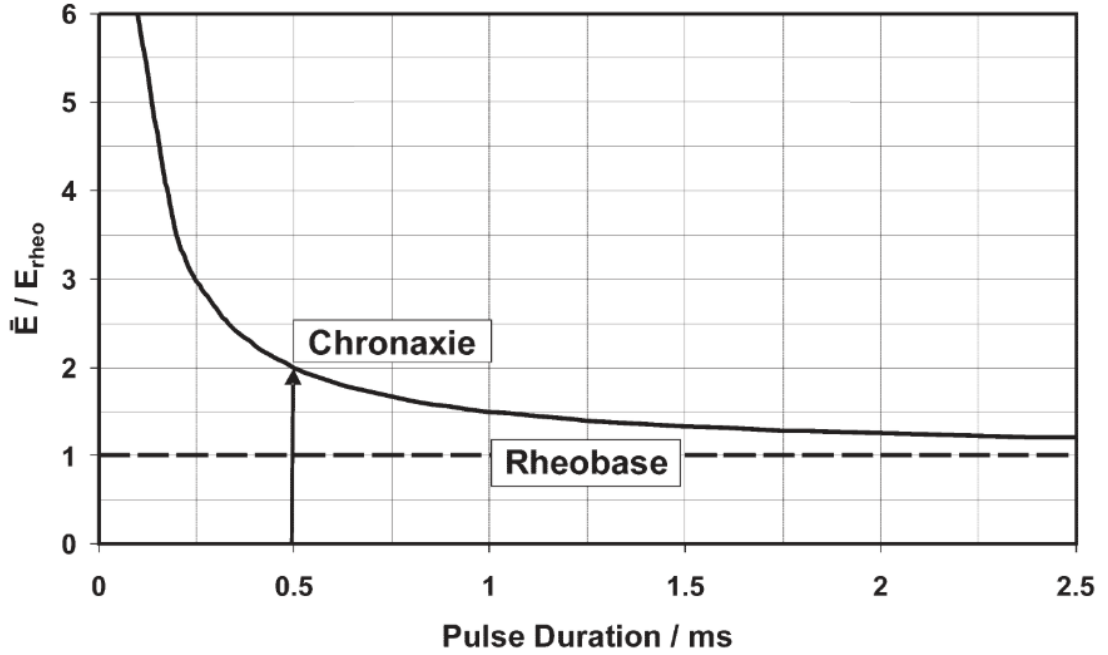
Figure 1.22: A strength-duration curve with stimulus strength in E [V/m] and stimulus duration in [ms]. Rheobase is the stimulus level under which no stimulation is possible, regardless of how long the stimulus is applied for. At twice this level, stimulation can occur with minimum energy. The duration of minimum energy stimulation is known as chronaxie. Figure adapted from [64].

Mansfield modelled a nerve-cell with a much simpler circuit model [66], fed by a time-varying current source $j(t)$, to derive the following equation

$$j(t) = \frac{c\sigma r}{2\tau_m} e^{-t/\tau_m} \int_0^t e^{t'/\tau_m} \frac{dB}{dt'} dt'. \tag{1.150}$$

Equation 1.150 could be solved for transient and steady-state responses, which corresponds to the response from short pulses or to the steady-state response from repetitive stimuli. Mansfield's derived equation allows analysis for a range stimuli shapes, and another major contribution from this work was made by evaluating stimuli thresholds when using trapezoidal and sinusoidal waveforms as can often be used in EPI readouts. It was found that in cases where $t/t_m << 1$ and dB/dt remained consistent over an extended period of time, it was the gradient excursion which best predicted possible PNS rather than dB/dt, and this assertion was backed up with experimental data. Moreover, solving Equation 1.150 for a mono-polar block-shaped stimulus arrives to the same expression as the one found by Reilly, in Equation 1.148.

Irnich in 1995 [63] avoided the link between magnetostimulation and a nerve-model. Instead, he used a more general expression for electrostimulation, derived in 1909 by Lapicque [61], which can be expressed as

$$\int^t E(\tau)d\tau \geq E_{rheo} \cdot t_{chron} \cdot (1 + t/t_{chron}) \tag{1.151}$$

where E_{rheo} is the rheobase stimulation level, and t_{chron} is the chronaxie stimulus duration.

Substituting Equation 1.147 into the left-hand side gives

$$\int^t \frac{dB(\tau)}{d\tau} d\tau \geq \frac{E_{rheo} \cdot t_{chron}}{c \cdot r}(1 + t/t_{chron}) \tag{1.152}$$

which can be rewritten as

$$B(t) \geq \frac{E_{rheo} \cdot t_{chron}}{c \cdot r}(1 + t/t_{chron}) \tag{1.153}$$

When t/t_{chron} approaches zero, the stimulation level can be approximated by

$$B_{min} = \frac{E_{rheo} \cdot t_{chron}}{c \cdot r} \tag{1.154}$$

Irnich hereby states that regardless of pulse duration, magnetostimulation is impossible as long as the gradient excursion $\Delta B < B_{min}$. This is denoted by Irnich as the rheobase condition [64].

Furthermore, dividing both sides of Equation 1.152 by t gives

$$\frac{1}{t} \int^t \frac{dB(\tau)}{d\tau} d\tau \geq \frac{E_{rheo}}{c \cdot r}(1 + t_{chron}/t) \tag{1.155}$$

where now the left-hand side of the equation is a time-average of changing magnetic fields, which is a more realistic description in MRI. Finally, Equation 1.155 can be simplified to

$$\bar{B}(t) \geq B_{rheo}(1 + t_{chron}/t) \tag{1.156}$$

where $B_{rheo} = E_{rheo}/(c \cdot r)$. This results in a strength-duration curve which is hyperbolic in nature rather than exponential. Moreover, the right-hand side of Equation 1.156 implies that the shape of $B(t)$ is irrelevant in determining stimulation, as long as the rheobase value B_{rheo} is lower than the gradient excursion. Irnich thus came to the same conclusion as Mansfield that what really mattered was gradient excursion rather than dB/dt, and that the gradient shape that resulted in this excursion is irrelevant to determining magnetostimulation.

Recent literature has been focused on incorporating the above findings into gradient coil design, including translating Equation 1.155 into pulse sequence parameters [67,68]. Moreover, a body of literature exists for developing electromagnetic simulation techniques for a greater understanding of how nerve networks respond to MR stimulation [69–72]. Interested readers are also directed to a review by Glover [73]. However common among these methods is the issue of solving computationally heavy simulations for fixed gradient waveforms, as is important for gaining an understanding of PNS, or designing gradient coils. Using such methods to evaluate PNS safety quickly enough for routine scanning remains unfeasible.

1.5.2 PNS safety evaluation

Having covered some of the theory surrounding the drivers amongst the sources of PNS and electro-physiology, the question remains how it can best be managed during scans.

The SAFE model proposed by Hebrank [74] suggested a simple circuit, based on dB/dt, to predict possible PNS. Gradient waveforms are differentiated to find $dB(t)/dt$, which are consequently filtered using two different time constants; one of which responds to relatively fast time-varying magnetic fields, and the other which accounts for slower varying magnetic fields. In addition, in one parallel branch the dB/dt is filtered before rectification, and vice versa on the other. This is justified by modelling the excitement of an action potential on the pre-synatpic side of a nerve, which diffuses charge into the post-synaptic side and are therefore rectified [75]. Whilst no biological references were found to justify this reasoning, it could be possible that the fast-responding filter emulates the exponential (or hyperbolic) functions from Equations 1.149,1.150 and 1.156, whilst the slow-responding filter emulates the averaging effect from Equation 1.155.

The filtered function are subsequently summed, to produce a time-varying stimulation function. The peak amplitude of this function is compared against a stimulation limit to determine the likelihood of PNS. A diagram of the SAFE model is shown in Figure 1.23. The marked annotations in this figure relate to an SAFE evaluation example for a balanced SSFP sequence, as shown in Figure 1.24.
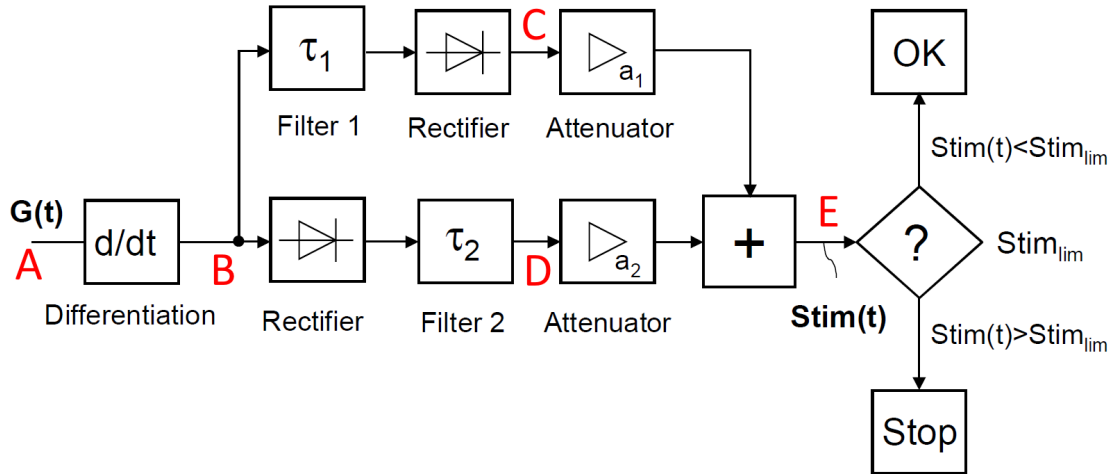
Figure 1.23: An example of the SAFE model for evaluating PNS. The model uses the derivative of gradient waveforms, and filters this function with two different filters, before adding them together using weights a_1 and a_2. The peak amplitude of the weighted signal is compared against a stimulation limit. The annotations A-E relate to excerpts shown in Figure 1.24. Figure adapted from [74].

Hebrank claimed that whilst the Irnich model fitted experimental data, it could not predict stimulation levels in cases where one stimulation shape is surrounded by a different one [75]. This would for example, violate Mansfield's assumption on having no large variation in dB/dt over the course of a sequence. This model thus takes the view that shapes are not irrelevant and that stimulation cannot be predicted using only a measure of gradient excursion. The SAFE model parameters (including filter constants and at-
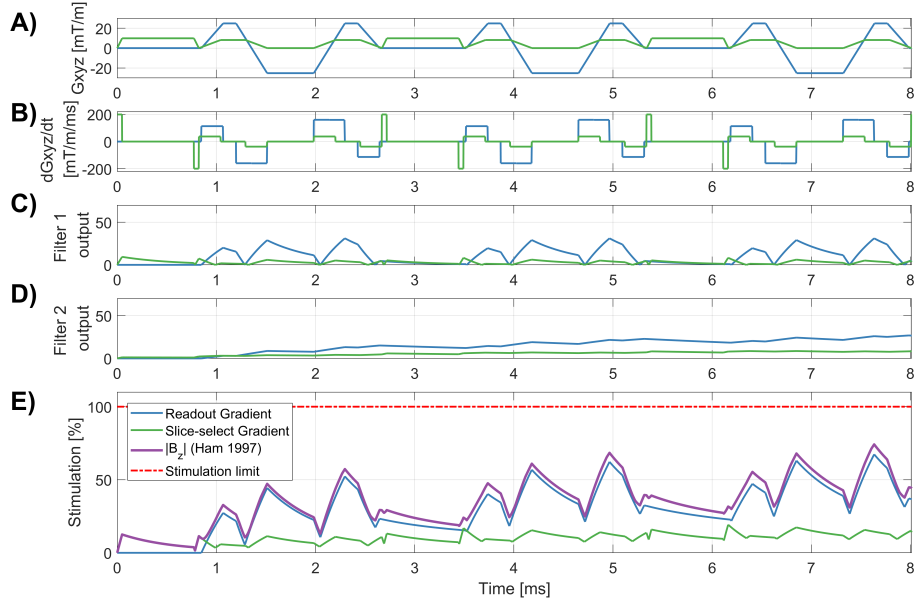
Figure 1.24: Excerpts from the SAFE model ($t_1 = 0.5ms$, $t_2 = 4ms$, $a_1 = a_2 = 0.5$). **A)** shows gradient waveforms for a balanced SSFP sequence, only showing the slice-select and the read-out gradients. **B)** shows the first time-derivatives which act as nerve stimuli. **C)** and **D)** shows response from a fast-responding Filter 1 and slow-responding Filter 2, respectively. **E)** shows the weighted-added stimulation signal, as a function of time, scaled in percentage of stimluation limit. It also show the vector-norm definition, which relates to the definition in Equation 1.157. A sequence can be reported unsafe if the stimulation limit is violated.

tenuation weights) were set experimentally, and produced by Siemens employees using 64 volunteers [74].

Around the same time, Ham et al. [60] worked on a more reliable predictor than dB/dt for Philips systems, and found that a vector magnitude definition of all B fields produced by three gradients was a better indicator for PNS stimulation. Using the notation $B_{coil,field-component}$, the definition can be expressed as

$$|B| = \sqrt{\Big(\sum_{i=x,y,z} B_{AP,i}(\bar{k}) \Big)^2 + \Big(\sum_{i=x,y,z} B_{LR,i}(\bar{k}) \Big)^2 + \Big(\sum_{i=x,y,z} B_{FH,i}(\bar{k}) \Big)^2} \qquad (1.157)$$

where $\bar{k}$ is spatial position (x, y, z). For a fixed point in space, this definition will give the maximum change of total magnetic fields when all gradient coils are energised simultaneously. To determine threshold values, the above definition can be used for a cylinder of fixed diameter, set to 0.2m in references ([60, 76]. This will be proportional to the vector norm definition considering only B_z components, allowing Equation 1.157 to be simplified to

$$|B_z| = \sqrt{\big(B_{AP,z}\big)^2 + \big(B_{LR,z}\big)^2 + \big(B_{FH,z}\big)^2} \qquad (1.158)$$

In Den Boer et al. [76] Siemens, Philips and GE healthcare employees collaborated on identifying whether this definition of gradient output could be used as an indicator for

mean PNS threshold, independent of gradient coil design. Results measurements from Hebrank, Ham and Bourland were combined, and reformatted for experimental differences to reveal that it was possible to reliably use the measure proposed by Ham et al. The $|B_z|$ definition can be incorporated in the SAFE model, by taking the vector magnitude of the three gradient axes. An example of this is shown in Figure 1.24E.

However later work by Irinch and Hebrank reiterated that gradient shapes with similar excursion produced the same PNS, and showed this by relating sinusoidal and trapezoidal stimuli waveforms to the same dataset [64].

1.6 Thesis outline

The remaining chapters of this thesis consist of research results, which will present the following.

Chapter 2 will present common RF hardware issues associated with implementing optimized multiband RF pulses. Existing hardware struggles to cope with rapidly varying FM waveforms, which can result in strong slice profile artefacts. MB RF pulse techniques are shown to be more stable when modified to produce equivalent designs using only amplitude modulation (AM). The benefit of doing so is demonstrated experimentally, and the relative cost in pulse duration is quantified over a range of designs.

Chapter 3 investigates how root-flipped MB pulses can lead to a disparity in T_2 and T_2^* contrast across different slices when used in a spin-echo sequence. This is quantified in terms of disparity in echo-arrival times and transverse magnetisation times, and an alternative root-flip design strategy is proposed to circumvent this effect completely.

Chapter 4 will present practical gradient hardware issues associated with MB RF pulses using time-variable selection gradients. This can be challenging for gradient systems to reproduce due to rapid gradient modulation, which is similar in nature to the cause of issues in Chapter 2. We propose an alternative MB RF pulse design strategy which produces temporally smooth gradient waveforms, show that this effectively avoids known issues, and demonstrate this experimentally. The design strategy is compared to existing techniques and the duration cost of this modification is reported.

Chapters 2-4 present work which minimise RF pulse duration, however this does not directly link to the reduction of overall imaging duration. This is because short RF pulses contain high RF energy, which lead to high SAR. Chapter 5 investigates how RF pulse design can be used to directly reduce acquisition duration for rapid gradient-echo sequences, by reducing the sequence repetition time (TR). The use of time-variable selection gradients, similar to those from chapter 4, is shown to reduce TR, and this is demonstrated in a MB2 cardiac balanced SSFP sequence.

Chapter 2

Optimized Amplitude Modulated Multiband RF Pulse Design

2.1 Contributions

The findings in the following chapter have been fully discussed in the following publications.

S Abo Seada, AN Price, JV Hajnal, SJ Malik. Optimized Amplitude Modulated Multiband RF Pulse Design. Magnetic Resonance in Medicine January 2017
DOI: https://doi.org/10.1002/mrm.26610
MatLab code to perform these findings is publically available at
`https://github.com/mriphysics/AM_multiband`

2.2 Preface

A common theme across this thesis will be on how to make multiband imaging workable in practice. This is highly relevant at a time when MB imaging is experiencing a renaissance associated with the Human Connectome Project, and locally with the developing Human Connectome Project. However highly efficient multiband pulses require rapid modulation, which existing MR hardware struggle to reproduce in practice as they were not designed for this type of imaging. This can affect the RF as well as the gradient system. This chapter will discuss issues surrounding the reproduction of multiband RF pulses, and propose a solution on overcoming common RF related errors.

As discussed in section 1.4.1 complex-valued RF pulses for our scanner (Philips Achieva 3T) need to be expressed in terms of amplitude and frequency modulation (AM and FM). However in practice we found that RF systems were unable to deal with the rapid temporal modulation associated with MB RF pulses.

A common pulse sequence implementation is to store RF pulses in a tabulated format with a fixed number of time-points, which can consequently be resampled to desired pulse durations. Such an implementation is harmless for singleband waveforms with smooth envelopes, but becomes problematic for highly modulated MB waveforms, which have much higher frequency content. As an example, we designed a phase-optimized MB6 pulse with 2048 time-points, and let the common implementation resample this to a waveform of $2.25ms$, described by 352 time-points. Slice-profile measures in Figure 2.1 show that this causes large problems, caused by aliasing during the resampling procedure [77]. The FM component of the complex-valued waveform has much higher frequency content than the AM-waveform, making them particularly vulnerable for this implementation. This is problematic, as unconstrained optimization of MB pulses usually leads to complex-valued pulses, which need to be described with FM.

This resampling step can be avoided altogether by specifying the waveform directly as a shape with the correct pulse duration (i.e. direct-sampling). A repeated experiment showed that the complex-valued waveform defined with FM still contained inter-slice artefacts, whereas the AM waveform specified without any FM did not produce such artefacts.
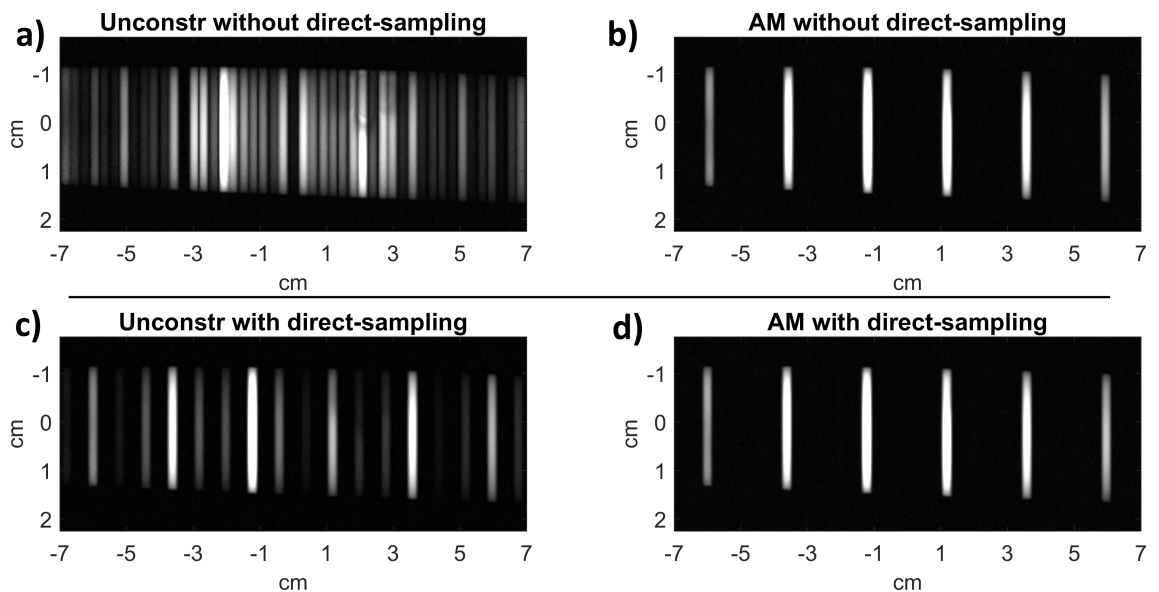
Figure 2.1: Slice profile measurements using a cylindrical phantom. **Top row:** A multiband 6 RF pulse was specified using 2048 time-points, and down-sampled by the MR scanner software to a duration 2.25 ms, using 352 time-points. In the first case **a)** an RF pulse specified with frequency modulation (FM) produces strong artifacts. **b)** Shows that these artefacts are avoided when repeated using an amplitude modulated (AM) RF pulse. **Bottom row:** Shows similar data when RF pulses were directly sampled at 2.25ms. **c)** Artefacts in the FM-case are still visible, but not in **d)** the AM case.

This suggested that something other than a software implementation was responsible for this type of artefact, and it could be avoided by designing optimized multiband RF pulses constrained to contain only amplitude modulation. From anecdotal reports, we were

aware that other users were experiencing similar RF-related issues, and also found that real-valued pulses behaved more stable. We therefore investigated how to modify existing multiband RF pulse techniques to produce equivalent designs described by real-valued envelopes (i.e. only using amplitude modulation) as well as quantify the relative cost of doing so.

The following text is reproduced as published.

2.3   Optimized Amplitude Modulated Multiband RF Pulse Design

Optimized Amplitude Modulated Multiband RF Pulse Design

Samy Abo Seada,* Anthony N. Price, Joseph V. Hajnal, and Shaihan J. Malik

Purpose: Multiband pulses are characterized by highly temporally modulated waveforms. Rapid phase or frequency modulation can be extremely demanding on the performance of radiofrequency (RF) pulse generation, which can lead to errors that can be avoided if pulses are restricted to amplitude modulation (AM) only. In this work, three existing multiband pulse design techniques are modified to produce AM waveforms.

Theory and Methods: Multiband refocusing pulses were designed using phase-optimization, time-shifting, and root-flipping. Each technique was constrained to produce AM pulses by exploiting conjugate symmetry in their respective frequency domain representations. Pulses were designed using the AM and unconstrained techniques for a range of multiband factors (ie, number of simultaneously excited slices), time-bandwidth products, and slice separations. Performance was compared by examining the resulting effective pulse durations. Phantom and in vivo experiments were conducted for validation.

Results: Acquired data confirmed that AM pulses can produce precise results when unconstrained designs may produce artifacts. The average duration of AM pulses is longer than the unconstrained versions. Averaged across a range of parameters, the duration cost for AM pulses was 26, 38, and 20% for phase-optimizing, time-shifting and root-flipping, respectively.

Conclusions: Amplitude modulation multiband pulses can be produced for a relatively small increase in pulse duration.

Division of Imaging Sciences and Biomedical Engineering, King's College London, London, United Kingdom.

*Correspondence to: Mr Samy Abo Seada, Division of Imaging Sciences and Biomedical Engineering, St. Thomas' Hospital, King's College London, Westminster Bridge Road, London SE1 7EH, United Kingdom.
E-mail: samy.abo_seada@kcl.ac.uk; Twitter: @tweetingsamy

INTRODUCTION

Simultaneous multislice imaging (1,2) can accelerate image acquisition, particularly for single-shot imaging sequences used for diffusion and functional MRI. Simultaneous multislice imaging uses multiband radiofrequency (RF) pulses, which can be technically difficult to realize, especially for high acceleration factors. This is because the simple multiband pulse design method of time-domain modulation leads to high-peak RF power requirements (or correspondingly long durations). Recently, three methods have been proposed to tackle the peak power problem: phase-optimizing (3), time-shifting (4), and root-flipping (5).

These three methods will usually produce complex-valued RF pulses with rapid modulation of both amplitude and phase components. We observed that some clinical MRI systems struggle to recreate this rapid modulation. Specifically, we found that limitations in pulse generation when using an amplitude/frequency (AM/FM) representation lead to a rather noticeable degradation in performance, making use of this type of pulse problematic. We hypothesized that designing equivalent pulses that contain only amplitude modulation (ie, real-valued waveforms) can effectively circumvent this issue. We present experimental results which demonstrate that this is indeed the case. In this work, we examine the three major multiband pulse design methods mentioned previously, demonstrate how each can be modified to produce AM-only RF pulses, and show that in many cases the performance cost of doing so is modest. Hence, the use of AM-only designs is a viable alternative for users experiencing this type of hardware issue.

THEORY

The challenge of pulse design is to determine a RF magnetic field (B_1) pulse that excites a desired transverse magnetization profile M_{xy}. The change in magnetization in the presence of B_1 and gradient fields is given by the Bloch equations, for which no analytic inversion exists with respect to B_1. One solution to this problem is to assume that the change in longitudinal magnetization is null. This is known as the small flip angle approximation, and simplifies the relation between B_1 pulses and resultant transverse magnetization to a Fourier relation (6). This is pertinent to multiband pulse design, as the simplest method for producing a multiband pulse $b(t)$ is to take a single-band pulse $p(t)$ and multiply it by a modulation function $f(t)$ as follows (1):

$$b(t) = p(t) \sum_{n=1}^{MB} e^{i\omega_n t} = p(t)f(t) \qquad [1]$$

Here, ω_n are the frequency offsets for the replica slices, numbered from $n = 1$ to MB (multiband factor). This is

2.3. Optimized Amplitude Modulated Multiband RF Pulse Design

referred to as in-phase modulation, as all modulation functions are in phase with each other. The Fourier convolution theorem dictates that in the Fourier domain

$$\tilde{b}(\omega) = \tilde{p}(\omega) * \tilde{f}(\omega) \qquad [2]$$

where $\tilde{f}(\omega)$ is an array of delta functions centered on ω_n. A key property is that conjugate symmetric Fourier series have real coefficients. The conjugate symmetric condition for a function $x(t)$ with Fourier transform $\tilde{x}(\omega)$ is $\tilde{x}(\omega)^* = \tilde{x}(-\omega)$. Conjugate symmetric Fourier series have even magnitude functions and odd phase functions. In the following sections, we describe how each of the existing pulse design techniques can be modified to produce AM pulses.

Phase-Optimizing

Wong (3) showed that the peak of $|f(t)|$ can be reduced by adding arbitrary phase offsets ϕ_n, such that the overall modulation function is given by

$$f(t) = \sum_{n=1}^{MB} e^{i(\omega_n t + \phi_n)} \qquad [3]$$

The peak amplitude of $|f(t)|$ can be minimized by numerically optimizing the values of ϕ_n. For the typical case in which ω_n are separated by a constant slice separation, distributed around ω_0 (the center frequency of the slice group), the optimization can produce real-valued multiband pulses if pairs of slices equidistant from ω_0 have an antisymmetric phase offset as follows (7,8):

$$\phi_i = -\phi_j \text{ for } i,j \text{ such that } \omega_i - \omega_0 = \omega_0 - \omega_j. \qquad [4]$$

When MB is odd valued, the central slice must be dealt with separately. Note that the optimal set of phase offsets for a multiband factor is independent of the single-band pulse and the constant slice separation. The frequency behavior of in-phase modulation and phase-optimizing is illustrated in Figures 1a and 1b, respectively.

Time-Shifting

Auerbach et al (4) proposed an alternative to phase-optimizing in which individual single-band pulses are temporally offset to minimize constructive interference (with additional optimal phase offsets also calculated). It is no longer possible to separate the optimization design as the product between a single-band waveform and a modulation function. Instead, the aggregated multiband pulse is characterized as

$$b(t) = \sum_{n=1}^{MB} p(t - \tau_n) e^{i(\omega_n t + \phi_n)} \qquad [5]$$

where τ_n is the temporal-shift variable for each single-band pulse. To create AM time-shifted pulses, time-shifting must be constrained such that single-band pulses corresponding to slices equidistant from the center frequency are shifted in pairs, as follows:

$$\tau_i = \tau_j \text{ for } i,j \text{ such that } \omega_i - \omega_0 = \omega_0 - \omega_j. \qquad [6]$$

Similar to the phase-optimizing method, when MB is odd, the middle slice must be dealt with separately. Because this method typically also includes optimized phase offsets, the condition from Equation 4 must also
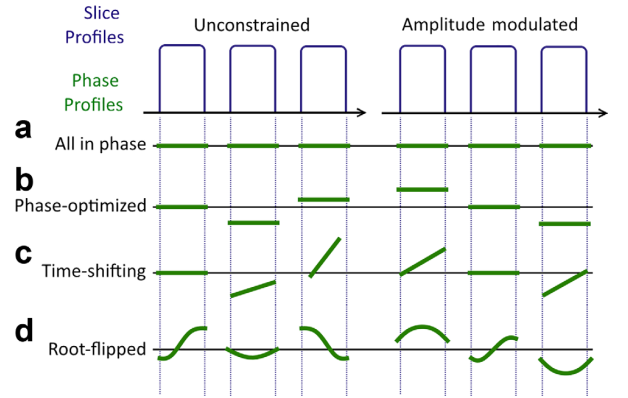
FIG. 1. Illustration of multiband 3-slice profiles for 90° excitation. The slice magnitude profiles are equivalent in all four methods: in phase, phase-optimization, time-shifting, and root-flipping. The important difference between the unconstrained and amplitude modulated phase profiles is that the AM pulses result in antisymmetric phase profiles, such that the frequency response is conjugate symmetric.

hold. When these conditions are met, the Fourier shift theorem implies that equidistant slices will gain similar linear phase ramps, allowing for conjugate symmetry to exist. This is in contrast to the original time-shifting method, in which equidistant slices were effectively shifted in opposite directions in time. In contrast to phase-optimizing, the optimal solution depends on the single-band waveform $p(t)$, so that optimal time and phase offsets must be evaluated for each design case. Figure 1c illustrates the relevant frequency behavior.

Root-Flipping

Root-flipping, as proposed by Sharma et al (5), takes a direct approach to multiband pulse design using the Shinnar-Le Roux (SLR) method (9). Briefly, this method involves designing a pair of polynomials of complex exponentials $\tilde{\alpha}$ and $\tilde{\beta}$, whose frequency representations yield the desired slice profile. Typically, the polynomial coefficients of $\tilde{\beta}$ are obtained using digital filter design; $\tilde{\alpha}$ can then be inferred using the equations (9)

$$|\tilde{\alpha}_k| = \sqrt{1 - \tilde{\beta}_k \tilde{\beta}_k^*} = \sqrt{1 - |\tilde{\beta}_k|^2} \qquad [7]$$
$$\angle \tilde{\alpha}_k = \mathcal{H}(\log|\tilde{\alpha}_k|) \qquad [8]$$
$$\tilde{\alpha}_k = |\tilde{\alpha}_k| e^{i \angle \tilde{\alpha}_k} \qquad [9]$$

where $\mathcal{H}$ denotes the Hilbert transform. The time-domain representations α_n and β_n are then subjected to the inverse SLR transform to recover the required RF pulse $b(t)$. $\tilde{\beta}_k$ can be expressed in polynomial form (as a sum of products) or in factored form (as a product of sums) as follows:

$$\tilde{\beta}_k = \sum_{n=0}^{N-1} \beta_n e^{-2\pi i k n / N} = \beta_0 \prod_{n=1}^{N-1} \left(1 - r_n e^{-2\pi i k / N}\right) \qquad [10]$$

where β_n are the polynomial coefficients, r_n are the roots of the polynomial $\tilde{\beta}_k$, and N is the degree of the polynomial.

Table 1
Optimized Phase Offsets for AM Multiband Pulses

MB	Phase Offsets (deg)										
3	73.6	0	−73.6								
4	55.8	78.6	−78.6	−55.8							
5	66.3	−56.9	0	56.9	−66.3						
6	96.9	161.1	66.3	−66.3	−161.1	−96.9					
7	147.9	−32.2	5.9	0	−5.9	32.2	-147.9				
8	121	12.6	83.9	114.1	−114.1	−83.9	−12.6	−121			
9	27.5	−152.8	−37	−24	0	24	37	152.8	−27.5		
10	96.4	−137.2	166.9	17.4	42.2	−42.2	−17.4	-166.9	137.2	−96.4	
11	80.5	50.8	−106.2	4	−85.6	0	85.6	−4	106.2	−50.8	−80.5
12	99.1	25.4	41.3	125.5	−125.8	56.4	−56.4	125.8	−125.5	−41.3	−25.4	−99.1

Note: Phases are ordered such that the central value corresponds to the middle slice.

When the roots are plotted on the complex plane, they are scattered around the unit circle. Flipping the passband roots radially from inside to outside or outside to inside the unit circle, changes the through-slice phase profile without affecting the magnitude profile. In the time domain, root-flipping redistributes the contributions associated with those frequencies across the duration of the RF pulse. The redistribution depends on the flipping pattern across the passband. Placing all roots inside (or outside) the unit circle leads to a maximum (or minimum) phase arrangement, and aligns the associated main amplitude peak at the start (or end) of the pulse. A search strategy can be used to find a flipping pattern that results in the distribution which leads to the minimum peak amplitude.

Amplitude modulated root-flipped pulses can be designed by ensuring roots are located inside or outside the unit circle symmetrically about the real axis. This ensures that $\tilde{\beta}_k$ is conjugate symmetric, such that its time domain representation β_n is real-valued. When $\tilde{\alpha}_k$ is designed using Equations 7-9, in which $|\tilde{\beta}_k|$ is an even function, its magnitude function $|\tilde{\alpha}_k|$ will be even. Moreover, the phase response will be odd because the Hilbert transform of an even function is odd (10). Hence, $\tilde{\alpha}_k$ will be conjugate symmetric, and finally the inverse SLR transform (9) yields an AM RF pulse when both α_n and β_n are real-valued. An illustration for the conjugate symmetric condition for each of the three techniques is shown in Figure 1.

METHODS

Pulses were designed for multiband factors 3 to 16, time-bandwidth products (TBP) 2, 4, 6, 8 and 10, and slice separations of 3 to 22 slice thicknesses in integer steps. Thus, a total of $14 \times 5 \times 20 = 1400$ cases were examined.

Single-band SLR refocusing pulses were generated from filters designed using a modified version of the minimization proposed as Equation 1 in (5); the ripple limits on the minimization were modified to produce linear phase pulses, whereas in (5) the method was used to make minimum phase designs. Refocusing pulses were designed to produce matched excitation spin-echo profiles with 1% ripples in and out of slice. These were used as a starting point for the phase-optimization and time-shifting results, to make them comparable with root-flipping. Optimal phase offsets were found using the fmincon function in MATLAB (MathWorks, Natick, MA, USA) with 100 different random

start points. Table 1 lists the optimized AM phase offsets for different multiband factors. For time-shifting, multiband pulses were created by summing up uniformly time-shifted single-band pulses, as in (4). For the AM case, the shifts were still spaced linearly over the extended duration of the pulse, but with equidistant slices shifted in pairs as discussed previously. For each design case, 50 candidate time shifts were tested, with overall pulse durations ranging from 100% of the single-band duration (no shift) to 200% (doubled duration). In each case, optimal phase offsets were found by using the genetic algorithm in MATLAB with population size 50, to then seed a local optimization with the fmincon function. Out of the 50 candidate solutions for each design case, the one with the lowest product between resulting pulse amplitude and duration was selected as optimal. The AM pulses were produced in the same way, except time shifts and phase offsets were applied in pairs, as described previously.

Root-flipped refocusing pulses were designed using code made available online by Sharma et al (www.vuiis.vanderbilt.edu/~grissowa/), again with 1% passband and stopband ripple constraints. The AM pulses were designed by modifying this code to flip roots as described previously. Half of the stopband roots at frequencies beyond the outermost passband were also flipped to prevent the accumulation of high coefficients at the pulse edges (Supporting Fig. S1). The Monte-Carlo approach used by Sharma et al to find optimal root-flipping patterns was replaced by the genetic algorithm toolbox in MATLAB, which we found to produce slightly improved results. For simplicity, we refer to the original root-flipping method as "unconstrained," even though it was constrained to be time-symmetric.

In all three cases, optimal pulses were found independently for the proposed AM constrained and unconstrained cases. Because amplitudes and durations of RF pulses can be traded off, we have quantified the relative performance of each design by computing the "effective duration" t_{eff}, which we define as the duration relative to a hard pulse of equivalent peak amplitude and flip angle:

$$t_{eff} = \frac{T\gamma\, b_{max}}{\theta} \qquad [11]$$

where T is the pulse duration; b_{max} is the maximum B_1 amplitude; θ is the design flip angle; and γ is the gyromagnetic ratio. A doubling of t_{eff} indicates a pulse that requires twice the amplitude for a given duration or vice versa. For
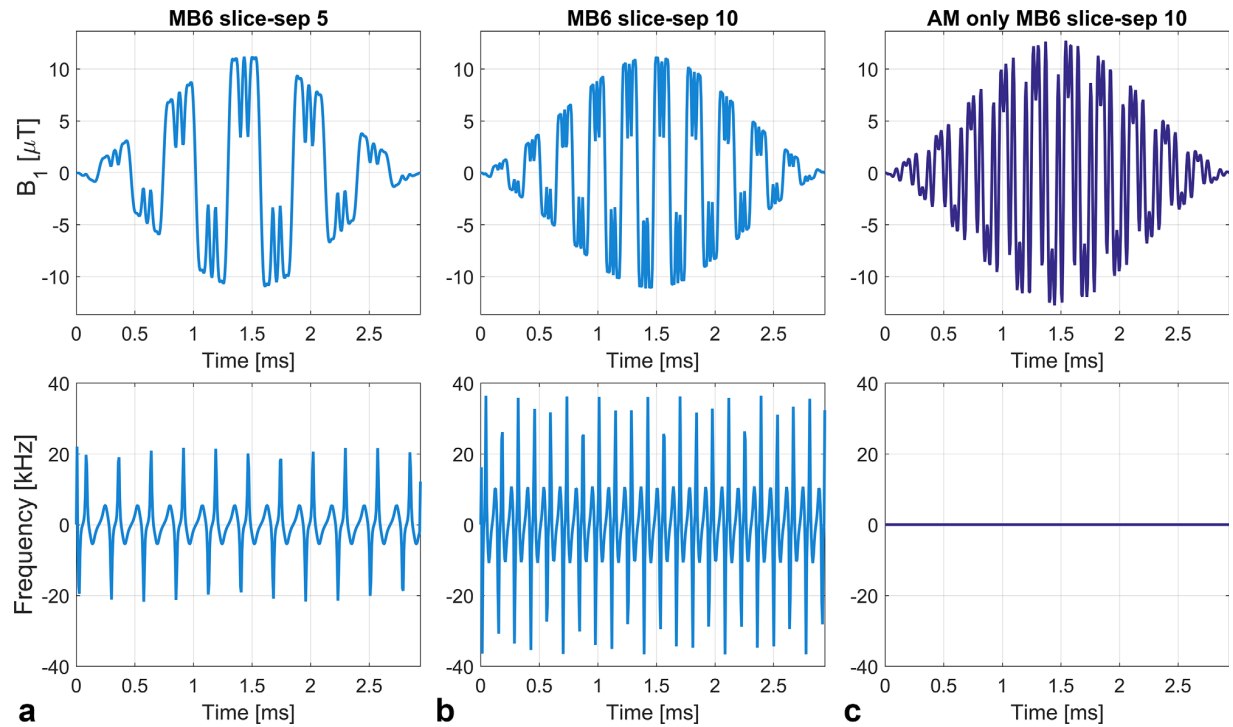
FIG. 2. Sample multiband 6 waveforms designed using phase-optimization, expressed as signed AM and FM. (**a, b**) Unconstrained phase-optimized pulses. Doubling the slice separation from 5 slices to 10 increases the amplitude of the FM waveforms. (**c**) Using AM phase-optimization, there is no FM. All three pulses are matched in duration. The AM pulse in (c) has a higher peak amplitude. The pulses in (b) and (c) have equivalent simulated slice profiles (eg, same magnitude profiles, ripple characteristics).

comparison, the single-band refocusing pulses used in this work had $t_{eff} = 3.637$, 8.270, 13.231, 18.156, and 23.051 for TBP from 2, 4, 6, 8 and 10, respectively.

Other investigators (11) have found that pulses with a large degree of "roughness" in the RF envelope can lead to errors on some systems. Constraining pulses to be amplitude modulated could conceivably increase this roughness by removing the degrees of freedom associated with phase modulation. To investigate this effect, pulse envelope roughness was quantified using the measure suggested in (11) as follows:

$$Roughness = \sqrt{\frac{1}{N-1}\sum_{n=1}^{N-1}\left(\frac{|b_{n+1}| - |b_n|}{dt}\right)^2} \qquad [12]$$

where N is the number of time points used, and dt is the dwell time for which the pulse is evaluated.

The MATLAB code to reproduce all of the designs used in this work is available at https://github.com/mriphysics/AM_multiband/, including modifications made to the original root-flipped design code, which was downloaded from www.vuiis.vanderbilt.edu/~grissowa/.

Experiments

All experiments were conducted using a 3T Philips Achieva TX (Philips Healthcare, Best, the Netherlands) scanner with software release R3.2. This scanner uses analog spectrometer technology and requires RF pulses to be specified using an AM/FM representation.

Slice-profile measurements were performed on a long cylindrical phantom containing 100 mL saline doped with 1% gadolinium contrast agent (0.5 mmol/mL Gd-DOTA, Dotarem, Guerbet LLC, Bloomington, IN, USA). For this experiment, phase-optimized 90° multiband excitation pulses with 6 slices were designed based on a standard vendor pulse (TBP = 2.13) using both the AM and unconstrained approaches. Slice thickness was 1 mm and a range of slice gaps were included; increasing the slice gap leads to an increase in the size of frequency modulation, as shown by the examples in Figure 2. All pulses were designed at the scanner's RF dwell time (6.4 µs) to avoid additional artifacts from resampling; durations were matched at 2.94 ms and peak amplitudes were allowed to vary accordingly so that the flip angle remained constant. Slice profiles of the individual excitation pulses (ie, not spin echo pairs) were measured using a 2D gradient-echo sequence with the read-out gradient moved to the slice-select direction. The acquired resolution was 0.1 mm through-slice with repetition time (TR) = 100ms, echo time (TE) = 13 ms.

An in vivo imaging experiment was conducted with unconstrained and AM phase-optimized versions of an MB4 pulse, for which the underlying single-band waveform was a standard vendor pulse with TBP 3.05. A gradient echo single-shot EPI sequence with blipped-CAIPI acquisition scheme (12) (1 mm isotropic resolution, flip angle 52°, TR 2 s, TE 25 ms) was used for acquisition with a 32-channel head coil. Axial brain images (total coverage 120 mm) were acquired on a single healthy
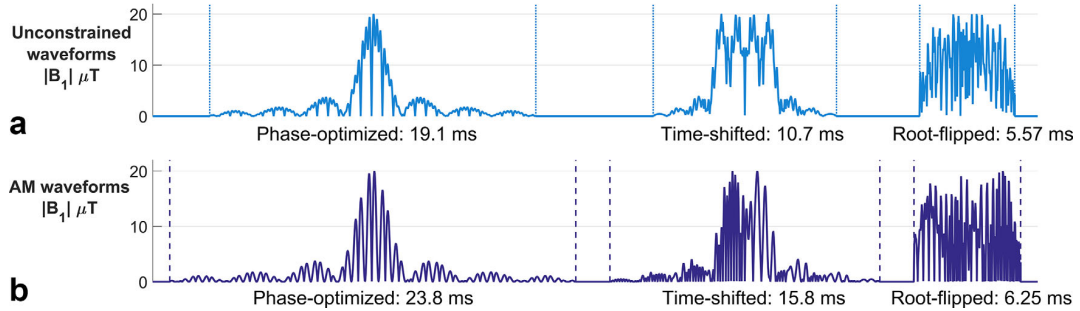
FIG. 3. Multiband RF refocusing pulses for multiband factor 4, time-bandwidth product 6, and slice separation of 5 slices, for each of the three design methods with unconstrained (**a**) and amplitude modulated (**b**) designs. Each pulse has been scaled to 20 µT peak amplitude. The AM condition results in longer pulse durations.

volunteer (written, informed consent obtained before enrollment), and data were reconstructed with a SENSE-based algorithm using ReconFrame (GyroTools GmbH, Zurich, Switzerland). As with phantom experiments, the pulse duration was the same for the unconstrained and AM pulses (2.39 ms), so that the bandwidth properties were the same in both acquisitions.

RESULTS

Simulations

Figure 3 shows sample magnitude waveforms for refocusing pulses with MB = 4, TBP = 6, and slice separation = 5 slice thicknesses, designed using the three techniques with and without the AM constraint.

Figure 4 plots the mean t_{eff} averaged over slice separations against multiband factor for each of the unconstrained (4a) and AM (4b) methods at a fixed time-bandwidth product of 6; error bars indicate the maximum and minimum durations found across the 20 different slice separations tested. Phase-optimizing is outperformed by time-shifting, which in turn is outperformed by root-flipping, as expected. Some variability is observed with respect to slice separation for all methods. This is the case for phase-optimizing, even though the solutions are independent of slice separation, because the peak of the modulation function is not always

directly aligned with the peak of the underlying single-band waveform. The effect is more pronounced for closely spaced slices.

Figure 5 displays the ratio of the effective durations of each AM pulse and its unconstrained counterpart for each method when plotted against multiband factor. The spread of values for each multiband factor is associated both with slice separation and time-bandwidth product. Averaged across slice separations and time-bandwidth products, the AM constraint results in effective durations that are longer by 26% for phase-optimizing, 38% for time-shifting, and 20% for root-flipping. Phase-optimizing results vary insignificantly across the various designs, but there is a significant amount of variance particularly in the latter two methods. Time-shifting has the largest variation; relative performance of AM-constrained solutions is particularly poor for time shifting at low multiband factors, but improves as this increases. For the phase-optimization method, multiband factors of 5 (19%) and 6 (14%) are particularly favorable for AM pulses. Average performance for root-flipped designs is relatively stable across multiband factor and time-bandwidth product but varies moderately with slice separations. The breakdown of this performance among different time-bandwidth products can be found in Supporting Figure S2. A notable exception to the general trend occurs for root-flipped pulses
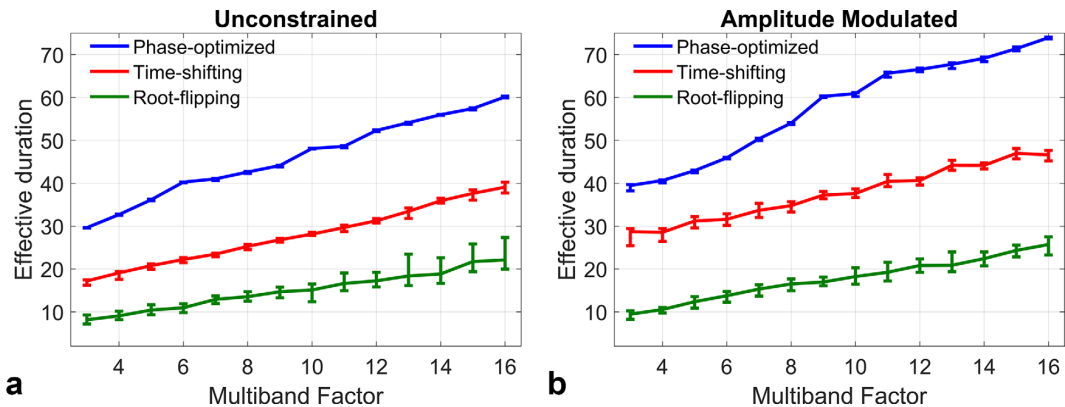
FIG. 4. The effective durations of the three techniques in relation to each other, as a function of the multiband factor in the unconstrained (**a**) and AM (**b**) case. All pulses were refocusing pulses designed for a time-bandwidth product of 6 and averaged over 20 different slice separations. Error bars indicate the maximum and minimum amplitude found in the group of 20 slice separations.
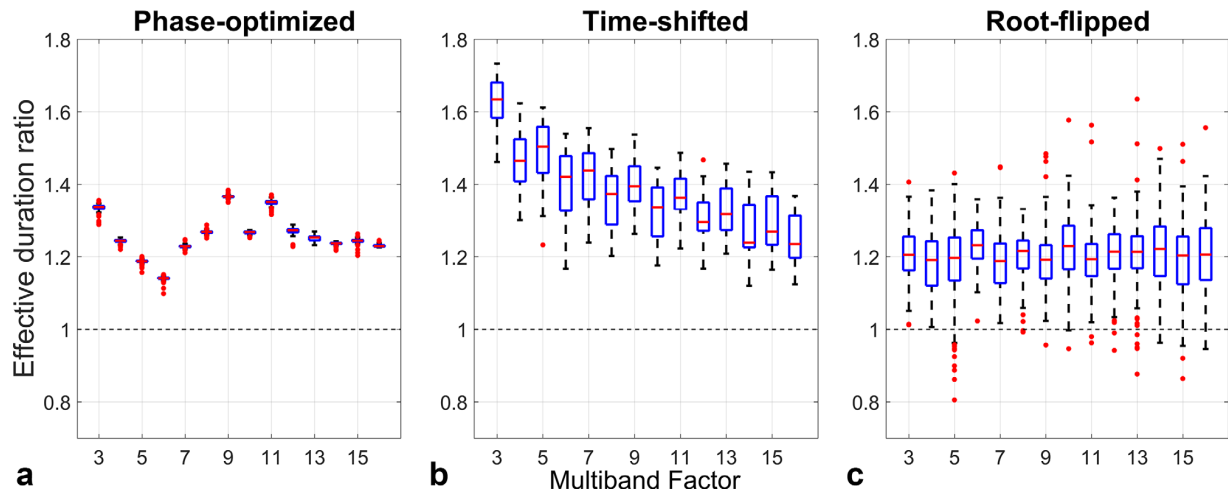
FIG. 5. Effective durations of AM multiband pulses relative to their unconstrained design equivalent, for the three techniques. Each AM design is compared with its unconstrained equivalent over all time-bandwidth products and slice separations (100 different cases for each multiband factor). Phase offsetting shows some variation with the multiband factor, but little variation for different TBP/slice separation, as expected, as this method is independent of the single-band starting waveforms. Time-shifting and root-flipped results show significantly more variation. The AM time-shifting is comparatively worse at lower multiband factors, whereas root-flipping is relatively constant across multiband factors. There are some cases in which the AM root-flipped designs outperform the original method (ie, ratio < 1).

designed for TBP $= 2$, MB $= 5$; in this case the AM designs outperform the original method on average.

Sharma et al (5) showed that combining root-flipped refocusing pulses with minimum-duration matched excitation pulses leads to a dispersion of echo times. The effect was visualized by averaging transverse magnetization from Bloch simulations for isochromats over a range of frequency offsets $\pm$ 50 Hz. Figure 6 shows the result for designs with TBP $= 6$, MB $= 8$, and slice separation $= 3$ slices; the green bars mark the effective time of excitation (peak $|M_{xy}|$ during excitation) and red bars mark the effective echo times (peak of the refocused $|M_{xy}|$).

Figure 7 shows the pulse envelope roughness for both unconstrained and AM-only MB6 TB4 waveforms designed using all three methods. The roughness values differ among the three design methods, with root-flipped

pulses perhaps unsurprisingly giving the highest roughness. For root-flipped and phase-optimized methods, there does not appear to be a systematic difference between the AM constrained and unconstrained approaches. However, there is a significant increase in roughness when using the AM constraint for time-shifted RF pulses.

Experiments

Figure 8 shows the experimental results from imaging a water phantom at 3T. At low slice separations, the unconstrained waveforms produce small artifacts that become more significant at higher slice separations. Figure 2 demonstrates that increasing the slice gap leads to larger amplitude of the FM waveform. These artifacts are not present when using the AM waveforms, even at high slice
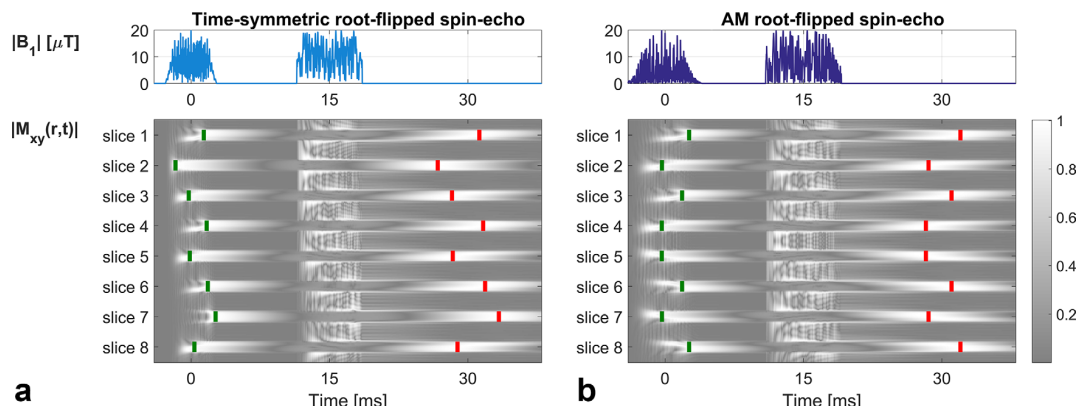
FIG. 6. A spin-echo simulation with a single refocusing pulse for a multiband factor 8 root-flipped pulse pair of time-bandwidth product 6, and 3 slice separations. In both the original (time-symmetric) and AM method, the pulses are scaled to a maximum B_1 of 20 μT (ie, minimum duration). Green boxes denote the peak M_{xy} during excitation (effective time of flip-down), and red boxes denote the peak of the refocused echo. Root-flipped pulses show a spread in both of these times across the group of slices, meaning that each slice will be read out with a different combination of T_2 and T_2^* weighting. The effect of conjugate symmetry in the AM case is to make equidistant slices have the same timing.

2.3. Optimized Amplitude Modulated Multiband RF Pulse Design
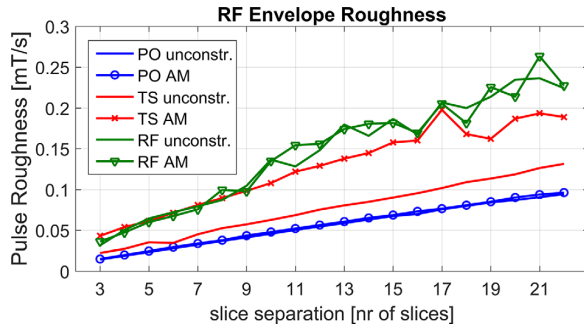
FIG. 7. Pulse envelope roughness defined by Equation 12 for the different design cases for MB = 6 TBP = 4. For this analysis, pulses were matched to the same amplitude but varied in duration.

separations. The pulses use matched durations and sampling rates that were matched to the system dwell time, to avoid resampling that can lead to additional errors, particularly for FM waveforms.

Results from the in vivo experiments are shown in Figure 9, which compares the unfolded simultaneously acquired (MB4) slices using both the unconstrained and AM-only RF pulses. Despite the design properties of these pulses being precisely matched, so that in an ideal system they would produce almost identical signals, it is evident that there are additional artifacts in the images from the FM pulse (top row, arrows).

DISCUSSION

We have presented a methodology for the constrained design of AM-multiband RF pulses, which have the potential advantage of being less demanding for some types of scanner pulse generator. The motivation for doing so is

illustrated by Figure 8, which shows the experimentally measured slice profiles for unconstrained RF pulses (ie, AM and FM modulation) compared with AM-only RF pulses, which are designed with nominally the same characteristics (eg, TBP, ripple). The unconstrained pulses result in artifacts that are not present when using AM-only designs, and are not predicted from simulating the slice profiles. The severity of the artifacts gets worse as the slices are moved apart (hence, the degree of frequency modulation increases). The effect of this is to produce imaging artifacts of the type shown in Figure 9. The additional interslice excitation is not unfolded by the reconstruction and produces interference across the field of view. This effect has been consistently observed with the scanner used for these experiments; the prevalence of this issue across other hardware is not known. Emerging fully digital hardware systems could avoid this issue; nevertheless, the AM-only designs explored in this work provide an alternative that is compatible with systems that suffer from this type of issue.

AM-constrained designs yield equivalent magnitude slice profiles, but are on average 20 to 38% less efficient than unconstrained solutions, depending on the design method used. This conclusion is based on tests using three design methods (phase-optimizing (3), time-shifting (4), root-flipping (5)), which were modified by imposing conjugate symmetry on the relevant frequency domain representation. Results were expressed in terms of the effective pulse duration (t_{eff}) relative to a hard pulse of the same flip angle. This provides a neutral basis for comparing pulses without having to specify RF amplitude or pulse duration settings.

Root-flipping produced the most efficient RF pulses (shortest t_{eff}) for both the AM and unconstrained cases, with time-shifting second and phase-optimizing last (Fig. 4). This
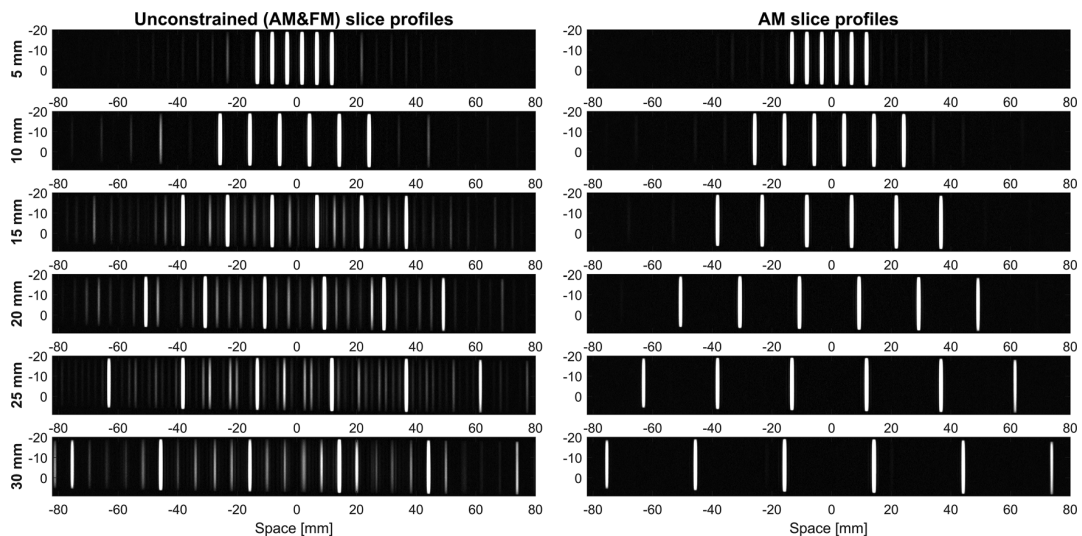
FIG. 8. Slice profiles from phantom experiments at 3T with MB = 6, TBP = 2.13 phase-optimized excitation pulses at different slice separations. All images are windowed in the same way. At low slice separations, the unconstrained waveforms—which are specified using both AM and FM— produce noticeable artifacts that become more significant at higher slice separations. This is not the case for slices excited by AM waveforms, even at high slice separations. All pulses were designed with the same underlying single-band waveform, and therefore should display the same level of between-slice ripple; the observed artifacts are interpreted as a pulse generation issue. Sample pulse waveforms are shown in Figure 2.
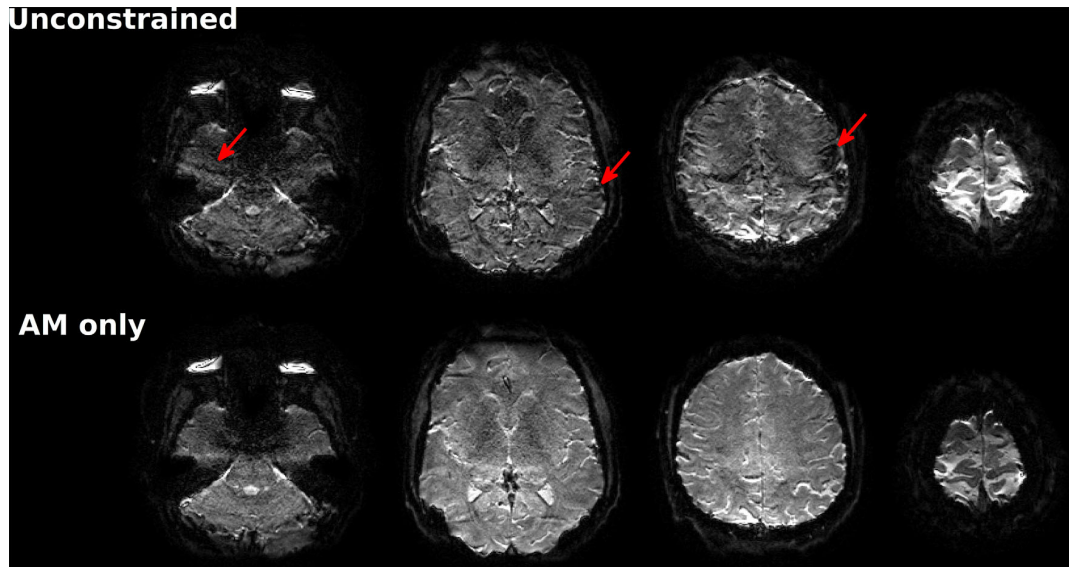
FIG. 9. In vivo MB4 GE-EPI images (1 mm isotropic resolution) using unconstrained and AM-only phase-optimized excitation pulses. Images are windowed in the same way. Images from the unconstrained (ie, AM and FM) pulse are affected by incoherent artifacts (arrows) that are attributed to unwanted interslice excitation seen on the slice profile measurements shown in Figure 8. In comparison, the images from the AM-only pulses are free from this type of artifact. As with the phantom experiment, the RF pulses were matched in design properties and in duration, with the only difference being that the unconstrained pulses were specified using AM and FM, whereas the AM-only pulses had no FM component.

hierarchy is consistent with the results of Sharma et al (5), and should be expected, as the performance mirrors the number of degrees of freedom available to each method. Sample waveforms from each method (Fig. 3) illustrate this difference, as the root-flipping allows for the most even distribution of RF energy throughout the duration of the pulse.

Constraining each method to produce purely AM RF pulses generally leads to a loss of performance, as shown in Figure 5. Given the reduction in number of degrees of freedom, the loss of performance is perhaps surprisingly small, particularly for root-flipping in which the average difference is 20%. Of all of the methods examined, time-shifting suffers the largest loss in performance, particularly at low multiband factors. We suspect this is because the required constraints (slices must be time-shifted in pairs and have paired phase offsets) are more limiting for this method.

However, it is striking that there are some design cases in which AM pulses incur very low penalties compared with their conventional counterparts. The phase-optimization and time-shifting AM designs are never better than unconstrained designs; indeed this is to be expected, as the AM case is a subset of the general optimization problem. However, AM phase-optimization performance is particularly good for MB = 5 and 6, in which the duration penalties are only approximately 19 and 14%, respectively. For root-flipping, there are cases in which the AM designs are better (the relative duration is less than 1). Figure 5 indicates that some AM designs are better than the conventional case, which is true for TBP = 2 and MB = 5 (Supporting Fig. S2). This is possible for the root-flipping method, because the AM solutions are not a simple subset of the original solutions. In the original root-flipping method, if a root is flipped on one half of the

complex plane, the conjugate root (the mirror root about the real axes) on the bottom half is not flipped, and vice versa, resulting in time-symmetric RF pulses. In the proposed AM root-flipping approach, roots must appear symmetrically about the real axis, which means equidistant slices have symmetric root patterns and the RF pulse is not time-symmetric. Hence, the two are designed using mutually exclusive symmetry constraints on the root-flipping. This suggests that there may be even more efficient solutions for truly unconstrained root-flipped pulses, which could merit further investigation.

Time-shifting and root-flipping can lead to spin echoes from different slices that are not aligned in time; the precise timing depends on the design of the matched excitation pulse in each case. A consequence of the AM constraint is that, in the case of time-shifting, the underlying single-slice waveforms must be shifted in pairs, so these pairs of slices have the same temporal properties. Similarly, we observed that a consequence of the AM root-flipping patterns when combined with minimum duration excitations is that spin echoes also form in pairs, with slices spaced equally about the center frequency, forming echoes at the same point in time (Fig. 6b). This is in contrast to the original method, which created time-symmetric pulses resulting in antisymmetric echo times for equidistant slices (Fig. 6a and Fig. 7 in (5)). Discrepancies in echo times are an inevitable aspect of multiband excitation/refocusing with these techniques, and characterization of these effects could be an interesting topic for future investigation.

In addition to the hardware issues that have motivated this study, there are other more practical benefits of using AM pulses, which although not the main motivation for this work, could prove to be useful. For example, AM waveforms are typically less susceptible to resampling

errors, and calculation of flip angles can be achieved by integrating the waveform directly (for odd-numbered MB). Our key motivation was to produce a practical workaround for hardware issues that arise from the strong demands placed on the RF system by multiband designs. Although our work focused on a pulse generation issue, other authors have examined related problems with rapidly modulated RF pulses. Grissom et al (11) found that rough RF pulse envelopes can lead to fidelity errors on systems with simpler RF amplifier designs. Another study (13) found that a specific absorption rate (SAR) monitoring device with low temporal resolution leads to overestimation of SAR, and hence overly conservative operational limits when using multiband pulses. Multiband pulses clearly have much rougher profiles than traditional single-band pulses; however, Figure 7 suggests that for the root-flipped and phase-optimized methods there is no systematic difference in "envelope roughness" between the AM and unconstrained approaches. There is, however, a consistent increase in roughness when using time-shifted pulses. The AM constraint generally leads to poorer performance with time-shifted designs, largely because of the requirement that pulses be shifted in pairs. Although the aforementioned power amplifier and SAR monitoring issues were not a concern for the hardware used in this work, additional design constraints on roughness are a possibility for some design approaches (11).

CONCLUSIONS

Existing multiband pulse design methods can be modified to produce real AM-only multiband pulse waveforms. The AM-only waveforms can be realized more reliably on some hardware, as illustrated in this study. These pulses come at a cost in duration, compared with their corresponding unconstrained versions; however, this cost is relatively modest for phase-optimizing (26%) and root-flipping (20%), but larger for time-shifting (38%). The required symmetry constraint also leads to different timing of spin-echo formation when used with root-flipping.

REFERENCES

1. Larkman DJ, Hajnal JV, Herlihy AH, Coutts GA, Young IR, Ehnholm G. Use of multicoil arrays for separation of signal from multiple slices simultaneously excited. J Magn Reson Imaging 2001;13:313–317.

2. Feinberg DA, Setsompop K. Ultra-fast MRI of the human brain with simultaneous multi-slice imaging. J Magn Reson 2013;229:90–100.

3. Wong E. Optimized phase schedules for minimizing peak RF power in simultaneous multi-slice RF excitation pulses. Proc Intl Soc Mag Reson Med 2012;20:2209.

4. Auerbach EJ, Xu J, Yacoub E, Moeller S, Ugurbil K. Multiband accelerated spin-echo echo planar imaging with reduced peak RF power using time-shifted RF pulses. Magn Reson Med 2013;69:1261–1267.

5. Sharma A, Lustig M, Grissom WA. Root-flipped multiband refocusing pulses. Magn Reson Med 2016;75:227–237.

6. Pauly J, Nishimura D, Macovski A. A k-space analysis of small-tip-angle excitation. J Magn Reson 1989;81:43–56.

7. Malik SJ, Price AN, Hajnal JV. Optimized amplitude modulated multi-band RF pulses. Proc Intl Soc Mag Reson Med 2013;21:1405.

8. Abo Seada S, Hajnal JV, Malik SJ. Optimized amplitude modulated multiband RF pulses. Proc Intl Soc Mag Reson Med 2016;24:1883.

9. Pauly J, Le Roux P, Nishimura D, Macovski A. Parameter relations for the Shinnar-Le Roux selective excitation pulse design algorithm. IEEE Trans Med Imaging 1991;10:53–65.

10. Poularikas AD. The Hilbert Transform. In: Hahn S, ed. The Handbook of Formulas and Tables for Signal Processing, 3rd Ed. Boca Raton, FL: CRC Press; 2010.

11. Grissom WA, Kerr AB, Stang P, Scott GC, Pauly JM. Minimum envelope roughness pulse design for reduced amplifier distortion in parallel excitation. Magn Reson Med 2010;64:1433–1440.

12. Setsompop K, Gagoski B A., Polimeni JR, Witzel T, Wedeen VJ, Wald LL. Blipped-controlled aliasing in parallel imaging for simultaneous multislice echo planar imaging with reduced g-factor penalty. Magn Reson Med 2012;67:1210–1224.

13. Vu AT, Auerbach E, Ugurbil K, Yacoub E. Online SAR measurement error in high resolution slice accelerated 2D EPI. Proc Intl Soc Mag Reson Med 2014;22:1377.

SUPPORTING INFORMATION

Fig. S1. The "edge spike" of a minimum-phase filter can be moved by flipping stop-band roots. Just as flipping passband roots controls passband energy across the pulse duration, so does flipping stopband roots control the distribution of stopband energy. The top row shows an untouched problematic minimum-phase filter with all stopband roots outside the unit circle and the spike at the end of the filter in the time domain. This spike (annotated with arrows) will remain, regardless of how the passband roots are flipped. The second row shows that when most of the stopband roots are flipped inside the unit circle, the spike moves to the start. When stopband roots are flipped alternatively, the spike moves to the center. We found that a good solution is to divide the stopband on each half-circle into subbands (six was found to work well), and flip each band alternatively (ie, like a square waveform). This increases roughness around the pulse edges, without the stopband energy accumulating at any coefficient in particular.

Fig. S2. The relative AM performance for the three methods for different time-bandwidth products, as in Figure 5 but now resolved for different TBP. The general trends follow those in Figure 5 with some exceptions. For example, for TBP = 2, the AM-constrained root-flipped pulses are on average better than the unconstrained versions for MB = 5.

2.4   Concluding remarks

In this work we identified a problematic issue with the reproduction of multiband RF pulses when defined as FM waveforms. In the preface it became clear that a FM pulses were exposed to resampling issues and reproduction issues. The approach we took was to modify existing techniques, to design similar RF pulses with the additional constraint of producing multiband RF pulses which can be defined using only amplitude modulation.

Since its publication, the AM multiband implementation has been the standard implementation for the developing human connectome project, which formed the basis of other publications [78, 79]. Moreover, it has also become part of the multiband SENSE product from Philips Healthcare.

One of the striking realisations from this work was the misaligned echoes associated with time-shifted and root-flipped pulses. While investigating this issue, it was realised that the misalignment for root-flipped pulses was associated with the arrangement of their roots. The natural question was to investigate how this would affect imaging, and whether it was possible to avoid such misalignment. This is demonstrated in the following chapter.

2.5   Supporting Material for publication

Below is supporting information that was published online with the article.
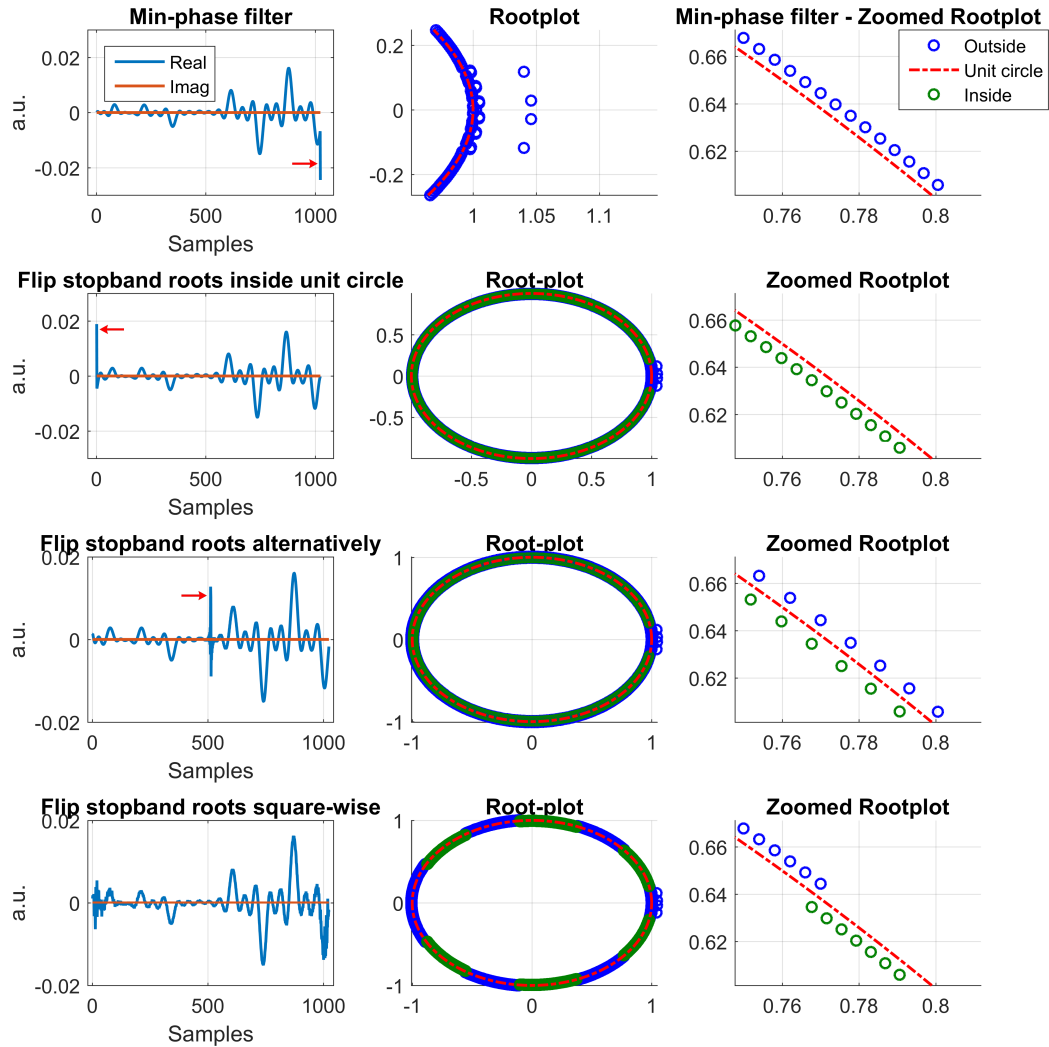
Figure 2.11: The "edge-spike" of a minimum-phase filter can be moved by flipping stop-band roots. Just as flipping passband roots controls passband energy across the pulse duration, so does flipping stopband roots control the distribution of stopband energy. The top row shows an untouched problematic minimum-phase filter with all stop-band roots outside the unit circle and the spike at the end of the filter in the time-domain. This spike (annotated with arrows) will remain regardless of how the passband roots are flipped. The second row shows that when most of the stopband roots are flipped inside the unit circle, the spike moves to the start. When stop-band roots are flipped alternatively, the spike moves to the center. We found that a good solution is to divide the stop-band on each half-circle into sub-bands (six was found to work well), and flip each band alternatively (i.e. like a square waveform). This increases roughness around the pulse edges, without the stopband energy accumulating at any coefficient in particular.

Figure 2.12: The relative AM performance for the three methods for different time-bandwidth products; as Figure 5 but now resolved for different TBP. The general trends follow those in Figure 5 with some exceptions. For example for TBP=2 the AM constrained root-flipped pulses are on average better than the unconstrained versions for MB=5.

Chapter 3

Root-flipped pulses with inherently aligned echoes

3.1   Contributions

The findings in the following chapter have been largely discussed in the following publications.

S Abo Seada, JV Hajnal, SJ Malik. Root-flipped pulses with inherently aligned echoes.
Proceedings of ISMRM 2017. Abstract Number 3955
Furthermore, MatLab code to perform these findings is publicly available at
`https://github.com/mriphysics/Rootflip-AlignEcho`

3.2   Introduction

The design of multiband RF pulses is problematic due to the high B_1-amplitude demands
from exciting multiple slices simultaneously. This often results in multiband RF pulses
with pulse durations which are too long to become feasible in existing sequences [15].
As discussed in section 1.2.7, three recently proposed design methods to reduce pulse
duration are phase-optimization [37], time-shifting [39] and root-flipping [7]. The latter
two techniques are more time-efficient, because different slices are excited at different times
across the duration of an RF pulse. This makes such pulses only suitable for spin-echo
sequences, as the excitation and refocusing pulses for these methods need to be matched
to have conjugate phase profiles. This is to ensure that the refocusing phase profile undoes
the phase profile of the excitation pulse, and that each slice refocuses fully at the echo-time
(TE).

Because different slices get excited and refocused at different times across the RF pulses,
the spin-echo formation develops differently in each slice, leading to misaligned echoes.

This phenomenon was first shown in an ISMRM abstract by Yao et al [80], and its effect has been considered for time-shifting [39], root-flipping [7] and in the modified AM-only method discussed in chapter 2 (see Figure 6 in chapter 2). For MB data acquired with a spin-echo EPI sequence, this means that different slices will have different T_2 and T_2^* weightings.

There are two quantities of interest; firstly, the time of arrival (T_{arr}) of the echo in each slice, for which alignment with the nominal echo-times determines the T_2^*-weighting for that slice. Secondly, the time that magnetization in each slice spends in the transverse plane (T_{xy}) will determine the T_2-weighting of that slice. The largest spread in these parameters across the set of simultaneously excited slices can be denoted by ΔT_{xy} and ΔT_{arr}. Note that in the case of a conventional single-slice spin-echo (see Figure 1.18) $T_{xy} = T_{arr}$, which are both equal to TE. Previous work [7,39] has proposed three excitation methods to categorize this effect:

1) Aligned-echo excitation: Matching the selection gradient of the excitation pulse to that of the refocusing pulse. Echoes arrive simultaneously but with different T_2-weighting. At readout, $\Delta T_{arr} = 0$ and $\Delta T_{xy} \neq 0$.
2) Align-TE excitation: Matching the duration of the excitation pulse to that of the refocusing pulse. Echoes arrive at different times with equal T_2-weighting. At readout, $\Delta T_{arr} \neq 0$ and $\Delta T_{xy} = 0$.
3) Minimum-duration excitation: Matching the peak amplitude of the excitation pulse to that of the refocusing pulse. Echoes arrive at different times with different T_2-weighting. At readout, $\Delta T_{arr} \neq 0$ and $\Delta T_{xy} \neq 0$.

As an example, Figure 3.1 shows a spin-echo simulation for a root-flipped MB5 example, with a minimum-duration excitation method.

It is however possible to constrain the root-flipping method from having asymmetric single-band components, and as will be shown, this results in having almost fully aligned echoes regardless of the excitation method. In this work root-flipped spin-echo simulations are performed using the three existing excitation methods, such that ΔT_{arr} and ΔT_{xy} can be investigated for each case. In addition, we also propose a novel root-flipping technique, referred to as "align-all",which inherently aligns the echoes such that $\Delta T_{arr} \approx 0$ and when combined with align-TE excitation results in $\Delta T_{xy} = 0$. The align-all technique comes at a cost in RF pulse duration, as will be shown. These excitation methods are summarised in Table 3.1.

3.3 Theory

In the root-flipping [7] method the multiband slice profile is evaluated as a multiband band-pass filter $\tilde{\beta}_k$. As described in 1.2.2, this can be expressed as a sum of complex exponentials with filter coefficients β_n, or represented as product of polynomial roots r_n

3.3. Theory
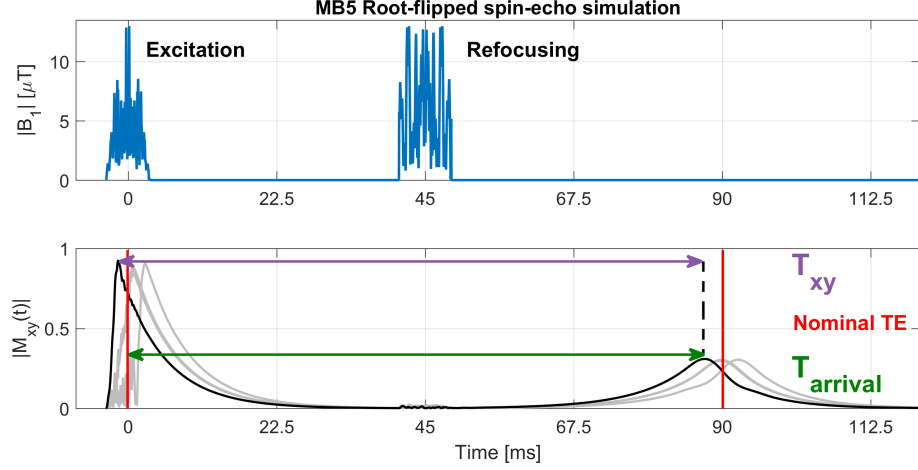
Figure 3.1: Top: A pair of 90°-180° root-flipped MB5 excitation and refocusing pulses for a nominal TE of 90ms. The excitation pulse shown is a minimum-duration variant. **Bottom:** Transverse magnetization as a function of time for the five slices. All bar one slice evolution have been faded out for clarity. T_{xy} is the time from excitation to the moment the slice fully refocuses. T_{arr} is the time from the center of the excitation pulse to the moment the slice fully refocuses. For conventional spin-echo sequences these two values are equal to the nominal echo-time.

Method	Excitation	Refocusing	ΔT_{arr}	ΔT_{xy}
Aligned-echo	$G_{exc} = G_{ref}$	Normal	$\Delta T_{arr} = 0$	$\Delta T_{xy} \neq 0$
Align-TE	$T_{exc} = T_{ref}$	Normal	$\Delta T_{arr} \neq 0$	$\Delta T_{xy} = 0$
Minimum-duration	minimal T_{exc}	Normal	$\Delta T_{arr} \neq 0$	$\Delta T_{xy} \neq 0$
Align-all	$T_{exc} = T_{ref}$	Align-all	$\Delta T_{arr} \approx 0$	$\Delta T_{xy} = 0$

Table 3.1: Summary of (left to right) each method, and their corresponding excitation condition, refocusing pulse and expected difference in echo arrival time ΔT_{arr} and difference in time spent transverse ΔT_{xy}. The align-all approach uses the same excitation condition as align-TE, but has to be derived from the align-all refocusing pulse.

along the unit circle on the complex plane.

$$\tilde{\beta}_k = \sum_{n=0}^{N-1} \beta_n e^{\frac{-2\pi i k n}{N}} = \beta_0 \prod_{n=1}^{N-1} (1 - r_n e^{\frac{-2\pi i k}{N}}) \tag{3.1}$$

The stopband frequencies have roots on the unit circle and the passband frequencies have roots away from this. Flipping roots inside or outside the unit circle redistributes the pulse energy in the time-domain. In the original method from Sharma et al., the root-pattern across each passband was unconstrained. Having an unequal number of roots inside and outside the unit circle across a passband leads to temporal displacement, which leads to the misalignment in spin-echo development.

Ensuring an equal number of roots inside and outside the unit circle for each passband restricts temporal displacement, which results in $\Delta T_{arr} \approx 0$ regardless of the excitation method. Figure 3.2 illustrates how these two root-flip pattern are different. Using this constrained root-flip pattern in conjunction with the align-TE excitation (i.e. matched-

duration) method also gives the desired property, $\Delta T_{xy} = 0$. We refer to this as the align-all approach.
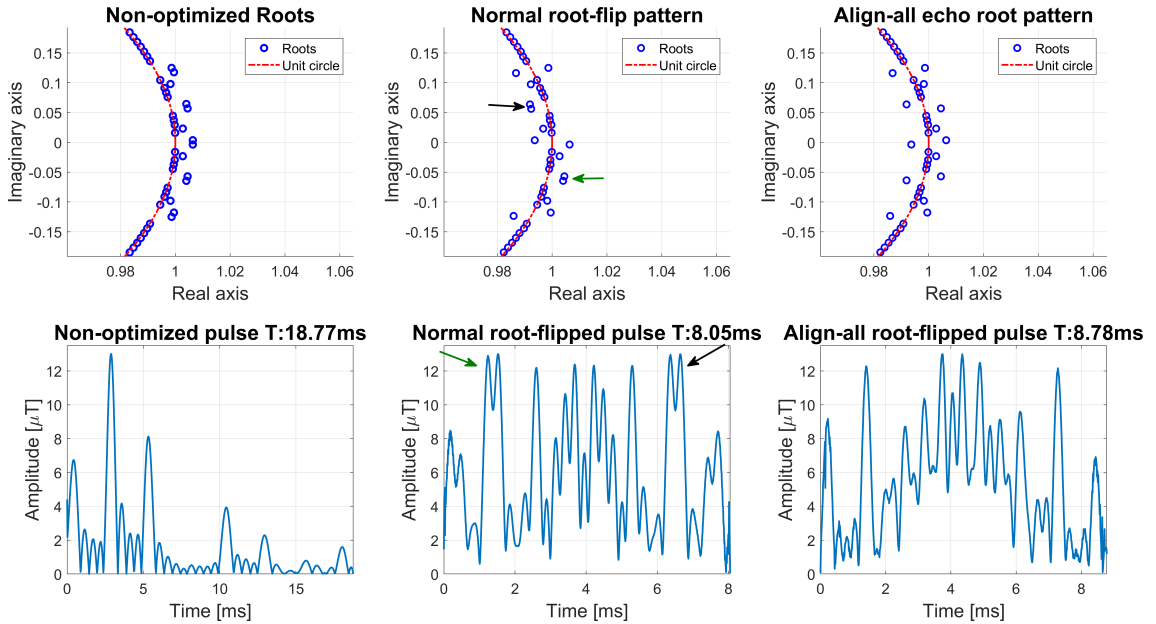
Figure 3.2: Left Column: Root-plots on the complex plane for a Non-optimized (maximum-phase) MB5 pulse, before any optimization. Five distinct passbands, with roots away from the unit circle can be seen. All passband roots are still outside the unit circle, and therefore RF lobes are concentrated towards the beginning of the RF pulse (bottom-left). **Middle column:** An optimized root-pattern after unconstrained optimization. The passbands with two roots inside (black arrow) and outside (green arrow) the unit circle deposit their RF energy away from the center of the pulse, which can be seen by increased RF lobes in those regions (bottom center). **Right column:** Align-all pulses have even number of passband roots for all passbands and consequently excite and refocus the center of the slices simultaneously. The resulting RF pulse contains more RF lobes concentrated to the center, and an increased pulse duration (bottom right).

3.4 Methods

3.4.1 RF pulse design

Root-flipped RF pulses were designed as described in [7] using code made available by Sharma et al. downloaded from `http://www.vuiis.vanderbilt.edu/~grissowa/`. As proposed in the original method, the refocusing pulse was optimized by flipping passbands inside and outside the unit circle, to find the root-flipping pattern which resulted in an RF pulse with the lowest peak amplitude. The Monte-carlo based search method from the original study was replaced by a Genetic Algorithm implementation, as this was found to slightly enhance performance [81]. Once the optimal refocusing pulse was determined, the excitation RF pulse is derived from the refocusing pulse using any of the three excitation methods (aligned-echo, align-TE or minimum-duration). Thus note that for these three methods, the root-flipped refocusing pulse remained unchanged.

Root-flipped RF pulses with inherently aligned echoes (align-all pulses) were designed by forcing the root-flipping pattern for each passband to have an equal number of passband roots inside as outside the unit circle. Such a root-flip pattern requires an even number of passband roots, which is related to the time-bandwidth product (TBP) of the target design. For example, TBP=4 gives two roots per passband; and thus all pulses in this work were designed with this TBP. This relationship between the number of passband roots and TBP was found through trial and error. The modified root-flipping algorithm selects an even number of roots per passband closest to the passband center and flips them evenly across the unit circle, as shown in Figure 3.2.

To minimize the peak RF amplitude, this was repeated in a Monte-Carlo optimization with different patterns in each slice. This constrained root-pattern results in pulses with $\Delta T_{arr} \approx 0$ regardless of the excitation method. To additionally benefit from $\Delta T_{xy} = 0$, the align-TE excitation pulse is derived from the optimal align-all refocusing pulse, to have a pair of align-all pulses. All excitation and refocusing pulses were designed with a flip-angle of 90º and 180º respectively, with 2mm slices, for a range of multiband factor 3-12 and a range slice-separations of 6-32mm in steps of 2mm. The peak RF amplitude was set to $B_{1,max} = 13\mu T$.

3.4.2 Spin-echo simulation

The magnetization vector in the presence of ΔB_0-induced dephasing and T_2 relaxation was simulated by solving Bloch equations, using matrix decomposition to evaluate its matrix exponential. As described in 1.3.3, dephasing within each voxel was simulated by an additional frequency-axis, along which a background gradient simulated the dephasing of isochromats in the transverse plane.

The predicted signal was estimated by Lorentzian weighted-averaging along this axis for T_2^* of 45ms, and T_2-relaxation was set to 80ms, which corresponded to white matter values at 3T [82]. For each slice, 7 spatial points were simulated across 30% of the slice-width. The nominal echo time of this sequence was 90ms, and T_1-relaxation was ignored ($T_1 = \infty$).

3.5 Results

Figure 3.3 shows temporal profiles of the resultant RF pulses, as well as the simulated time-evolution of magnitude transverse magnetization in a 90º-180º spin-echo sequence, for a multiband-5 example and a nominal TE of 90ms. For align-TE or aligned-echo, either T_{arr} or T_{xy} differs through the group of five simultaneously excited slices. Going further, the minimum-duration approach leads to a discrepancy in both T_{arr} and T_{xy}. All

these approaches will thus lead to a slice-by-slice discrepancy in T_2^* and/or T_2-weighting. However, Figure 3.3d shows that the proposed align-all approach results in nearly complete alignment of the echoes, and thus a consistent T_2^* and T_2-weighting for all excited slices.
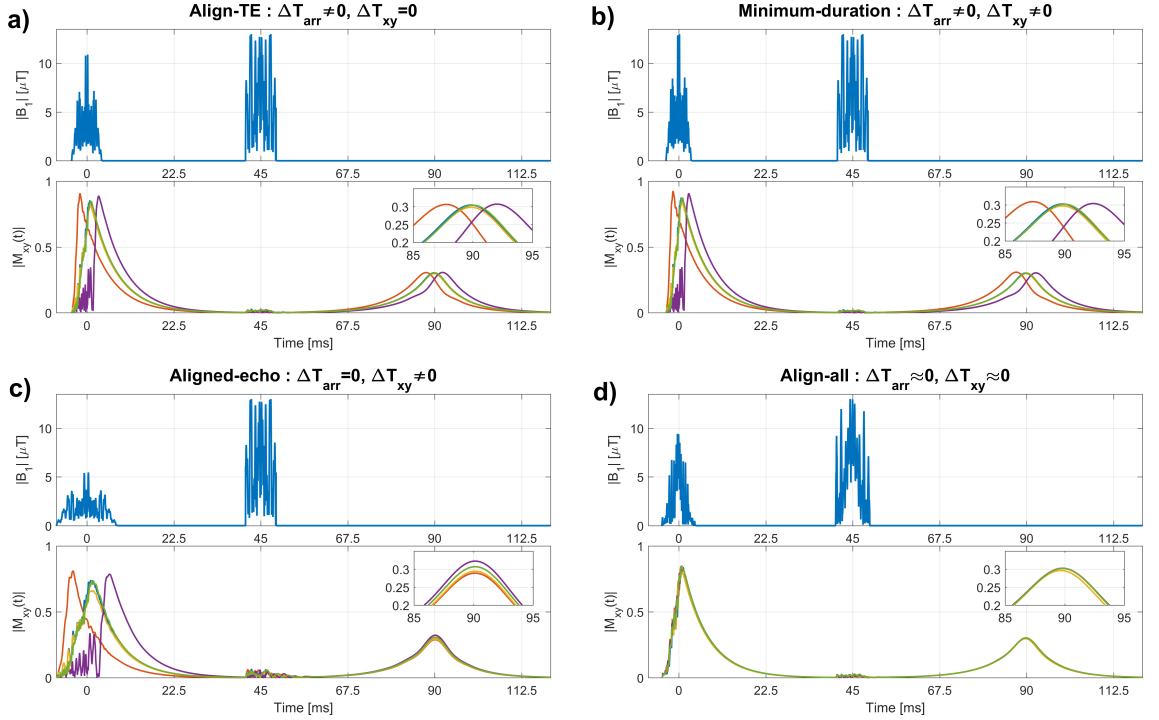
Figure 3.3: Example spin-echo simulations for multiband 5 pulses with different excitation methods for a nominal echo time of 90ms. The five slices were simulated with T_2 and T_2^* relaxation. The spin-echo sequences in subfigures **a)**, **b)** and **c)** all use the same refocusing pulse, with align-TE, minimum-duration and aligned-echo excitation respectively. The echoes from different slices in a) and b) arrive a few milli-seconds apart from each-other, but with only a small amount of difference in T_2-weighting. c) shows all slices with aligned echoes, but with different T_2-weighting. d) shows an example of an align-all simulation, where the echoes arrive almost simultaneously with equal T_2-weighting.

Figure 3.4 shows the maximal expected differences in echo arrival time, ΔT_{arr}, as well as the maximal expected time-difference of slices being transverse, ΔT_{xy}. The analysis is shown for the four types of root-flipped spin-echo modes considered in this work, for a range of multiband factors and slice-separations. The top row show the expected ΔT_{arr} to be virtually zero for the aligned-echo case, where-as align-TE shows a 2-6ms difference and minimum-duration an average of 4-8ms difference. Both these excitation methods will thus lead to a difference in T_2^*-weighting, and this analysis shows that the maximal difference will be proportional to the excited number of slices. This is to be expected, as the excitation and refocusing pulse durations both increase with respect to multiband factor, leaving more space for discrepancy. This effect however is not present for the align-all method, which closely resembles the aligned-echo case thanks to the constrained root-flipping pattern, inherent to its design. The bottom row shows how ΔT_{xy} is expected to vary, and again is shown to be virtually non-existent in the align-TE case. In the

aligned-echo case it will vary 6-14 ms on average, depending on the excited number of slices, whilst in the minimum-duration case it remains consistent around 2.5ms. This is expected to result in a difference in T_2-weighting for different slices. The align-all method explicitly makes use of the align-TE excitation method, and therefore results in a similar ΔT_{xy} performance.
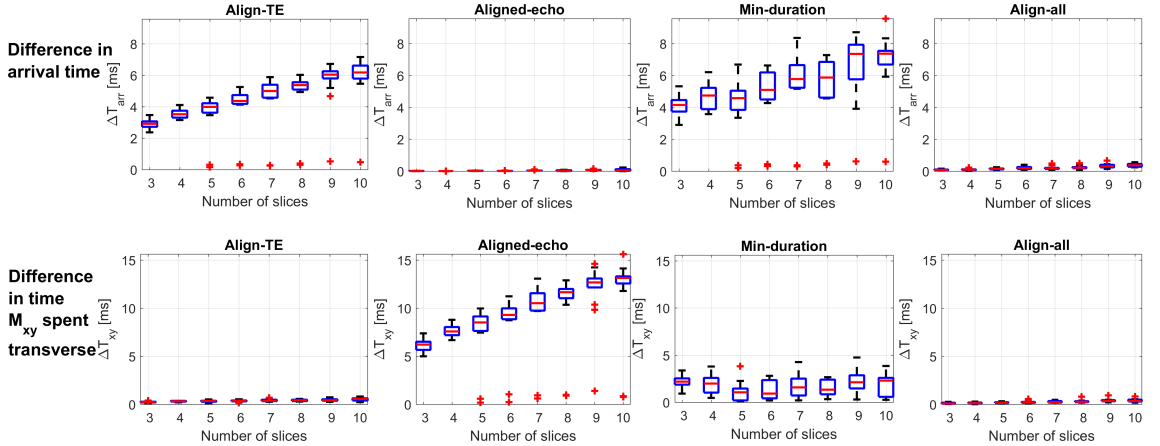
Figure 3.4: Top row: Difference in echo arrival time (ΔT_{arr}) for a range of multiband factors and slice separations. The aligned-echo has perfect time-alignment, where-as the align-TE and minimum-duration have a few milli-seconds of mismatch. This will lead to a difference in T_2^*-weighting. Align-all comes very close to aligning the echoes, which will happen regardless of the excitation method used. **Bottom row:** Difference between the longest and shortest T_{xy}. This value is near zero for the align-TE method and similar for the align-all method. Outliers show that align-all solutions can also be found without imposing the constraint.

Figure 3.5 shows that on average the align-all root-flipped pulses are 18.5% longer in duration than those from the original method. This is expected, since they are more constrained designs. Align-all pulses remain on average 50% more efficient than phase-optimized pulses. To assess how each of the excitation-refocusing technique would compare in a spin-echo EPI type sequence, both pulse durations must be taken into account. This is shown in Figure 3.5b, where the minimum-duration method outperforms all other methods. Align-TE is only slightly worse, but both these methods have misaligned echoes. The align-all method comes out on top amongst the three methods which align all echoes in time, outperforming phase-optimization by 41.6% and the aligned-echo method by 11.1%, on average. However, by the same measure it is also 27.2% longer than the minimum-duration pulses.

3.6 Discussion

Time-shifted and root-flipped pulses are both novel methods in multiband spin-echo imaging. Being more time-efficient than earlier phase-optimized MB pulses, they are a promising technique for multiband EPI, which could be useful for diffusion-weighted imaging (DWI) and spin-echo functional MRI. However, the topic of misaligned echoes was an
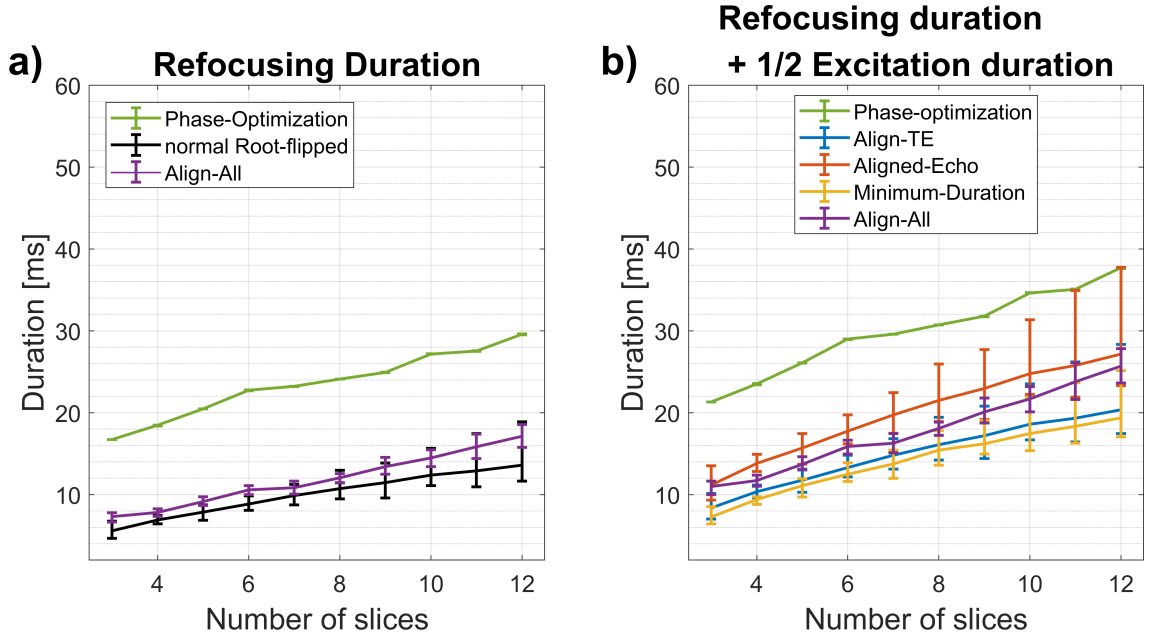
Figure 3.5: a) Duration of refocusing pulses designed using phase-optimization, root-flipping and align-all root-flipping. On average, the proposed align-all method incurs a 18.5% increase in pulse duration compared to unconstrained root-flipping. However it is still 50% more efficient than phase-optimization, which is the only other method which inherently aligns all echoes. **b)** To fully appreciate how each method performs, this graph shows the refocusing duration plus halve the excitation duration. This score takes into account how each pulse-pair either allows for a reduction in TE or more diffusion encoding time. Minimum-duration performs best in this respect, with align-TE only slightly worse. Out of the three methods that align the echoes in time, the proposed align-all methods performs best, outperforming phase-optimization by 41.6% and the aligned-echo method by 11.1%. However, when considered as a excitation-refocusing pulse set it is 27.2% longer than minimum-duration.

unresolved issue since first identified by Auerbach et al [39]. Figure 3.1 shows temporal signal evolutions which results in problematic misaligned echoes when using conventional root-flipped RF pulses. This work has investigated the potential discrepancies one can expect to encounter, when using root-flipped RF pulses in a sequence with timing and relaxation parameters representative of spin-echo DWI imaged using EPI [83].

Figure 3.3 validates that existing methods will inevitably result in a discrepancy in T_2 and/or T_2^*-weighting. Only our newly proposed align-all root-flipping algorithm achieves a nearly complete alignment in echoes for all slices. Arguably, this method is designing a root-flipped pulse without the time-shifting attribute. The time-alignment for the align-all method is only approximate, as it can still be a fraction of a millisecond larger than the echoes from the aligned-echo approach. This is because the time-alignment is achieved in different ways; in the aligned-echo approach the net phase accumulation is set to perfectly align at the echo-time [39, 80], such that all echoes align simultaneously. However in the align-all approach the similar effect is achieved by forcing the magnetic center for each slice at the center of the root-flipped pulse. This effect however highly resembles the aligned-echo approach.

3.6. Discussion

Figure 3.4 quantitatively shows how ΔT_{arr} and ΔT_{xy} vary across the number of excited slices and different slice-separations. It validates that align-TE and aligned-echo excitation methods result in a near-zero cancellation of ΔT_{arr} and ΔT_{xy}, respectively. The minimum-duration method has no cancellation for either, but benefits from having a shortest possible excitation pulse. However the align-all methods results in a consistent removal of both ΔT_{arr} and ΔT_{xy}.

Such cancellation however is not unique to the align-all method. As can be seen from the outliers in Figure 3.4 at $\Delta T_{xy} = 0$ or $\Delta T_{arr} = 0$ for existing excitation methods, sometimes the align-all solution was found without imposing the root-flipping constraint.

Generally, both ΔT_{arr} and ΔT_{xy} increase with respect to the number of excited slices. This was an expected result as it relates to an increase in both excitation and refocusing duration. The exception to this is ΔT_{xy} for the minimum-duration condition, which remains roughly consistent. This is because the excitation and refocusing pulse durations increase consistently with each other, as the number of excited slices is increased, and therefore no increase in ΔT_{xy} is found.

The highest discrepancy in ΔT_{xy} was 5-15ms, and 2-8ms for ΔT_{arr}. The connection between a timing mismatch and signal attenuation can be found by exponentially weighing such time-measures for our proposed T_2 and T_2^* values. For example, a difference of ΔT_{xy}=10ms (roughly corresponding to MB6 in an aligned-echo case) would lead to a 11.7% reduction in signal amplitude. Similarly, a typical ΔT_{arr} for MB4 using minimum-duration excitation is 4ms, which translates to a 8.5% signal dropout. Such signal reductions are considered small, but not insignificant as an discrepancy across slices interferes with volumetric-based analysis. Further work could investigate the effect on the point spread function thanks to such echo behaviour.

Figure 3.5a shows the refocusing pulse durations, which show that the cost of using align-all refocusing pulses comes at an average duration increase of 18.5% compared to the conventional root-flipped refocusing pulses. Figure 3.5b also shows how each pulse-pair of excitation and refocusing would perform in a single spin-echo style sequence. This score indicates how each method can be used to reduce the sequence TE, which leads to higher SNR, or allow for more diffusion encoding which might be desirable for high b-values, which give different micro-structural contrast. When using an excitation and refocusing pair, the align-all method outperforms phase-optimization by 41.6% and the aligned-echo method by 11.1%. However the combination is still 27.2% longer than the minimum-duration pulse set. It is also possible to combine a minimum-duration excitation pulse with an align-all refocusing pulse, which together would produce $\Delta T_{arr} \approx 0$ and $\Delta T_{xy} \neq 0$, but produce a shorter combined excitation-refocusing duration.

The align-all method successfully eliminates a spread of echoes for different slices. However it is limited to cases where there an even number of roots per passband, and thus a limited regime of time bandwidth products. An exact derivation between the number of roots and

time-bandwidth product could not be found. In this work only RF pulses with constant valued gradients were considered. More advanced pulse design methods can use time-variable gradients, such as PINS [48], VERSE [42] or optimal control methods [84]. As will be shown in the next chapter, when using time-optimal VERSE [45] the duration difference between phase-optimized and root-flipped pulses becomes insignificant.

In this work only white matter tissue was considered at a single field-strength, but it is expected that the T_2^*-values are critical in this investigation, with shorter relaxation leading to more signal attenuation. A more comprehensive investigation could consider both white and gray matter, at different field strengths.

3.7 Conclusion

Root-flipped multiband pulses as proposed result in a discrepancy in spin-echo formation for different slices. The discrepancy in echo-time arrival and transverse evolution was investigated using spin-echo Bloch simulations and reported to be of the order of 2-14ms, depending on excitation method and the excited number of slices. An alternative root-flipping algorithm was proposed which makes these discrepancies negligible, and outperforms the existing phase-optimization method by 50% in refocusing duration.

Chapter 4

Multiband RF pulse design for realistic gradient performance

4.1 Contributions

The findings in the following chapter have been fully discussed in the following publications.

S Abo Seada, AN Price, TS Schneider, JV Hajnal, SJ Malik. Multiband RF pulse design for realistic gradient performance. Magnetic Resonance in Medicine September 2018 DOI: 10.1002/mrm.27411

MatLab code to perform these findings is publically available at
`https://github.com/mriphysics/verse-mb`

4.2 Preface

In late 2015 the ISMRM RF pulse design challenge (`http://challenge.ismrm.org/`) was announced, inviting RF pulse designers to participate ahead of the ISMRM meeting in 2016. The challenge had two sub-challenges; to design the shortest possible multiband refocusing pulses, and the design of parallel transmit excitation pulses. All RF designs had to adhere to fixed hardware constraints (peak B_1 amplitude, and peak gradient amplitude and slew-rate) as well as a fixed slice-profile. Participants submitted their designs online, and an up-to-date leaderboard showed updated results.

The first sub-challenge was highly relevant to the work of this thesis, and it was soon realised that a very effective method to deliver a time-optimal design incorporating hardware constraints was the time-optimal VERSE framework, discussed in section 1.2.7.

The multiband sub-challenge was to design two separate pulses, one for a multiband 12 with a linear-phase constraint applicable to a multiband TSE sequence, and a second for a multiband 5 without a phase constraint, which could be useful for a spin-echo diffusion sequence. The total score for each submission was the summed durations.

Figure 4.1a shows the progress of the leaderboard, adapted from [46] marked with our team-name "Nothing Exciting". Our team finished 5th in the first phase of the challenge, and the winning rfcontrol team made use of a time-optimal control framework which designed time-variable RF and gradient waveforms based on the Bloch equations [85] An MB5 example is shown in Figure 4.1b.
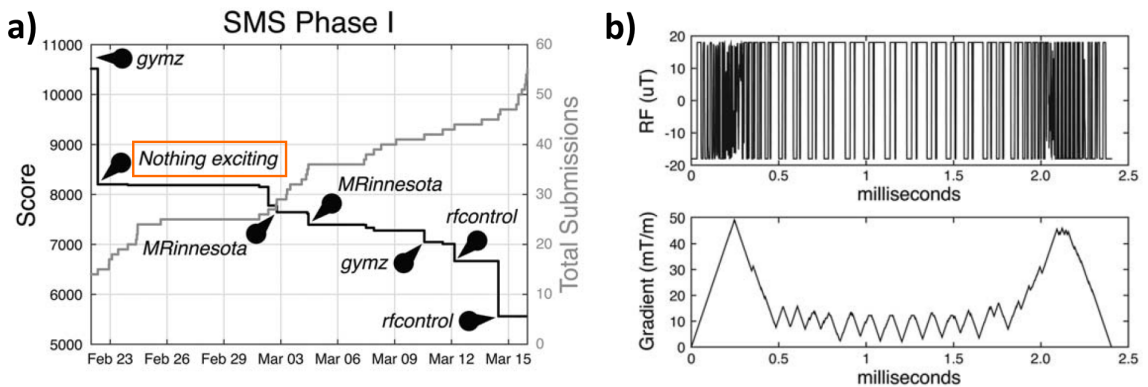
Figure 4.1: a) A graph of the submissions for the ISMRM RF pulse design challenge leaderboard in 2016. Our team "Nothing exciting" participated and came 5th in the first phase. **b)** An example of the winning submission, used rapidly varying RF and gradient waveforms. Figures adapted from [46].

As a result of the ISMRM challenge, it became clear that MB designs with time-variable gradient were likely to become components of future multiband applications, where RF and selection gradients share the burden of transmit-based image acceleration. However this assumes that RF and gradient systems have a similar bandwidth performance, and from previous work [86] it was known that gradient systems often struggled with faithfully reproducing rapidly varying waveforms. As discussed in section 1.4.2 this can be modelled by a measured gradient impulse response function (GIRF). Figure 4.2 shows a reproduction of the VERSE example from the introduction (Figure 1.15) including the GIRF effects.

The first approach we took was to correct for GIRF-distortions using an iterative VERSE correction method, as shown in an ISMRM abstract [87]. The down-side to such methods is that they require an accurate GIRF, and that they tend to create gradient waveforms which are actually more demanding on MR hardware.

A more elegant solution is to avoid such high temporal modulation from being passed onto the gradient waveform in the first place. This can be done by applying time-optimal VERSE on a singleband pulse, before applying multiband modulation to it with necessary time adjustments. This accounts for the knowledge that current gradient systems are not
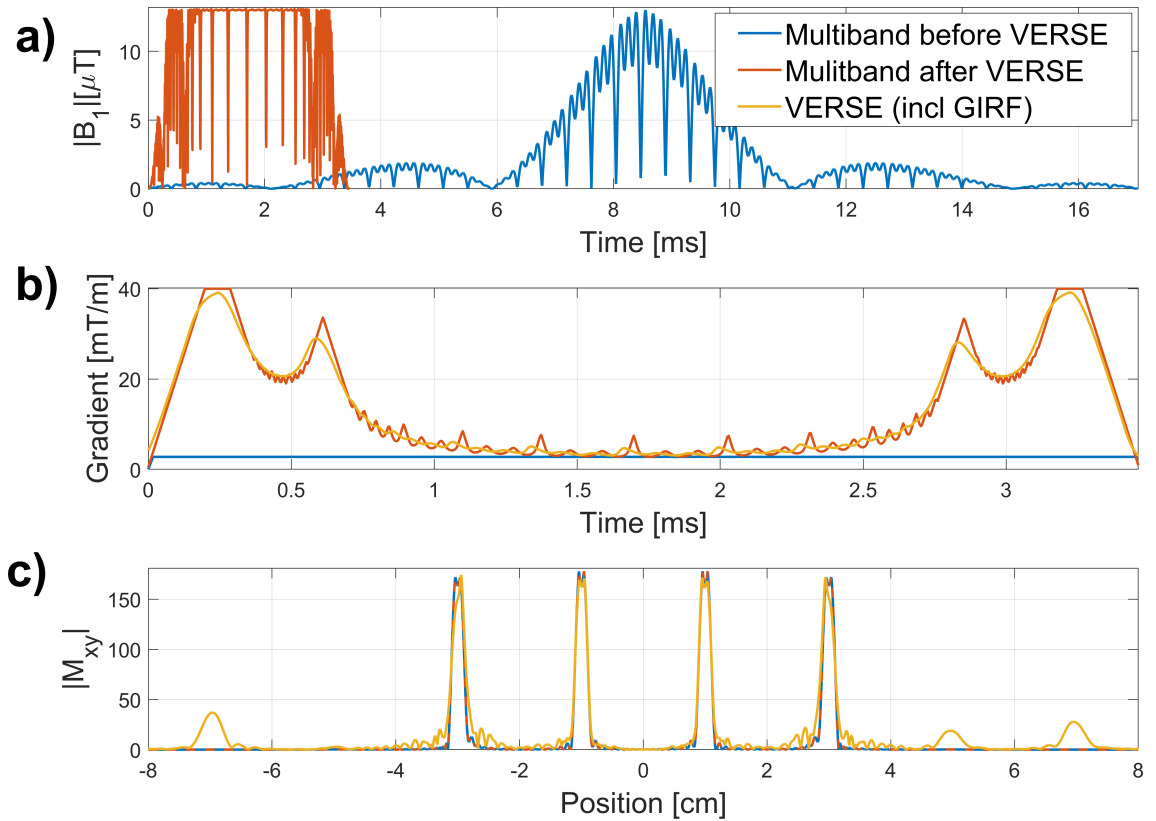
Figure 4.2: The example from Figure 1.15 repeated, incorporating GIRF effects (see 1.4.2). The predicted gradient distortion results in slice-distortions as well as spurious excitation outside the field-of-view. Note that the gradient shape here is similar to the one in Figure 4.1b.

able to reproduce temporal modulations at the frequencies of multiband pulses. However most of the benefit from VERSE can still be achieved from optimizing the gradient for a singleband RF pulse.

This chapter presents a study of this approach, and the following text is reproduced as published.

4.3 Multiband RF pulse design for realistic gradient performance

Magnetic Resonance in Medicine

Multiband RF pulse design for realistic gradient performance

Samy Abo Seada[1] iD | **Anthony N. Price**[1] iD | **Torben Schneider**[2] |
Joseph V. Hajnal[1] iD | **Shaihan J. Malik**[1] iD

[1]School of Biomedical Engineering & Imaging Sciences, King's College London, King's Health Partners, St Thomas' Hospital, London, United Kingdom
[2]Philips UK, Guildford, United Kingdom

Correspondence
Shahain J. Malik, Faculty of Life Sciences & Medicine, School of Biomedical Engineering & Imaging Sciences, King's College, London, United Kingdom.
Email: shaihan.malik@kcl.ac.uk
Twitter: @shaihanmalik

Funding information
This work was supported by the Wellcome Trust/EPSRC Centre for Medical Engineering at King's College London [WT 203148/Z/16/Z]; the Medical Research Council [MR/K006355/1]; the National Institute for Health Research (NIHR) Biomedical Research Centre based at Guy's and St Thomas' NHS Foundation Trust and King's College London. The views expressed are those of the author(s) and not necessarily those of the NHS, the NIHR or the Department of Health. This work was additionally supported by Imperial College London EPSRC Centre for Doctoral Training in Medical Imaging [EP/L015226/1]; and EPSRC [EP/L00531X/1] Philips Healthcare.

Purpose: Simultaneous multi-slice techniques are reliant on multiband RF pulses, for which conventional design strategies result in long pulse durations, lengthening echo-times so lowering SNR for spin-echo imaging, and lengthening repetition times for gradient echo sequences. Pulse durations can be reduced with advanced RF pulse design methods that use time-variable selection gradients. However, the ability of gradient systems to reproduce fast switching pulses is often limited and can lead to image artifacts when ignored. We propose a time-efficient pulse design method that inherently produces gradient waveforms with lower temporal bandwidth.

Methods: Efficient multiband RF pulses with time-variable gradients were designed using time-optimal VERSE. Using VERSE directly on multiband pulses leads to gradient waveforms with high temporal bandwidth, whereas VERSE applied first to singleband RF pulses and then modulated to make them multiband, significantly reduces this. The relative performance of these approaches was compared using simulation and experimental measurements.

Results: Applying VERSE before multiband modulation was successful at removing out-of-band slice distortion. This effectively removes the need for high frequency modulation in the gradient waveform while preserving the benefit of time-efficiency inherited from VERSE.

Conclusion: We propose a time-efficient RF pulse design that produces gradient pulses with lower temporal bandwidth, reducing image artifacts associated with finite temporal bandwidth of gradient systems.

KEYWORDS
gradient frequency characterization, minimum duration, multiband, RF pulse design, time optimal, VERSE

1 | INTRODUCTION

Simultaneous multi-slice (SMS) imaging uses multiband (MB) RF pulses to accelerate MR image acquisition by acquiring data from multiple slices simultaneously.[1,2] A simple method for designing an MB pulse is to multiply a singleband (SB) pulse by a modulation function that replicates the slices in the frequency domain.[1,3] This method quickly reaches hardware limits on peak amplitudes as the number of slices increases, forcing pulse designers to either increase the pulse duration or reduce the flip angle, both of which are problematic for sequences such as spin-echo diffusion imaging and turbo spin echo (TSE) where high signal and short echo times are important.[4-6] Similarly, specific absorption rate (SAR) constraints in MB SSFP applications force the use of sub-peak amplitude MB RF pulses, which have long pulse durations and become difficult to fit within TR constraints.[7,8]

A range of solutions have been proposed to reduce the peak amplitude of MB waveforms including phase-optimization,[9-13] time-shifting,[10,14] and root-flipping.[15] These methods aim to reduce the peak amplitude for a given constant slice selection gradient. Alternatively, "power independent of number of slices" (PINS)[16] pulses use a different paradigm in which an SB waveform is split into discrete subpulses and undersampled to create a periodic excitation in the slice-select direction. This method has low RF energy but generally long pulse durations, especially for designs with large slice-gaps. It can be made more efficient (either in time or RF energy) in combination with more traditional MB pulses—this method is known as MultiPINS.[17]

PINS pulses do not use a constant selection gradient, rather the gradient is switched on and off periodically. Taking this further, there has been recent interest in designing combinations of RF pulses and time-variable selection gradients, which together yield the minimum possible duration. Such pulses were designed for the ISMRM pulse design challenge in 2016[18] where participants used time-optimal VERSE algorithms[19-21] and the winning technique used an algorithm that designed RF pulses using an optimal control approach.[22-24] These solutions are typically associated with very fast temporal modulation of both RF and gradient waveforms, which can be problematic if the temporal output bandwidth of the RF and gradient systems is not sufficient. In practice, however, the output bandwidth for RF chains far exceeds that of a gradient system, which implies that fast switching gradient waveforms are unlikely to be reproduced with high fidelity.

Recent work has demonstrated that for both RF pulse design[25] and image reconstruction,[26] limited temporal bandwidth of commercial MRI gradient systems leads to errors when gradient waveforms with high temporal bandwidth are demanded. The effective bandwidth of a gradient system relates to eddy currents,[27,28] but also to the design of the gradient coil and amplifier bandwidth.[19] Performance can vary between manufacturers, different models and types (body vs.

head), and also different orientations. Under the assumption that the system is linear time invariant (LTI), however, all of these factors can be captured by measuring the gradient impulse response function (GIRF)[26] for any particular system.

Although hardware limits such as peak slew rate and amplitudes can be enforced as static constraints, it is not straightforward to directly incorporate a GIRF into a time-optimal design as temporal bandwidth is a function of the complete waveform. The result is that such pulses are prone to gradient distortion related artifacts, as will be demonstrated later.

The focus of this work was to produce time-optimal MB designs that avoid very high bandwidth demands on the gradient system. As shown in Hargreaves et al.,[19] when VERSE is applied on SB gradients, the gradient pulses retain manageable bandwidth demands. With this in mind, we combined multiband pulses and VERSE in 2 different ways and compared their associated gradient waveforms. Firstly, the time-optimal VERSE method[20,29] was applied directly on an MB pulse. Secondly, we applied VERSE first to an SB pulse, before applying MB modulation (which alters the RF pulse and leaves the VERSE gradient pulse intact). We hypothesized that the latter approach would benefit from a gradient waveform with lower temporal bandwidth and therefore suffer less from slice profile distortions. This concept is shown in Figure 1.

In this work, we investigate the slice profile effect because of imperfect gradients on time-optimal MB pulses by using VERSE (for both linear and non-linear phase pulses), PINS, and MultiPINS. We report on slice profile error, pulse durations, RF energy, and off-resonance effects. We show that optimizing a time-variable gradient for a SB waveform before MB modulation produces short duration RF pulses, while effectively reducing slice profile errors, and demonstrate this experimentally.

2 | THEORY

The time-optimal VERSE approach as applied to RF pulse design is described in Lee et al.[20] and is referred to as VERSE in this work. For a given combination of RF and gradient pulses, it returns revised versions of these that minimize transmit time, subject to peak B_1 ($B_{1,max}$), gradient amplitude (G_{max}) and slew rate (S_{max}) constraints. We consider 2 approaches to combining this with MB RF pulse design: (1) design an MB pulse for a constant gradient, then apply the VERSE algorithm (MBv); and (2) design an SB pulse for a constant gradient, apply VERSE, then modulate it to form an MB pulse (vMB).

For the first approach phase-optimized[11] MB RF pulses were designed, which were then optimized using VERSE. The second approach applies VERSE to a standard SB pulse before applying a modulation function to produce an MB pulse. For a constant gradient MB pulse, exciting N slices, this function is defined as

$$f_N(t) = \sum_{n=1}^{N} e^{i(\gamma G t x_n + \phi_n)},$$

(1)

ABO SEADA ET AL.
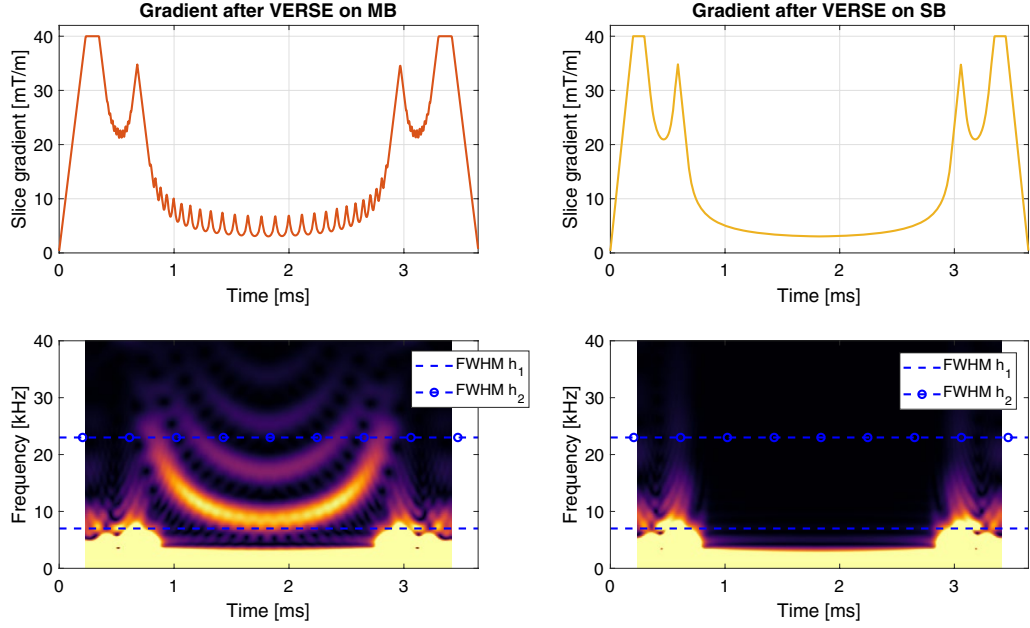
FIGURE 1 A time-variable gradient as a result of VERSE, when applied to a multiband (MB) pulse (left column) and a singleband (SB) pulse (right column), both stretched to have matched durations. The gradient pulses have similar shapes, but the left pulse contains additional high-frequency components, which the VERSE method translates from a highly-modulated MB RF pulse. The bottom row shows spectrograms with 2 dotted lines marking the FWHM of a measured and duplicated gradient impulse response function (GIRF), h_1 and h_2, respectively. Any high-frequency (HF) components from beyond the FWHM will be attenuated because of the GIRF. These HF components are not present in the right pulse, leading to reduced slice profile distortions

where γ is the gyromagnetic ratio, G is the amplitude of the constant selection gradient, t is a time-variable, x_n is the spatial location of the nth excited slice and ϕ_n is the phase-offset of this slice, numerically optimized as in Wong[11] and Abo Seada et al.[30] After application of VERSE the gradient waveform is time-variable, and this must be accounted for in the modulation function $f_N^v(t)$

$$f_N^v(t) = \sum_{n=1}^{N} e^{i(k(t)x_n + \phi_n)}, \quad (2)$$

where the spatial frequency variable $k(t)$ is defined as

$$k(t) = -\gamma \int_t^T G(s)\, ds. \quad (3)$$

When using the vMB method (i.e., performing VERSE on an SB pulse) the $B_{1,max}$ constraint must be reduced to account for the fact that after MB modulation the amplitude will be increased. In other words, for vMB, the $B_{1,max}$ amplitude constraint for exciting N slices becomes:

$$B_{1,max,N}^{SB} = B_{1,max} \max \left\{ \left| f_N^v(t) \right| \right\}. \quad (4)$$

Constant gradient MB pulse design methods that use non-linear through-slice phase patterns enhance performance when this phase dispersion is acceptable. To design MBv pulses with non-linear through-slice phase, we applied VERSE to MB pulses designed using the root-flipping method.[15] We refer to this method as non-linear MBv. Furthermore, we can design vMB pulses of this kind by applying VERSE to a non-linear SB waveform (in our case, quadratic phase)[31] and then apply modulation function $f_N^v(t)$. We refer to this method as non-linear vMB.

3 | METHODS

3.1 | RF pulse design

All methods were used to design refocusing pulses (180° flip) with a slice-thickness of 2 mm, maximum RF amplitude of $B_{1,max} = 13\ \mu T$, maximum gradient slew rate of $S_{max} = 200\ mTm^{-1}ms^{-1}$ and $G_{max} = 40\ mTm^{-1}$. Time bandwidth products (TBP) 2 and 4 were used, and the number of slices "N" was varied from 2 to 12. For each N, we designed 1 set of pulses with a fixed slice-separation of 14 slices (i.e., 28 mm from center to center) and 1 set with a fixed FOV of 200 mm, so a slice-separation of $\frac{200mm}{2mm}\frac{1}{N}$ slices. All pulse designs were implemented in MATLAB 2015b (The MathWorks, Natick, MA), each pulse

4.3. Multiband RF pulse design for realistic gradient performance

starting with 2048 samples and a sufficiently high sampling rate to avoid aliasing and numerical inaccuracies at high frequencies.

All the linear phase examples studied in this work started with the same Shinnar-Le Roux (SLR)-designed SB pulse. The SLR refocusing (assuming crusher gradients) pulse was designed using a finite impulse response (FIR) filter design approach, solved using a convex optimization approach, adapted from Sharma et al.[15] In- and out-of-slice ripples were set to 1%. MBv and vMB pulses were designed as described above. MB modulation was completed using a phase-optimized scheme as in Wong.[11] Optimal phase-offsets were obtained using MATLAB's fmincon function—these were always the same for a given *N*, and so phase-offsets were not adapted to match individual pulse designs.

Non-linear MBv pulses were root-flipped pulses, which were designed as described in Sharma et al.[15] with publicly available code (https://www.vuiis.vanderbilt.edu/~grissowa/software.html). For this work, the ripple relations were set to design a single refocusing pulse instead of a matched-excitation as originally proposed. Moreover, the Monte Carlo

search for optimal root-patterns was replaced by a genetic algorithm as implemented in MATLAB 2015b, which we previously found to give slightly improved results.[30]

Non-linear vMB were chosen as quadratic phase pulses, which were designed by first designing a minimum phase pulse with the same slice characteristics as the linear phase pulse. The minimum phase pulse was reduced in RF power by evaluating its equivalent Cayley-Klein β representation[32] and inverting all its β-roots on the bottom half of the unit circle, as described in Shinnar.[31]

PINS[16] pulses were designed by appropriately undersampling the same linear phase SB waveform depending on the ratio of slice-thickness to slice-separation. Code to produce such pulses was based on source files downloaded from https://bitbucket.org/wgrissom/lowpeakpowermbrf/overview. PINS RF blips were made as short as possible to minimize pulse duration, putting it in line with other time-optimal approaches in this study. Therefore, per PINS pulse, RF blips varied in duration (as dictated by $B_{1,max}$) but gradient blip duration was fixed (as limited by gradient slew-rate).
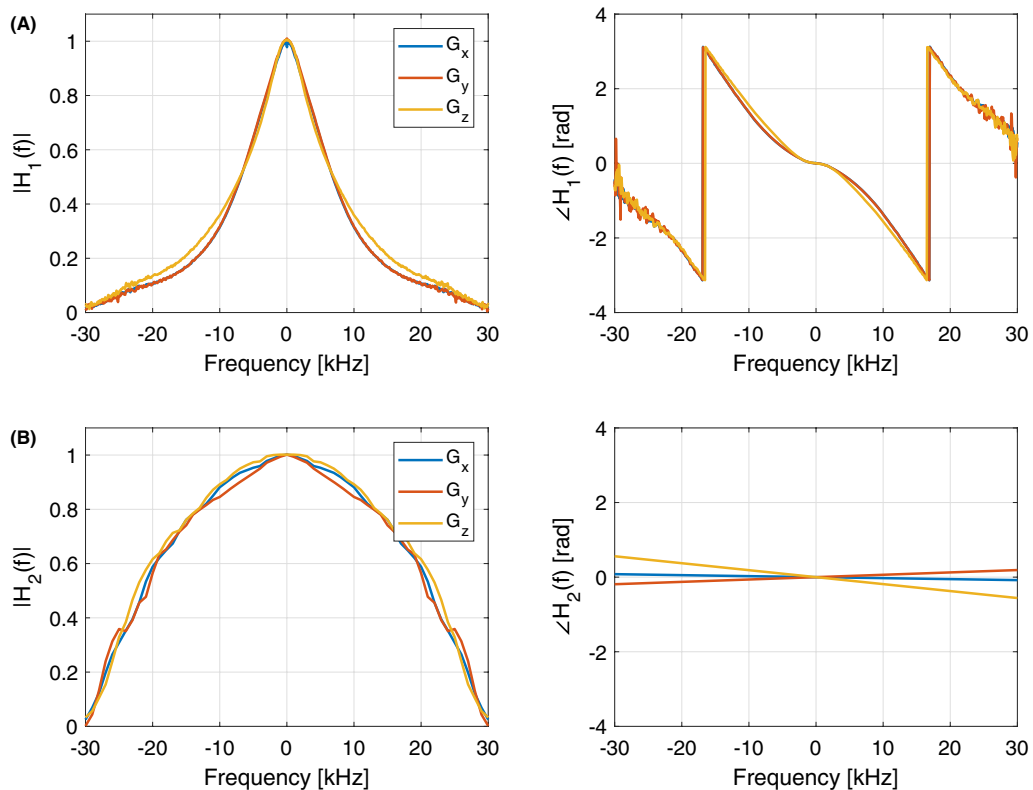
FIGURE 2 (a) Measured impulse response function h_1 in the frequency domain for all gradient axes at frequency resolution 156 Hz. The x- and y-axes are very similar, while the z performance is slightly different. (b) h_2 based on a published measurement from a different vendor, reconstructed with a frequency resolution of 1 kHz. The phase profile on the right is estimated to be linear (i.e., constant time-delay for all frequencies) for simplicity. Please note that although h_1 is a true experimental measurement, h_2 is only an approximation reconstructed from Testud[34]

MultiPINS pulses were designed by first designing a PINS pulse and then adding a reshaped MB pulse using a mixing ratio "M," defined in Eichner et al.[17] as

$$RF_{MultiPINS} = MRF_{MB} + (1-M) RF_{PINS}. \quad (5)$$

The mixing-ratio was increased from 0 to 1 (in steps of 0.005) to minimize pulse duration without exceeding $B_{1,max}$ (see Supporting Information Figure S1). For each value of M in Equation (5), RF_{PINS} was designed as described earlier. To design RF_{MB}, the same singleband waveform used for RF_{PINS} was multiplied by a modulation function without phase-optimization. Subsequently RF_{MB}, as defined for a constant gradient, was reshaped for the blipped PINS gradient using a VERSE algorithm, as described by Equation 8 in Eichner et al.[17] For time-optimal PINS and MultiPINS, better performance can be achieved with short sampling times thanks to shorter RF blips. In this work, the sampling time was set to 1.21 μs for all time bandwidth product 2 designs and 3.37 μs for all time bandwidth product 4 designs.

3.2 | Evaluation of gradient distortion

In this work, we use 2 different GIRFs $h_1(t)$ and $h_2(t)$ that are related to scanners from 2 different manufacturers, corresponding to a Philips Achieva 3T (Philips Healthcare, Best, The Netherlands) and a Siemens Magnetom 3T (Siemens Healthcare GmbH, Erlangen, Germany), respectively. $h_1(t)$ was measured experimentally using an image-based procedure similar to that reported in Papadakis et al.,[33] and $h_2(t)$ was reconstructed manually from Testud.[34] The 2 frequency responses are shown in Figure 2 and are quite different. Please note, however, that although $h_1(t)$ was measured experimentally, $h_2(t)$ should only be treated as an approximation. Both GIRFs included measurements for all 3 gradient axes, but in this work we used only the z-axis gradient coils (i.e., exciting purely transverse slices). Unless specified, h_1 was used for the results presented in this article.

For each candidate pulse design, the predicted gradient after distortion $G_{actual}(t)$ can be computed from the target waveform $G_{target}(t)$ by convolution:

$$G_{actual}(t) = G_{target}(t) * h(t). \quad (6)$$

In practice, the convolution was computed using frequency domain multiplication, and the GIRF was linearly interpolated beforehand to account for any differences in frequency resolution. Bloch equation simulations (using Cayley-Klein representation) were then performed using $G_{target}(t)$ and $G_{actual}(t)$ to find the target and predicted distorted slice profiles, respectively. Slice profiles were represented using flip angles $\theta(z) = arccos(M_z(z))$, and the

normalized RMS error (NRMSE) was computed between the 2 profiles and normalized to the target profile. Flip angle representation was chosen to make our analysis independent of the final use of these pulses. A specific measure relevant to spin-echo refocusing is the β^2 profile from the Cayley-Klein parameters, which was also calculated along with the phase deviation for β^2 and flip-angle profiles. Slice profile error was computed for both the FOV of a single pack of slices and 3 times this FOV. This distinguishes between distortions inside and outside the FOV being imaged, as the former relates to slice distortions leading primarily to blurred images, and the latter leads to residual ghosting and saturation effects. These errors are referred to as ϵ_{inside} and $\epsilon_{outside}$ respectively. Phase errors were also evaluated. Because phase is not well-defined when simulating a 180° pulse, we quantified the through-slice phase distortion for the pulses when scaled down to ~45° flip angle and also considered the phase profiles of β^2 without rescaling. In both cases, linear phase rolls common to all slices were discounted, because these could be balanced by appropriate rewinders/crushers. Finally, RF pulses with time-variable gradients are known to suffer more from off-resonance effects. To investigate this, off-resonance simulations were conducted for an outer slice of an MB4 TB4 example at off-resonance frequencies from 0 to 200 Hz.

3.3 | Experimental validation

Slice profile measurements were performed on Philips Achieva 3T system (Philips Healthcare, Best, the Netherlands) whose frequency response is close to $h_1(t)$. Phantom experiments used a cylindrical phantom containing 100 mL of saline (9 g/L) doped with 1% gadolinium contrast agent (0.5 mmol/L Gd-DOTA, Dotarem, Guerbet LLC, Bloomington, IN). RF pulses used were designed, based on a vendor SB waveform, as MB3 TB4.4 180° refocusing pulses, slice-thickness 2 mm, center-to-center gap of 20 mm, and optimized for the constraints $B_{1,max} = 13\,\mu T$, $G_{max} = 31\,mTm^{-1}$, $S_{max} = 200$ $mTm^{-1}ms^{-1}$. Both RF and gradient waveform were designed at a sufficiently short sampling time, before being downsampled to the MR system sampling time of 6.4 μs. To visualize the slice profile from these RF pulses in isolation, the pulses were scaled down by a factor of 3 (flip angle ~60°) and then incorporated into a 2D gradient-echo sequence (TR = 500 ms, TE = 25 ms, 0.2 × 0.48 mm in-plane resolution), with the read-out gradient moved to the same direction as the slice-selection gradient. Optimal phase-offsets were chosen to produce real-valued RF pulses (i.e. not complex-valued), which could be described using purely signed AM.[30] This was done to circumvent an additional known hardware issue with faithfully reproducing rapidly varying FM waveforms. This issue also led us to choose linear vMB rather than non-linear vMB

4.3. Multiband RF pulse design for realistic gradient performance

pulses, because the starting SB pulse in the non-linear case is not real-valued.

In vivo imaging was conducted on the same MR system, using a single healthy volunteer (male, 27 y) after the sequence, and the study was approved by our local ethics board. The same RF and gradient designs as those from the phantom experiment were used, with exception that the original 180° RF refocusing pulses were scaled down by a factor of 6 so that they could be used as low-tip excitation pulses. A gradient-echo sequence (TR = 100 ms, TE = 14 ms, slice-thickness 2 mm, 0.75×0.6 mm in-plane resolution) with a blipped-CAPI shift acquisition scheme was used,[35] and MB data were reconstructed with a SENSE-based algorithm using ReconFrame (GyroTools GmbH, Zurich, Switzerland).

Code to reproduce such VERSE and PINS RF and gradient pulses (and to perform the related simulations) has been made publically available on our GitHub repository (https://github.com/mriphysics/verse-mb).

4 | RESULTS

Figure 3 shows the temporal profiles of MB3 RF and target gradient pulses (G_{target}), as well as the predicted distorted gradient (G_{actual}) assuming GIRF $h_1(t)$. Application of VERSE leads to a compression of the RF waveforms with the MBv methods (Figures 3b, d) showing the smallest durations for this design, with little difference between linear and
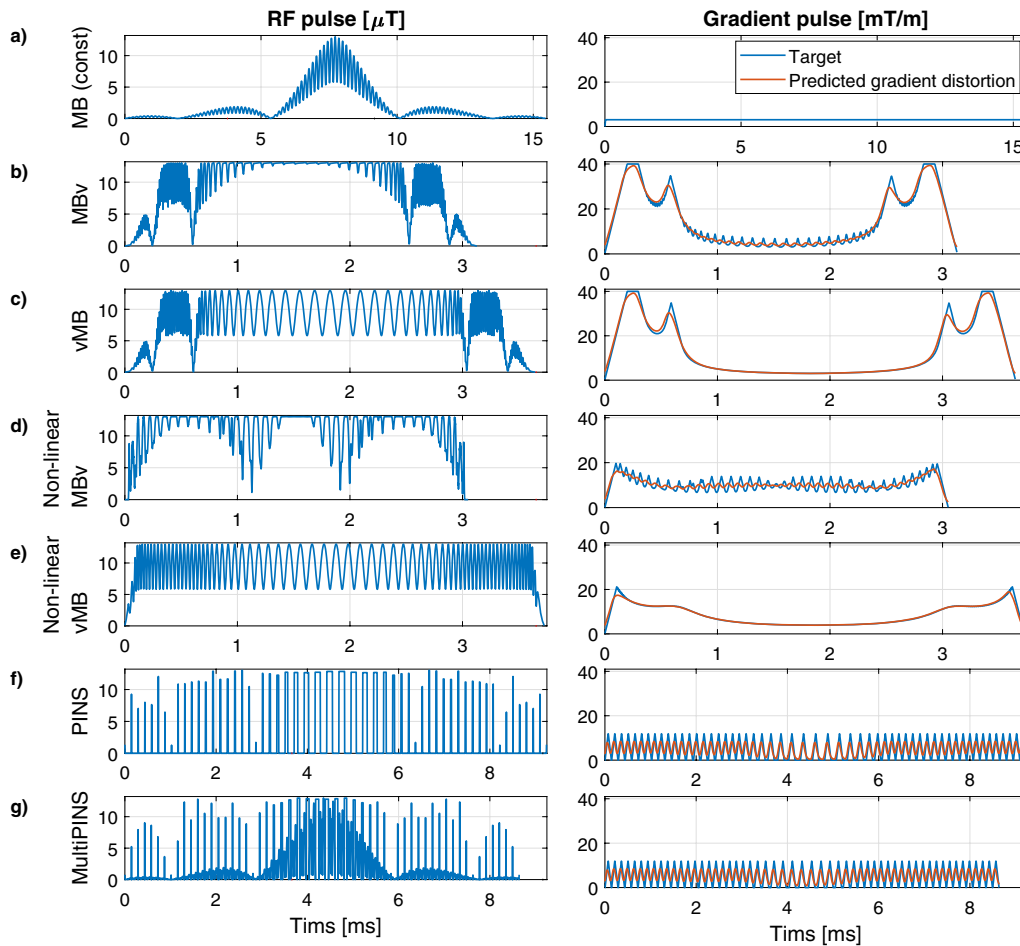
FIGURE 3 Example RF and gradient waveforms for every technique used in this work for an MB3, time bandwidth product 4 design with 2 mm slices and 28 mm slice-gap. The 2 columns display RF (only the modulus is shown for simplicity) and gradient waveforms, respectively, on different time scales. The effect of gradient distortion from GIRF h_1 is shown in orange. (a) Linear phase constant gradient MB pulse. (b) Multiband modulation followed by VERSE (MBv), linear phase. (c) VERSE followed by multiband modulation (vMB), linear phase. (d) MBv for non-linear phase. (e) vMB for non-linear phase. (f) PINS. (g) MultiPINS. The impact of the gradient distortion is shown in Figure 4
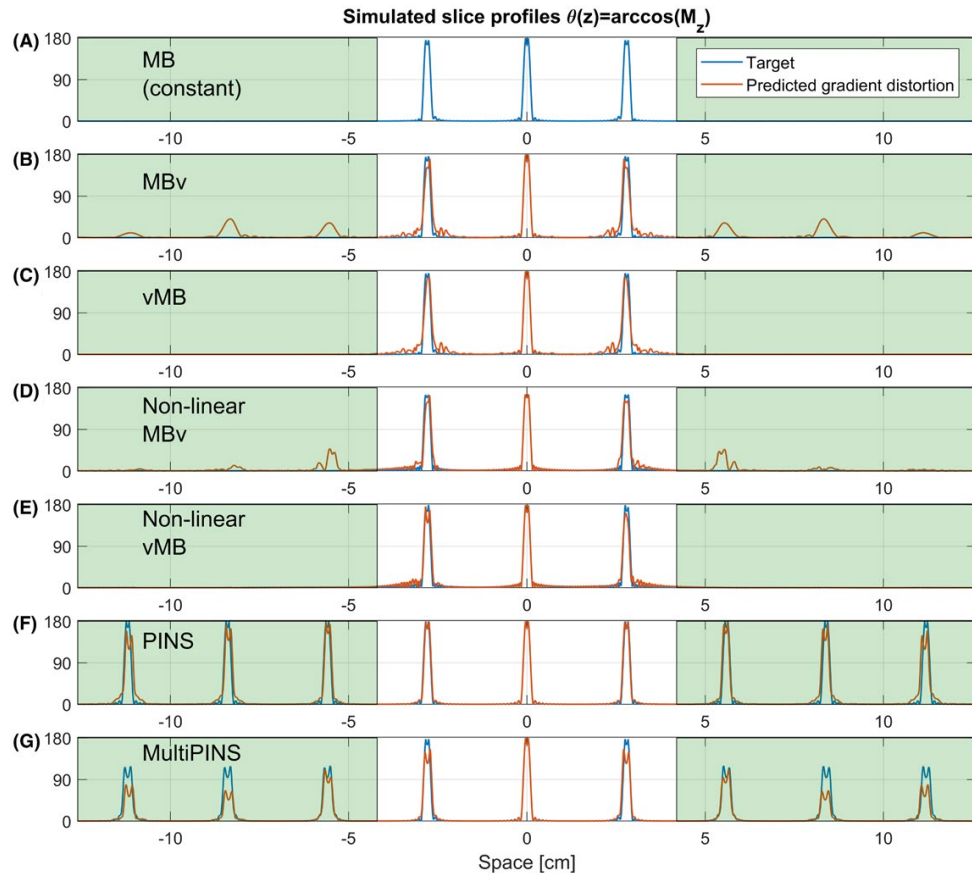
FIGURE 4 Slice profile distortions for the MB3, time bandwidth 4 refocusing pulses shown in Figure 3. Slice profiles are shown in flip-angle representation. For VERSE methods, the gradient distortions seen in Figures 3b–3e lead to distortion within the imaging slice-pack, as well as the additional excitation of ghost slices outside the imaging FOV for MBv methods. For PINS methods, gradient distortion leads to slice distortion within and outside the FOV, but often the error outside the FOV is ignored. The shaded and unshaded region shows where $\epsilon_{outside}$ and ϵ_{inside} are defined. A quantitative analysis of these errors across different designs is shown in Figure 5

non-linear phase. The gradient waveforms from Figures 3b, d show that when VERSE is performed on the MB pulses, the resulting gradient waveforms have high temporal bandwidth. The slice profile simulations in Figure 4 show that these designs result in artifacts at ghost-slice locations when the effect of limited gradient-system bandwidth is included. For PINS pulses, although temporal gradient distortion is relatively severe, because RF and gradients are not usually active at the same time, the effect of distortion as shown in Figure 4f is relatively minor. This is not the case for MultiPINS (Figure 4g) because RF and gradients are active simultaneously.

Figure 5 compares the slice profile errors inside (ϵ_{inside}) and outside ($\epsilon_{outside}$) the imaging slice-pack for various different N as predicted by both GIRFs (h_1 and h_2). As expected, the lower bandwidth GIRF shows greater distortion. All methods have some error within the FOV—this is also visible on Figure 4 and is mainly attributed to slice profile distortion and localized

ringing. The MBv methods (linear and non-linear phase) are noticeably more susceptible to error outside the FOV—this corresponds to the ghost slices that are excited because of distortion of gradient pulses with high temporal bandwidth. This is absent in the vMB methods, demonstrating the benefit of this approach. Supporting Information Figure S2 shows similar results for the case of fixed field-of-view, and Supporting Information Figure S3 shows such results when considering spin-echo refocusing profiles (β^2) instead of flip-angle representation. In Supporting Information Figure S3, it can be seen that $\epsilon_{outside}$ decreases for MBv and PINS methods, but the relations between all methods remain the same. Supporting Figures S4 and S5 show the additional average phase deviation across the slice profile because of gradient distortion, which was found to be of 1–5° additional loss in phase coherence.

The primary objective for our designs was to produce time-optimal RF pulses. Figure 6 shows the pulse durations for the
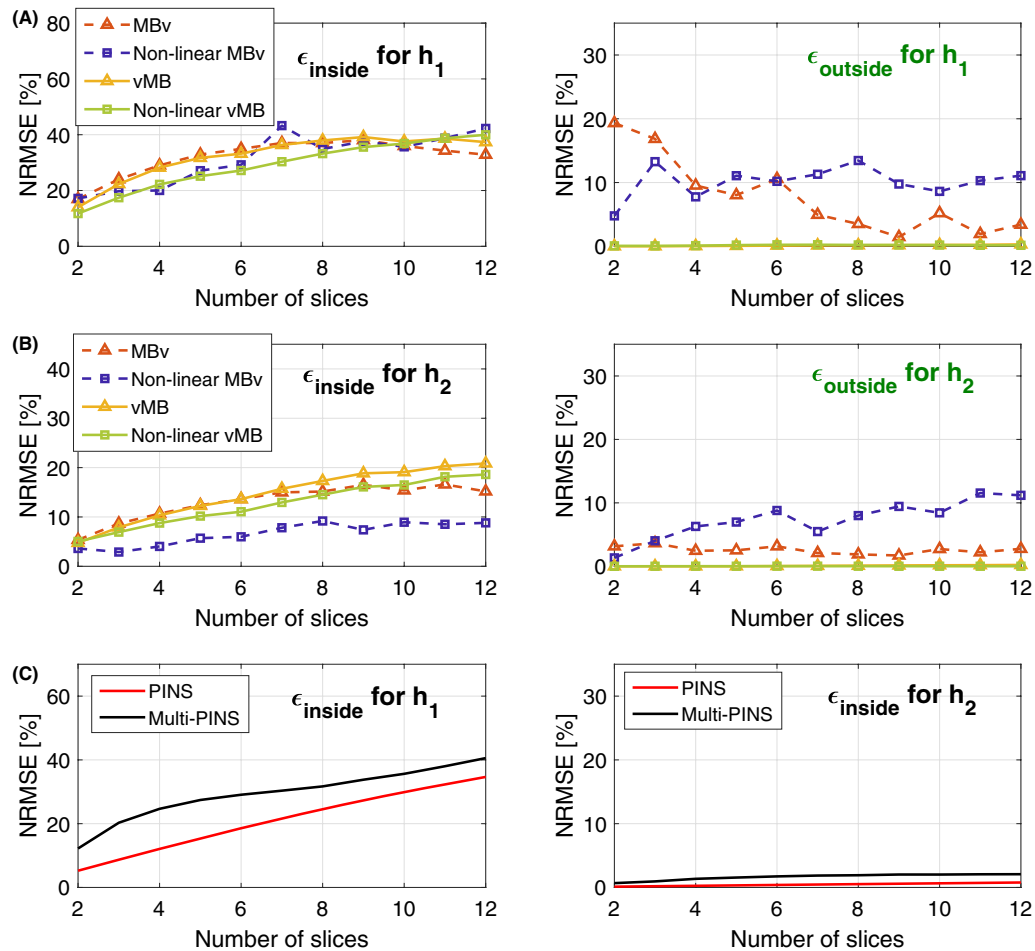
FIGURE 5 Slice profile error for the different techniques investigated inside and outside an imaging slice-pack (as illustrated in Figure 4). (a) Results found for a measured GIRF h_1. The error induced by finite temporal bandwidth of gradient systems is fairly consistent within the slice-pack (left-plot), but outside the slice-pack there is negligible error from vMB methods. (b) Same principle for a second GIRF h_2 with higher temporal bandwidth. (c) PINS and MultiPINS results in less slice profile error than VERSE methods. When temporal bandwidth is increased to h_2, PINS methods benefit greatly. $\epsilon_{outside}$ is not shown here as it is irrelevant in practice. These results are for the set of pulses calculated for a fixed slice-separation of 28 mm. A similar plot for a fixed FOV is shown in Supporting Information Figure S2, and an analysis for refocusing profiles is shown in Supporting Information Figure S3. Further analysis of distortion of through-slice phase coherence is presented in Supporting Information Figure S4 and S5, for flip-angle and refocusing profiles, respectively

proposed vMB and MBv methods, alongside existing methods, for designs with a fixed FOV of 200 mm and therefore varying relative slice-separation with N. The figure shows that VERSE can be used to drastically reduce the duration of the original linear phase constant gradient RF pulse by around a factor of 5. vMB is only slightly less time-efficient than MBv (10.7%) even though the former has been shown to suffer from fewer slice profile distortion effects. Similarly, non-linear vMB was on average 9.3% longer than non-linear MBv. Duration of PINS and MultiPINS is invariant with respect to N, but varies with slice-separation. To highlight this, Figure 6c shows the

case for variable separation as described, but also for variable N with fixed separation (dashed lines). The other (non-PINS) methods are not as sensitive to changes in slice-separation.

Figure 7 shows RF energy associated with each of the methods, calculated by integrating the square amplitude of each pulse (units are $\mu T^2 ms$ which is proportional to the energy). The graph shows a reciprocal relation to pulse duration. Supporting Figures S6 and S7 show similar results for the case of time bandwidth product 2.

Time-variable gradients also lead to complex off-resonance behaviour as shown by Figure 8. The top row of this
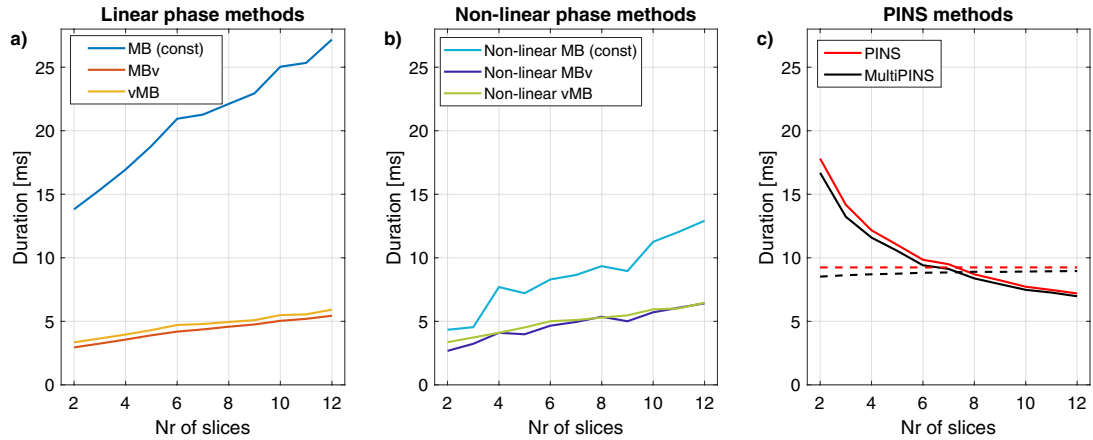
FIGURE 6 RF pulse durations associated with each method (split in (a) linear phase, (b) non-linear phase, and (c) PINS designs) as a function of N, for TBP = 4, maximum G_{max} = 40 mT m^{-1}, and $B_{1,max}$ = 13 μT. All results are shown for the case of a fixed imaging FOV, except for the dashed lines in (c) that are for a fixed slice-separation of 14 slice-thicknesses for every N. vMB methods are only slightly longer in duration than the MBv methods (10.7% and 9.1% on average for linear and non-linear phase, respectively). Depending on the ratio of slice-separation to slice-thickness, they can be more time-efficient than PINS and MultiPINS pulses. Supporting Information Figure S6 shows a similar figure for TBP = 2
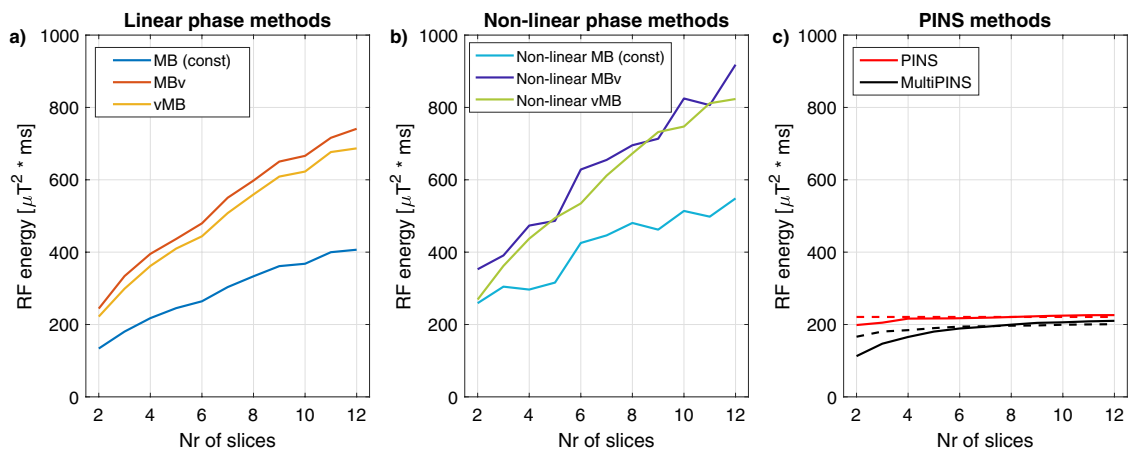
FIGURE 7 RF energy (units μT^{2}ms, proportional to energy) as a function of the number of slices excited for the case of fixed FOV of 200 mm for (a) linear phase pulses, (b) non-linear phase pulses, and (c) PINS methods. Results for the case of fixed slice-separation is shown in dashed lines. An equivalent version for TBP = 2 pulses is available in Supporting Information Figure S7

image shows the simulated profile of a MB4 time bandwidth product 4 example, in a constant gradient MB case (Figure 8a) as well as a verse MB case (Figure 8b). Off-resonance results in a shifting of the slices and a degradation of the slice profile. We quantitatively distinguish these 2 effects for all pulse design methods from this work by reporting the shift experienced by an outer-slice of the MB4 pack in Figure 8c and the NRMSE for the degraded slice when corrected for their spatial displacement (found by maximal cross-correlation) in Figure 8d. The latter method was also used in

Eichner et al.[17] The largest shifts are experienced by the longest pulses, as they spend more time off-resonant. The linear phase vMB and MBv methods perform the least favorably in terms of slice distortion off-resonance. The effect is less pronounced for lower time bandwidth (i.e., shorter) pulses (shown in Supporting Information Figure S8). The effect of gradient bandwidth-related distortion on off-resonance sensitivity was found to be insignificant.

Figure 9 shows experimentally measured slice profiles for an MB3 pulse for constant gradient, MBv, and vMB methods
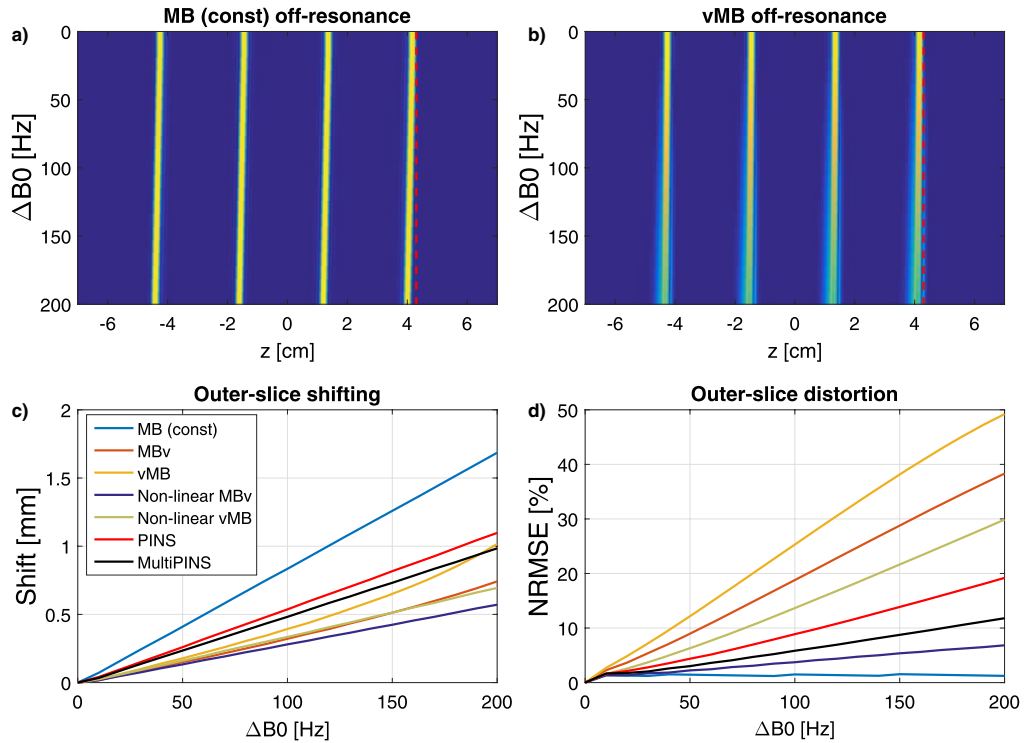
FIGURE 8 Off-resonance simulations for the MB4 pulses, shown for the (a) constant gradient MB and (b) vMB case, with a vertical dashed line as a visual cue. Constant gradient MB pulses experience more slice-shifting than vMB pulses because of their longer durations, but vMB suffers more from slice distortion at off-resonance frequencies. Subfigure (c) shows how much the outer-slice for each technique experiences a spatial shift as a function of frequency. This shows that longer pulses experience a larger shift. (d) Outer-slice distortion as compared in NRMSE from its on-resonant equivalent. MBv and vMB experience the worst off-resonance distortion. A similar plot for TBP = 2 pulses is shown in Supporting Information Figure S8

(linear phase). The relevant gradient system is characterized by h_1. Both MBv and vMB have some distortion in the outer slices (as expected from simulation, see Figure. 4) but the MBv method also has strong ghost slices (as indicated by the red arrows) that are not seen for vMB, again as expected. The pulses used in this experiment were also simulated using the predicted distorted gradient, and in Figure 9e are shown to resemble the measured results. Note that in this experimental validation, the difference in duration between linear MBv and vMB pulses was 30.9% which is greater than the average of 10.7% reported above. This is because MB pulses were constrained to have real-valued (AM) modulation, and it was found that this constraint affects the performance of vMB much more than MBv.

Figure 10 shows in vivo gradient-echo images acquired using a similar pulse. The ghost slices lead to significant reconstruction artifacts because of unresolved aliasing in the MBv case, which are avoided by using vMB pulses. Figure 9 shows that there is a small residual artifact at the ghost slice location (±4 mm), in both the constant gradient and vMB results, which was attributed to a residual RF chain instability

that we could not correct for. Because the artifact is present in the standard constant gradient case, it can be assumed to be unrelated to gradient bandwidth artifacts, and as evidenced by Figure 10, this does not lead to an obvious imaging artifact.

5 | DISCUSSION

In this work, we examined the effect of limited temporal bandwidth of gradient systems on the performance of multiband (MB) RF pulses with time-variable gradients. We explored the use of VERSE to create short MB pulses and compared performance of using VERSE on MB pulses (called MBv) with VERSE on singleband (SB) pulses that are subsequently modulated to make them MB (called vMB). As hypothesized, the vMB method resulted in temporally smoother gradient waveforms with reduced distortion artifacts.

The general problem of gradient distortion is illustrated in Figures 3 and 4, showing the type of effect that would be expected from a gradient system characterized by impulse response function (GIRF) h_1 (shown Figure 2). Figure 9 shows
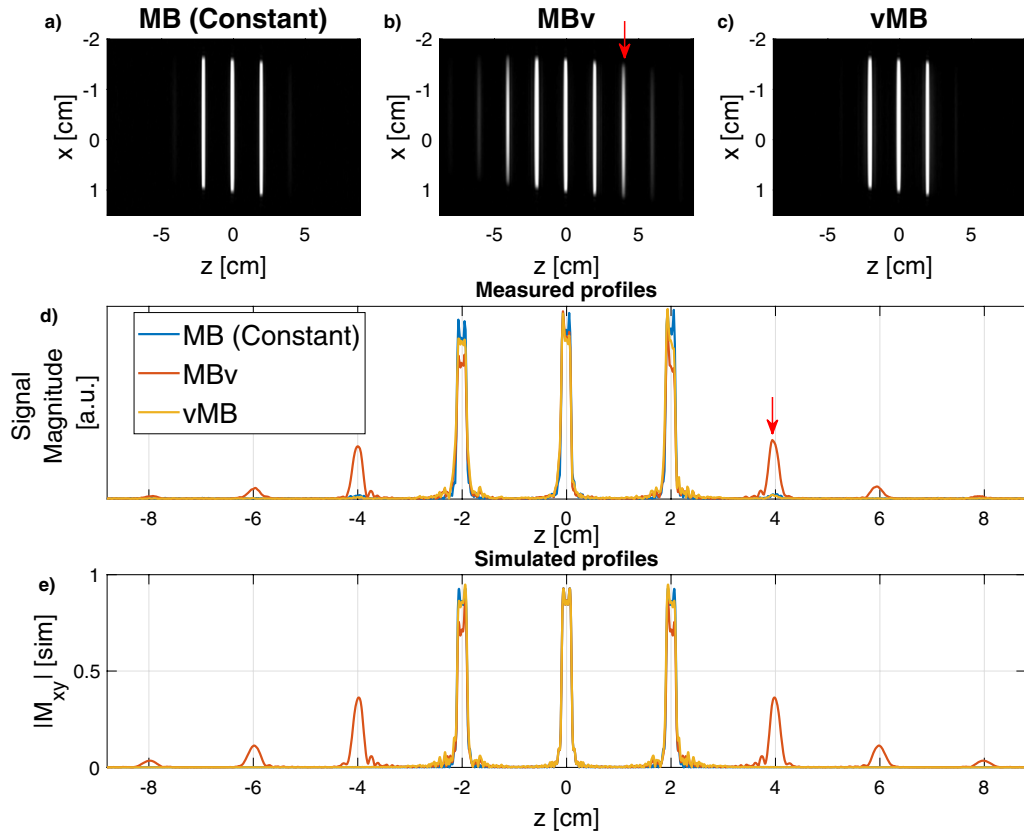
FIGURE 9 Slice profile measurements using RF and gradient pulses ($N = 3$, TBP = 4.4 refocusing pulse, slice-thickness = 2 mm, gap = 20 mm). After VERSE, RF refocusing pulses were scaled down by a factor of 3 such that they could be used as excitation pulses. (a) Slice profile produced with a constant gradient shows very low artifact level. The MBv slice profile in (b) shows significant artifacts at well-defined ghost locations at multiples of the slice-gap outside the original FOV (red arrows in b and d), which would lead to image artifacts. The vMB method in (c) effectively avoids this problem. (d) More clearly illustrates the artifacts, which corresponds with the simulated predictions in (e)

some equivalent experimental measurements and simulated errors, confirming this prediction. Figure 10 shows the resulting errors in SMS image acquisition.

In general, gradient distortion leads to distortion of the individual slice profiles quantified by ϵ_{inside} and excitation of "ghost slices" that tend to appear at multiples of the multiband slice locations (see Figures 4 and 9) quantified by $\epsilon_{outside}$. Results (Figure 5 and Supporting Information Figures S2 and S3) show that ϵ_{inside} is similar between MBv and vMB methods, but was much lower for the higher bandwidth gradient system characterized by h_2. This is to be expected because the individual slice profiles are related to the SB RF and gradient waveforms—these are affected in a similar way by both MBv and vMB approaches and are more strongly distorted by h_1 than h_2. The only anomaly for the ϵ_{inside} results is the surprisingly good performance of non-linear MBv (Figure 5b, purple trace) that we cannot explain.

MBv and vMB approaches differ in that MBv results in gradient waveforms that are modulated at the multiband modulation frequency—distortion therefore leads to "ghost slices" that are not present in the vMB method. Figure 5 shows that this is the case, and these unwanted slices can be seen in Figure 9. When these ghost slices fall within the anatomy they appear as unreconstructed artifacts, as in Figure 10. In this work, we used 180° refocusing pulses as a main example application, to allow comparison with other existing pulse design methods. In the refocusing case, the image artifacts seen would depend on the β^2 profile (Supporting Information Figure S3) as well as the excitation pulse used. Refocusing pulse errors outside the FOV would only lead to image artifacts if used in combination with an excitation pulse with a similar artifact problem. It would therefore be possible to avoid these artifacts by using excitation pulses with better performance, however, it should be expected that to obtain
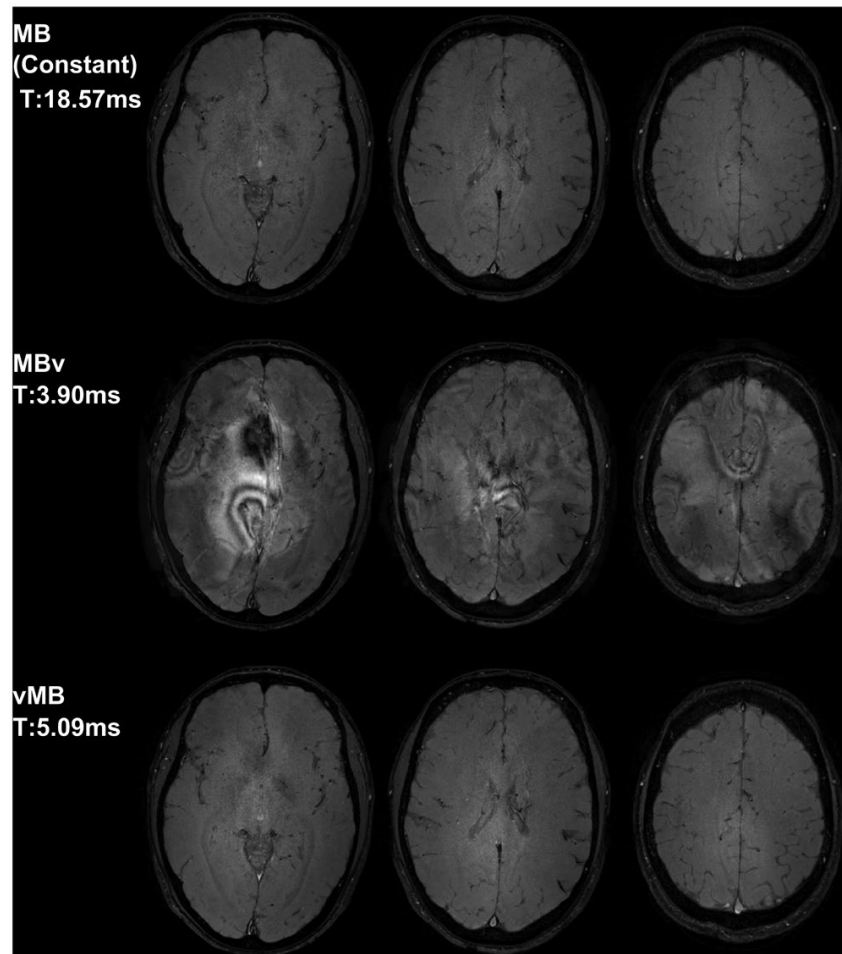
FIGURE 10   In-vivo results for MB3 pulses (gradient-echo, 2 mm slice-thickness, 0.75 × 0.56 mm in-plane FA = 30°, B_1 = 2.17 μT, TE = 14 ms, TR = 100 ms, real-valued RF pulses) using constant gradient (top), MBv (middle), and vMB pulses (bottom). MBv pulses excite regions outside the FOV, which introduce signal into other images, creating strong artifacts. The vMB pulses avoid this behavior and produce equivalent image quality as the constant gradient pulses, but with a 3.6× shorter pulse duration. The relative performance between MBv and vMB pulses (vMB pulse duration is 30% longer than MBv) is above the average (10.9%) partly because the design in this case was constrained for AM-only modulation; this is required to avoid further artifacts on our system

short echo times, excitation pulses may be designed with the same approach and would be likely to have similar ghosts. Excitation for short TR gradient echo sequences is another possible use of these pulses,[36] and Figure 10 used this application as a demonstration, because it allows for a straightforward visualization without the need to design an additional excitation pulse.

In addition to magnitude errors, phase distortions were also investigated (Supporting Information Figures S4 and S5). In general, these errors were found to be small, at ~1–5° in average phase-deviation in both refocusing and flip-angle profiles.

The MBv method studied here creates RF pulses that are similar in both RF and gradient waveform to those created by an optimal control method (see Figure 10a in Grissom et al.[18]). Pulses from the latter method are expected to be shorter in duration than those created by the MBv method, because RF and gradient are jointly optimized instead of being done sequentially. The resulting waveforms have similar temporal characteristics, so we expect the gradient bandwidth related errors to also be similar. In contrast, the proposed vMB method does not suffer from these effects because the gradient waveforms have an inherently lower temporal bandwidth.

4.3. Multiband RF pulse design for realistic gradient performance

Gradient-related slice profile errors are more pronounced for gradient systems with lower temporal bandwidth, however, they are still expected to be present on gradient systems with a higher temporal bandwidth. Predictions made using a higher bandwidth GIRF h_2 constructed from published results on a system from an alternative vendor (Testud[34]; Figure 2) still show higher $\epsilon_{outside}$ for the MBv methods, compared with vMB (Figure 5). In general, the variability of gradient system bandwidth that causes the reported differences in performance has not been problematic for MB methods in mainstream use, because these use constant selection gradients that are faithfully reproduced on all systems. A move to more rapidly varying gradient waveforms places more demand on the gradient system and can lead to the errors shown in this work. Aside from reducing errors, another advantage of the vMB approach is that cross-platform performance would be expected to be more similar, which may be desirable for standardized protocols.

Previous work has also considered the gradient bandwidth-related slice profile errors. In Hargreaves et al.,[19] the gradient waveform after VERSE was low-pass filtered up to 50 kHz to smooth out such effects. Another study showed how small mismatches between RF and gradient timings can lead to excitation errors.[37] The solution proposed was to avoid RF and gradient amplitude being high simultaneously, which hampers the effectiveness of VERSE. RF characterization was not incorporated in this study, however, previous literature has identified that this can be problematic.[38,39]

The penalty in terms of pulse duration is illustrated by Figure 6. The use of time-variable gradients significantly reduces duration when compared with constant gradient pulses, in comparison the difference between vMB and MBv is relatively minor, with vMB being only 10.7% and 9.1% longer than MBv (linear and non-linear phase, respectively). These designs are typically shorter in duration than PINS/MultiPINS pulses for lower N (fixed FOV)—duration of PINS type pulses is not explicitly dependent on N but falls as the ratio of slice-separation to slice-thickness falls. It is also apparent that once time-variable gradient waveforms are used, there is no longer a big difference in duration between the linear and non-linear phase designs. For example, before use of VERSE, the linear phase MB pulses are on average 252% longer than the non-linear phase versions, however, after application of VERSE this difference drops to below 8% for both MBv or vMB variants. This is because VERSE is more effective at reducing durations for constant gradient RF shapes with regions of low-and-high amplitude RF lobes. A more comprehensive design approach such as Rund et al.[24] could potentially outperform VERSE and increase the gap between linear and non-linear phase designs.

As Figure 7 shows, another cost of producing very short duration pulses is increased RF energy. In this respect, the PINS-related designs are more effective—this work focused on short duration, which inevitably leads to higher energy. The choice of which approach to take is application-dependent.

A limitation of all VERSE-based methods is that they can lead to poor off-resonance performance. Our results (Figure 8) also show this to be the case, however, the significance of this error depends on the application (and whether fat suppression is applied, for example). It is also significantly less for low TBP pulses (see Supporting Information Figure S8).

Simulation and experiment (Figures 4 and 9) both suggest that low temporal gradient bandwidth also leads to additional ringing effects local to each slice, even with the vMB method. In previous work, we have shown that these errors can be effectively mitigated by using an iterative correction scheme[40] with knowledge of the GIRF. In Supporting Information Figure S9, we show an experimental proof that the same method can correct the vMB method to reduce additional slice profile errors. The disadvantage from this method, however, is that the iterative correction requires knowledge of the scanner GIRF, must be computed online, and is potentially gradient-axis-dependent meaning that it may need to be recomputed if the slice orientation changes.

An additional benefit for vMB methods is that they are potentially simpler to implement. Phase-offsets and peak amplitude of the MB modulation function that leads to time-optimality are known beforehand. In practice, this means that for a combination of SB RF shape and slice-thickness, one only needs to store a library of time-optimal SB RF and gradient shapes constructed using VERSE (depending on number of slices and hardware limitations). The required modulation function to then produce an MB pulse (see Equation 2) is easily calculated online.

As discussed previously, although we expect optimal control MB pulse designs such as in Rund et al.[23] will outperform the MBv designs in this work, we would also expect them to suffer from similar slice profile errors because the gradient pulses have similarly high temporal bandwidth. Design approaches based on optimizing a SB RF pulse and gradient waveform based on some other method, before subsequent MB modulation, may be a useful area for future development.

6 | CONCLUSION

We propose a novel method for designing time-optimal multiband RF pulses that are less susceptible to distortion related to the finite temporal bandwidth of real-world gradient systems. We assessed our work with a measured and reconstructed GIRF, based on 2 major vendors. We conclude that such pulses would benefit future SMS imaging applications.

ABO SEADA ET AL.

ORCID

Samy Abo Seada http://orcid.org/0000-0003-3221-433X
Anthony N. Price http://orcid.org/0000-0002-6907-7554
Joseph V. Hajnal http://orcid.org/0000-0002-2690-5495
Shaihan J. Malik http://orcid.org/0000-0001-8295-9032

REFERENCES

1. Larkman DJ, Hajnal JV, Herlihy AH, Coutts GA, Young IR, Ehnholm G. Use of multicoil arrays for separation of signal from multiple slices simultaneously excited. *J Magn Reson Imaging*. 2001;13:313–317.
2. Barth M, Breuer F, Koopmans PJ, Norris DG, Poser BA. Simultaneous multislice (SMS) imaging techniques. *Magn Reson Med*. 2016;75:63–81.
3. Glover GH. Phase-offset multiplanar (POMP) volume imaging: a new technique. *J Magn Reson Imaging*. 1991;1:457–461.
4. Setsompop K, Fan Q, Stockmann J, et al. High-resolution in vivo diffusion imaging of the human brain with generalized slice dithered enhanced resolution: simultaneous multislice (gSlider-SMS). *Magn Reson Med*. 2018;79:141–151.
5. Gagoski BA, Bilgic B, Eichner C, et al. RARE/turbo spin echo imaging with simultaneous multislice Wave-CAIPI. *Magn Reson Med*. 2015;73:929–938.
6. Norris DG, Boyacioglu R, Schulz J, Barth M, Koopmans PJ. Application of PINS radiofrequency pulses to reduce power deposition in RARE/turbo spin echo imaging of the human head. *Magn Reson Med*. 2014;71:44–49.
7. Price AN, Cordero-Grande L, Malik SJ, Hajnal JV Accelerated cine imaging of the heart using blipped multiband SSFP. In Proceedings of the 25th Annual Meeting of ISMRM, Honolulu, HI, 2017. Abstract 0631.
8. Wang Y, Shao X, Martin T, Moeller S, Yacoub E, Wang D. Phase-cycled simultaneous multislice balanced SSFP imaging with CAIPIRINHA for efficient banding reduction. *Magn Reson Med*. 2016;76:1764–1774.
9. Hennig J. Chemical shift imaging with phase-encoding RF pulses. *Magn Reson Med*. 1992;25:289–298.
10. Goelman G. Two methods for peak RF power minimization of multiple inversion-band pulses. *Magn Reson Med*. 1997;37:658–665.
11. Wong E Optimized phase schedules for minimizing peak RF power in simultaneous multi-slice RF excitation pulses. In Proceedings of the 20th Annual Meeting of ISMRM, Melbourne, Australia, 2012. Abstract 2209.
12. Malik SJ, Price AN, Hajnal JV Optimized amplitude modulated multi-band RF pulses. In Proceedings of the 21st Annual Meeting of ISMRM, Salt Lake City, UT, 2013. p. 1405.
13. Sbrizzi A, Poser BA, Tse D, Hoogduin H, Luijten PR, van den Berg C. RF peak power reduction in CAIPIRINHA excitation by interslice phase optimization. *NMR Biomed*. 2015;28:1393–1401.
14. Auerbach EJ, Xu J, Yacoub E, Moeller S, Ugurbil K. Multiband accelerated spin-echo echo planar imaging with reduced peak RF power using time-shifted RF pulses. *Magn Reson Med*. 2013;69:1261–1267.
15. Sharma A, Lustig M, Grissom WA. Root-flipped multiband refocusing pulses. *Magn Reson Med*. 2016;75:227–237.
16. Norris DG, Koopmans PJ, Boyacioglu R, Barth M. Power independent of number of slices (PINS) radiofrequency pulses for low-power simultaneous multislice excitation. *Magn Reson Med*. 2011;66:1234–1240.
17. Eichner C, Wald LL, Setsompop K. A low power radiofrequency pulse for simultaneous multislice excitation and refocusing. *Magn Reson Med*. 2014;958:949–958.
18. Grissom WA, Setsompop K, Hurley SA, Tsao J, Velikina JV, Samsonov AA. Advancing RF pulse design using an open-competition format: report from the 2015 ISMRM challenge. *Magn Reson Med*. 2017;78:1352–1361.
19. Hargreaves BA, Cunningham CH, Nishimura DG, Conolly SM. Variable-rate selective excitation for rapid MRI sequences. *Magn Reson Med*. 2004;52:590–597.
20. Lee D, Lustig M, Grissom WA, Pauly JM. Time-optimal design for multidimensional and parallel transmit variable-rate selective excitation. *Magn Reson Med*. 2009;61:1471–1479.
21. Kobayashi N, Ugurbil K, Wu X. Shortening nonlinear phase multiband refocusing pulses with VERSE. In Proceedings of the 24th Annual Meeting of ISMRM, Singapore, 2016. p. 3253.
22. Aigner CS, Clason C, Rund A, Stollberger R. Efficient high-resolution RF pulse design applied to simultaneous multi-slice excitation. *J Magn Reson*. 2016;263:33–44.
23. Rund A, Aigner CS, Kunisch K, Stollberger R. Magnetic resonance RF pulse design by optimal control with physical constraints. *IEEE Trans Med Imaging*. 2018:461–472.
24. Rund A, Aigner CS, Kunisch K, Stollberger R. Simultaneous multislice refocusing via time optimal control. *Magn Reson Med*. 2018; 18:1416–1428.
25. Malik SJ, Hajnal JV. Phase relaxed localized excitation pulses for inner volume fast spin echo imaging. *Magn Reson Med*. 2016;76:848–861.
26. Vannesjo SJ, Haeberlin M, Kasper L, et al. Gradient system characterization by impulse response measurements with a dynamic field camera. *Magn Reson Med*. 2013;69:583–593.
27. Boesch C, Gruetter R, Martin E. Temporal and spatial analysis of fields generated by eddy currents in superconducting magnets: optimization of corrections and quantitative characterization of magnet/gradient systems. *Magn Reson Med*. 1991;20:268–284.
28. Liu Q, Hughes DG, Allen PS. Quantitative characterization of the eddy current fields in a 40-cm bore superconducting magnet. *Magn Reson Med*. 1994;31:73–76.

29. Lee D, Grissom WA, Lustig M, Kerr AB, Stang PP, Pauly JM. VERSE-guided numerical RF pulse design: a fast method for peak RF power control. *Magn Reson Med*. 2012;67:353–362.

30. Abo Seada S, Price AN, Hajnal JV, Malik SJ. Optimized amplitude modulated multiband RF pulse design. *Magn Reson Med*. 2017;78:2185–2193.

31. Shinnar M. Reduced power selective excitation radio frequency pulses. *Magn Reson Med*. 1994;32:658–660.

32. Pauly J, Le Roux P, Nishimura D, Macovski A. Parameter relations for the Shinnar-Le Roux selective excitation pulse design algorithm. *IEEE Trans Med Imaging*. 1991;10:53–65.

33. Papadakis NG, Wilkinson AA, Carpenter TA, Hall LD. A general method for measurement of the time integral of variant magnetic field gradients: application to 2D spiral imaging. *Magn Reson Imaging*. 1997;15:567–578.

34. Testud F. *Dynamic magnetic field estimation for magnetic resonance imaging [dissertation on the Internet]*. Freiburg: Albert Ludwich University of Freiburg; 2014. Available from: https://www.freidok.uni-freiburg.de/volltexte/9288/.

35. Setsompop K, Gagoski BA, Polimeni JR, Witzel T, Wedeen VJ, Wald LL. Blipped-controlled aliasing in parallel imaging for simultaneous multislice echo planar imaging with reduced g-factor penalty. *Magn Reson Med*. 2012;67:1210–1224.

36. Abo Seada S, Beqiri A, Price AN, Hajnal JV, Malik SJ. Minimum-TR pulse design for rapid gradient echo sequences Samy. In Proceedings of the 26th Annual Meeting of ISMRM, Paris, France, 2018. p. 5800.

37. Kerr AB, Zhu K, Middione MJ, Wu H, Doughtery RF, Pauly JM. Delay-insensitive variable-rate selective excitation (DIVERSE). In Proceedings of the 23rd Annual Meeting of ISMRM, Toronto, Canada, 2015. p. 921.

38. Grissom WA, Kerr AB, Stang P, Scott GC, Pauly JM. Minimum envelope roughness pulse design for reduced amplifier distortion in parallel excitation. *Magn Reson Med*. 2010;64:1433–1440.

39. Zhu K, Dougherty RF, Middione MJ et al. RF amplifier nonlinearity correction for multiband RF pulses. In Proceedings of the 23rd Annual Meeting of ISMRM, Toronto, Canada, 2015. p. 3763.

40. Abo Seada S, Hajnal JV, Malik SJ. A simple optimisation approach to making time efficient VERSE-multiband pulses feasible on non-ideal gradients. In Proceedings of the 25th Annual Meeting of ISMRM, Honolulu, HI, 2017. 5049.

SUPPORTING INFORMATION

Additional Supporting Information may be found in the online version of this article.

FIGURE S1 MultiPINS pulses in this study were optimized for time-optimality. As more MB is added to the pulse, the duration of the pulse decreases. The time-optimal solution is found by maximizing M without violating the peak B1 amplitude constraint. This is a 1D version of Figure 2 found in Eichner et al.[17]

FIGURE S2 Slice profile error for the case of fixed FOV and flip-angle represented slice profiles (compare with Figure 5)

FIGURE S3 Slice profile error for the case of fixed slice-separation of 28 mm and using refocusing profiles (evaluated using β^2 parameters). The error of ghost slices is reduced,

but the overall relationship between different methods remain the same. The same representation here was used to evaluate phase profile distortion in Supporting Information Figure S5

FIGURE S4 Phase profile deviation across slices for MBv, vMB, PINS, and MultiPINS methods across the number of slices refocused. This figure shows the average phase error in the excited slices when the pulses are scaled down to 45°. Linear phase rolls common to all slices were excluded. Therefore, the above results only show the increase in non-linear phase deviation that cannot be corrected for using linear gradient fields. A 3° under-tip is not a significant effect, even considering TSE sequences where CPMG conditions ought to be respected

FIGURE S5 Phase profile deviation across slices for MBv, vMB, PINS, and MultiPINS methods across the number of slices refocused. This analysis is similar as shown in Supporting Information Figure S4 except the pulses were not rescaled. Instead, the phase corresponds to the phase of the β^2 profile.

FIGURE S6 RF pulse durations for fixed FOV, TBP = 2 as a function of the number of slices (compare with Figure 6, which was TBP = 4). The dashed lines in the graph for PINS methods show the durations for the case of fixed slice-separation. The RF energy for these pulses are shown in Supporting Information Figure S7

FIGURE S7 RF energy versus number of slices for fixed FOV and TBP = 2, corresponding to the pulses of Supporting Information Figure S5. The dashed lines in the graph for PINS methods show the RF energy for fixed slice-separation. Compare with Figure 7, which was TBP = 4. As with Figure 7, the unit used here (μT^2 ms) is proportional to the energy

FIGURE S8 Simulated slice-shifting and slice-distortion as a result of off-resonance behavior, as a function off-resonance frequency $\Delta B0$. This is a TBP = 2 version of Figure 8. For VERSE pulses, off-resonance effects are less damaging for lower TBP, making such pulses suitable candidates when spatial selectivity is less important

FIGURE S9 Experimental results showing how remaining slice distortions for the vMB method can be improved if the system GIRF is known. The same sequence as Figure 9 was used. (A) Measured slice profile for an MB3 RF pulse with a constant gradient. (B) The MB3 profile from a vMB pulse without GIRF-correction. (C) Improvement achieved when the vMB RF pulse is iteratively corrected using the technique described in Abo Seada et al.[40] (D) Accurate depiction of the slightly improved passband and decreased side lobes in the GIRF-corrected case. When used in vivo, no clear benefit was visible when using vMB with GIRF correction, as such side lobes barely affect imaging

4.4   Iterative GIRF correction

As mentioned in the preface, we also investigated an approach for reducing GIRF-associated errors by iteratively correcting MB pulses based on a GIRF [87]. This section will discuss this technique in more detail.

A demanded VERSE gradient G_{demand}^v will be distorted by a GIRF $H(t)$, and the actual gradient can be predicted as

$$G_{actual}^v(t) = G_{demand}^v(t) * H(t) \tag{4.1}$$

A consequence of this is that the condition under which VERSE preserves the slice-profile in Equation 1.112 is now violated, as the RF pulse was designed for G_{demand}^v but experiences the distorted gradient field G_{actual}^v, and thus the slice-profile will be distorted.
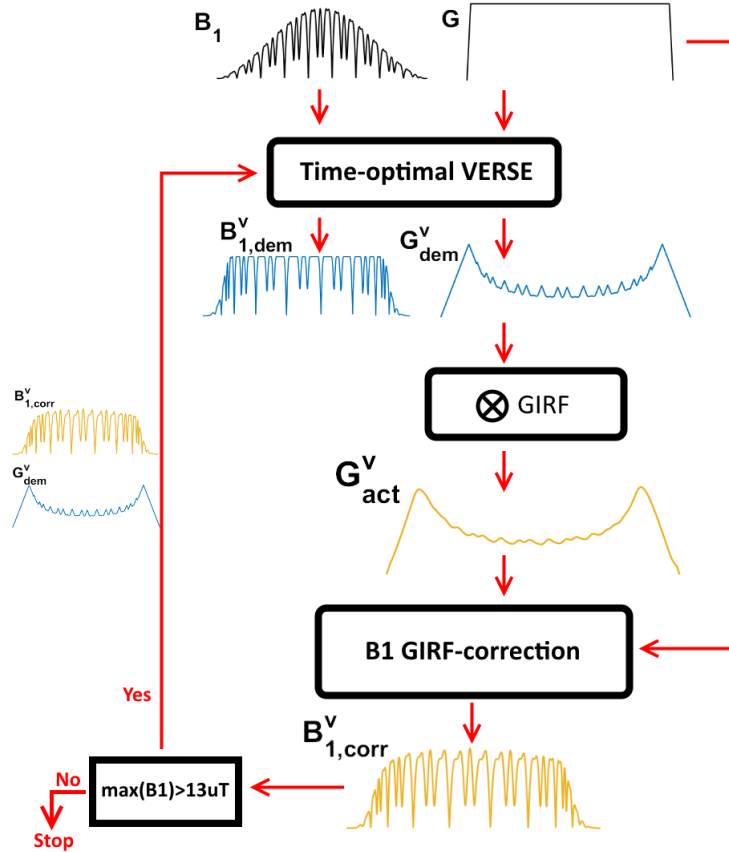
Figure 4.13: Work-flow of the iterative GIRF-correction scheme. In the first iteration, a corrected RF is designed which corrects the slice-profile but exceeds the desired B_1 limit. The corrected RF and demanded gradient are inputs to the VERSE algorithm in the next iteration, and $B_1^{v,corr}$ is found using the newly distorted gradient G_{actual}^v and $W(s)$ from the first iteration. This procedure is repeated until the corrected RF reaches a peak B_1 below the amplitude limit.

It is however possible to correct for the distorted gradient field by altering the RF waveform. The actual k-space trajectory can be found by rephrasing Equation 1.109.

$$s_{act}(t) = \gamma \int_0^t G_{actual}^v(\tau) d\tau \tag{4.2}$$

and the ratio of amplitudes for the realized k-space trajectory $W(s_{act})$ can be found by resampling $W(s)$ onto $s_{act}(t)$. If $H(t)$ is known, the corrected RF pulse can be found as

$$B_1^{v,corr}(s_{act}) = G_{actual}^v(s_{act})W(s_{act}) \qquad (4.3)$$

and is reparametrized to time using Equation 4.2. $B_1^{v,corr}$, when experiencing the distorted gradient G_{actual} will produce a slice-profile free from distortion. However $B_1^{v,corr}$ might not adhere to the peak RF amplitude constraint, and will almost certainly violate it.

Additionally, an iterative correction scheme can be used to ensure $B_1^{v,corr}$ meets the prescribed peak RF amplitude constraint. In the first iteration, a corrected RF is designed which corrects the slice-profile but exceeds the desired B_1 limit. The corrected RF and demanded gradient are inputs to the VERSE algorithm in the next iteration, and $B_1^{v,corr}$ is found using the newly distorted gradient G_{actual}^v and $W(s)$ from the first iteration. This procedure is repeated until the corrected RF reaches a peak B_1 below the amplitude limit , and the algorithm converges. To regularize this algorithm the target B_1-amplitude in each iteration can be reduced by about 1% [88], which usually ensures convergence within 20 iterations. A work-flow diagram is shown in Figure 4.13, and excerpts from this iterative algorithm are shown in Figure 4.14.

On close inspection of Figure 4.14 it becomes clear that the demanded gradient waveform becomes progressively more violent, such that the actual gradient contains sufficiently high amount of modulation to minimise the overhead of RF correction necessary.
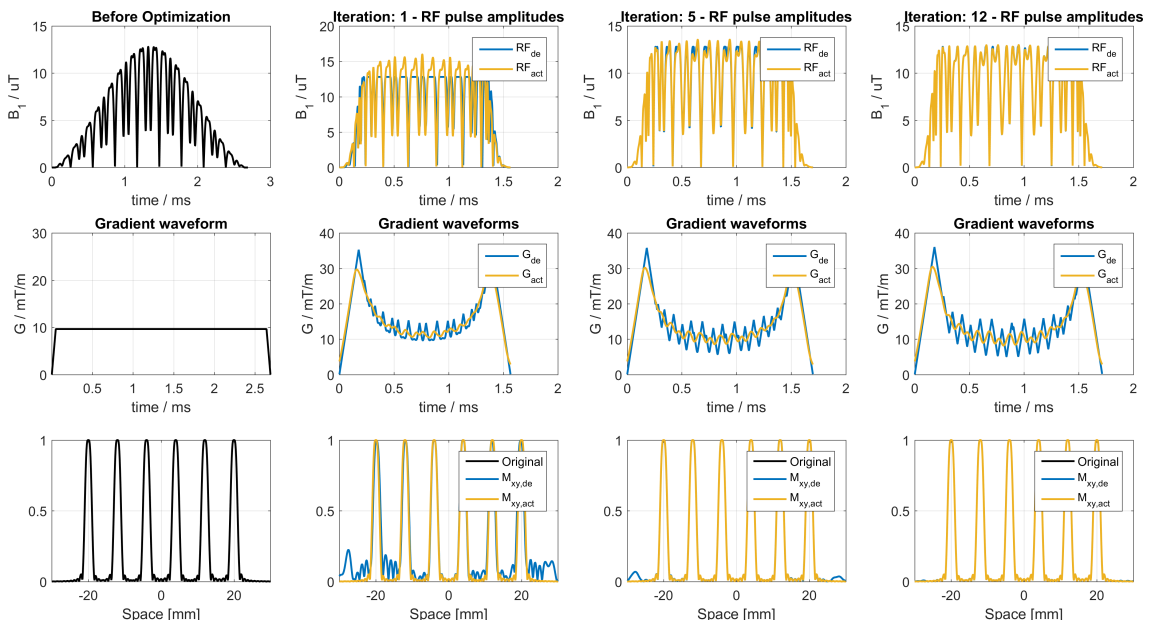
Figure 4.14: An excerpt from an iterative VERSE-based GIRF correction. In each iteration, the GIRF is used to distort the VERSE gradient. Based on this distorted gradient a corrected RF is designed (Top row, yellow) which corrects the slice-profile, but exceeds the desired B_1 limit. The corrected RF and distorted gradient are input to the next iteration, and the procedure is repeated until the corrected RF reaches a peak B_1 below the amplitude limit.

We have also shown that this is possible using vMB methods, as shown experimentally in Supporting Figure S9 (reproduced in Figure 4.25).
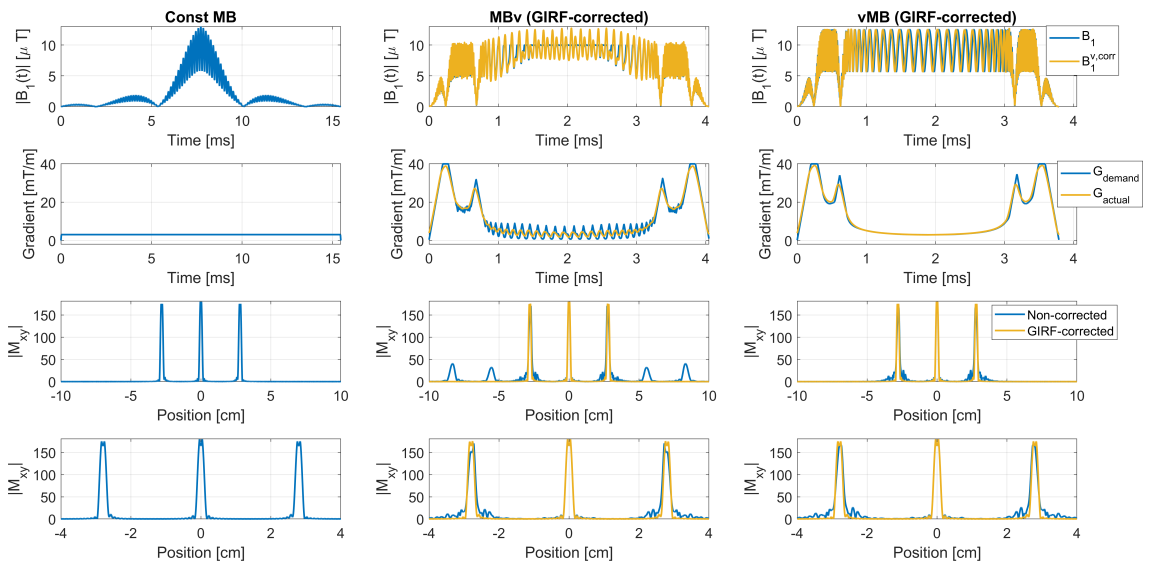
Figure 4.15: GIRF-corrected MBv and vMB pulses. For MBv pulses (middle column) the correction leads to highly demanding gradient waveforms, which leads to long RF pulse durations. In the right-most column it is shown that the vMB gradient is easier to correct for thanks to its inherent smoothness, and this leads to shorter RF durations.

In Figure 4.15 an example is shown for an iteratively GIRF-corrected MBv pulse as well as a vMB version. It is possible to correct both pulses, however due to the rapid gradient modulation in the MBv case (middle column) this RF-correction becomes unstable and results in a more rapidly varying selection gradient, as well as a longer RF pulse. In the vMB case (right column) the gradient is smoother and it is easier to correct for, leading to an overall improved result.

Figure 4.16 shows RF pulse durations before and after GIRF-correction. The iterative optimization increases the RF pulse durations for linear MBv method, and becomes unstable for high multiband factor designs. For both linear and non-linear phase designs however, GIRF-corrected vMB methods only increase marginally in duration.

4.5 Concluding remarks

Multiband RF pulses based on time-variable selection gradient have been shown to be highly effective at reducing RF pulse durations. However gradient waveform with high temporal bandwidth become problematic to realise, and can produce image artefacts when ignored. In this work we proposed a new concept surrounding the design of such multiband pulses, which is to optimize the gradient waveform for a singleband waveform before applying multiband modulation which turns it into a multiband RF pulse. The benefit of these pulses has been shown experimentally in phantoms as well as in-vivo. A good
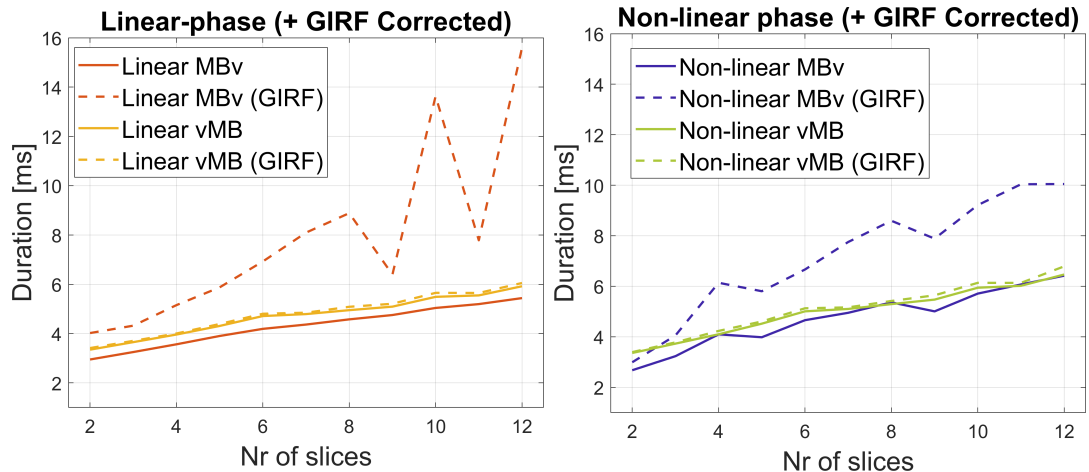
Figure 4.16: RF pulse duration for TBP=4 fixed FoV RF pulses (same as in Figure 6 in this chapter) and their GIRF-corrected versions using an iterative scheme as in [87]. The iterative optimization increases the RF pulse durations for Linear MBv method, and becomes unstable for high multiband factor designs. For both Linear and non-linear phase designs however, GIRF-corrected vMB methods only increase marginally in duration.

application for such pulses would be in spin-echo diffusion sequences, where short RF pulses result in shorter echo-times.

An alternative approach to the published method is to remove slice profile distortions by iteratively correcting RF and gradient waveforms. The limitations of this approach however are that they require an accurate GIRF model, and that the performance is axis-dependent and so a different pulse might be needed for different slice orientation. We have however shown that the vMB method is particularly well-suited for GIRF-correction, and this will become useful for rapid gradient echo imaging, as will be demonstrated in the following chapter.

4.6 Supporting Material for publication

Below is supporting material that was published online with the article.
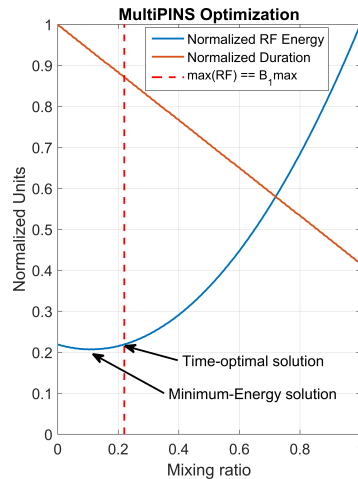
Figure 4.17: Supporting Figure S1: MultiPINS pulses in this study were optimized for time-optimality. As more MB is added to the pulse, the duration of the pulse decreases. The time-optimal solution is found by maximizing M without violating the peak B1 amplitude constraint. This is a 1D version of Figure 2 found in Eichner et al. [50]
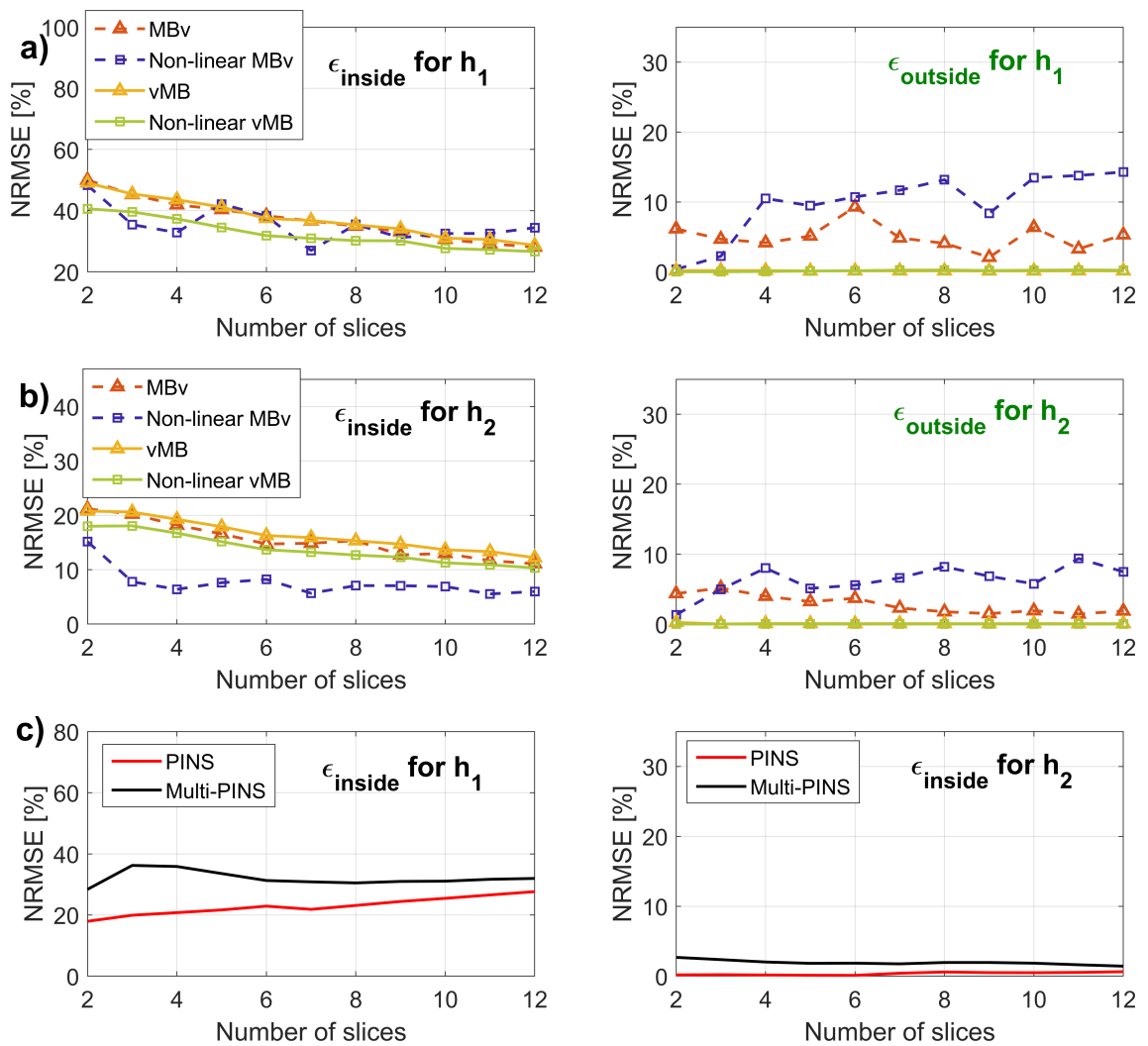
Figure 4.18: Supporting Figure S2: Slice profile error for the case of fixed FOV and flip-angle represented slice profiles (compare with Figure 5).
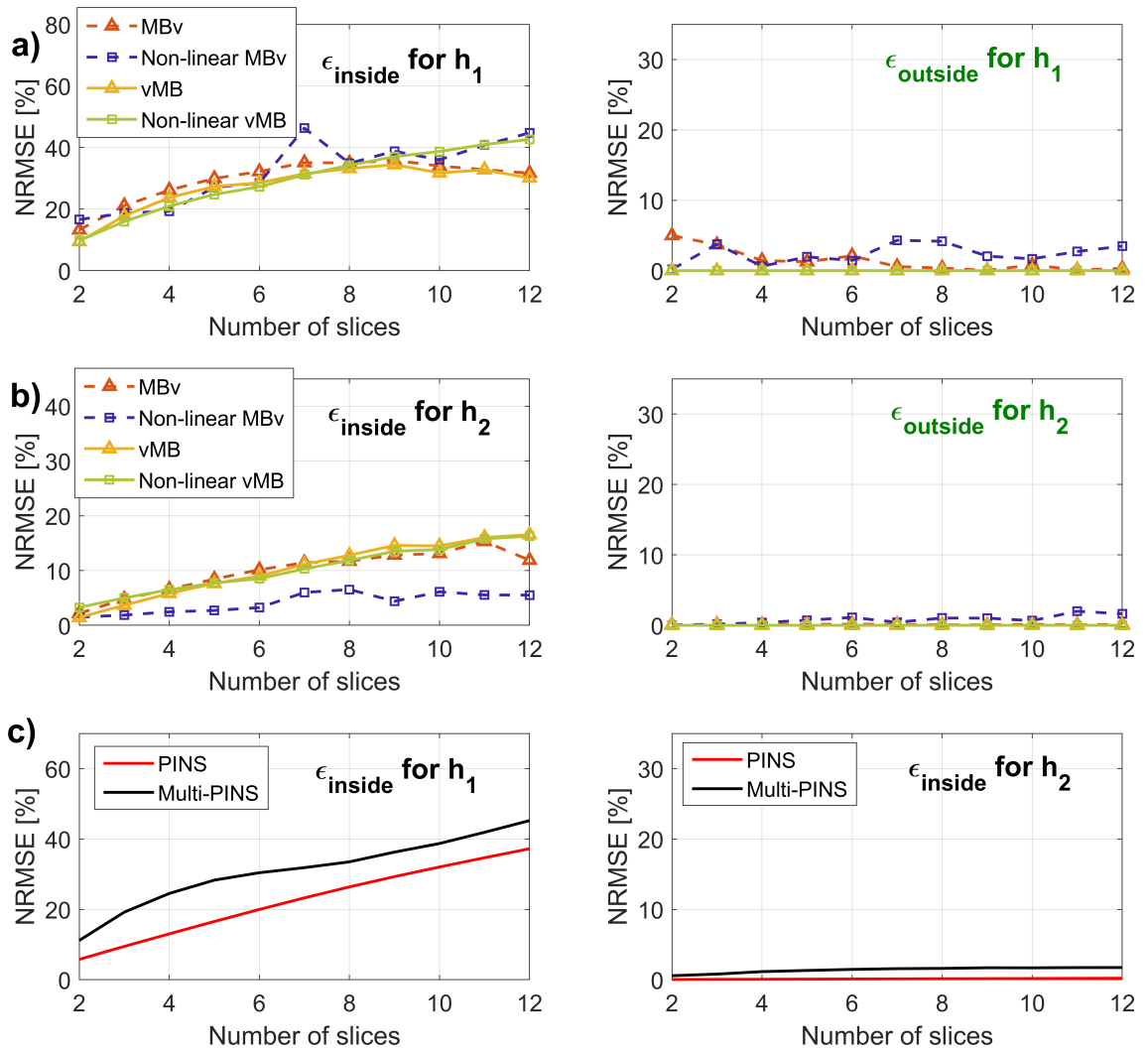
Figure 4.19: Supporting Figure S3: Slice profile error for the case of fixed slice-separation of 28mm and using refocusing profiles (evaluated using β^2 parameters). The error of ghost slices reduces, however the overall relationship between different methods remain the same. The same representation here was used to evaluate phase profile distortion in Supporting Figure S5.
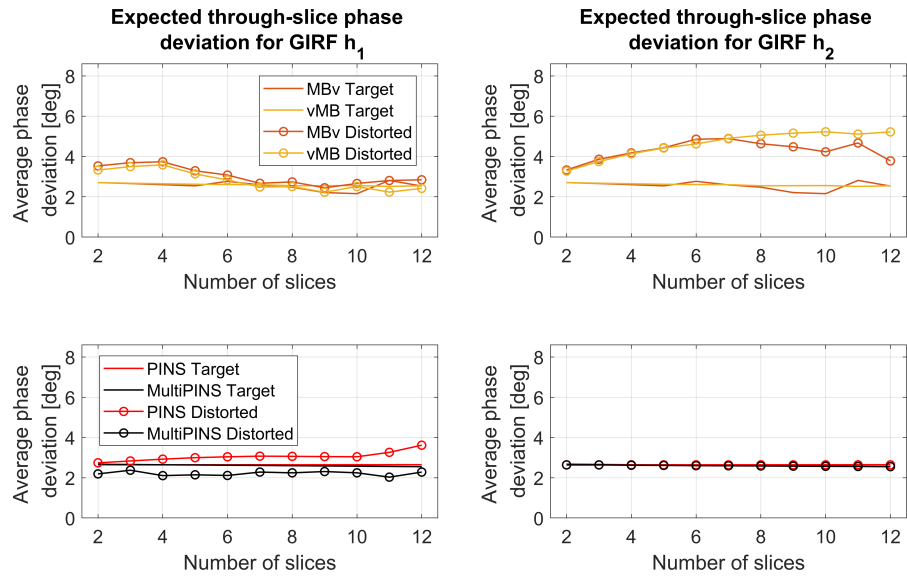
Figure 4.20: Supporting Figure S4: Phase profile deviation across slices for MBv, vMB, PINS and MultiPINS methods across the number of slices refocused. This figure shows the average phase error in the excited slices when the pulses are scaled to 45°. Linear phase rolls common to all slices were excluded. Therefore, the above results only show the increase in non-linear phase deviation which cannot be corrected for using linear gradient fields. A 3° under-tip is not a significant effect, even considering TSE sequences where CPMG conditions ought to be respected.
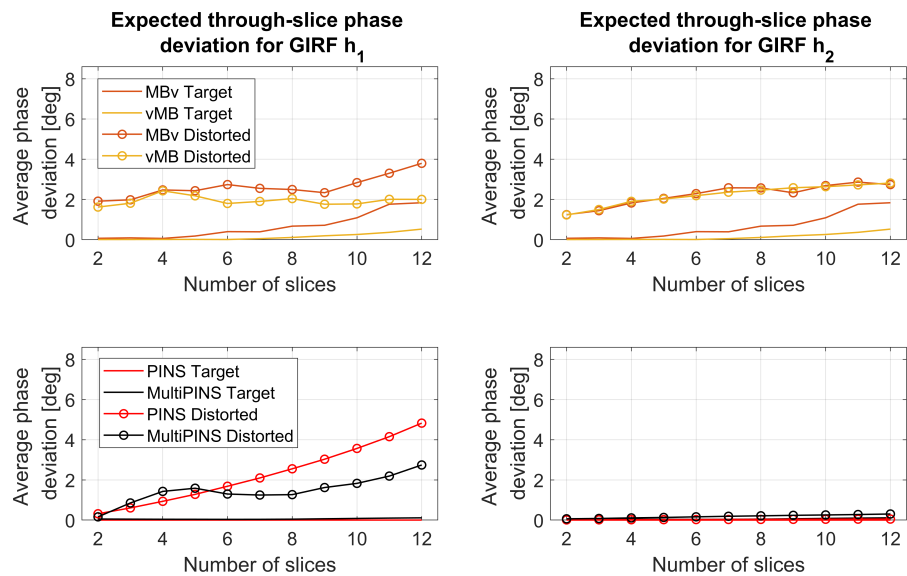
Figure 4.21: Supporting Figure S5: Phase profile deviation across slices for MBv, vMB, PINS and MultiPINS methods across the number of slices refocused. This analysis is similar as shown in Supporting Figure S4 except the pulses were not rescaled, instead the phase corresponds to the phase of the β^2 profile.
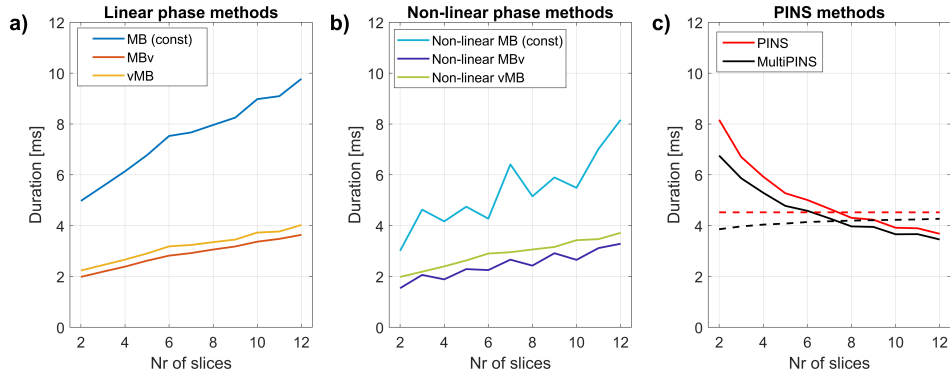
Figure 4.22: Supporting Figure S6: RF pulse durations for fixed FOV, TBP = 2 as a function of the number of slices (compare with Figure 6, which was for TBP=4). The dashed lines in the graph for PINS methods show the durations for the case of fixed slice-separation. The RF energies for these pulses are shown in Supporting Figure S7.
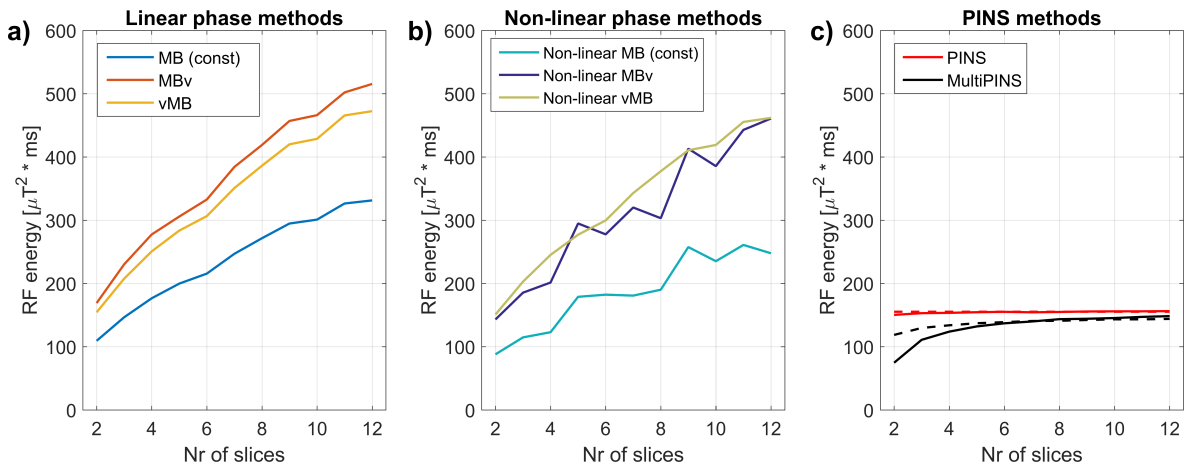
Figure 4.23: Supporting Figure S7: RF energy vs Number of slices for fixed FOV and TBP = 2, corresponding to the pulses of Supporting Figure S5. The dashed lines in the graph for PINS methods show the RF energy for fixed slice-separation. Compare with Figure 7, which was for TBP=4. As with Figure 7, the unit used here $\mu T^2 ms$ is proportional to the energy.
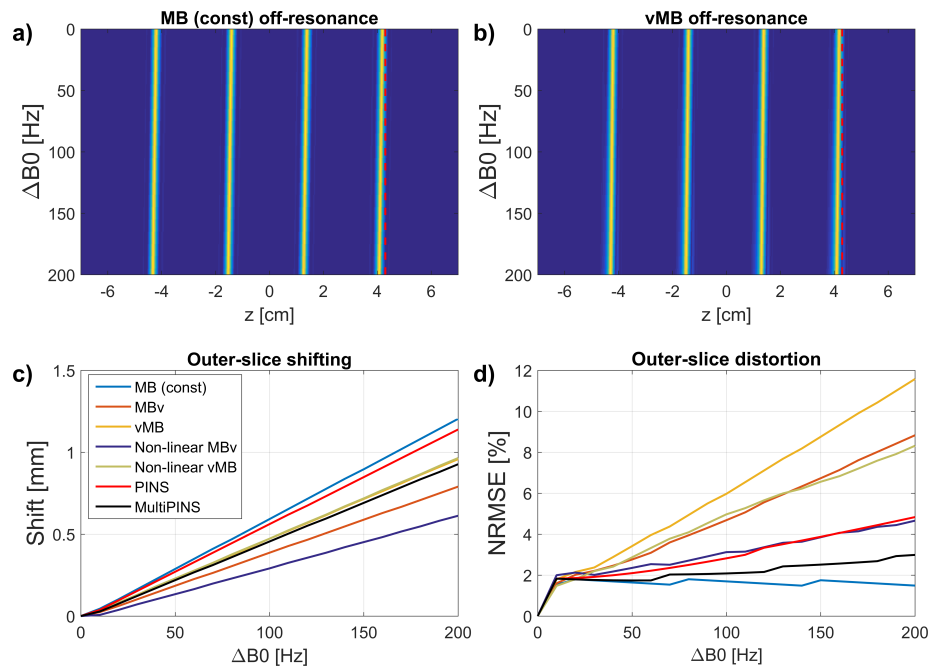
Figure 4.24: Supporting Figure S8: Simulated slice-shifting and slice-distortion as a result of off-resonance behaviour, as a function off-resonance frequency $\Delta B0$. This is a TBP = 2 version of Figure 8. For VERSE pulses, off-resonance effects are less damaging for lower TBP, making such pulses suitable candidates when spatial selectivity is less important.
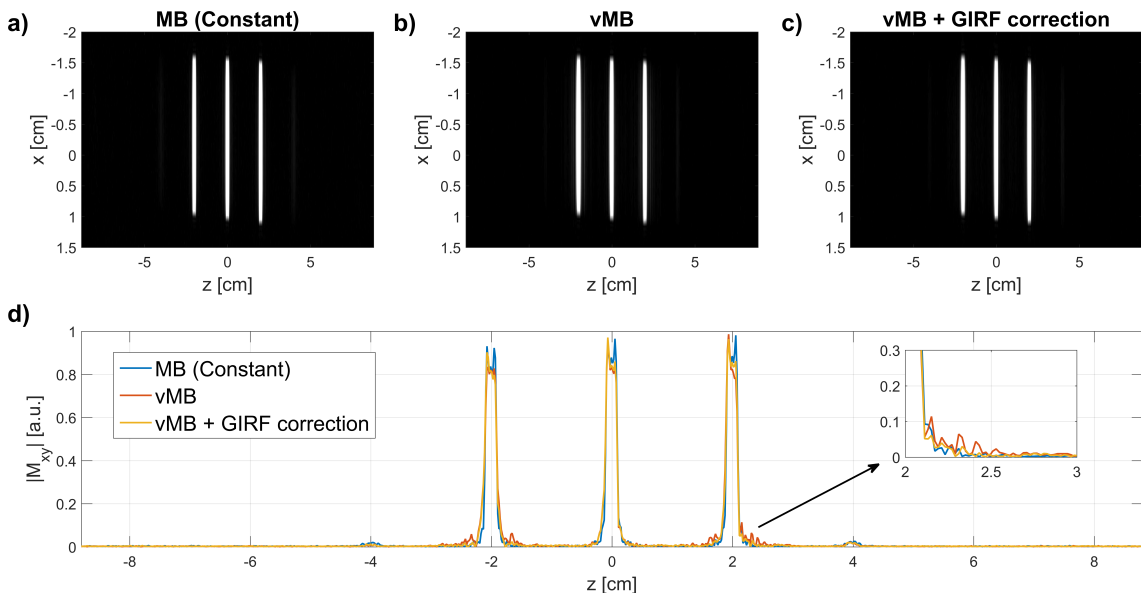
Figure 4.25: Supporting Figure S9: Experimental results showing how remaining slice distortions for the vMB method can be improved if the system GIRF is known. The same sequence as Figure 9 was used. a) shows a measured slice profile for an MB3 RF pulse with a constant gradient. b) shows the MB3 profile from a vMB pulse without GIRF-correction. c) shows the improvement achieved when the vMB RF pulse is iteratively corrected using the technique described in [87]. d) more accurately shows the slightly improved passband and decreased sidelobes in the GIRF-corrected case. When used in-vivo, no clear benefit was visible when using vMB with GIRF correction, as such sidelobes barely affect imaging.

107

Chapter 5

Minimum-TR RF pulse design for rapid gradient echo sequences

5.1 Introduction

Rapid gradient echo sequences are widely used across MRI. This family of pulse sequences include balanced SSFP [89], which is clinically popular thanks to its high SNR and T_2/T_1-contrast. A range of rapid gradient-echo sequences form the basis of nonenhanced MR angiography [90], such as Time-of-Flight (TOF) techniques as well as flow quantification with phase-contrast. Recent years have seen gradient echo sequences used in a range of quantitative methods such as MR fingerprinting [29] as well as multi-echo steady-state sequences, such as DESS [91] and TESS [32, 33]. All such sequences are based on a fixed TR, and differ in having different gradient structuring and RF phase cycling. The scan duration is directly proportional to the Repetition Time (TR) and hence a reduction in TR is a vital aspect to be traded of against image resolution, Field-of-View (FOV) and RF pulse properties. Balanced SSFP sequences particularly benefit from reduced TR thanks to reduced banding artefacts, which can become problematic for challenging B_0-shimming scenarios such as cardiac CINE. Aside from image quality, breath-holds can be uncomfortable experiences for patients but necessary for imaging situations sensitive to respiratory motion, and scan time reduction can help to reduce this as much as possible.

Rapid gradient echo sequences are usually limited by SAR, which is quadratically proportional to RF amplitude. This can constrain pulse sequence designers from achieving their desired flip-angle, for example in attempting maximal contrast between cardiac muscle and blood [92, 93]. Cardiac bSSFP accelerated with multiband (MB) pulses could allow a great reduction in breath-holds, but is heavily constrained by SAR and can lead to an unacceptably long TR for image quality [26, 27]. In coronary imaging, such as TOF angiography, high flip-angles are desirable to saturate background tissue within the imaging slab. Specifically for multi-slab TOF angiography, so-called "venetian blinds" artefacts

can be reduced by using high slice quality with long RF pulses. Both high flip-angles and slice quality are parameters which increase TR and thus acquisition time [90].

Much recent RF pulse design development, including the previous chapters in this thesis, has focused on minimum-duration techniques subject to hardware constraints, which are shown to benefit greatly from time-variable selection gradients designed using time-optimal VERSE [45], non-uniform SLR [94] or optimal control approaches [84, 95]. However the problem of minimizing RF pulse duration and minimizing TR are not equivalent, because minimum TR is constrained by SAR which is usually increased by reducing pulse duration. How best to utilize time-variable gradient techniques for the purpose of minimizing TR is not trivial, and we have found that this can only be achieved by considering both SAR constraints and sequence timing. In this work we will use VERSE as an example for time-variable gradient design methods, to show that minimum-duration and minimum-TR are inherently separate operating points, and present a framework which achieves minimum-TR for gradient-echo sequences.
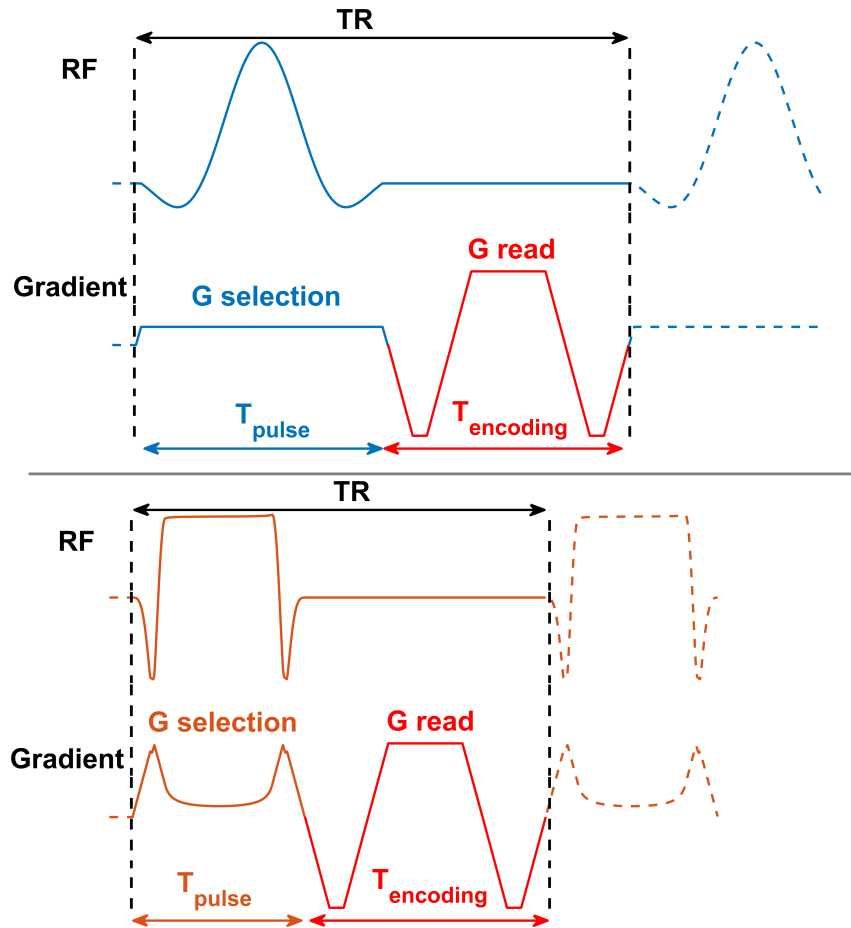
Figure 5.1: Top: An example balanced SSFP sequence diagram, only showing the selection and balanced read-out gradient. A TR is comprised of a pulse duration and readout duration. This repeated after each TR to maintain the balanced NMR effect.
Bottom: An example balanced SSFP sequence with a VERSE RF and Gradient waveform. This work explains how to design time-variable gradient pulses (such as VERSE) for minimum-TR sequences.

5.2 Theory

RF pulses are designed to achieve a flip angle θ, and can either be short in duration but high in amplitude, or vice-versa. The measure that is proportional to SAR however is RF energy, calculated as

$$E_{RF} = \int_0^{T_{pulse}} B_1(t)^2 dt \tag{5.1}$$

where T_{pulse} is the RF pulse duration, and E_{RF} is expressed in $\mu T^2 ms$. RF energy can be related to minimum Repetition Time (TR) using the relationship

$$TR_{min} = \frac{E_{RF}}{SAR_{limit}} \alpha \tag{5.2}$$

where SAR_{limit} is a regulatory set value in W/kg, and α is a conversion factor in $W/kg/\mu T^2$ which relates to how effectively RF transmission leads to RF heating, and thus SAR.

Independent of RF pulse design, the image encoding time is set by a range of imaging parameters such as the imaging resolution, Field-of-View in the read-out direction, and its water-fat shift. These parameters can be summarised with a single time-value, T_{enc}. Moreover, RF systems can have duty cycle limitations, which bars them from being active for more than a percentage of a sequence TR. Encoding time and RF duty cycle can be formalized into an minimum TR function as

$$TR_{min} = max\left(T_{enc} + T_{pulse}, \frac{T_{pulse}}{\delta_0}\right) \tag{5.3}$$

where δ_0 is the RF duty cycle with a value between 0 and 1.
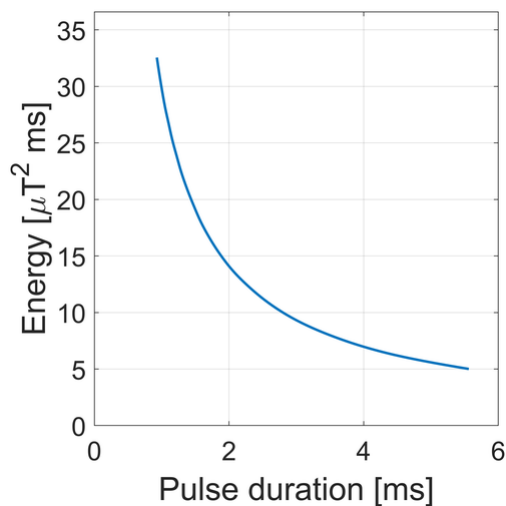
Figure 5.2: Pulse energy as a function of pulse duration, where the pulse duration is varied by changing the peak B_1-amplitude and all other pulse parameters are left intact (FA=40º, TBP = 4)

For a fixed imaging situation (i.e. slice-thickness and encoding constraint), and a fixed RF pulse properties (flip-angle, time bandwidth product), the only parameter that can be changed is the RF shape. The RF shape is defined for a certain slice-quality, but once
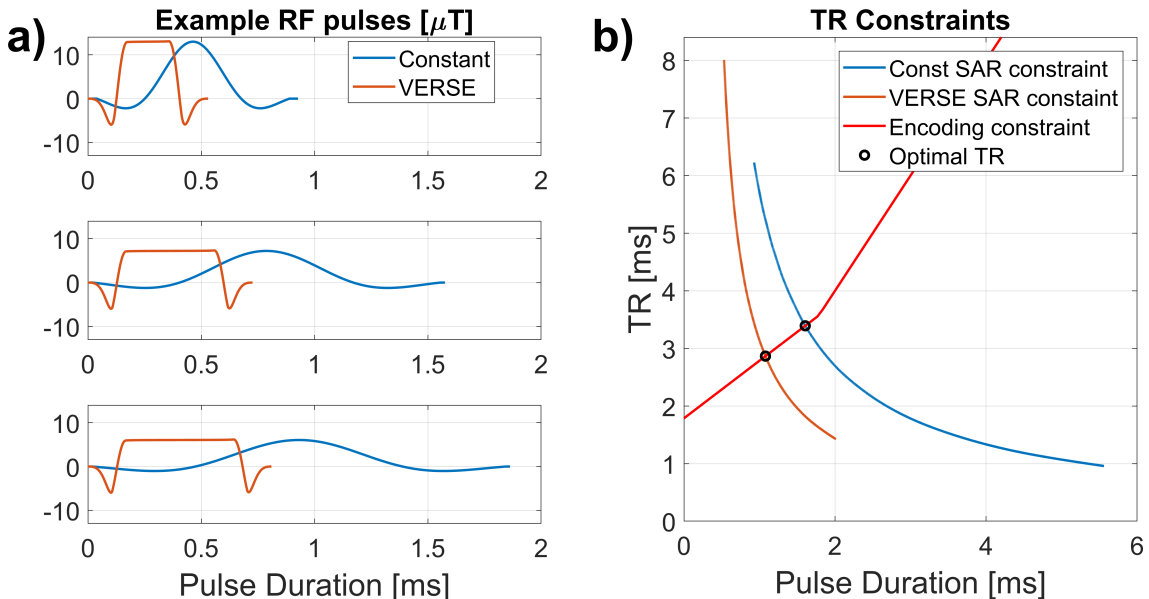
Figure 5.3: a) Shows constant gradient and VERSE designed RF pulses for three different B_1-amplitudes. The shape of the constant gradient pulse remains the same, but the VERSE shape changes for every peak B_1 amplitude. **b)** Shows the TR constraints from Equations 5.2 and 5.3, for constant and time-variable VERSE gradients. Any solutions below these traces are infeasible, and minimum TR is achieved at the marked intersection. The SAR constraint for VERSE intersects the encoding constraint curve lower, and thus allows for a shorter TR.

designed [1,2] it can be reshaped using VERSE [42]. For different peak B_1-amplitudes the shape of the constant gradient pulse remains the same, but the VERSE shape changes. This is shown in Figure 5.3a.

From Equation 5.3, it seems that a short RF pulse will minimize TR. However Equation 5.2 tells us that a pulse with short duration will have high RF energy and thus will actually lead to a high TR. The trade-off between the SAR constraint and encoding constraint is shown in Figure 5.3b where it is shown that TR is minimized at the intersection of the two curves. Because VERSE changes RF shapes, it will also change the shape of the SAR constraint in 5.3b and lead to a reduction in TR when all other parameters are left the same, showing the benefit that VERSE can give.

5.3 Methods

5.3.1 RF pulse design

Conventional RF pulses with constant gradients were calculated to be minimum duration, for a maximum $B_1(t)$ amplitude varying from $2\mu T$ to $13\mu T$, in 20 intermediate steps. This ensured that pulse duration and pulse energy were simultaneously controlled by the pulse amplitude, for a given flip-angle and all other design parameters fixed. Additionally, the selection gradient amplitude was limited to $31mT/m$, and when pulse bandwidth

exceeded this the pulse was stretched to achieve this limit. The pulse duration included gradient slopes at either end, driven at a slew-rate of $200mT/m/ms$, and the RF pulse was zero-padded appropriately, to match duration. Multiband pulses, to excite N slices, were designed in the same manner but with an additional step of applying a multiband modulation function

$$f_n(t) = \sum_{n=1}^{N} e^{i(\gamma G x_n t)} \tag{5.4}$$

where γ is the gyromagnetic ratio, t is a time-variable, x_n is the nth slice position. Note that in this work, there is no gain in using slice-specific phase-optimization [35, 37, 81] as the RF energy is more constraining than the peak RF amplitude.

VERSE pulses were calculated using the time-optimal VERSE algorithm [45] constrained with the same hardware limits (B_1-amplitude, gradient amplitude and slew-rate) as in the constant gradient case. Gradient slopes were incorporated in the optimization, and RF was allowed to be active during the gradient slopes. VERSE MB pulses were designed using the vMB method described in chapter 4. This method applies VERSE to a singleband waveform, which becomes a multiband pulse by applying a modified multiband modulation function $f_N^v(t)$

$$f_N^v(t) = \sum_{n=1}^{N} e^{ik(t)x_n} \tag{5.5}$$

where the spatial frequency variable $k(t)$ is defined as

$$k(t) = -\gamma \int_t^T G(\tau)d\tau \tag{5.6}$$

In contrast to the original vMB method, here we again omit any multiband phase-optimization for $f_N^v(t)$.

With two applications in mind, we focused on two separate designs. The first, with body balanced SSFP in mind [26], we designed pulses with low time bandwidth product (TBP = 2.13) singleband and multiband 2-3 with slice-thickness 1-9mm in steps of 2mm and centered slice-to-slice gaps to cover an imaging FOV of 100mm. For the second application, with 3D multi-slab TOF angiography in mind [96], we designed singleband pulses with TBP 4 and 6, and slice-thicknesses 10, 15, 40 and 60mm. Both applications were designed for flip-angles 25 to 90 degrees, in steps of 5 degrees.

5.3.2 Minimum TR

Pulse energy was converted to TR using Equation 5.2 using the regulatory local SAR limit of $20W/kg$ for operating at 3T, which is always stricter than the whole-body SAR limit. The encoding time in Equation 5.3 was set to 1.786ms , which was fixed for a read-out resolution of 2mm and a water-fat shift of 0.4mm. The intersection between the encoding and SAR constraint curves was found by highly interpolating both, and the corresponding B_1-amplitude for that solution was considered TR-optimal.

5.3.3 Slice-shifting

Time-variable selection gradients results in a variable velocity in excitation k-space during RF transmission. Off-center slice-positioning can no longer be conducted in the same manner as for constant-valued gradients. The relationship between the spatial position of a slice x, and a time-modulated RF pulse in the small-tip approximation is [1]

$$M_{xy}(x) = i\gamma M_0 \int_0^T B_1(t) e^{-i\gamma x \int_t^T G(s)ds} dt \tag{5.7}$$

where the integral $\int_t^T G(s)ds$ in the case of a constant-valued gradient of amplitude G, simplifies to $(T-t)G$. To shift a slice by position Δx, the RF pulse can be induced to operate at a shifted frequency shift given by

$$\omega = \pm\gamma\Delta x G \tag{5.8}$$

which can be achieved using a phase modulation function

$$\theta(t) = \pm\gamma\Delta x G t. \tag{5.9}$$

Multiplying Equation 5.7 with $e^{i\theta(t)}$ from Equation 5.9 then results in (ignoring the non-variable T-term)

$$M_{xy}(x) = i\gamma M_0 \int_0^T B_1(t) e^{-i\gamma(x\pm\Delta x)Gt} dt \tag{5.10}$$

To achieve the similar effect for time-variable gradient shapes, shifting must be completed using a complex exponential with the gradient integral left intact, and thus

$$\theta^v(t) = \pm\gamma\Delta x \int_t^T G(s)ds. \tag{5.11}$$

This is the same as applying a frequency modulation during RF transmission as described in section 1.4.1, where the frequency modulated component of the RF is equivalent to the VERSE gradient, scaled in frequency to achieve the desired off-center excitation Δx. Note that the mechanism between a modified multiband modulation function in Equation 5.5 and Equation 5.11 are similar. Equation 5.5 describes how a singleband slice is duplicated and shifted for a variable velocity excursion of excitation k-space, whereas Equation 5.11 describes how a composite multiband slice-profile, excited in this way, is shifted in space as a pack of slices.

5.3.4 GIRF-based RF correction

Time-variable selection gradients also lead to increased fidelity issues due to limited temporal bandwidth of practical gradient systems. As discussed in 1.4.2, assuming such imperfections are linear time-invariant effects they can be modelled using a gradient impulse response function (GIRF) [57], and as shown in chapter 4 the GIRF can be used to predict slice-profile errors. When the GIRF of a system is known, it is possible to design

an RF waveform which corrects for such errors, as described in section 4.4. In this work no iterative correction was necessary, as the RF pulses are not constrained by the available peak-amplitude. The GIRF of our scanner is shown in Figure 2 in chapter 4, which in the frequency domain can be well approximated using a Lorentzian-shaped function. In the time-domain we can therefore estimate our GIRF as

$$H(t) = \frac{1}{\tau} e^{-t/\tau} \tag{5.12}$$

where τ is a time-constant which we set $42\mu s$, as we found this to resemble our measured GIRF without further optimization necessary. As discussed, FM-based slice-shifting in Equation 5.11 depends on the time-variable gradient, and may also benefit from knowledge of the GIRF. Therefore, the distorted waveform is used in specifying $\theta^v(t)$.

5.3.5 Peripheral nerve stimulation

The usage of time-variable selection gradients raises the question on whether peripheral nerve stimulation (PNS) should be considered as an additional physiological constraint, similar to SAR. PNS is caused by fast switching gradients and depends on the rate of time-varying fields, as well as slice orientations and read-out directions (See section 1.5.2). Our Philips 3T system made use of the SAFE-model to predict stimulation [74,75]. This model uses the first-derivative of a gradient waveform as peripheral nerve stimuli. These stimuli are then filtered using low-pass filters, and recombined with set weights to produce a SAFE model output. The maximum value of this output is directly reported as a percentage of a fixed PNS threshold.

To investigate whether the minimum TR would be affected due to the insertion of a VERSE gradient, we implemented the SAFE model off-line with two parallel low-pass filters, and manually specified trapezoid gradients associated with a typical in-vivo imaging scenario. This was repeated for all three gradients axes independently.

5.3.6 Experiments

The B_1-amplitude which led to an optimal TR solution was used to design a new pulse, which can be recalculated at run-time. Slice profile measurements were conducted on a 3T Philips Achieva (Philips Healthcare, Best, Netherlands) using a cylindrical phantom containing 100mL of saline (9g/L) doped with 1% gadolinium contrast agent (0.5 mmol/L Gd-DOTA, Dotarem, Guerbet LLC, Bloomington, IN, USA). All pulses were designed for a flip-angle of 45 degrees, slice-thickness of 7mm and a gap of 42mm. All slices were shifted from isocenter by Δx =21mm using the FM-shifting approach described above. This includes the constant gradient MB2 pulse, for which the FM-shape is constant valued and scaled to $\gamma G \Delta x$. Slices were visualized using a 2D gradient-echo sequence(TR = 50ms, TE=8.5ms,0.55x0.575mm in-plane resolution) with the read-out gradient moved to the slice-select direction.

Cardiac bSSFP imaging was performed using the same MRI system, on a healthy volunteer (27yo, male) using a 32channel receiver coil. MB2 and vMB2 RF pulses were designed for a flip-angle of 40°, TBP=2.13, slice thicknesses 7mm and a slice-gap of 49mm. No other forms of in-plane acceleration (SENSE or half-Fourier) were used. B_0-shimming was performed using a custom slice-by-slice tool, and cardiac traces were synchronised using an ECG trigger. Aliased multiband images were unfolded and reconstructed with a SENSE-based algorithm as used in ReconFrame (GyroToools GmbH, Zurich, Switzerland). Implementation issues arose with user-defined RF and gradient shapes close to 100% SAR, and as a compromise, pulses in this demonstration were designed to fit just below 93% of permitted SAR (i.e. maximum SAR limit of 18.6W/kg) which alleviated such issues.

5.4 Results

5.4.1 Simulations

Figure 5.4 shows the minimized TR when using time-variable VERSE selection gradients in the case for low time bandwidth product (TBP=2) RF pulses, for different flip-angles. Figure 5.4a shows that the TR can always be reduced by using time-variable selection gradients, for multiband factors 1-3. Figure 5.4b shows the same results, expressed as time spent per slice, which directly relates to scan reduction. When accelerating a singleband acquisition with conventional multiband 2, an average of 36% of reduction in time-per-slice can be achieved. However this acceleration comes at an average increase of 29% in TR, which for cardiac bSSFP introduces more banding artefacts in an already challenging B_0-shimming situation. By using a sequence-level minimum-TR framework, a VERSE MB2 implementation reduces the time-per-slice by 43% with only an average increase of 15% in TR.

Figure 5.5 shows the minimum TR for VERSE singleband pulses, which for example are applicable to 3D multi-slab TOF angiography as an application which benefits both from high flip angles and high time bandwidth products. A VERSE implementation for TB4 and TB6 can lead to an average reduction in TR by 24% and 32% respectively, compared to constant gradient pulses. The relative benefit between a constant and VERSE implementation is greater at higher flip-angles, and higher time bandwidth products. Moreover, for constant gradient pulses, an increase in time bandwidth from TB4 to TB6 comes at a TR cost of 12%, where-as for the VERSE pulses this increase comes with a negligible TR increase of 1.7%.

Figure 5.6 shows how the minimum TR varies as a function of slice-thickness, for two different flip-angles (30° and 80°) and TBP=2,4,6. For the TBP=2, low-flip angle case the minimum TR is significantly higher for a 1mm slice than for the other cases (left-most column). This is because the pulse bandwidth exceeds the maximum gradient amplitude of $31mT/m$, and the RF pulse needs to be stretched in compensation. This however is
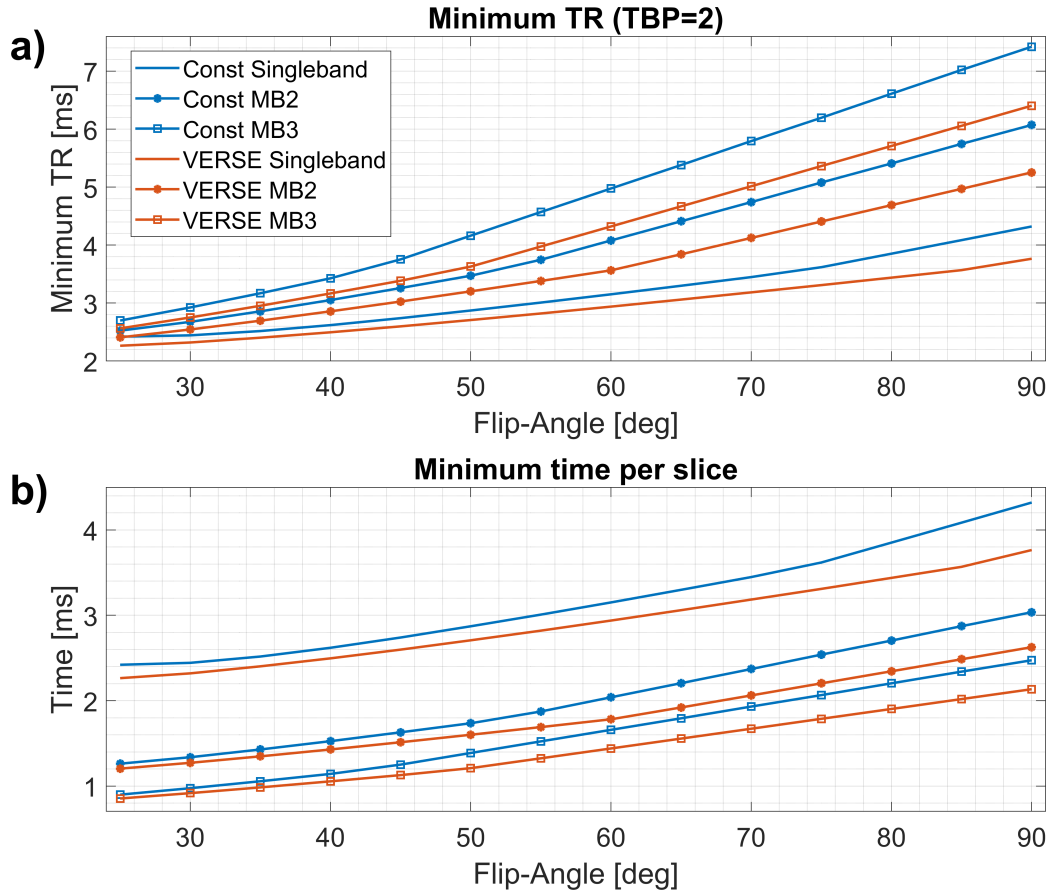
Figure 5.4: a) Shows the minimum TR achievable for a TBP=2 case, for constant and VERSE gradients, as well as for singleband and multiband 2-3 pulses. Using VERSE always reduces the TR. **b)** Shows the time per slice for the same pulses. An MB2 acceleration with constant gradients can reduce scan durations by an average of 36% with a TR-increase of 29%. A VERSE minimum-TR implementation can reduce the scan time by 43% with only a 15% TR increase. This would be useful, for example, for a cardiac bSSFP sequence with reduced breath-holds.

not induced by the usage of time-variable gradients. For higher flip-angles and TBP, a similar behaviour can be seen, but to a much smaller degree as the pulse bandwidth is significantly lower. MB2-3 and vMB2-3 pulses (not shown here) are longer versions of the SB pulses, and thus also show this effect, if to a lesser degree. For TBP=4 and TBP=6 (middle and right column, respectively) minimum TR does not depend on slice-thickness as the gradient amplitude is not limited for thicker slabs.

Introducing VERSE gradients impacts PNS, which could pose as an additional constraint to achieving minimum TR. Figure 5.7 shows excerpts of the SAFE model during two TR periods at the start of a bSSFP sequence. Gradient waveforms, their first derivatives and the SAFE model outputs are shown from in sections a,b, and c respectively. From the model output in Figure 5.7c it can be seen that the biggest contributor towards PNS are the slopes on either side of the read-out gradient. This result is shown for the excitation of a transverse slice (i.e. slice-select on the FH direction) and read-out along the LR direction. PNS evaluation however depends on slice orientation and read-out
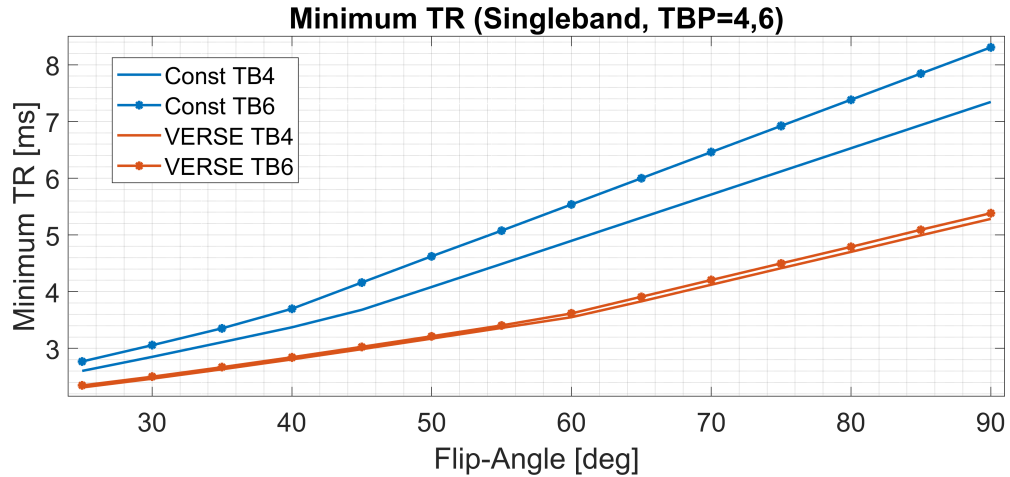
Figure 5.5: Minimum TR achievable for TBP=4 and 6, for constant and VERSE gradients. The average benefit of VERSE for a singleband with a time bandwidth product of 4 and 6 is 24% and 32% respectively, compared to constant gradient pulses. The TR reductions are more significant at higher flip-angles. Moreover, an increase from TB4 to TB6 comes almost at no extra cost in TR. This would be useful for a Multi-slab TOF angiography sequence, or a 3D bSSFP sequence.
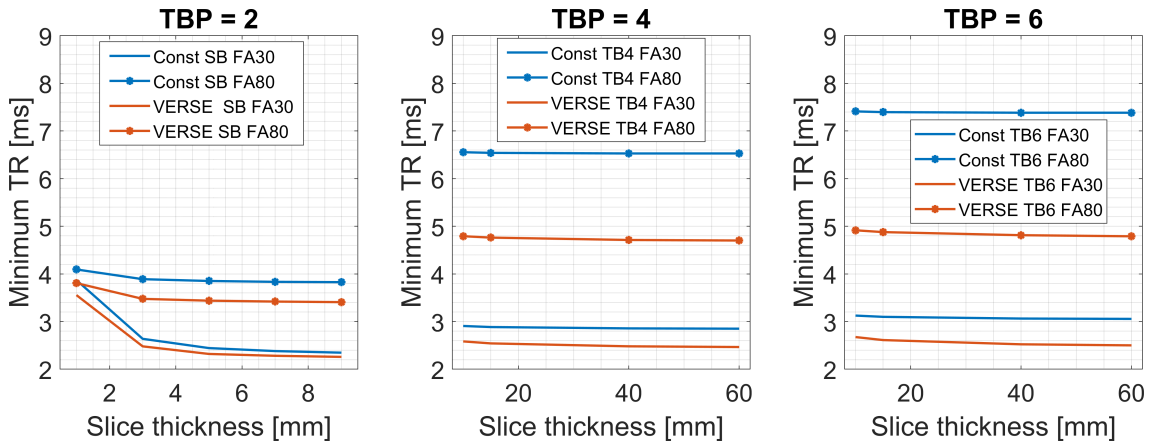
Figure 5.6: Minimum TR as a function of slice-thickness, for two different flip-angles and TBP=2,4 and 6. In most cases the minimum TR is largely independent of slice-thickness, with the exception of low TBP and low flip-angle. In this case the RF pulse is short, has high bandwidth and requires stretching to meet the gradient amplitude limitation of $31mT/m$. Note that this effect is not induced by using time-variable VERSE gradients, and in fact VERSE can help reduce TR. This can become problematic for imaging with low flip-angle and high-resolution isotropic voxels.

direction. Furthermore, due to the filtering of repeated stimuli with fixed time intervals, the filter output will develop a steady-state response, which cannot be seen in the first few repetitions of the model output.

Figure 5.8 therefore shows a similar graph, but with shaded patches along the filtered outputs, showing the worst (highest stimulation) and best (lowest stimulation) that can be experienced for any slice orientation. For example, the highest shaded patch of the read-out gradient filter output corresponds to reading out along the AP direction on an either coronal or transverse slice, whereas the lowest shaded patch would correspond to reading
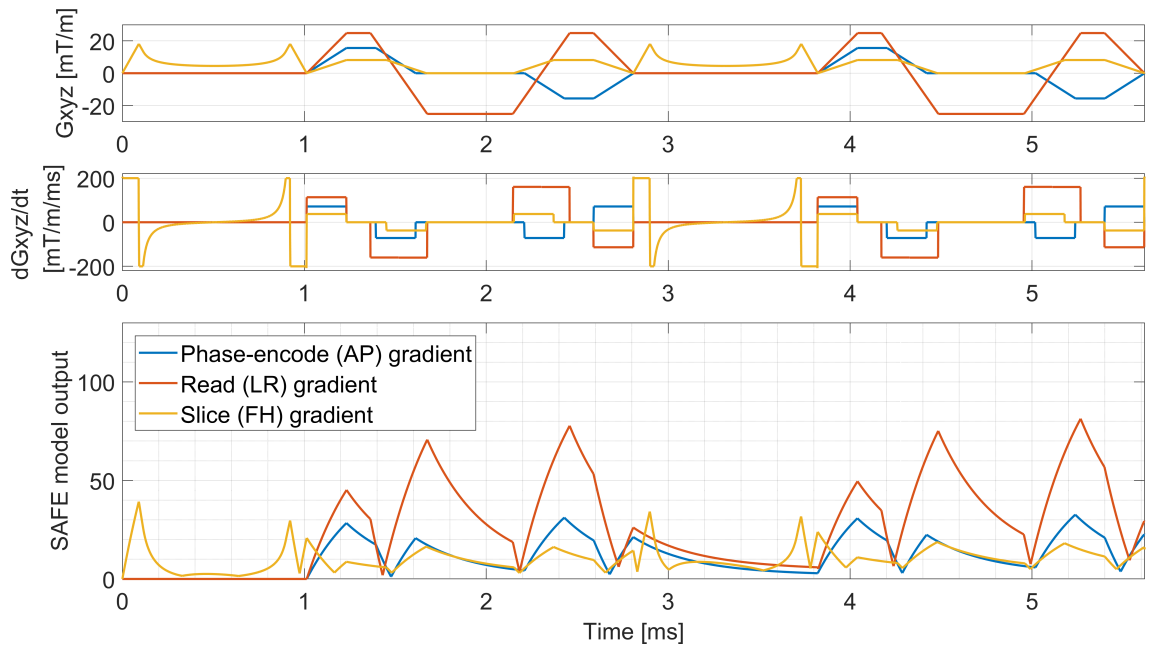
Figure 5.7: Analysis for Peripheral Nerve Stimulation (PNS) when using VERSE selection gradients.
Top: Gradient diagram for a 2D balanced SSFP sequence, exciting a transverse slice and reading along the LR direction. **Middle:** Shows the derivative of all three gradient axes, which relate to nerve stimuli that could cause PNS. **Bottom:** shows the output from the SAFE model. The highest peak amplitude is reported as the stimulation level, as a percentage of a set PNS threshold level. The biggest contributor towards stimulation level are the gradient slopes either side of the balanced read-out gradient, which overshadows the VERSE gradient. However a few aspects are missing from this results, namely the dependence on slice orientation and read-out direction, and the steady-state response of the SAFE model. These are addressed in Figure 5.8

out along the FH direction on either coronal or sagittal slice. Any slice with a single- or double-oblique angulation will result in a less extreme PNS situation [97]. This figure shows the repeated stimuli after 10 TRs, and the repetition of filter output peaks verify a steady-state response. For comparison an constant slice gradient with matched duration is shown along side the VERSE slice gradient. For clarity, the balanced phase-encoding blips are omitted.

The SAFE model output shows that replacing a constant gradient with a VERSE gradient increase the contribution of the slice-select gradient towards PNS. However, it remains relatively low in comparison with the contribution of the read gradient.

5.4.2 Experiments

Figure 5.9 shows off-center slice-profile measurements from a constant gradient MB2 pulse, as well as from three different vMB2 pulses, which were excited away from isocenter as described above. The bottom row shows a zoomed version of the top row. Comparing the MB2 and the vMB2 profile without any GIRF correction, the vMB2 measurement contains
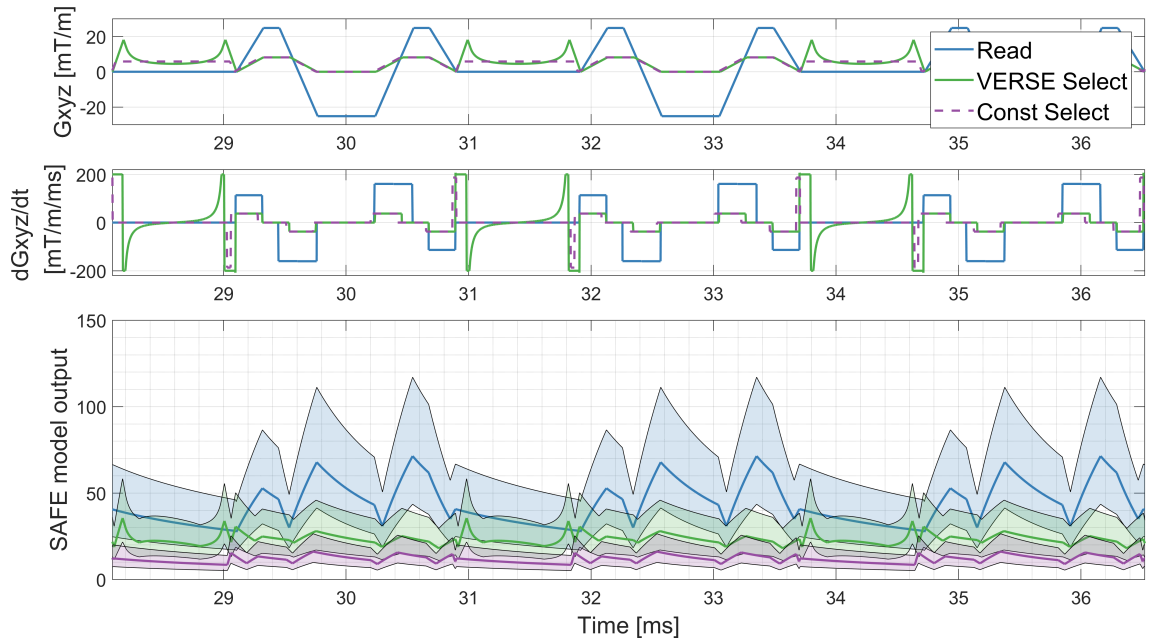
Figure 5.8: Further analysis for estimating PNS when using VERSE selection gradients.
Top: shows the same sequence diagram as in Figure 5.7, including a duration-matched constant selection gradient for comparison. The phase-encoding blips are omitted for clarity. **Middle:** Gradient waveform derivatives which act as nerve stimuli.
Bottom: SAFE model output, where the solid traces are similar to those shown in 5.7. The shaded regions above and below relate to worst and best PNS cases respectively, depending on slice orientation and read-out direction. The model output has reached a steady state, as can be seen by the repeated peaks. This shows that there are extreme imaging cases where the stimuli of VERSE gradients are equivalent to that of read-out gradients. However in most cases, the read-out gradient is remains the biggest contributor, and PNS can be best avoided by limiting the slew-rate on the balancing read-out gradient, using a lower read-out resolution, or a higher water-fat shift.

increased side-lobes which are more prominent at around the right slice, as it is further away from isocenter. In addition, spurious signal is inadvertently excited in between the slices. This latter component can be avoided by using a GIRF-distorted FM-waveform to shift the slice-pack, as shown in yellow. However this only reduces artefacts in the center of the slicepack, but actually increases the side-lobes on the left slice and again shows side-lobes on the right slice. The best way to reduce both effects is to design a vMB2 with GIRF-corrected RF and GIRF-corrected FM for slice-shifting, as shown in purple. This profile most closely resembles the MB2 profile, however some small side-lobes remain visible. The full GIRF-corrected pulses were used in the in-vivo demonstration.

Figure 5.10 shows balanced SSFP acquisitions in a healthy volunteer with T_{enc}=1.786ms. The left-most column shows a standard singleband acquisition using a single 14 second breath-hold. The column to the right shows a MB2 accelerated acquisition of this using a constant-valued gradient, acquired in an 8 second breath-hold. In the next column a vMB2 pulse was designed to have the same peak RF amplitude as the MB2 pulse, leading to a short RF pulse which leads to high RF energy. This however leads to a $0.8ms$ increase in
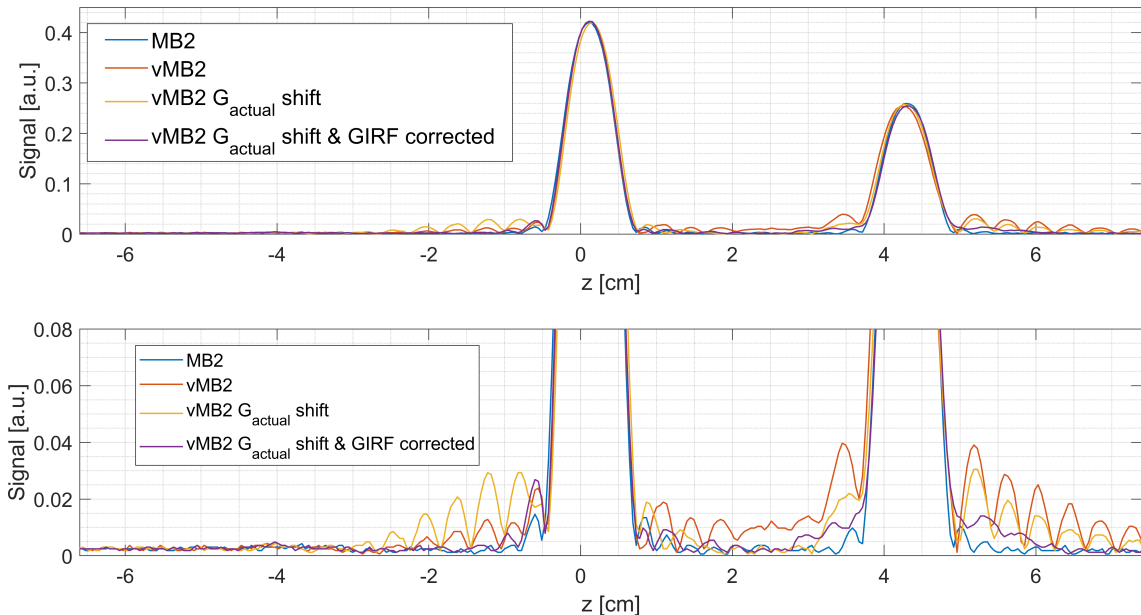
Figure 5.9: Mulitband 2 and vMB2 slice profiles, shifted 21mm from isocenter using FM-shifting, acquired in a gradient-echo sequence (FA=45°, TE=8.9ms, TR=50ms,slice thickness 7mm, 42mm gap). The **top row** is duplicated in the **bottom row** with a smaller view. Using vMB2 without any GIRF-correction shows an increase in side-lobes, which is worse around the right slice as it is further away isocenter. Using a vMB2 pulse with a GIRF-corrected FM-shape reduces the noise-level in between the slices, but cannot correct for the sidelobes around the slices. Using a GIRF-corrected FM shape as well as a GIRF-corrected RF waveform results in shifted VERSE slices which best resemble the constant gradient profile. Remnant side-lobes could be due to an mismatch in the GIRF model used.

TR, increasing banding artefacts and distorting the image. Using our proposed framework a VERSE RF pulse and gradient were designed to minimize TR, which leads to a TR of 2.9ms. This is twice as much imaging data than the singleband case, with only a 11% increase in TR, rather than the 19.2% increase required for the constant gradient MB2. Both mininmum-TR MB2 and vMB2 scans were acquired in an 8 second breath-hold, which is a 43% reduction from the SB acquired data. In this case the TR-reduction from using VERSE was not significant enough to see a scan-time reduction. This might be more plausible when using higher flip-angles.

5.5 Discussion

Rapid gradient echo sequences are some of the most widely used MR sequences. RF pulse design parameters are sacrificed in the competition for SAR and imaging demands. Time-variable selection gradients can give a novel leeway to this family of sequences, as shown by many recent developments [24, 42, 43, 96]. This work has proposed an optimization framework which allows RF pulse design specifically for minimum-TR gradient echo sequences.
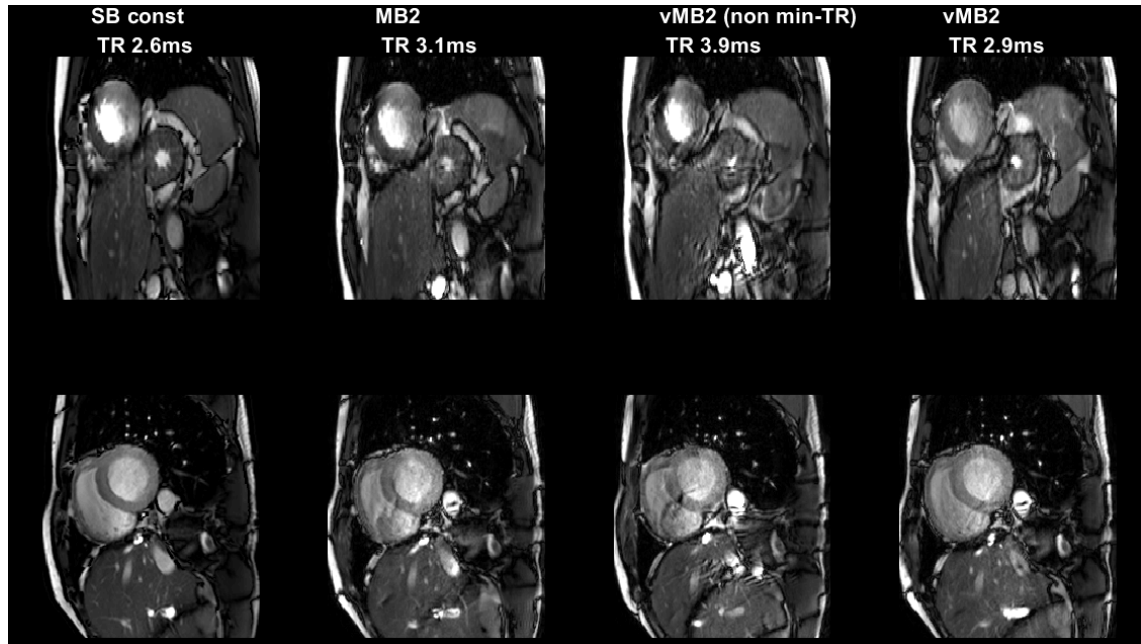
Figure 5.10: Cardiac MB2 -bSSFP experiments using conventional MB2, and two different vMB2 pulses (TB=2.13, FA=40°,slice thickness = 7mm, 1.6x2mm in-plane resolution. No in-plane acceleration). **a)** Shows singleband data acquired using a 14s breathold. **b)** Using a MB2 pulse designed for minimum-TR, this can be reduced to a 8s breath-hold, which comes at a TR increase of 19%. The constant-gradient MB2 pulse can be optimized in the same way as the singleband pulse. **c)** A vMB2 pulse designed to have the same peak B_1-amplitude as the MB2 pulse, results in an RF pulse shorter than the MB2 pulse, however leads to a $0.8ms$ increase in TR due to high RF energy. This also leads to a 11s breath-hold. **d)** A vMB2 pulse designed using our minimum TR framework results in an VERSE RF pulse which lead to a reduced 8s breath-hold with only a 11% increase in TR compared to the singleband data.

Equation 5.4 shows how RF energy can be equated to minimum TR for a fixed SAR-limit, and Equation 5.3 describes how the sequence timing constraints of a rapid gradient echo sequence can be described in terms of minimum TR. Figure 5.3 shows how these two constraints interact, and when image encoding parameters are fixed, the framework only needs to know the encoding duration, to determine the RF and gradient pulse which result in the minimum-TR achievable. The key to this framework is that knowledge about the sequence timing allows for minimum-TR design. This is different from past VERSE implementations, where RF pulses are designed independently from the sequence they are used in.

Figures 5.4 and 5.5 show the benefit achievable by moving from a constant-valued gradient to a time-variable VERSE gradient. We have looked at two imaging scenarios; firstly, multiband pulses with low TBP, which proved useful for cardiac (body) bSSFP, and secondly singleband pulses with high TBP for exciting thick slabs, which could be useful for multi-slab TOF angiography. A significant finding is that VERSE is always able to reduce TR. Moreover, this framework is incredibly flexible, being applicable to a wide range of RF pulse design parameters. Time-variable gradients are more effective at TR-reduction

when using high time bandwidth product pulses, such as for multi-slab angiography to prevent cross-slab saturation artefacts, which lead to "venetian blinds" artefacts. Another potential advantage could come from using higher TBP pulses in a 3D slab acquisition, where better defined slices will provide more homogeneous contrast across the slab [43] or require less extra phase-encoding, and thus lead to shorter acquisition times.

Figure 5.6 shows the minimum TR dependency on slice-thicknesses, for two different flip-angles. It is shown that minimum TR performance is independent of slice-thickness in most cases, with the exception of TBP=2 and low flip-angle case. In this case the required selection gradient amplitude exceeds our limit of $31mT/m$, and thus the pulse cannot be further reduced in duration to arrive at the minimum-TR operating point. This effect is not due to the time-variable method, but depends on the maximum gradient amplitude available, and could constrain imaging situations where high-resolution isotropic voxels are desired. The results for the higher TBP cases show that minimum TR is largely independent of slice-thickness. This was an expected result, as in this analysis we have focused on thicker slabs (10-60mm), which in addition to higher TBP further relieve on pulse bandwidth.

Figures 5.7 and 5.8 investigated the effect on PNS when inserting time-variable gradients in a balanced SSFP sequence. The conclusion from this analysis is that the read-out gradient is the largest contributor towards PNS. However, when considering all possible slice orientations and read-out directions, it is possible that VERSE slice gradients have similar contributions towards PNS as the read-out gradients (i.e. a coronal slice with a FH readout). Whether or not this means that VERSE gradients will increase stimulation levels depends on the implemetation of specific systems. When only the maximum stimulation from each gradient coil is considered [74, 76] VERSE slice gradients would almost always be overshadowed by the read-out gradient. For our analysis, we considered the gradient waveforms for a balanced SSFP sequence, as this was our target demonstration. This type of imaging typically has highly anisotropic voxel sizes, with slice-thicknesses being greater than in-plane resolution. This inherently implies that slice selection bandwidth is lower than the read-out bandwidth, and so in terms of PNS a more isotropic imaging scenario is likely to more constrained than an anisotropic imaging situation, when using a VERSE slice-select gradient.

The practical implementation of such time-variable gradients required special care with off-center excitation. Slice-shifting can no longer be done using conventional frequency modulation, but requires time-variable frequency modulation adjusted to the rate at which excitation k-space is traversed. Moreover, low temporal bandwidth of current gradient systems lead to the demanded excursion not being fully realized, as shown in chapter 4. In this work this led to increased sidelobe errors as well as spurious excitation between slices as shown in Figure 5.9. Such small sidelobes can lead to high signal leakage as they approach SSFP bands. However, these side-lobes can be largely corrected for by using GIRF-based RF correction and GIRF-corrected frequency-modulated slice-shifting. Small

errors remain visible, which could be due to an incorrect GIRF, which we assumed to be an mono-exponential model. We tested this imaging method with a GIRF described by an analytic function with an approximate parameter, to report findings which could be easily reproducible by other imaging centers. In previous work we have shown that these errors can be corrected for when using a measured GIRF correction [87].

Figure 5.10 shows cardiac MB-bSSFP results acquired on the same system. The purpose of this demonstration was to show how a short RF pulse with time-variable gradients can have too much RF energy, which inadvertently leads to a high TR due to SAR constraints. As our proposed framework has shown, both RF energy and sequence timing constraints must be considered to achieve minimum TR, and this concept is key to designs with time-variable selection gradients. Using this framework a conventional singleband breath-hold of 14s was reduced to 8s with vMB2, with only a 11% increase in TR. A conventional multiband implementation could have led to a similarly short breath-hold, but with a 19% increase in TR.

A range of applications can benefit from this framework, thanks to its simplicity and flexibility. For example, MR fingerprinting [29] aims to accurately map MR signal evolution to T1/T2 maps, and relies on achieving a prescribed flip-angle in an imaging volume. This assumption often does not hold for low time bandwidth product pulses in rapid gradient echo sequences, and makes the use of higher TBP pulses beneficial. MR fingerprinting has also been shown to be accelerated using multiband pulses [30,31]; both higher time bandwidth pulses and multiband acceleration can be fully maximized using our framework, however the most optimal solution should jointly optimize variable TR and flip-angles. This would also be true for other variable-flip angle methods, as proposed in [98]. Another recent quantitative imaging method [32,33] uses three echo pathways in MB2 and MB4 acquisitions, which can be further optimized using our proposed framework. Alternative-TR bSSFP [99,100] is an imaging method where two different TRs combine to place fat-signals in suppressed bands. This method will only suppress fat effectively with specific pairs of TR-values, and is a design problem of fitting the best possible pulse within such a TR, which is an analogous problem to the one discussed in this work.

In this work we found the optimal TR solution by evaluating a range of pulses, and once their pulse energy traces (Fig 5.3a) were found, other imaging parameters determined the optimal operating point in an ad-hoc manner. In practice, once imaging parameters are set, an iterative root-finding method based on the B_1-amplitude should quickly arrive at the TR-optimal solution without full knowledge of the pulse energy trace. An inclusion of the GIRF-based RF correction will not dramatically change the pulse energy trace, and so this can be easily incorporated into a practical design.

Furthermore, we considered hardware constraints (maximum B_1, gradient amplitude and slew-rate) and SAR as the physiological constraint. We found that PNS could potentially be another physiological constraint. An enhanced framework could make use of the SAFE model to further optimize for minimum TR by considering all gradient waveforms in the

sequence.

Time-optimal VERSE was used in this work due to our past experience and relatively fast calculation. Other methods which allow for the design of time-variable gradients, such as NUSLR [94] or optimal control [84, 95] might outperform our implementation - however the general minimum-TR framework is expected to apply extend to all time-variable gradient designs, as long as pulse energy traces (5.3a) are smooth with respect to peak B_1-amplitude. It should be noted that existing techniques for designing optimised RF pulses with time-variable gradients have focused on the challenging applications with large tip inversion and refocusing pulses in mind [46,94] or multi-dimensional pulses [101]. What our proposed framework would benefit most from is a similar one-dimensional approach for small-tip designs which can calculate time-optimal pulses fast enough for usage in routine imaging.

Previous work on cardiac MB-bSSFP [27] has noted that SAR and short TR was not a constraint in their sequence optimisation for a 3T Siemens Prisma. This difference might relate to how different vendors implement SAR evaluation, which implies that a minimum-TR framework might need system-based adjusting for maximum performance.

Other work has experienced RF artefacts associated with MB bSSFP [28]. In this work we have not seen similar artefacts, however as we use different MR systems with RF systems it is challenging to assimilate results.

5.6 Conclusion

We propose a novel VERSE algorithm to design RF pulses which are optimised for minimum-TR in rapid gradient echo sequences. Such pulses are shown to reduce cardiac bSSFP acquisition time by 43% in an in-vivo demonstration, and could further reduce TOF angiography acquisition time by 32%. The flexibility of this framework allows for benefit in other gradient-echo applications such as MR fingerprinting and other quantitative imaging methods.

Chapter 6

Conclusion

6.1   Thesis summary

This thesis has focused on implementing multiband RF pulses in existing MRI sequences, with the aim of accelerating imaging by reducing scan duration.

At the start of the project, the main challenge was to produce multiband RF pulses with sufficiently short durations to fit within existing sequences. Several techniques were already available to reduce the duration of RF pulses, such as phase-optimization, time-shifting and root-flipping. During the process of implementing these techniques we encountered practical difficulties, which over time were isolated to engineering considerations. The question we aimed to answer was how well we could do in terms of time-efficiency given limited RF and gradient hardware.

Multiband RF pulses place unconventionally high demands on RF hardware. Specifically, the rapid time-modulation of multiband pulses is easily an order of magnitude higher than that of conventional RF pulses. We discovered an issue relating to rapid time modulation, and discovered that the reproduction of rapidly varying frequency-modulated waveforms proved difficult. In response to this we demonstrated how three existing multiband pulse design techniques can be modified to produce equivalent results without frequency modulation, but using only amplitude modulation. This modification proved to be inherently kinder to our RF system, and avoided the strong image artefacts shown in Chapter 2. The results showed that the cost for avoiding such artefacts lead to an increase in RF pulse duration of 20-26%, but can be as little as only 14%. This technique is currently being used in data collection for the developing human connectome project, and is part of the Philips Healthcare Multiband SENSE product for designing multiband RF pulses.

Multiband RF pulse durations can be further reduced by using time-variable selection gradients, which was an idea ignited during the ISMRM RF pulse design challenge in 2016. However we found that rapidly modulating selection gradients place unconventional

strain on the gradient hardware. A simple and effective way of describing how gradient hardware responds to time-varying gradient waveform demands, is the gradient impulse response function (GIRF). We found that this affects multiband imaging when using such highly accelerated multiband waveforms, and in chapter 4 proposed a simple procedure of producing multiband RF pulses with time-variable gradients, which inherently have lower temporal bandwidth demands. This places less strain on the gradient hardware, and comes at a roughly 10% cost in time-efficiency compared to time-optimal time-variable gradient designs.

Discovering limitations in current MR hardware was only natural, given that current systems were not designed for modern demands. Multiband imaging has experienced a revival since the beginnings of the human connectome project, and we have investigated the effects of such accelerations from a hardware perspective. This provides pulse sequence developers with software-based solutions for existing hardware, but hopefully also sets the need the next generation of MR hardware to meet such demands in the future.

Hardware limitations were a first encounter with imaging considerations, but we also discovered limitations driven by physics. Chapter 3 focused on the formation of spin-echoes when using root-flipped multiband pulses, a recently proposed type of pulse with non-linear phase behaviour. Such pulses, even for the singleband case are unconventional and the extension to multiband implied that the spin-echoes for different slices misaligned in time. This meant that in an imaging experiment, different slices could contain different T_2 and T_2^* contrast. To develop an understanding for this effect, a spin-echo simulation model was developed and it was found that a difference in echo-arrival time could lead to an approximate 8.5% signal reduction, whilst the difference due to spin-echoes spending different amounts of time in the transverse plane could lead to a signal reduction of about 11.7%.

Most work in this thesis has been focused on designing the shortest possible multiband pulses, for EPI-type sequences where RF pulses are followed by relatively long read-out periods. This is motivated by the desire for short echo-times in diffusion MRI sequences, or high acceleration factors in functional MRI sequences for high temporal resolution. Another family of sequences are those with a balanced amount of transmit and receive periods. Examples are rapid gradient echo sequences and turbo spin-echo sequences, which when compared to the former family of sequences are much more SAR constrained, even in a conventional singleband scenario.

In addition to previous hardware considerations, this also exposed us to physiological constraints of SAR and PNS, which became the focus of chapter 5. We extended our work on using time-variable gradients in such sequences, and used a sequence-level framework to minimise TR. We demonstrated the potential benefit for multiband accelerated cardiac balanced SSFP, and found that when combined with multiband accelerations a 43% reduction in TR was possible compared to conventional imaging, achieved when using our proposed framework.

6.2   Other relevant literature

During the progression of work that contributed to this thesis, other research has aimed to improve image acceleration through different avenues. One of direct relevance was the work by Rund and Aigner [95], who won the ISMRM RF pulse design challenge. They propose a time-optimal control RF pulse design method, which iteratively calculates time-variable RF and gradient shapes. This problem is computationally expensive, and can be reduced in complexity using a topic known as adjoint optimization in PDE constrained calculus. In recent work, I have collaborated with Aigner to incorporate the GIRF method into the time-optimal control framework, which was presented at the annual ISMRM meeting in 2018 [102].

Apart from RF pulse design, image acceleration by the use of multiband is often limited by the technology surrounding receiver coil arrays. For instance, multiband acceleration in brain MRI is aided by multi-channel receiver coils which are well spatially distributed to unfold aliased slices. Multiband imaging in body MRI on the other hand, is usually limited to acceleration factors of 2-3, due to patient motion, as well as coil geometries which are not as well spatially distributed.

Other current research uses non-linear higher-order gradients during read-out, which has been shown to improve parallel imaging [103]. This is noted research as it makes use of novel MR hardware towards the same goal of reducing image acquisition duration, albeit with improved parallel imaging.

On the topic of gradient modelling, other work has used the GIRF to improve EPI-acquired data for improved reconstruction [58]. On the topic of reconstruction, recent years have seen a lot of interest of machine learning approaches to reconstructing parallel imaging data [104]. It will be interesting to see to what extent future rapid MR will be driven by transmit-based acceleration versus receive-based acceleration.

6.3   Future work

The general result from our thesis are methods and considerations of practically implementing multiband RF pulses. Further work can be developed in a wide range of applications.

Shorter multiband RF pulses, designed using VERSE or other time-variable gradient techniques, can benefit spin-echo EPI diffusion weighted imaging. In particular, by reducing the refocusing pulse duration in a spin-echo pulse pair, a shorter echo-time can result in higher SNR, which can be valuable in diffusion imaging. Alternatively, by using such shorter pulses a higher multiband factor can be achieved for a similar echo-time, or the same multiband factor can be used with higher b-values. This can prove valuable in brain

MRI, as well as in body MRI. For instance, liver tissue has short T_2 relaxation values and would be another useful application for multiband accelerations.

The majority of this thesis has been focused on implementing multiband RF pulses into clinical sequences. This paved the way for the minimum-TR framework for time-variable gradients. This can be extended to all rapid gradient echo sequences, but ultimately also to all RF designs, including conventional singleband RF pulses with time-variable selection gradients. One application would be to implement the minimum TR framework for multi-slab Time-of-Flight (TOF) angiography.

Another possibility is to include the gradient waveforms, which are responsible for image encoding, into the minimum-TR framework. Such a framework could deliver the shortest possible TR based on both SAR and PNS, which are physiological limitations, as well as any hardware limitations which were the focus chapters 2 and 4.

In terms of RF pulse design, we would be interested to reimplement minimum-TR design for time-variable gradient waveforms designed using a time-optimal control [95], which have been shown to outperform VERSE methods. In order to do this, we would need to develop an algorithm which is sufficiently fast to calculate minimum-TR solutions in real-time.

Multiband TSE sequences have similar structures to rapid gradient echo sequences, however typically require a much larger flip-angle for every refocusing pulse [105, 106]. Further work should investigate how the time-variable multiband pulses can be optimized for this purpose, where SAR constraints can further be alleviated by using variable flip angles [107, 108], or GRASE-type sequences [109].

In conclusion, much more work can be done in the area of optimizing RF and gradient pulse design techniques which take into account both hardware limitations as well as physiological limitations. I hope that readers will have appreciated how RF pulse design methods can resolve such limitations. Where possible, I think that future generations of MRI scanners will be better adapted to multiband imaging, however it might prove that the software-based solutions will remain relevant as long as current MR hardware remains used.

Bibliography

[1] John M. Pauly, Dwight G. Nishimura, and Albert Macovski. A k-space analysis of small-tip-angle excitation. *Journal of Magnetic Resonance*, 81:43–56, 1988.

[2] John Pauly, P. Le Roux, Dwight Nishimura, and Albert Macovski. Parameter relations for the Shinnar-Le Roux selective excitation pulse design algorithm (NMR imaging). *IEEE Transactions on Medical Imaging*, 10(1):53–65, mar 1991.

[3] N Damera-Venkata, B L Evans, and S R McCaslin. Design of optimal minimum-phase digital FIR filters using discrete Hilbert transforms. *Signal Processing, IEEE Transactions on*, 48(5):1491–1495, 2000.

[4] O Herrmann, L R Rabiner, and D S K Chan. Practical Design Rules for Optimum Finite Impulse Response Low-Pass Digital Filters. *Bell System Technical Journal*, 52(6):769–799, 1973.

[5] Thomas W. Parks and James H. McClellan. Chebyshev Approximation for Non-recursive Digital Filters with Linear Phase. *IEEE Transactions on Circuit Theory*, 19(2):189–194, 1972.

[6] Hong Shang, Peder E.Z. Larson, Adam Kerr, Galen Reed, Subramaniam Sukumar, Adam Elkhaled, Jeremy W. Gordon, Michael A. Ohliger, John M. Pauly, Michael Lustig, and Daniel B. Vigneron. Multiband RF pulses with improved performance via convex optimization. *Journal of Magnetic Resonance*, 262:81–90, 2016.

[7] Anuj Sharma, Michael Lustig, and William A. Grissom. Root-flipped multiband refocusing pulses. *Magnetic Resonance in Medicine*, 75(1):227–237, 2016.

[8] Rolf F. Schulte, Jeffrey Tsao, Peter Boesiger, and Klaas P. Pruessmann. Equi-ripple design of quadratic-phase RF pulses. *Journal of Magnetic Resonance*, 166(1):111–122, 2004.

[9] Meir Shinnar. Reduced power selective excitation radio frequency pulses. *Magnetic Resonance in Medicine*, 32(5):658–660, 1994.

[10] Patrick Le Roux, Raymond J. Gilles, Graeme C. McKinnon, and Pierre G. Carlier. Optimized outer volume suppression for single-shot fast spin-echo cardiac imaging. *Journal of Magnetic Resonance Imaging*, 8(5):1022–1032, 1998.

[11] R. F. Schulte, A. Henning, J. Tsao, P. Boesiger, and K. P. Pruessmann. Design of broadband RF pulses with polynomial-phase response. *Journal of Magnetic Resonance*, 186(2):167–175, 2007.

[12] S. P. Souza, J. Szumowski, C. L. Dumoulin, D. P. Plewes, and G. Glover. Sima: Simultaneous multislice acquisition of MR images by hadamard-encoded excitation. *Journal of Computer Assisted Tomography*, 12(6):1026–1030, 1988.

[13] S. Müller. Multifrequency selective rf pulses for multislice MR imaging. *Magnetic Resonance in Medicine*, 6(3):364–371, 1988.

[14] Gary H. Glover. Phase-offset multiplanar (POMP) volume imaging: A new technique. *Journal of Magnetic Resonance Imaging*, 1(4):457–461, 1991.

[15] David J. Larkman, Joseph V. Hajnal, Amy H. Herlihy, Glyn A. Coutts, Ian R. Young, and Gsta Ehnholm. Use of multicoil arrays for separation of signal from multiple slices simultaneously excited. *Journal of Magnetic Resonance Imaging*, 13(2):313–317, 2001.

[16] Felix A. Breuer, Martin Blaimer, Robin M. Heidemann, Matthias F. Mueller, Mark A. Griswold, and Peter M. Jakob. Controlled aliasing in parallel imaging results in higher acceleration (CAIPIRINHA) for multi-slice imaging. *Magnetic Resonance in Medicine*, 53(3):684–691, 2005.

[17] Felix A. Breuer, Martin Blaimer, Matthias F. Mueller, Nicole Seiberlich, Robin M. Heidemann, Mark A. Griswold, and Peter M. Jakob. Controlled aliasing in volumetric parallel imaging (2D CAIPIRINHA). *Magnetic Resonance in Medicine*, 55(3):549–556, 2006.

[18] R.G. Nunes, J.V. Hajnal, X. Golay, and D.J. Larkman. Simultaneous slice excitation and reconstruction for single shot EPI . *Proc Intl Soc Mag Reson Med*, 14(2):293, 2006.

[19] K. Setsompop, J. Cohen-Adad, B. A. Gagoski, T. Raij, A. Yendiki, B. Keil, V. J. Wedeen, and L. L. Wald. Improving diffusion MRI using simultaneous multi-slice echo planar imaging. *NeuroImage*, 63(1):569–580, 2012.

[20] Benjamin Zahneisen, Thomas Ernst, and Benedikt A. Poser. SENSE and simultaneous multislice imaging. *Magnetic Resonance in Medicine*, 74(5):1356–1362, 2015.

[21] Benjamin Zahneisen, Benedikt A. Poser, Thomas Ernst, and Andrew V. Stenger. Simultaneous Multi-Slice fMRI using spiral trajectories. *NeuroImage*, 92:8–18, 2014.

[22] Stephen F. Cauley, Jonathan R. Polimeni, Himanshu Bhat, Lawrence L. Wald, and Kawin Setsompop. Interslice leakage artifact reduction technique for simultaneous multislice acquisitions. *Magnetic Resonance in Medicine*, 72(1):93–102, 2014.

[23] Kamil Ugurbil, Junqian Xu, Edward J. Auerbach, Steen Moeller, An T. Vu, Julio M. Duarte-Carvajalino, Christophe Lenglet, Xiaoping Wu, Sebastian Schmitter, Pierre Francois Van de Moortele, John Strupp, Guillermo Sapiro, Federico De Martino, Dingxin Wang, Noam Harel, Michael Garwood, Liyong Chen, David A. Feinberg, Stephen M. Smith, Karla L. Miller, Stamatios N. Sotiropoulos, Saad Jbabdi, Jesper L.R. Andersson, Timothy E.J. Behrens, Matthew F. Glasser, David C. Van Essen, and Essa Yacoub. Pushing spatial and temporal resolution for functional and diffusion MRI in the Human Connectome Project. *NeuroImage*, 80:80–104, 2013.

[24] Kawin Setsompop, Qiuyun Fan, Jason Stockmann, Berkin Bilgic, Susie Huang, Stephen F. Cauley, Aapo Nummenmaa, Fuyixue Wang, Yogesh Rathi, Thomas Witzel, and Lawrence L. Wald. High-resolution in vivo diffusion imaging of the human brain with generalized slice dithered enhanced resolution: Simultaneous multislice (gSlider-SMS). *Magnetic Resonance in Medicine*, 79(1):141–151, 2018.

[25] B.A. Gagoski, B. Bilgic, C. Eichner, H. Bhat, P.E. Grant, L.L. Wald, and K. Setsompop. RARE/ Turbo Spin Echo Imaging with Simultaneous MultiSlice Wave-CAIPI. *Magn Reson Med.*, 73(3):929–938, 2015.

[26] Anthony N Price, Lucilio Cordero-Grande, Shaihan J Malik, and Joseph V Hajnal. Accelerated Cine Imaging of the Heart using Blipped Multiband SSFP. *International Society for Magnetic Resonance in Medicine*, page 0631, 2017.

[27] Yi Wang, Xingfeng Shao, Thomas Martin, Steen Moeller, Essa Yacoub, and Danny J.J. Wang. Phase-cycled simultaneous multislice balanced SSFP imaging with CAIPIRINHA for efficient banding reduction. *Magnetic Resonance in Medicine*, 76(6):1764–1774, 2016.

[28] Vanessa Landes, Terrance Jao, and Krishna Nayak. Practical implementation of SMS bSSFP in the Heart. In *Proc. Intl. Soc. Mag. Reson. Med. 26*, pages 18–20, 2018.

[29] Dan Ma, Vikas Gulani, Nicole Seiberlich, Kecheng Liu, Jeffrey L. Sunshine, Jeffrey L. Duerk, and Mark A. Griswold. Magnetic resonance fingerprinting. *Nature*, 495(7440):187–192, 2013.

[30] Huihui Ye, Dan Ma, Yun Jiang, Stephen F. Cauley, Yiping Du, Lawrence L. Wald, Mark A. Griswold, and Kawin Setsompop. Accelerating magnetic resonance fingerprinting (MRF) using t-blipped simultaneous multislice (SMS) acquisition. *Magnetic Resonance in Medicine*, 75(5):2078–2085, 2016.

[31] Huihui Ye, Stephen F. Cauley, Borjan Gagoski, Berkin Bilgic, Dan Ma, Yun Jiang, Yiping P. Du, Mark A. Griswold, Lawrence L. Wald, and Kawin Setsompop. Simultaneous multislice magnetic resonance fingerprinting (SMS-MRF) with direct-spiral slice-GRAPPA (ds-SG) reconstruction. *Magnetic Resonance in Medicine*, 77(5):1966–1974, 2017.

[32] Rahel Heule, Carl Ganter, and Oliver Bieri. Triple echo steady-state (TESS) relaxometry. *Magnetic Resonance in Medicine*, 71(1):230–237, 2014.

[33] Rahel Heule, Zarko Celicanin, Sebastian Kozerke, and Oliver Bieri. Simultaneous multislice triple-echo steady-state (SMS-TESS) T1, T2, PD, and off-resonance mapping in the human brain. *Magnetic Resonance in Medicine*, 80(3):1088–1100, 2018.

[34] Markus Barth, Felix Breuer, Peter J. Koopmans, David G. Norris, and Benedikt A. Poser. Simultaneous multislice (SMS) imaging techniques. *Magnetic Resonance in Medicine*, 75(1):63–81, 2016.

[35] J Hennig. Chemical shift imaging with phase-encoding RF pulses. *Magnetic resonance in medicine : official journal of the Society of Magnetic Resonance in Medicine / Society of Magnetic Resonance in Medicine*, 25(2):289–298, 1992.

[36] Gadi Goelman. Fast 3D T2-weighted MRI with Hadamard encoding in the slice select direction. *Magnetic Resonance Imaging*, 18(8):939–945, 2000.

[37] E Wong. Optimized Phase Schedules for Minimizing Peak RF Power in Simultaneous Multi-Slice RF Excitation Pulses. *Proceedings of the 20th Annual Meeting of ISMRM, Melbourne, Australia*, 20:2209, 2012.

[38] Alessandro Sbrizzi, Benedikt A. Poser, Desmond H.Y. Tse, Hans Hoogduin, Peter R. Luijten, and Cornelis A.T. van den Berg. RF peak power reduction in CAIPIRINHA excitation by interslice phase optimization. *NMR in Biomedicine*, 28(11):1393–1401, 2015.

[39] Edward J. Auerbach, Junqian Xu, Essa Yacoub, Steen Moeller, and Kâmil Ugurbil. Multiband accelerated spin-echo echo planar imaging with reduced peak RF power using time-shifted RF pulses. *Magnetic Resonance in Medicine*, 69(5):1261–1267, 2013.

[40] Michael Lustig, Charles H. Cunningham, and John M Pauly. A Monte Carlo Algorithm for Designing Ultra High Time Bandwidth Minimum Peak B1 Selective Saturation and Inversion RF Pulses. In *Proceedings of the ENC*, 2006.

[41] Jun Ma, Thomas Witzel, William A Grissom, and Kawin Setsompop. Minimum peak power root- flipped gSlider-SMS RF pulses for high-resolution in vivo diffusion imaging. In *Minimum peak power root-flipped gSlider-SMS RF pulses for high-resolution in vivo diffusion imaging*, page 0523, 2017.

[42] Steven Conolly, Dwight Nishimura, Albert Macovski, and Gary Glover. Variable-rate selective excitation. *Journal of Magnetic Resonance (1969)*, 78(3):440–458, 1988.

[43] Brian A. Hargreaves, Charles H. Cunningham, Dwight G. Nishimura, and Steven M. Conolly. Variable-rate selective excitation for rapid MRI sequences. *Magnetic Resonance in Medicine*, 52(3):590–597, 2004.

[44] Michael Lustig, Seung Jean Kim, and John M. Pauly. A fast method for designing time-optimal gradient waveforms for arbitrary k-space trajectories. *IEEE Transactions on Medical Imaging*, 27(6):866–873, 2008.

[45] Daeho Lee, Michael Lustig, William A. Grissom, and John M. Pauly. Time-optimal design for multidimensional and parallel transmit variable-rate selective excitation. *Magnetic Resonance in Medicine*, 61(6):1471–1479, 2009.

[46] William A. Grissom, Kawin Setsompop, Samuel A. Hurley, Jeffrey Tsao, Julia V. Velikina, and Alexey A. Samsonov. Advancing RF pulse design using an open-competition format: Report from the 2015 ISMRM challenge. *Magnetic Resonance in Medicine*, 78(4):1352–1361, 2017.

[47] Naoharu Kobayashi, Kamil Ugurbil, and Xiaoping Wu. Shortening nonlinear phase multiband refocusing pulses with VERSE. In *Proc. Intl. Soc. Mag. Reson. Med. 24*, page 3253, 2016.

[48] David G. Norris, Peter J. Koopmans, Rasim Boyacioglu, and Markus Barth. Power independent of number of slices (PINS) radiofrequency pulses for low-power simultaneous multislice excitation. *Magnetic Resonance in Medicine*, 66(5):1234–1240, 2011.

[49] Ed X. Wu, Christopher W. Towe, and Haiying Tang. MRI cardiac tagging using a sinc-modulated RF pulse train. *Magnetic Resonance in Medicine*, 48(2):389–393, 2002.

[50] Cornelius Eichner, Lawrence L. Wald, and Kawin Setsompop. A low power radiofrequency pulse for simultaneous multislice excitation and refocusing. *Magnetic Resonance in Medicine*, 72(4):949–958, 2014.

[51] Robert Turner. Gradient coil design: A review of methods. *Magnetic Resonance Imaging*, 11(7):903–920, jan 1993.

[52] C. B. Ahn and Z. H. Cho. Analysis of the Eddy-Current Induced Artifacts and the Temporal Compensation in Nuclear Magnetic Resonance Imaging. *IEEE Transactions on Medical Imaging*, 10(1):47–52, 1991.

[53] Michael A. Morich, David A. Lampman, Wayne R. Dannels, and Frederick T D Goldie. Exact Temporal Eddy Current Compensation in Magnetic Resonance Imaging Systems. *IEEE Transactions on Medical Imaging*, 7(3):247–254, 1988.

[54] CH Boesch, R. Gruetter, and E. Martin. Temporal and spatial analysis of fields generated by eddy currents in superconducting magnets: Optimization of corrections and quantitative characterization of magnet/gradient systems. *Magnetic Resonance in Medicine*, 20(2):268–284, 1991.

[55] Q. Liu, D. G. Hughes, and P. S. Allen. Quantitative characterization of the eddy current fields in a 40cm bore superconducting magnet. *Magnetic Resonance in Medicine*, 31(1):73–76, 1994.

[56] Bernd U. Foerster, Dardo Tomasi, and Elisabeth C. Caparelli. Magnetic field shift due to mechanical vibration in functional magnetic resonance imaging. *Magnetic Resonance in Medicine*, 54(5):1261–1267, 2005.

[57] Signe J. Vannesjo, Maximilan Haeberlin, Lars Kasper, Matteo Pavan, Bertram J. Wilm, Christoph Barmet, and Klaas P. Pruessmann. Gradient system characterization by impulse response measurements with a dynamic field camera. *Magnetic Resonance in Medicine*, 69(2):583–593, 2013.

[58] Adrienne E. Campbell-Washburn, Hui Xue, Robert J. Lederman, Anthony Z. Faranesh, and Michael S. Hansen. Real-time distortion correction of spiral and echo planar images using the gradient system impulse response function. *Magnetic Resonance in Medicine*, 75(6):2278–2285, 2016.

[59] Samy Abo Seada, Arian Beqiri, Anthony N Price, J.V. Hajnal, and Shaihan J Malik. Minimum-TR pulse design for rapid gradient echo sequences. In *Proc. Intl. Soc. Mag. Reson. Med. 26*, page 5800, 2018.

[60] C. L G Ham, J. M L Engels, G. T. Van de Wiel, and A. Machielsen. Peripheral nerve stimulation during MRI: Effects of high gradient amplitudes and switching rates. *Journal of Magnetic Resonance Imaging*, 7(5):933–937, 1997.

[61] F. Schmitt, W. Irnich, and H. Fischer. Physiological Side Effects of Fast Gradient Switching. In *Echo-planar Imaging*, pages 201–252. Springer, 1998.

[62] J. Patrick Reilly. Principles of Nerve and Heart Excitation by Time-varying Magnetic Fields. *Annals of the New York Academy of Sciences*, 649(1):96–117, mar 1992.

[63] Werner Irnich and Franz Schmitt. Magnetostimulation in MRI. *Magnetic Resonance in Medicine*, 33(5):619–623, 1995.

[64] Werner Irnich and Franz X. Hebrank. Stimulation threshold comparison of time-varying magnetic pulses with different waveforms. *Journal of Magnetic Resonance Imaging*, 29(1):229–236, 2009.

[65] J. Patrick Reilly, Vanda T. Freeman, and Willard D. Larkin. Sensory Effects of Transient Electrical Stimulation - Evaluation with a Neuroelectric Model. *IEEE Transactions on Biomedical Engineering*, BME-32(12):1001–1011, dec 1985.

[66] P. Mansfield and P. R. Harvey. Limits to neural stimulation in echo-planar imaging. *Magnetic Resonance in Medicine*, 29(6):746–758, 1993.

[67] Blaine A. Chronik and Brian K. Rutt. A comparison between human magnetostimulation thresholds in whole-body and head/neck gradient coils. *Magnetic Resonance in Medicine*, 46(2):386–394, 2001.

[68] Blaine A. Chronik and Brian K. Rutt. Simple linear formulation for magnetostimulation specific to MRI gradient coils. *Magnetic Resonance in Medicine*, 45(5):916–919, 2001.

[69] Mathias Davids, Bastien Guérin, Matthias Malzacher, Lothar R. Schad, and Lawrence L. Wald. Predicting Magnetostimulation Thresholds in the Peripheral Nervous System using Realistic Body Models. *Scientific Reports*, 7(1):1–14, 2017.

[70] Martin Bencsik, Richard Bowtell, and Roger M. Bowley. Using the vector potential in evaluating the likelihood of peripheral nerve stimulation due to switched magnetic field gradients. *Magnetic Resonance in Medicine*, 50(2):405–410, 2003.

[71] Poman P M So, Maria A. Stuchly, and John A. Nyenhuis. Peripheral nerve stimulation by gradient switching fields in magnetic resonance imaging. *IEEE Transactions on Biomedical Engineering*, 51(11):1907–1914, 2004.

[72] Martin Bencsik, Richard Bowtell, and Roger Bowley. Electric fields induced in the human body by time-varying magnetic field gradients in MRI: Numerical calculations and correlation analysis. *Physics in Medicine and Biology*, 52(9):2337–2353, 2007.

[73] P. M. Glover. Interaction of MRI field gradients with the human body. *Physics in Medicine and Biology*, 54(21), 2009.

[74] Franz X. Hebrank and Matthias Gebhardt. SAFE-Model – A new method for predicting peripheral nerve stimulations in MRI. *Proc Intl Soc Mag Reson Med*, 8:2007, 2000.

[75] Franz Hebrank, Matthias Gebhardt, and Helmut Lenz. Method and MR device for simulating electrical simulations in a subject by MR stimulation, 2001.

[76] Jacques A. Den Boer, Joe D. Bourland, John A. Nyenhuis, Cornelis L G Ham, Johan M L Engels, Franz X. Hebrank, Georg Frese, and Daniel J. Schaefer. Comparison of the threshold for peripheral nerve stimulation during gradient switching in whole body MR systems. *Journal of Magnetic Resonance Imaging*, 15(5):520–525, 2002.

[77] Gennaro Evangelista and Heinz G. Gockler. Arbitrary Sampling Rate Conversion of Complex Signals. Technical report, 2002.

[78] Lucilio Cordero-Grande, Emer J. Hughes, Jana Hutter, Anthony N. Price, and Joseph V. Hajnal. Three-dimensional motion corrected sensitivity encoding recon-

struction for multi-shot multi-slice MRI: Application to neonatal brain imaging. *Magnetic Resonance in Medicine*, 79(3):1365–1376, 2018.

[79] Jana Hutter, J. Donald Tournier, Anthony N. Price, Lucilio Cordero-Grande, Emer J. Hughes, Shaihan Malik, Johannes Steinweg, Matteo Bastiani, Stamatios N. Sotiropoulos, Saad Jbabdi, Jesper Andersson, A. David Edwards, and Joseph V. Hajnal. Time-efficient and flexible design of optimized multishell HARDI diffusion. *Magnetic Resonance in Medicine*, 79(3):1276–1292, 2018.

[80] C. Yao, L. Shen, J. Wu, and M. Kritzer. Parallel Multi-slice Imaging with Limited Peak RF Power. In *Proceedings of the 12th Annual Meeting of SMRM*, page 427, 1993.

[81] Samy Abo Seada, Anthony N. Price, Joseph V. Hajnal, and Shaihan J. Malik. Optimized amplitude modulated multiband RF pulse design. *Magnetic Resonance in Medicine*, 78(6):2185–2193, 2017.

[82] Janaka P. Wansapura, Scott K. Holland, R. Scott Dunn, and William S. Ball. NMR relaxation times in the human brain at 3.0 Tesla. *Journal of Magnetic Resonance Imaging*, 9(4):531–538, 1999.

[83] David A. Feinberg, Alexander Beckett, and Liyong Chen. Arterial spin labeling with simultaneous multi-slice echo planar imaging. *Magnetic Resonance in Medicine*, 70(6):1500–1506, 2013.

[84] Armin Rund, Christoph Stefan Aigner, Karl Kunisch, and Rudolf Stollberger. Magnetic Resonance RF Pulse Design by Optimal Control with Physical Constraints. *IEEE Transactions on Medical Imaging*, 37(2):461–472, 2018.

[85] Christoph Stefan Aigner, Christian Clason, Armin Rund, and Rudolf Stollberger. Efficient high-resolution RF pulse design applied to simultaneous multi-slice excitation. *Journal of Magnetic Resonance*, 263:33–44, 2016.

[86] Shaihan J. Malik, Shiva Keihaninejad, Alexander Hammers, and Joseph V. Hajnal. Tailored excitation in 3D with spiral nonselective (SPINS) RF pulses. *Magnetic Resonance in Medicine*, 67(5):1303–1315, 2012.

[87] Samy Abo Seada, Joseph V Hajnal, and Shaihan J Malik. A simple optimisation approach to making time efficient VERSE-multiband pulses feasible on non-ideal gradients. *Proc. Intl. Soc. Mag. Reson. Med. 25*, page 5049, 2017.

[88] Daeho Lee, William A. Grissom, Michael Lustig, Adam B. Kerr, Pascal P. Stang, and John M. Pauly. VERSE-guided numerical RF pulse design: A fast method for peak RF power control. *Magnetic Resonance in Medicine*, 67(2):353–362, 2012.

[89] Klaus Scheffler and Stefan Lehnhardt. Principles and applications of balanced SSFP techniques. *European Radiology*, 13(11):2409–2418, 2003.

[90] Mitsue Miyazaki and Vivian S. Lee. Nonenhanced MR Angiography. *Radiology*, 248(1):20–43, 2008.

[91] Peter A. Hardy, Michael P. Recht, David Piraino, and David Thomasson. Optimization of a Dual Echo in the Steady State (DESS) free-precession sequence for imaging cartilage. *Journal of Magnetic Resonance Imaging*, 6(2):329–335, 1996.

[92] Michael Schär, Sebastian Kozerke, Stefan E. Fischer, and Peter Boesiger. Cardiac SSFP Imaging at 3 Tesla. *Magnetic Resonance in Medicine*, 51(4):799–806, 2004.

[93] Subashini Srinivasan and Daniel B. Ennis. Optimal flip angle for high contrast balanced SSFP cardiac cine imaging. *Magnetic Resonance in Medicine*, 73(3):1095–1103, 2015.

[94] William A. Grissom, Graeme C. McKinnon, and Mika W. Vogel. Nonuniform and multidimensional Shinnar-Le Roux RF pulse design method. *Magnetic Resonance in Medicine*, 68(3):690–702, 2012.

[95] Armin Rund, Christoph Stefan Aigner, Karl Kunisch, and Rudolf Stollberger. Simultaneous multislice refocusing via time optimal control. *Magnetic Resonance in Medicine*, 80(4):1416–1428, oct 2018.

[96] Sebastian Schmitter, Michael Bock, Sören Johst, Edward J. Auerbach, Kâmil Ugurbil, and Pierre François Van De Moortele. Contrast enhancement in TOF cerebral angiography at 7 T using saturation and MT pulses under SAR constraints: Impact of verse and sparse pulses. *Magnetic Resonance in Medicine*, 68(1):188–197, 2012.

[97] J Abart, K Eberhardt, H Fischer, W Huk, E Richter, F Schmitt, T Storch, B Tomandl, and E Zeitler. Peripheral nerve stimulation by time-varying magnetic fields. *Journal of computer assisted tomography*, 21(4):532–538, 1997.

[98] Subashini Srinivasan and Daniel B. Ennis. Variable flip angle balanced steady-state free precession for lower SAR or higher contrast cardiac cine imaging. *Magnetic Resonance in Medicine*, 71(3):1035–1043, 2014.

[99] Oliver J. Gurney-Champion, Aart J. Nederveen, Remy Klaassen, Marc R. Engelbrecht, Arjan Bel, Hanneke W.M. Van Laarhoven, Jaap Stoker, and Sonia I. Goncalves. Revisiting the potential of alternating repetition time balanced steady-state free precession imaging of the abdomen at 3 T. *Investigative Radiology*, 51(9):560–568, 2016.

[100] Krishna S. Nayak, Hsu Lei Lee, Brian A. Hargreaves, and Bob S. Hu. Wideband SSFP: Alternating repetition time balanced steady state free precession with increased band spacing. *Magnetic Resonance in Medicine*, 58(5):931–938, 2007.

[101] Sun Hao, Jeffrey A. Fessler, Douglas C. Noll, and Jon Fredrik Nielsen. Joint design of excitation k-space trajectory and RF pulse for small-tip 3D tailored excitation in MRI. *IEEE Transactions on Medical Imaging*, 35(2):468–479, 2016.

[102] Christoph Stefan Aigner, Armin Rund, Samy Abo Seada, Shaihan Malik, Joseph V Hajnal, and Karl Kunisch. Time-optimal control based RF pulse design under gradient imperfections. *Proc. Intl. Soc. Mag. Reson. Med. 26*, page 219, 2018.

[103] Haifeng Wang, Leo K. Tam, R. Todd Constable, and Gigi Galiana. Fast rotary non-linear spatial acquisition (FRONSAC) imaging. *Magnetic Resonance in Medicine*, 75(3):1154–1165, 2016.

[104] Kerstin Hammernik, Teresa Klatzer, Erich Kobler, Michael P. Recht, Daniel K. Sodickson, Thomas Pock, and Florian Knoll. Learning a variational network for reconstruction of accelerated MRI data. *Magnetic Resonance in Medicine*, 79(6):3055–3071, jun 2018.

[105] David G. Norris, Rasim Boyacioglu, Jenni Schulz, Markus Barth, and Peter J. Koopmans. Application of PINS radiofrequency pulses to reduce power deposition in RARE/turbo spin echo imaging of the human head. *Magnetic Resonance in Medicine*, 71(1):44–49, 2014.

[106] Berkin Bilgic, Borjan A. Gagoski, Stephen F. Cauley, Audrey P. Fan, Jonathan R. Polimeni, P. Ellen Grant, Lawrence L. Wald, and Kawin Setsompop. Wave-CAIPI for highly accelerated 3D imaging. *Magnetic Resonance in Medicine*, 73(6):2152–2162, 2015.

[107] Reed F. Busse, Hari Hariharan, Anthony Vu, and Jean H. Brittain. Fast spin echo sequences with very long echo trains: Design of variable refocusing flip angle schedules and generation of clinical T2 contrast. *Magnetic Resonance in Medicine*, 55(5):1030–1037, 2006.

[108] Reed F. Busse, Anja C.S. Brau, Anthony Vu, Charles R. Michelich, Ersin Bayram, Richard Kijowski, Scott B. Reeder, and Howard A. Rowley. Effects of refocusing flip angle modulation and view ordering in 3D fast spin echo. *Magnetic Resonance in Medicine*, 60(3):640–649, 2008.

[109] Koichi Oshio and David A. Feinberg. GRASE (Gradient-and Spin-Echo) imaging: A novel fast MRI technique. *Magnetic Resonance in Medicine*, 20(2):344–349, 1991.